Fat Unsaturation Quantification, Including ω-3 Measures, with *In-Vivo* Magnetic Resonance Spectroscopy

By

Clara Jodie Michele Fallone

A thesis submitted in partial fulfillment of the requirements for the degree of

Doctor of Philosophy

In

Medical Physics

Department of Oncology

University of Alberta

Abstract

Fat composition is relevant to disease and can be assessed non-invasively using Magnetic Resonance Spectroscopy (MRS). MRS studies do not usually account for the ω-3 (omega-3) fat content because of its low prevalence in human adipose tissue (≈ 1 %) and because the ω-3 (≈ 1.0 ppm) and non-ω-3 (≈ 0.9 ppm) methyl proton signals overlap at field strengths even as high as 9.4 T (Tesla). However, ω-3 fat content is altered in disease; therefore, there is motivation to quantify it non-invasively. Fat unsaturation can be estimated with MRS *in vivo* using the olefinic resonance (≈ 5.4 ppm). The thesis objectives are to enable relative ω-3 fat quantification at 9.4 T and 3 T and to enhance aspects of relative fat unsaturation assessment at 3 T.

High field strengths including 9.4 T have been used to investigate animal fat composition. When employing standard short TE (echo time) *in-vivo* MRS pulse sequences, the ω-3 and non-ω-3 methyl resonances overlap at 9.4 T, rendering relative ω-3 fat quantification challenging. The presented research uses product operator formalism to establish a PRESS (Point RESolved Spectroscopy) TE of 109 ms that separately quantifies the two methyl resonances at 9.4 T (the TE minimized signal from the side peaks of the methyl triplets). The optimized method measured relative differences in ω-3 fat content in abdominal tissue of mice fed varying amounts of ω-3 fat. A coefficient of determination (R^2) of 0.96 was calculated when assessing MRS results against the content measured with gas chromatography of excised mouse tissue.

Relative ω-3 fat quantification was also investigated at the clinical field strength of 3 T. The more weakly-coupled ω-3 methyl triplet includes side peaks that vary sinusoidally with TE. The response of the methyl resonances as a function of PRESS and STEAM (STimulated Echo

Acquisition Mode, TM (mixing time) of 20 ms) TE was investigated. It was found that a TE of 160 ms with both sequences yields ω-3 methyl side peaks that are positive in-phase and broaden the collective methyl linewidth, correlating methyl linewidth to relative ω-3 fat content in oil phantoms. The optimized methods yielded R^2 values ≥ 0.9 when comparing to the expected oil compositions obtained using 16.5 T high field NMR.

In addition, using MRS to quantify relative levels of fat unsaturation at 3 T *in vivo* was explored. PRESS (TE = 180 ms) and STEAM (TE = 120 ms, TM = 20 ms) yielded olefinic to methyl ratios that differed by 0.2 % and -1.8 %, respectively, from literature-obtained values for tibial bone marrow. The optimal timings depend on combined effects from J-coupling evolution and T_2 relaxation. Apparent (including J-coupling effects) T_2 relaxation times in several subjects were investigated in tibial bone marrow, subcutaneous and breast adipose tissue, to assess if the determined TE values in tibial bone marrow can be used to compare fat unsaturation measurements in the anatomical regions without applying correction factors for T_2 relaxation. Olefinic proton T_2 relaxation times were significantly higher in tibial bone marrow than in breast adipose. Fat unsaturation measures in the three tissues were also measured using olefinic to methylene (1.3 ppm) ratios. Fat unsaturation measures in breast have not been explored extensively. This thesis examined the use of an inversion recovery pulse prior to a PRESS sequence (delay = 613 ms, TE = 40 ms) for minimizing water contamination of the olefinic resonance when using a short TE. The technique yielded 5.9 times higher olefinic signal to noise ratio compared to using the previously determined long-TE of 200 ms, which relies on water T_2 relaxation to resolve the olefinic resonance.

Often, the glycerol CH (≈ 5.2 ppm) resonance contribution to that of the olefinic is ignored. This research estimates glycerol contaminations of ≈ 13 % for PRESS with a TE of 40

ms and ≈ 20 % for STEAM with a TE of 20 ms (TM = 20 ms) at 3 T. Furthermore, the response of the glycerol proton to PRESS and STEAM TE was studied to determine that PRESS with a TE of 200 ms and STEAM with a TE of 90 ms (TM = 20ms) minimizes the glycerol resonance area. The technique efficacies were verified on tibial bone marrow *in vivo.*

Preface

A version of Chapter 3 of the thesis has been published in *NMR in Biomedicine*:

Fallone, C.J., Tessier, A.G., Field, C.J. and Yahya, A. (2021). Resolving the ω-3 methyl resonance with long echo time magnetic resonance spectroscopy in mouse adipose tissue at 9.4 T. NMR Biomed 34: e4455 (11 pages).

A version of Chapter 4 of the thesis has been published in the *Journal of Magnetic Resonance Imaging*:

Fallone, C.J., McKay, R.T. and Yahya, A. (2018). Long TE STEAM and PRESS for estimating fat olefinic/methyl ratios and relative ω-3 fat content at 3T. J Magn Reson Imaging 48: 169-177.

A version of Chapter 5 of the thesis has been submitted for publication:

Fallone, C.J., Tessier, A.G. and Yahya, A. Apparent T_2 relaxation times and fat unsaturation measurements in breast, tibial, and subcutaneous adipose tissue at 3 T.

A version of Chapter 6 of the thesis has been published in the journal *Biomedical Physics and Engineering Express:*

Fallone, C.J. and Yahya, A. (2019). Effect of triglyceride glycerol CH signal on olefinic resonance quantification with proton magnetic resonance spectroscopy at 3 T. Biomed Phys Eng Express 5: 027004 (10 pages).

I, Clara J. Fallone, under the supervision of Dr. Yahya, contributed to the formation of the projects. I was responsible for project outputs, for obtaining all research data, completing all

data analysis, and writing the published or submitted manuscripts. Dr. Ryan T. McKay performed the 16.5 T NMR experiments and contributed to the methods concerning 16.5 T NMR in Chapter 4. Mr. A.G. Tessier was involved in planning and conducting the animal experiments at 9.4 T (Chapter 3). In addition, he helped with LCModel analysis in Chapters 3 and 5 and participated in manuscript review for those chapters. Dr. Catherine J. Field (and her laboratory) provided the designed animal diets and performed the excised tissue gas chromatography and its analysis. In addition, she contributed to the gas chromatography methods and manuscript review for Chapter 3. As my supervisor and the principal investigator, Dr. A. Yahya oversaw project development and the experimental procedures. She was also an integral part of all manuscript review and editing.

The research projects at 3 T involved healthy volunteers with ethics approval from the Health Research Ethics Board of Alberta Cancer Committee under the following protocol:

"Pulse Sequence Development on 3 T Magnetic Resonance Imaging/Spectroscopy", HREBA.CC-17-0478_REN3, October 30, 2017, which was based on a previous protocol administered by the Alberta Cancer Board:

"Pulse Sequence Development on 3 T Magnetic Resonance Imaging/Spectroscopy", ETH 22307 NCT00309504, March 2006.

The research project at 9.4 T was granted ethics approval from the Animal Care Committee at the Cross Cancer Institute under the following protocol:

"Nuclear Magnetic Resonance Spectroscopy Techniques for Fat Assessment in Rat and Mouse at 9.4 T", AC 18244, August 10, 2018

Acknowledgements

Most importantly, this work could not have been completed without my supervisor, Dr. Atiyah Yahya. She has been more supportive, knowledgeable, ambitious, and patient than I could have envisioned and no words can express my appreciation for her guidance on this graduate journey. I hope to someday emulate the expertise, fellowship, and mentorship that Dr. Yahya has graciously given me to others.

I extend my gratitude to the valued members of my supervisory committee, including Dr. Alan Wilman, Dr. Jonathan Sharp and Dr. Boguslaw Tomanek. The knowledge, and constructive criticism provided throughout my graduate studies have consistently driven me to complete stronger and more valuable research and to challenge the boundaries of my knowledge. My gratitude also extends to Dr. Warkentin and Dr. Rathee for being a part of my candidacy examination, and to Dr. Théberge and Dr. Mazurak for being a part of my PhD defense. Thank you to Dr. Underhill for chairing these important events and for being supportive of my studies and ambitions throughout graduate school.

I would like to thank all of the students, trainees, and office-mates I have had the opportunity to interact with throughout the years, including Brennen, Ray, Amanda, Gowan, Hongwei, Braden, Aaron, Radim, Neil, Andrei, Hali, Simon, Brie, Brian, Cam, Bryson, Niri, Michael, Eugene, Devin, Tania, Dylan, Simon, JD, Shima, Oleks, Mark, and Chris. You have made my experience as a graduate student fun and engaging with physics discussions, board games, and support, and I am very excited to see what you will all achieve in the years to come.

I would also like to thank the number of agencies and donors that provided graduate student funding, including the Natural Sciences and Engineering Research Council of Canada (NSERC), the Canadian Federation of University Women, the Jugdutt family, Cathy and Harold Roozen, and the Alberta Government and University of Alberta for numerous scholarships and awards. My gratitude also extends to NSERC and the Canadian Breast Cancer Foundation for grant funding for my supervisor's research program, which includes the work of this thesis.

I would like to thank all the staff at the Cross Cancer Institute, especially Mrs. Debbi Howorko, Mrs. Jocelyn Martin, Ms. Brenda Sheen, Ms. Tara Schuetz-Zawaduk, Ms. Mary Burns, and Ms. Yvette Labiuk for always being on top of everything administrative and award-related, Mrs. Heather Warkentin for her insightful clinical mentorship, Mr. Ernie Mah and Mr. Praful Shrestha for their countless help with IT issues, Mr. Anthony Tessier for his patience and help with the 9.4 T, and the vivarium staff, especially Mr. Dan McGinn, for their commitment to my project. Many thanks also go to Mr. Lance Spiridon in the mechanical shop, who has always been open to improving coil designs for my project and has consistently shared excellent ideas. Thank you also to Dr. Slava Volotovskyy for repairing a broken coil and always being willing to share your expertise. I would also like to thank Dr. Catherine Field and Mrs. Susan Goruk, from the Department of Agricultural, Food, and Nutritional Sciences, and Dr. Ryan McKay from the Chemistry Department, for their collaboration in some of my research projects.

Lastly, I would like to thank my family, who has always supported me in my goals and ambitions to pursue higher education. From a young age, my parents Angie and Gino enabled me to understand the value of education, encouraged me to challenge myself, and thought me the importance of devotion to one's goals, inside and outside of academia. My sister Alexia has always stood by me and provided unconditional support and love from her family. My brother Joey-Michael has never said no to discussing a mathematical or computer problem with me and has always been a wise audience and advisor. I would also like to thank my best friend Roopa, for believing in me and giving me confidence to push beyond my own expectations.

Table of Contents

List of Tables

Chapter 1: Introduction

Chapter 3: Resolving the ω-3 Methyl Resonance with Long Echo Time Magnetic Resonance Spectroscopy in Mouse Adipose Tissue at 9.4 T

Chapter 4: Long TE STEAM and PRESS for Estimating Fat Olefinic/Methyl Ratios and Relative ω-3 Fat Content at 3 T

Chapter 5: Apparent T_2 Relaxation Times and Fat Unsaturation Measurements in Breast, Tibial, and Subcutaneous Adipose Tissue at 3 T

Chapter 6: Effect of Triglyceride Glycerol CH Signal on Olefinic Resonance Quantification with Proton Magnetic Resonance Spectroscopy at 3 T

List of Figures

Chapter 1: Introduction

Chapter 2: Background Information, Methods, and Procedures

Chapter 3: Resolving the ω-3 Methyl Resonance with Long Echo Time Magnetic Resonance Spectroscopy in Mouse Adipose Tissue at 9.4 T

Chapter 4: Long TE STEAM and PRESS for Estimating Fat Olefinic/Methyl Ratios and Relative ω-3 Fat Content at 3 T

Chapter 5: Apparent T_2 Relaxation Times and Fat Unsaturation Measurements in Breast, Tibial, and Subcutaneous Adipose Tissue at 3 T

Chapter 6: Effect of Triglyceride Glycerol CH Signal on Olefinic Resonance Quantification with Proton Magnetic Resonance Spectroscopy at 3 T

List of Abbreviations

BW: Bandwidth

EMF: Electromotive force

FWHM: full width at half max (linewidth)

IR: Inversion Recovery

MRI: Magnetic Resonance Imaging

MRS: Magnetic Resonance Spectroscopy

NMR: Nuclear Magnetic Resonance

PRESS: Point RESolved Spectroscopy

RF: Radio-frequency

STEAM: STimulated Echo Acquisition Mode

T: Tesla

TE: Echo Time

TFE: Turbo Field Echo

TI: Inversion delay time

TM: Mixing Time

TR: Repetition Time

TSE: Turbo Spin Echo

ω: omega

Chapter 1

Introduction

1.1 Thesis Introduction

1.1.1 Hypothesis

Fat composition assessments, including ω-3 measures, with Magnetic Resonance Spectroscopy (MRS) at 9.4 T and at 3 T can be improved using spectral editing techniques.

1.1.2 Introduction to Magnetic Resonance Spectroscopy (MRS)

The concept of Nuclear Magnetic Resonance (NMR) describes how nuclei in a strong constant magnetic field ($\overrightarrow{B_o}$) are perturbed by a perpendicular oscillating magnetic field ($\overrightarrow{B_1}$), producing an electromagnetic signal with a characteristic frequency. The surrounding electronic molecular environment determines the chemical shift of the nucleus and its J-coupling interactions. The NMR phenomenon is used in MRS and MRI (Magnetic Resonance Imaging). MRS is similar to the more-widely known MRI, which provides an anatomical image non-invasively. Instead of providing an image, MRS yields information about molecular composition and metabolite quantification. This thesis exclusively conducts MRS of the ^{1}H nucleus. Since the hydrogen nucleus consists of a single proton, MRS of the ^{1}H nucleus is often referred to as proton MRS. The chemical shift effect leads to peaks at specific resonant frequencies for different ^{1}H protons in fatty acids, enabling their relative quantification with MRS.

1.1.3 Summary of MRS in Fat Composition Studies

Adipose tissue fat composition is relevant to the study of a number of diseases, including diabetes and obesity [1,2], breast cancer [3-6], liver disease [7,8], osteoporosis [9-11], and response to treatment for some cancers [12]. Adipose tissue *in vivo* is composed of ≈ 28% saturated fatty acids (primarily palmitic acid, no carbon-to-carbon double bonds), ≈ 51 % monounsaturated fatty acids (primarily oleic acid, one carbon-to-carbon double bond), ≈ 14 % di-unsaturated fatty acids (primarily linoleic acid, two carbon-to-carbon double bonds), and ≈ 1% tri-unsaturated fatty acids (three carbon-to-carbon double bonds) [13-16], most of which is the ω-3 fat α-linolenic acid (hereon referred to as linolenic acid). The ω-3 indicates that the first carbon-to-carbon double

bond in the fatty acid is on the third carbon from the methyl (CH_3) end of the fatty acid. Additional ω-3 fatty acids that are more unsaturated (docosahexaenoic acid and eicosapentaenoic acid) form less than 0.5 % of the total fatty acid content [14]. Proton MRS is a non-invasive method that facilitates fat composition measurements in humans *in vivo* [1,2,6,8,16-25]. The method provides a safer and non-invasive potential substitute to biopsies. The olefinic peak (≈ 5.4 ppm) is proportional to total unsaturation levels [17,22]. The allylic resonance (≈ 2.0 ppm) can also be used as a measure of total fat unsaturation if it is well-resolved [24]. The diallylic peak (≈ 2.8 ppm) is relevant because it denotes poly-unsaturation levels (fatty acid chains with more than one carbon-to-carbon double bond) [16]. The methylene (1.3 ppm) and methyl resonances (≈ 0.8 – 1.0 ppm) can be used as normalization factors [1,17,19,20,22,26,27]. *In-vivo* quantification is limited by the fact that some fat peaks overlap others, making their quantification difficult. For example, the ω-3 methyl resonance (≈ 1.0 ppm) cannot be adequately resolved from the non-ω-3 methyl resonance (≈ 0.8- 0.9 ppm) using standard MRS techniques, even at high field strengths [23]. Quantifying ω-3 fat levels is further impeded because ω-3 fat levels are typically only ≈ 1 % *in vivo* [13]. An additional challenge is that the water peak (≈ 4.7 ppm) overlaps that of the olefinic in tissues which contain both water and fat [17,18,26,27]. All fatty acid protons exhibit J-coupling interactions with neighboring protons; therefore, their response to MRS pulse sequences is further complicated [28]. Spectral editing can be used to improve spectral resolution of certain peaks, resolve overlapped peaks and optimize relative fat composition measures. Spectral editing methods exploit differences in J-coupling evolution of protons of interest and their overlapping proton resonances. MRS pulse sequences can be optimized such that J-coupling evolution yields prominent signal from a proton of interest and reduced signal from contaminating protons. One way of achieving this effect is to optimize the echo time (TE) of common MRS pulse sequences such as PRESS (Point RESolved Spectroscopy)[29] or STEAM (STimulated Echo Acquisition Mode) [30]. These sequences are both often used in *in-vivo* fat spectroscopy and are single voxel, single-shot sequences. This thesis explores the spectral editing method of optimizing pulse sequence TE values to improve quantification of fat methyl resonances (at 3 T and 9.4 T) and the olefinic resonance (at 3 T).

1.1.4 High Field Strength Fat MRS Animal Research

Higher magnetic field strengths are typically exploited in animal studies because of their enhanced spectral resolution. The higher spectral resolution results from increased frequency separation between peaks. Higher magnetic fields also yield improved SNR (signal to noise ratio) because SNR increases about linearly with field strength [31,32]. Several studies have used high field strengths to study fat composition in animals [33-37], and some research was done in humans at 7 T [23,24,38].

High field strength fat composition models have been developed for quantifying saturated, mono-unsaturated and di-unsaturated fatty acids in animals [33,36,38,39]; however, these studies still neglect or assume constant or negligible levels of ω-3 fatty acids (mostly tri-unsaturated fatty acids) [33,36,39], likely because of the low concentration of ω-3 fatty acids [13]. Furthermore, even at high field strengths, the ω-3 methyl resonance cannot be sufficiently resolved from that of the non-ω-3 using standard short-TE techniques. A study recently used PRESS with an ultra-long TE (1000 ms) to resolve the ω-3 methyl resonance [23]. The method exploited the shorter T_2 relaxation times of the methylene and non-ω-3 methyl resonances compared to the ω-3 methyl resonance.

1.1.5 Clinical Field Strength Fat MRS Human Research

Fatty acid composition quantification generally neglects the ω-3 fatty acid content [35,38,41]. It has been shown, however, that low levels of linolenic acid (an ω-3 fat) content in breast tissue correspond to increased breast cancer risk [40]. A study at 1.5 T used a long TE (540 ms) [41] and a study at 3 T used spectral editing to assess relative ω-3 fat content [42]. Research on breast cancer patients and healthy women revealed that a smaller methyl resonance linewidth from breast at 1.5 T is linked to women who are at a higher risk of breast cancer [43]. A larger methyl resonance linewidth is proposed to be an indication of a more varied group of methyl protons [43] and may correspond to differences in ω-3 fatty acid content (primarily linolenic acid).

Various MRS spectral peak areas have been used to quantify fat unsaturation *in-vivo* at clinical field strengths [1,17,20,22,25-27,41]. For instance, short TE PRESS and STEAM pulse

sequences have been used to quantify the olefinic (5.4 ppm resonant frequency) signal ratio as a measure of total fat unsaturation [1,10,25]. In tissues where water is present (for example, in spinal bone marrow, breast, and liver) the water resonance (≈ 4.7 ppm) obscures the olefinic resonance signal. Long-TE pulse sequences have been optimized to address the issue since the water signal decays by T_2 relaxation more quickly than the fat olefinic signal [18,26,27]. A long TE also offers better spectral resolution of methyl and methylene resonances [44], yielding more representative results [17,20]. Previous studies presented that olefinic to methylene (≈ 1.3 ppm) peak area ratios measured using PRESS with a TE of 200 ms [17,18,20,27] and STEAM with a TE of 100 ms [26] are representative of relative levels of fat unsaturation at 3 T. In addition to using olefinic to methylene area ratios as a measure of fat unsaturation, the methyl resonance is a practical normalization factor because every fatty acid has one methyl group regardless of chain length or degree of unsaturation [1]. Previous research made use of olefinic to methyl areas to assess the fat composition of rat tissue extracts with a 500 MHz system [45]. Optimized long-TE pulse sequences have not been previously determined for estimating olefinic to methyl ratios.

An additional challenge with fat unsaturation measures at clinical field strength is the glycerol proton signal contaminating (≈ 5.2 ppm) that of the olefinic [6,46-48]. The glycerol proton exists on the glycerol backbone to which the fatty acids are bound to as triglycerides. The contamination affects relative fat unsaturation assessments to different extents depending on the TE used.

1.1.6 Thesis Objectives

The overall objective of this thesis work is to develop MRS techniques to improve fat unsaturation assessment. Relative measures of ω-3 fat content at 9.4 T and 3 T are enabled, and *in-vivo* relative fat unsaturation assessment at 3 T is improved or facilitated.

The first objective was to determine a PRESS TE to quantify relative ω-3 fat content at 9.4 T, a high field strength that is often used for animal studies (Chapter 3). Product operator formalism was used to find TE values that best separated the two methyl resonances. Since both groups of methyl protons are weakly-coupled at 9.4 T, they exhibit a

triplet pattern that includes sinusoidally varying side peaks. Certain TE values yield zero in-phase signal of the side multiplets, improving the resolution of the ω-3 and non-ω-3 methyl central peaks. The method was verified *in vivo* in abdominal visceral fat of mice fed diets differing in ω-3 fat content. Previous high-field strength MRS studies neglected contributions from ω-3 fats [34,39]. In the study at 7 T that investigated ω-3 fat contributions, variations in ω-3 fat due to diet were not explored; furthermore, the ultra-long TE of 1000 ms yields sizable T_2 decay [23].

The second objective was to investigate the response of methyl protons at 3 T to STEAM and PRESS to optimize relative ω-3 fat quantification and olefinic to methyl measures for relative fat unsaturation assessment (Chapter 4). PRESS and STEAM TE values that enable quantifying relative levels of fat ω-3 content (mainly linolenic acid) in oil phantoms were determined by correlating the methyl linewidth to ω-3 fatty acid content. Previous work at clinical field strength either employed an ultra long TE (540 ms) [41] or multiple spectral acquisitions [42] to detect ω-3 fat content *in vivo*. Long TE STEAM and PRESS sequences were also optimized to yield olefinic/methyl ratios that agree most closely to ratios obtained with high resolution 16.5 T NMR for 9 edible oils, and literature composition for tibial bone marrow. The PRESS sequence has been previously optimized for olefinic to methylene ratio measures in tibial bone marrow [27]. The optimal timings determined in the previous work and in this work are based on both J-coupling interactions and T_2 relaxation times. J-coupling interactions are the same in different tissues; but T_2 relaxation times can differ [49]. Correcting for T_2 decay is essential if comparing ratios obtained in different tissues with varying T_2 relaxation times.

The third objective of this work was to compare apparent T_2 relaxation times (the term apparent is used because J-coupling evolution affects the T_2 relaxation time measured [17,24,36,41,50]) and fat unsaturation measures in tibial bone marrow, subcutaneous and breast adipose tissue (Chapter 5). Assessing apparent T_2 relaxation times will determine if comparisons of fat unsaturation can be made among the three anatomical regions without the need for correcting for T_2 differences. Determining differences in fat unsaturation levels in different anatomical regions can lead to insights about the role of fatty acids in human pathology [22]. Since fat unsaturation measures in breast have not been explored extensively in the literature,

an inversion recovery (IR) method was examined for olefinic peak quantification in breast with short TE.

The fourth objective of this work was to characterize the contamination of the olefinic signal from that of the glycerol proton, which is inherent at clinical field strengths and can impact fat unsaturation measurements (Chapter 6). Since edible oils and adipose tissue *in vivo* are primarily triglycerides [51,52], the glycerol proton signal (≈ 5.2 ppm) contaminates the olefinic proton signal [46-48,53]. The same overlap occurs in human adipose tissue due to the way fats are stored and metabolized; fatty acids are stored as triglycerides in fat depots and converted to free fatty acids that are released into the blood stream for energy [54-56]. The fatty acid tricaprylin was utilized in this study to characterize the behaviour of the glycerol proton because it is a pure, saturated triglyceride containing only glycerol protons and no olefinic protons. Similarly, the free fatty acid oleic acid was used to characterize the behaviour of the olefinic resonance because it does not contain any glycerol protons and only has olefinic protons. Utilizing these two phantoms permitted studying the impact of the glycerol contamination on the olefinic proton signal and enabled determining TE values for both PRESS and STEAM which minimized the glycerol signal.

1.1.7 Thesis Composition

The thesis consists of seven chapters. The remainder of Chapter 1 describes MRS concepts, including the physics of NMR, the MRS experiment, localization, relaxation, spectral acquisition, spin echoes, stimulated echoes, and relevant MRS parameters. Chapter 1 also includes information about pulse sequences (PRESS, STEAM, and IR), chemical shift, peak quantification, product operator formalism, and J-coupling and its evolution during PRESS and STEAM. The benefits and disadvantages of high field MRS are also briefly covered. Chapter 2 presents information on fatty acids and their quantification, including relevant coupling interactions. It also explains how product operator formalism was used to calculate timings which resolve the ω-3 and non-ω-3 methyl resonances at 9.4 T. Chapter 2 also outlines general MR hardware, and the experimental hardware and methods for phantom (9.4 T and 3 T), animal (9.4 T), and human experiments (3 T). Data analysis with LCModel peak fitting software is also

reviewed. The methodology used for the 16.5 T NMR scans to verify phantom oil composition is also outlined. Chapter 3 (published in *NMR in Biomedicine,* 2021) presents the research at 9.4 T on resolving the ω-3 from the non-ω-3 methyl resonance in mice for relative ω-3 fat quantification. The chapter outlines the methods to optimize the PRESS TE and demonstrates the efficacy of the sequence on oils with different ω-3 content and on mice that were fed diets with varying amounts of ω-3. Chapter 4 (published in *Journal of Magnetic Resonance Imaging*, 2018) explains the research on exploiting differences in J-coupling evolution between ω-3 and non-ω-3 methyl protons at 3 T to correlate the combined methyl linewidth to the relative ω-3 fat content. The efficacy of the PRESS and STEAM optimized TE values are verified on oils with different ω-3 content. Chapter 4 also presents the optimization of PRESS and STEAM TE values for olefinic to methyl ratio quantification in tibial bone marrow. Chapter 5 (submitted for publication) details the work on comparing apparent T_2 relaxation times in tibial bone marrow, subcutaneous and breast adipose tissue at 3 T, to evaluate if previously optimized TE values for fat unsaturation measures in tibial bone marrow can be used to make intra-individual comparisons with other tissues without the need for T_2 correction. Chapter 5 also investigates intra-individual variability of fat unsaturation and poly-unsaturation measures in the different adipose tissue depots. Since techniques for fat unsaturation measures have not been investigated extensively in breast, the IR method is explored as an alternative to a long TE for fat unsaturation measures in tissues with fat and water. Chapter 6 (published in *Biomedical Physics and Engineering Express*, 2019) demonstrates how tricaprylin (a saturated triglyceride) and oleic acid (a mono-unsaturated free fatty acid) were employed to characterize the independent behaviour of the glycerol protons and olefinic protons, respectively. PRESS and STEAM TE values which minimized the glycerol proton signal while providing adequate olefinic proton signal were reported as optimal for olefinic quantification. Furthermore, the expected contamination of the glycerol resonance on the olefinic resonance was estimated for PRESS and STEAM sequences with short TE. Conclusions of the research are summarized in Chapter 7.

1.2 Nuclear Magnetic Resonance (NMR) Physics

1.2.1 Spin and Magnetic Moments in NMR

Atomic nuclei are composed of combinations of protons and neutrons; these are responsible for spin and magnetic moments [57]. Spin is a quantized intrinsic angular momentum that is mathematically given by:

$$I = \frac{n}{2} \tag{1.1}$$

where n is a positive integer (or zero) [57]. From quantum theory, the spin number follows precise rules [57]. If the nuclei have even numbers of both protons and neutrons, then the spin number, I, equals 0. If the nuclei have an odd number of protons or neutrons, then the nucleus will have a spin. The mass number is the sum of the number of protons and neutrons in a nucleus [58]. Nuclei with odd mass numbers have half integer values (I= 1/2, 3/2...). Nuclei with even mass numbers, but an odd number of neutrons, have integer values of I. The spin number of ^{1}H nuclei is I = ½.

The magnitude of the total spin angular momentum is calculated as [59-61]:

$$S = \frac{h}{2\pi}\sqrt{I(I+1)} \tag{1.2}$$

where h is the Planck constant ($6.63 * 10^{-34}$J/s). For a spin ½ system, the total spin angular momentum is thus:

$$I = \frac{h}{2\pi}\frac{\sqrt{3}}{2} \tag{1.3}$$

The magnitude of the nuclear magnetic moment is written as [62]:

$$u = \gamma S \tag{1.4}$$

where γ denotes the gyromagnetic ratio, which is inherent to different nuclei. For this thesis, we are concerned only with the ^{1}H proton nucleus: γ = 2π rad*42.6 MHz/T [63]. In NMR, the component of angular momentum along the z-direction, S_z, is given by [61]:

$$S_z = \frac{mh}{2\pi} \tag{1.5}$$

Here, m denotes a second quantum number that can only be values of $I, I-1, I-2 \ldots -I$.

Rearranging and combining Equations (1.4) and (1.5) yields the magnitude of the magnetic moment in the z-direction:

$$u_z = \frac{\gamma h m}{2\pi} \tag{1.6}$$

1.2.2 Impact of an External Magnetic Field $\overrightarrow{B_o}$ and the Zeeman Energy

In the absence of a magnetic field, the nuclear magnetic moments of a population of spin ½ nuclei will not have a preferred direction. When the nuclei are subjected to an external magnetic field ($\overrightarrow{B_o}$), the net z-components of the spins of the nuclei will reach a thermal equilibrium aligned in a direction parallel (α state, m=1/2) or anti-parallel (β state, m= -1/2) to the direction of $\overrightarrow{B_o}$. Figure 1.1 displays the α and β states of the nuclei. The parallel state has lower energy than the anti-parallel state. Each given state has an energy, E, of [63]:

$$E = -\vec{\mu} \cdot \vec{\beta} = \gamma \left(\frac{h}{2\pi}\right) m B_o \tag{1.7}$$

For $m = \pm 1/2$, there will be a difference in energy between the two states, given by the Zeeman energy [59]:

$$\Delta E = \gamma \frac{h}{2\pi} B_o \tag{1.8}$$

The difference in distribution of spins in the α and β states yields the NMR phenomenon. Any spin state $|SS\rangle$ can be described as a linear superposition of the α and β states [64]:

$$|SS\rangle = p_\alpha |\alpha\rangle + p_\beta |\beta\rangle \tag{1.9}$$

where p_α and p_β are the probability amplitudes of spins in the parallel and anti-parallel states, respectively.

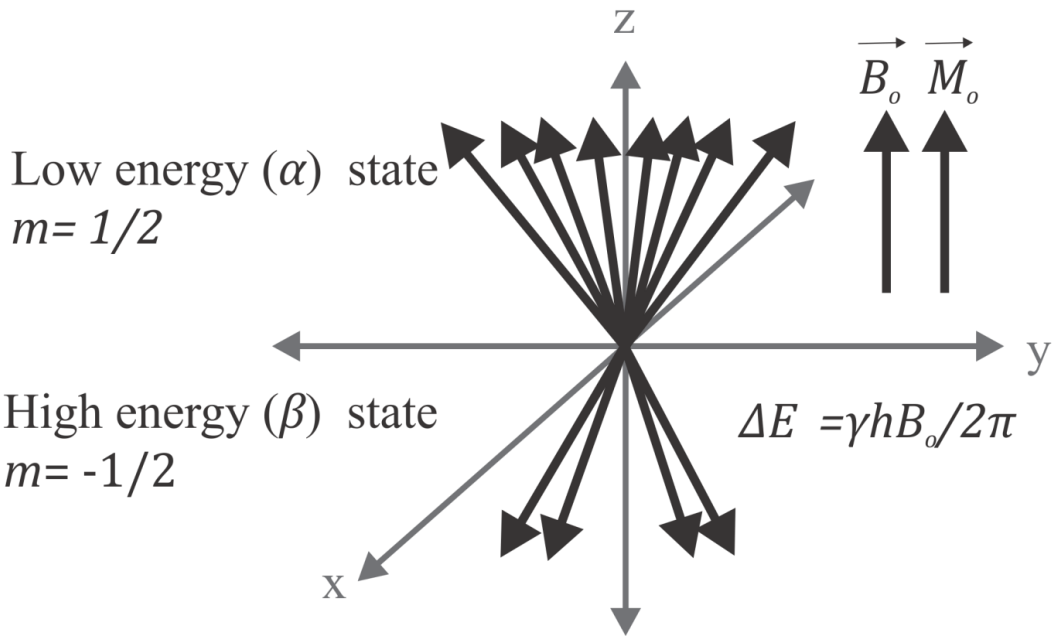

Figure 1.1: Low energy (α) and high energy (β) spin states of nuclei with a nuclear magnetic moment. The net z-components of low energy spins are aligned with the main magnetic field $\overrightarrow{B_o}$, whereas the net z-components of higher energy spins are aligned against the magnetic field $\overrightarrow{B_o}$. Spins exist pointing in all directions; for purpose of illustration only spins demonstrating a net magnetization in the z-direction are included.

1.2.3 Net Magnetization

A net magnetization vector arises from net excess of spins aligned in the parallel state. The population difference between nuclei in the parallel and anti-parallel states is given by the Boltzmann Distribution, which is a function of temperature, T [65]:

$$\frac{n_\alpha}{n_\beta} = e^{\frac{\Delta E}{kT}} = e^{\frac{\gamma h B_o}{2\pi kT}} \tag{1.10}$$

In Equation (1.10), n_α and n_β are the number of spins in the parallel and anti-parallel states, respectively, k is the Boltzmann constant ($1.38x10^{23}$ J/K) and T is the temperature in Kelvin. Because the parallel state is lower energy, more spins will align parallel to $\overrightarrow{B_o}$. As seen in Figure 1.1, the transverse components of the magnetization cancel each other, yielding a net longitudinal magnetization ($\overrightarrow{M_o}$) in the direction of $\overrightarrow{B_o}$. The magnitude of the net magnetization

is the difference of the z-components of the parallel magnetizations and the anti-parallel magnetizations [65]:

$$M_o = \sum_{i=1}^{n} u_i = n_\alpha u_z + n_\beta u_z = \frac{\gamma h}{4\pi}\left(n_\alpha - n_\beta\right) \tag{1.11}$$

Assuming that $\frac{\gamma h B_o}{2\pi kT}$ is much less than 1, one can approximate Equation (1.10) as [63,65]:

$$\frac{n_\alpha}{n_\beta} \approx 1 + \frac{\gamma h B_o}{2\pi kT} \tag{1.12}$$

Using Equation (1.12) and assuming that

$$n_\alpha \sim n_\beta = \frac{N}{2} \tag{1.13}$$

where N is the total number of spins, one can deduce [63]:

$$n_\alpha - n_\beta \approx \frac{N}{2}\frac{\gamma h B_o}{2\pi kT} \tag{1.14}$$

Utilizing Equations (1.11) and (1.14), the magnitude of the total magnetization vector, M_o, can be written as:

$$M_o = u_z\left(n_\alpha - n_\beta\right) = \frac{\gamma h}{4\pi}\,\frac{N}{2}\,\frac{\gamma h B_o}{2\pi kT} \tag{1.15}$$

The total net magnetization vector simplifies to [65]:

$$M_o = \frac{\gamma^2 \hbar^2 N B_o}{4kT} \tag{1.16}$$

where $\hbar = \frac{h}{2\pi}$.

1.2.4 Larmor Frequency v_o

When exposed to a radiofrequency field ($\overrightarrow{B_1}$), perpendicular to $\overrightarrow{M_o}$, transitions between the parallel and anti-parallel energy states occur through exchange of electromagnetic energy given by the Planck relation [63]:

$$E = hv \tag{1.17}$$

where h is the Planck constant and v is the frequency. Equating Equations (1.8) and (1.17) and rearranging gives the resonant frequency (Larmor Frequency) of the nuclei as [57]:

$$v_o = \frac{\gamma}{2\pi} B_o = \frac{\omega_o}{2\pi} \tag{1.18}$$

Any nucleus with a spin magnetic moment (such as ^{1}H, ^{31}P, ^{13}C) can be used in an NMR experiment. The ^{1}H nucleus (as used in this study) is most commonly used because it has high

abundance *in vivo* (99.985%). It also has a large gyromagnetic ratio and results in a resonant frequency of 127.8 MHz at 3 T and 400.4 MHz at 9.4 T ($\frac{\gamma}{2\pi}$= 42.6 MHz/T) [57].

1.3 The MRS Experiment- From Acquisition to Pulse Sequences

1.3.1 Excitation

Figure 1.2 displays the steps of the MRS experiment. To measure nuclear magnetization, or signal, the precession of the spins must be detected. However, nuclear magnetization cannot be observed when the net magnetization is fully along the z-axis and there are no components in the transverse plane [57]. Therefore, an oscillating magnetic field in the transverse plane, $\overrightarrow{B_1}$, is used to tilt all or some of the magnetization to the transverse plane by initiating the exchange of energy between the states. Magnetization that is fully in the transverse plane corresponds to states ($|SS_x\rangle$ and $|SS_y\rangle$) that can be written as superpositions of α and β states per Equation 1.9 [64]:

$$|SS_x\rangle = \frac{1}{\sqrt{2}}|\alpha\rangle \pm \frac{1}{\sqrt{2}}|\beta\rangle \tag{1.19}$$

$$|SS_y\rangle = \frac{1}{\sqrt{2}}|\alpha\rangle \pm \frac{i}{\sqrt{2}}|\beta\rangle \tag{1.20}$$

where i is the imaginary number and the x and y axes are chosen arbitrarily.

The type of pulse used (its amplitude and duration ($d\tau$)) dictates the final angle of rotation (θ) of the initial longitudinal magnetization vector $\overrightarrow{M_o}$ [57]:

$$\theta = \int \gamma B_1 d\tau \tag{1.21}$$

In Figure 1.2, a 90° RF pulse about x ($\overrightarrow{B_1}$) is applied. Such a pulse is written as 90°x, where the pulse phase direction is indicated by the subscript. For example, a 90°x pulse fully rotates $\overrightarrow{M_o}$ from the z-axis to the transverse plane along the y-axis. After the pulse is turned off, the transverse magnetization components $\overrightarrow{M_x}$ and $\overrightarrow{M_y}$ (collectively $\overrightarrow{M_T}$) are subject to a change in angular momentum described by [63]:

$$\frac{d\overrightarrow{M_T}}{dt} = \gamma\overrightarrow{M_T} \times \overrightarrow{B_o} = \gamma \begin{vmatrix} \hat{x} & \hat{y} & \hat{z} \\ M_x & M_y & 0 \\ 0 & 0 & B_o \end{vmatrix} = \gamma(M_y B_o \hat{x} - M_x B_o \hat{y}) \quad (1.22)$$

Using a complex number notation, M_T is written as [63]:

$$M_{xy} = M_x + iM_y \quad (1.23)$$

Solving Equation (1.22) in the complex number realm yields [59]:

$$M_{xy} = M_o \exp\left(i(-\gamma B_o t + \varphi)\right) \quad (1.24)$$

where φ is the initial angle of the magnetization in the transverse plane. Thus, a net magnetization rotates with a phase dictated by the Larmor Frequency. The rotating magnetization creates an oscillating magnetic field along the axis of a surrounding receiver coil. The changing magnetic flux over time induces an electromotive force (EMF), or voltage, in the receiver coil, with a magnitude given by Faraday's law of electromagnetic induction [66]:

$$\epsilon = -\frac{d\overrightarrow{\Psi_B}}{dt} \quad (1.25)$$

where ϵ is the magnitude of the electromotive force (voltage) and $\Psi_B$is the magnitude of the magnetic flux. The latter is calculated from [66]:

$$\Psi_B = \iint \vec{B} \cdot d\vec{A} \quad (1.26)$$

where $\vec{B}$ is the magnetic field and $d\vec{A}$ is the surface area element. The induced electromotive force is measured and forms the signal. The time-dependency of this force, which will be described in more detail in Section 1.3.6, is referred to as the free induction decay, or FID [57]. Figure 1.3 provides an illustration of Faraday's Law of Induction [66]. Figure 1.4 illustrates the effect of a 180°x pulse, which rotates the magnetization to the negative z-axis. This pulse is referred to as an inversion pulse [57]. In this case, no FID is shown and no voltage is induced since the magnetization is not precessing in the transverse plane. Additional experiments will be outlined in subsequent sections.

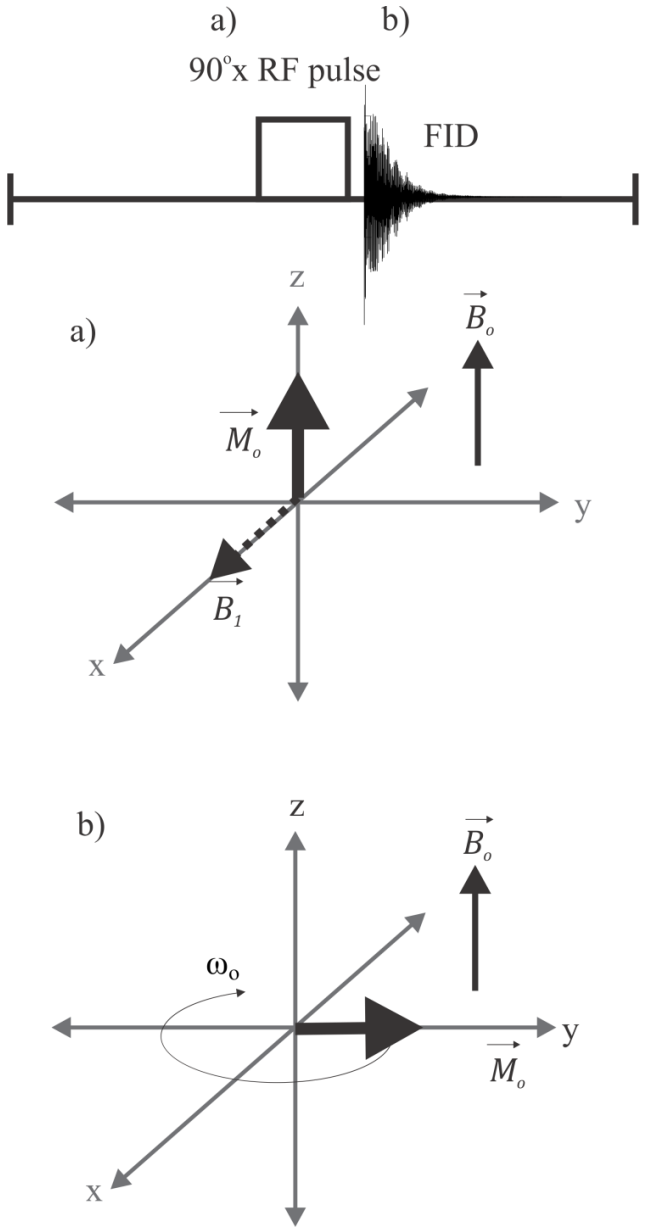

Figure 1.2: Illustration of the basic pulse-acquire MRS experiment. a) and b) denote the spin diagrams for each corresponding part of the pulse sequence diagram. a) The net magnetization ($\overrightarrow{M_o}$) is initially in the direction of the main magnetic field ($\overrightarrow{B_o}$). A 90°x RF pulse uses a magnetic field in the transverse plane ($\overrightarrow{B_1}$) to rotate the magnetization to the transverse plane. b) $\overrightarrow{M_o}$ precesses about $\overrightarrow{B_o}$, inducing an electromotive force in the RF coil. This signal is referred to as the free induction decay (FID). The magnetization shown in b) is at the start of the FID, before decay due to relaxation has taken place (see Section 1.3.7). The RF pulse and FID are plotted on the same axis of time but with different scales of the amplitude/voltage axis.

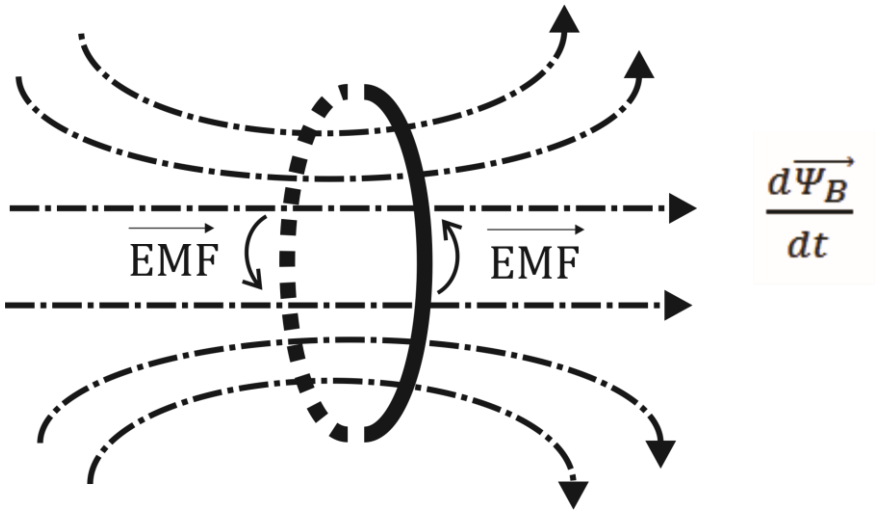

Figure 1.3: Faraday's Law of Induction. An electromotive force (EMF) is created to oppose the change in magnetic flux ($\frac{d\overrightarrow{\Psi_B}}{dt}$). Adapted from Griffiths [66].

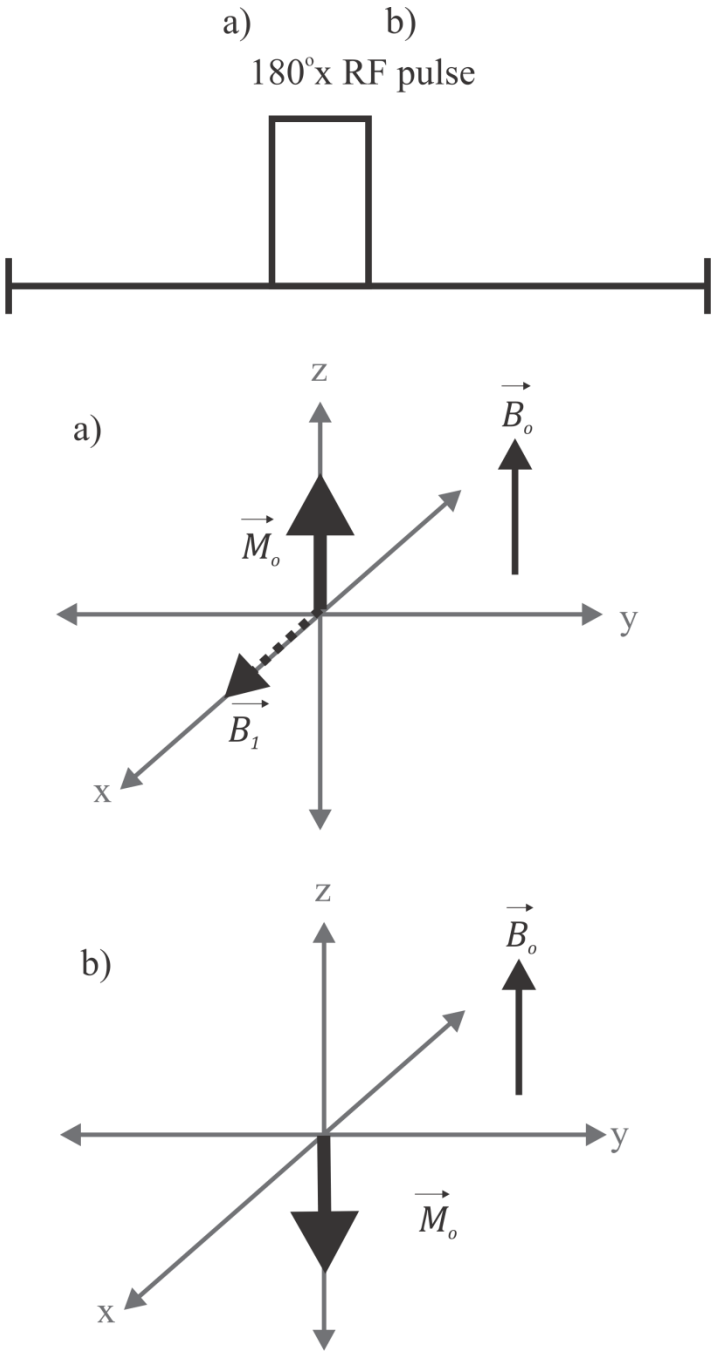

Figure 1.4: An inversion pulse. a) and b) denote the spin diagrams for each corresponding part of the pulse sequence diagram. The net magnetization ($\overrightarrow{M_o}$) is initially in the direction of the main magnetic field ($\overrightarrow{B_o}$). A 180°x inversion RF pulse uses a magnetic field in the transverse plane ($\overrightarrow{B_1}$) to rotate the magnetization to the negative z-axis. Since $\overrightarrow{M_o}$ is not precessing in the transverse plane, there is no FID.

1.3.2 The Rotating Reference Frame

A rotating reference frame is commonly used in MRS. The reader is likely familiar with the static laboratory frame ($\vec{x}$, $\vec{y}$, and $\vec{z}$), wherein the z-axis points along the direction of $\overrightarrow{B_o}$, as seen in Figure 1.2. The rotating reference frame consists of $\overrightarrow{x_\rho}$, $\overrightarrow{y_\rho}$, and $\overrightarrow{z_\rho}$. As in the Cartesian frame, $\overrightarrow{z_\rho}$ points in the direction of $\overrightarrow{B_o}$; however, the rotating frame of reference rotates at the frequency of $\overrightarrow{B_1}$ about the $\overrightarrow{z_\rho}$ axis with respect to the Cartesian reference frame [59]. The rotating reference frame is used because the behaviour of the magnetization during MR experiments is mathematically complex in the Cartesian frame. In the rotating frame, $\overrightarrow{M_T}$ only oscillates in a cone about $\overrightarrow{B_1}$; the oscillation about $\overrightarrow{B_o}$ is removed, simplifying the mathematics.

1.3.3 Oscillation of the $\overrightarrow{B_1}$ Field

To effectively tilt magnetization, the $\overrightarrow{B_1}$ field ideally moves at the resonant frequency of the nuclei in the experiment [65]. In the rotating frame, spins will experience an effective magnetic field $\vec{B}_{eff}$ [65]:

$$\vec{B}_{eff} = B_1\hat{x} + \left(B_o + \frac{\omega}{\gamma}\right)\hat{z} \tag{1.27}$$

where ω denotes the frequency of rotation of the $\overrightarrow{B_1}$ field. When $\overrightarrow{B_1}$ is applied exactly on resonance ($\omega = -\gamma B_o$) [65]:

$$\vec{B}_{eff} = B_1\hat{x} \tag{1.28}$$

and $\vec{M}$ will precess in the y-z plane with frequency $\omega_1 = \gamma B_1$.

1.3.4 Radio-Frequency (RF) Coils

RF coils are employed to apply excitation pulses and to detect the FID signal. As detailed in the previous section, the frequency of the oscillating magnetic field of the RF coil must be

tuned to the resonant frequency of the nuclei in the experiment to effectively rotate the magnetization. Many types of MRS coils exist. Two common coils are surface coils and volume coils.

Figure 1.5 illustrates how a simple surface coil can be used for RF generation and signal detection. These coils are composed of capacitors and inductors which yield resonance [67]. Surface coils typically yield higher signal to noise ratio (SNR), since they can be placed close to the region being imaged [63]. The disadvantage of surface coils is that the RF field is less homogeneous than that of a volume coil because the signal of the surface coils decreases with increasing depth in the object being imaged [63].

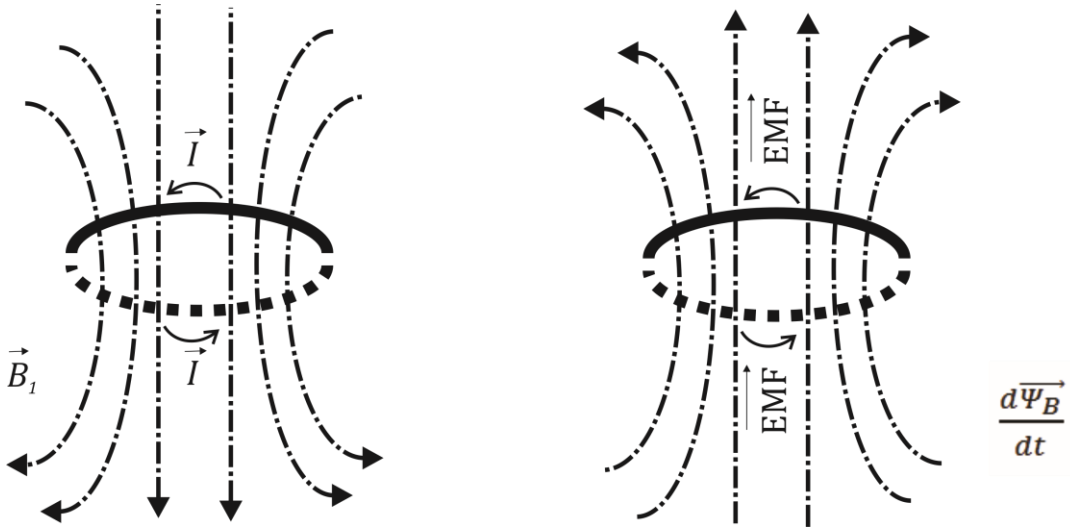

Figure 1.5: $\overrightarrow{B_1}$ formation using current $\vec{I}$ (left) and signal detection ($\overrightarrow{EMF}$) induced from fluctuating magnetic flux $\frac{d\overrightarrow{\Psi_B}}{dt}$ (right) using a surface coil. Adapted from Griffiths [66].

Figure 1.6 illustrates a common volume coil, the birdcage coil. The design yields a more homogeneous field inside the cylinder than a surface coil; however, the coil is often farther away from the sample being imaged, reducing the SNR [63]. Birdcage head coils are often used in both transmit and receive mode since they are close to the object of interest whereas birdcage body coils are often only used for RF-transmission, and another coil is used for reception [63]. A birdcage coil is composed of two circular conductive loops (end rings) attached by an even number of elements (rungs), usually 16-32, contingent on coil size [63]. The coils also have capacitors between the end rings which are placed accordingly depending on the frequency

characteristics needed for the experiment [63,68]. The coil becomes resonant from the innate inductance of the conducting elements [59]. When the birdcage coil is used for transmission, sinusoidal currents flow through each rung and are consequentially phased shifted about the coil's circumference [68,69]. The current is distributed over the surface with sinusoidal angular dependence. This relationship yields resonance within the coil [68,69].

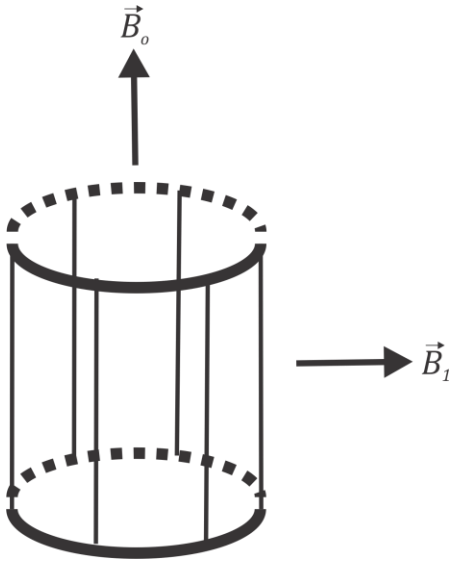

Figure 1.6: $\overrightarrow{B_1}$ formation using a birdcage coil. Current is applied to each rung of the birdcage and phase shifted by 60°, generating its own local field. A rotating $\overrightarrow{B_1}$ field is created.

1.3.5 Spatial Localization

In high field NMR experiments where small samples are being studies there is no need for spatial localization. In *in-vivo* MRS, it is necessary to only excite the spins in a voxel of interest. To achieve this localization, linear magnetic field gradients (G_x, G_y, G_z) are used to add to the existing static magnetic field in each of the x, y, and z directions, varying the frequency linearly over space. The gradients are defined as follows [69]:

$$G_z = \frac{\partial B_z}{\partial z} \tag{1.29}$$

$$G_y = \frac{\partial B_z}{\partial y} \tag{1.30}$$

$$G_x = \frac{\partial B_z}{\partial x} \tag{1.31}$$

The resonance frequency $\omega(x, y, z)$ for a magnetic field in the z direction can be made to depend on the position [69]:

$$\omega(x, y, z) = \gamma B_z = \gamma B_o + \gamma z G_z + \gamma y G_y + \gamma x G_x \tag{1.32}$$

where x, y, and z are the distances from the magnet isocenter. A range of frequencies selected, $\Delta\omega(z)$, across the slice thickness Δz is given as [69]:

$$\Delta\omega(z) = \gamma G_z \Delta z \tag{1.33}$$

The excited slice is perpendicular to the gradient direction. MRS experiments often require localizing a 3-D voxel in an object. This localization is accomplished by using three magnetic field gradients in three directions which overlap to form a 3-D volume. Figure 1.7 displays a linear gradient and the resulting $\Delta\omega(z)$.

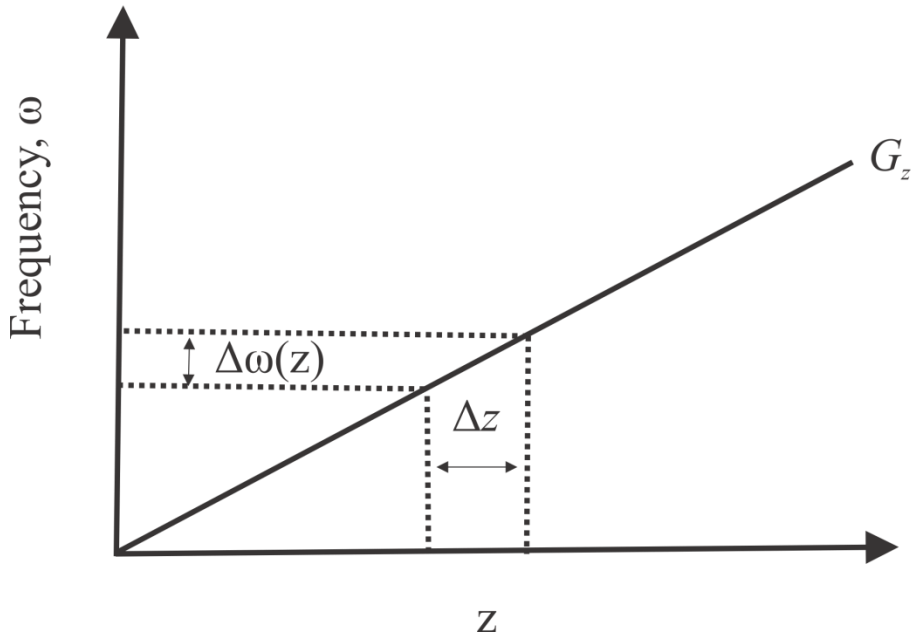

Figure 1.7: Linear gradient and the resulting $\Delta\omega(z)$. The gradient renders the frequency a function of position and enables selecting a slice of the object (Δz) with corresponding angular frequency range $\Delta\omega$.

1.3.6 The Fourier Transform of the FID

The free induction decay (FID) was previously introduced as the signal detected by the coil. Figure 1.8 illustrates the FID as an induced voltage that varies with time. The decay of the FID occurs exponentially according to:

$$e^{\frac{-t}{T_2^*}} \tag{1.34}$$

where T_2^* is a time constant [59]. The frequency of oscillations in the FID occur at the angular frequency ω_o. The Fourier Transform inter-converts between the frequency domain and the time domain. Converting from time domain data (FID) to frequency domain data is given by the following [57]:

$$F(\omega) = \int_{-\infty}^{\infty} f(t) e^{-2\pi i \omega t} dt \tag{1.35}$$

Applying the Fourier Transform to a FID oscillating at ω_o will yield a frequency domain with a peak at $\frac{\omega_o}{2\pi}$ Hz, as shown in Figure 1.8. The full-width-at-half-maximum (FWHM, or linewidth) of this peak is proportional to $\frac{1}{\pi T_2^*}$ [57]. The Fourier Transform thus translates the signal from the coil to a frequency spectrum.

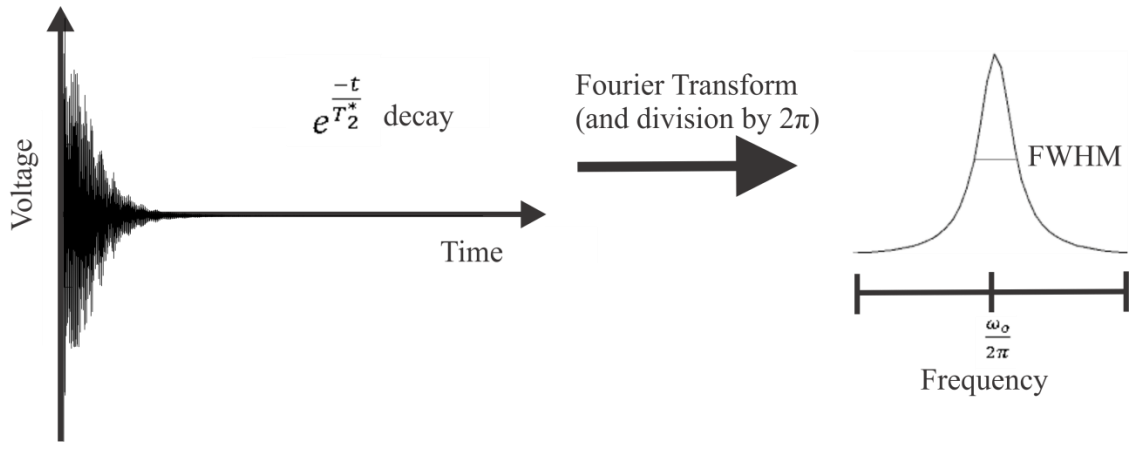

Figure 1.8: A free induction decay oscillating at ω_o and decaying exponentially with time constant T_2^*. Taking the Fourier Transform of this FID yields a peak with a Lorentzian line shape in the frequency domain at $\frac{\omega_o}{2\pi}$ Hz, with a linewidth (FWHM) of $\frac{1}{\pi T_2^*}$.

1.3.7 Relaxation

T_1 (longitudinal) and T_2 (transverse) relaxation are important for understanding MRS experiments [57,65]. Relaxation occurs due to several physical phenomena. The magnet producing the $\overrightarrow{B_o}$ field has inhomogeneities, meaning that an inherent spread of magnetic fields throughout the object of interest exists. Additionally, the nuclear dipoles themselves also produce and respond to magnetic fields. These various fields are experienced by the nuclear spins and can change with time, causing the spins to precess at different frequencies. The varying rates of precession yield to de-phasing, and ultimately to relaxation. Two types of relaxation occur; the transition of transverse magnetization back to $\overrightarrow{M_z}$ (T_1 relaxation) and the decay of transverse magnetization to null (T_2 relaxation) [57,65]. T_1 relaxation involves a transfer of energy from the spins to the lattice at the Larmor frequency whereas T_2 relaxation does not involve energy exchange but involves random fluctuations of the local field [65]. Mathematically, the change in the magnitude of magnetization $\overrightarrow{M_z}$, corresponding to T_1 relaxation, can be expressed as [57,65]:

$$\frac{dM_z(t)}{dt} = \frac{M_o - M_z(t)}{T_1} \tag{1.36}$$

where M_o is the original magnetization and T_1 denotes the T_1 relaxation time constant. This time constant represents the time required for the magnetization to recover 63 % of its equilibrium value following a 90° rotation. Solving the differential equation for a 90° RF excitation pulse yields the magnitude of the longitudinal magnetization as [57,65]:

$$M_z(t) = M_o - (M_o - M_z(0))\left(e^{\frac{-t}{T_1}}\right) \tag{1.37}$$

where t is the time for recovery. T_1 relaxation is relevant because it can affect experimental results. In a series of consecutive excitations, the degree of longitudinal magnetization recovery before the next excitation determines how much longitudinal magnetization is available to tip to the transverse axis. If $t > 5T_1$ [69], the longitudinal magnetization fully recovers and the transverse magnetization equals the initial longitudinal magnetization. If the magnetization is not fully recovered, the transverse magnetization is proportional to $M_o\left(1 - e^{\frac{-t}{T_1}}\right)$,[57] where t is the time allotted for relaxation. Spectra acquired under such conditions are T_1-weighted.

T_2 relaxation describes how the transverse magnetization will de-phase over time, losing coherence and eventually returning to its equilibrium value of zero [57,65]. Any process that yields T_1 relaxation will also cause T_2 relaxation [69]. More specifically, if a spin exchanges energy with its external environment (T_1 relaxation) and affects one of the spins contributing to the transverse magnetization, the angular momentum of the latter spin is changed and it loses phase coherence with the other spins. Mathematically, the change in magnitude of the components of magnetization in the transverse plane, corresponding to T_2 relaxation, are described by [57,65]:

$$\frac{dMx}{dt} = -\frac{Mx}{T_2} \tag{1.38}$$

$$\frac{dMy}{dt} = -\frac{My}{T_2} \tag{1.39}$$

where T_2 denotes the T_2 relaxation time constant. This time constant corresponds to the time required for the magnetization to decay to 37 % of its initial value. One can solve the differential equation for a 90° RF pulse to yield [57,65]:

$$M_T(t) = M_o e^{-\frac{t}{T_2}} \tag{1.40}$$

where M_T denotes the magnitude of the magnetization in the transverse plane and M_o is the original magnetization. Equation (1.40) illustrates that if t is much smaller than T_2, $M_T(t)$ approaches M_o. If t is not significantly smaller than T_2, the transverse magnetization depends on T_2; these spectra are T_2-weighted. Any time between excitation and signal acquisition adds to signal decay. Typically, the time between excitation and acquisition is not zero because gradients etc. require time to execute in MRS pulse sequences; thus there is some T_2 relaxation loss. Figure 1.9 displays the decay of transverse magnetization due to T_2 relaxation and recovery of longitudinal magnetization due to T_1 relaxation. The T_2 relaxation time is always shorter than the T_1 relaxation time [69].

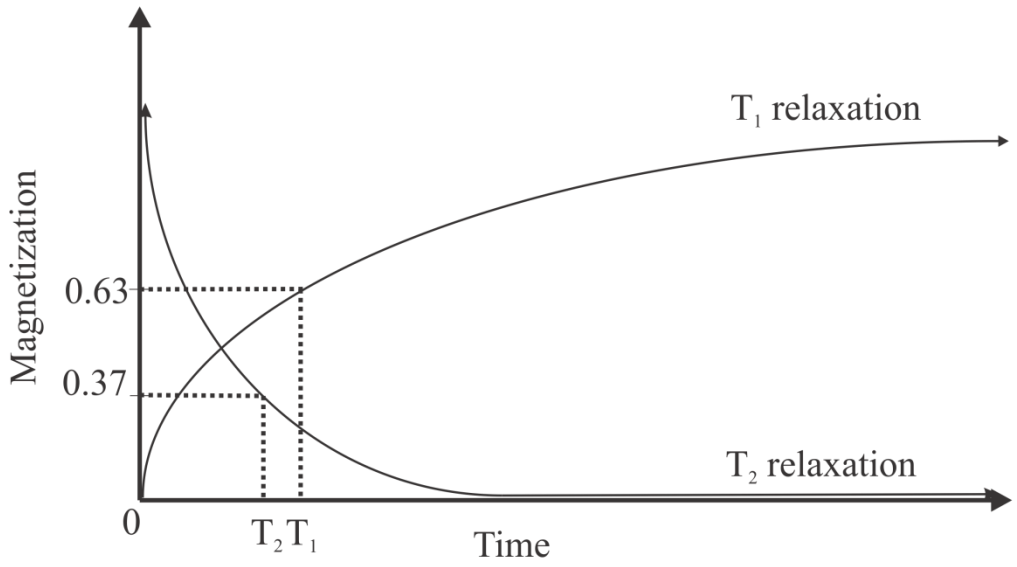

Figure 1.9: Decay of transverse magnetization due to transverse (T_2) relaxation and recovery of longitudinal magnetization due to T_1 relaxation, following a 90° pulse.

The experimentally observed relaxation is partly caused by time-independent static magnetic field inhomogeneities, typically due to imperfections in the static magnetic field. The overall transverse relaxation is due to a combination of these static field inhomogeneities and the actual transverse relaxation constant T_2 [57]. This experimentally observed overall relaxation constant (T_2*) is calculated with [69]:

$$\frac{1}{T_2^*} = \frac{1}{T_2'} + \frac{1}{T_2} \tag{1.41}$$

where T_2' is the contribution from static field inhomogeneities. The transverse relaxation due to T_2' can be reversed through certain MRS experiments (Section 1.3.9), but transverse relaxation due to T_2 cannot be reversed [59].

1.3.8 Spectral Acquisition

The most basic slice-selective method in spectral data acquisition is to acquire the signal immediately following spin excitation. Figure 1.10 describes the steps involved in a simple data acquisition, where one gradient is used to define the excitation slice. Section 1.3.5 explains how the selective pulse excites spins whose frequencies lie in a certain range.

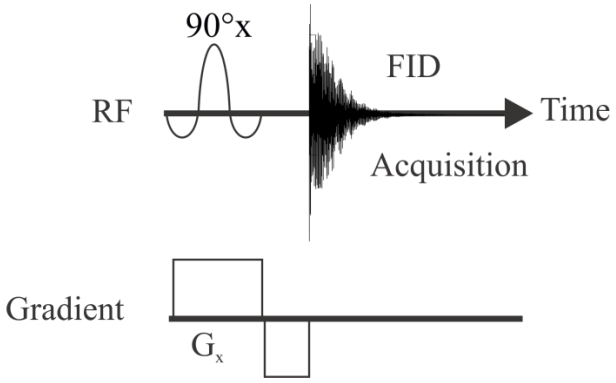

Figure 1.10: Simple slice-selective spectral acquisition using excite-acquire method. A 90°x RF pulse is applied in conjunction with a slice-selective gradient. The signal is acquired from the free induction decay following the 90°x pulse. A negative gradient with about half the area of the slice selection gradient is applied to refocus spins de-phased during the excitation process [70,71].

The fields of MRS and MRI include pulse sequences that are designed for various purposes. Example objectives include minimizing the effects from relaxation, elaborating contrast between certain tissues, or decreasing time of acquisition. Two of the most common and useful techniques are the spin echo and the stimulated echo.

1.3.9 Spin Echoes

The objective of the spin echo pulse sequence is to refocus de-phasing due to relaxation effects from static magnetic field inhomogeneities (T_2') and due to chemical shift [59,63]. As previously described, the MRS experiment consists of rotating all or part of the longitudinal magnetization into the transverse plane. This transverse magnetization will de-phase and lose coherence over time due to T_2* relaxation. The spin-echo experiment applies a 180°x refocusing

pulse at a time τ following the first 90°x excitation pulse. The refocusing pulse rotates the de-phasing spins about the x-axis. These spins continue to precess at their previous frequencies; spins that had a positive phase due to increased frequency before the inversion pulse will have a negative phase after the inversion pulse, and vice versa. At time 2τ, the spins that de-phased due to time-independent magnetic field variations will re-phase. At this point, the signal is acquired. Signal that is acquired using the spin-echo method will have a FID that decays with T_2* (Figure 1.8), but the signal amplitude as a function of TE (i.e the amplitude of the first point of the FID) only depends on T_2 and will not include contributions from static, time-independent inhomogeneities or chemical shift (Section 1.3.7). Figure 1.11 illustrates the state of the spins during all steps of a spin-echo experiment. The total time from the initial excitation pulse to height of the spin echo (2τ) is referred to as the echo time (TE).

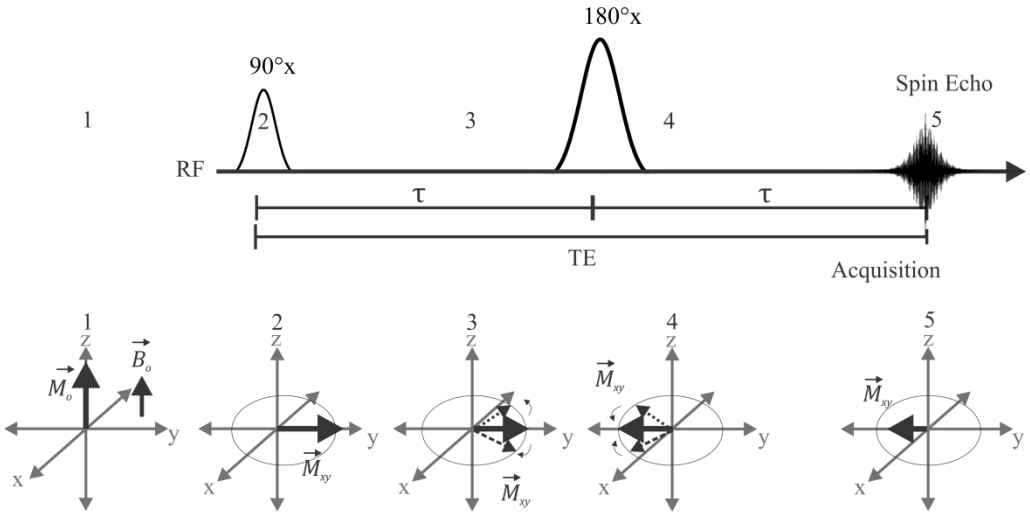

Figure 1.11: Spin echo which refocuses de-phasing from time-independent magnetic field variations or chemical shift. Before excitation (Part 1), the magnetization is aligned with the main magnetic field $\overrightarrow{B_o}$. Following the 90°x pulse, the magnetization is rotated to the transverse plane along the y-axis (Part 2). During time τ, the spins de-phase as depicted (Part 3). A 180°x pulse is applied, which flips the spins as depicted in Part 4. After time τ, the spins re-phase, forming a spin echo. The spin echo is acquired after time TE following the initial excitation pulse (Part 5).

1.3.10 Stimulated Echoes

Whereas a spin echo arises from two radio-frequency (RF) pulses, a stimulated echo arises from three RF pulses [63]. In the case of an experiment with three pulses, the first 90°x pulse rotates $\overrightarrow{M_o}$ into the x-y plane. The transverse magnetization de-phases during time τ. A second 90°x pulse rotates the spins about the x-axis into the x-z plane. After time T following the second pulse, a third 90°x pulse rotates the magnetization in the x-z plane back to the transverse x-y plane. After another period of time τ, a stimulated echo is formed as the spins re-phase. The time from the initial excitation to the middle of the stimulated echo (2τ+T) is the TE. Figure 1.12 illustrates the pulses applied and the signals acquired during all steps of the stimulated echo experiment. As seen in the figure, the stimulated echo experiment also produces several spin echoes (Signals 1, 3, 4, and 5). Signal 2 is the stimulated echo. The second pulse only rotates half of the transverse signal (signal along the rotation axis is not rotated) to be stored along the longitudinal axis [63]. This stored signal also undergoes T_1 relaxation [63]. Since only half the original spins come into phase at the same time, the stimulated echo is of weaker magnitude compared to a signal acquired under the same TE with a spin-echo sequence [69]. A stimulated echo sequence, however, permits for a shorter TE to be used since it employs 90° pulses. Figure 1.13 displays the behaviour of the spins during the stimulated echo experiment.

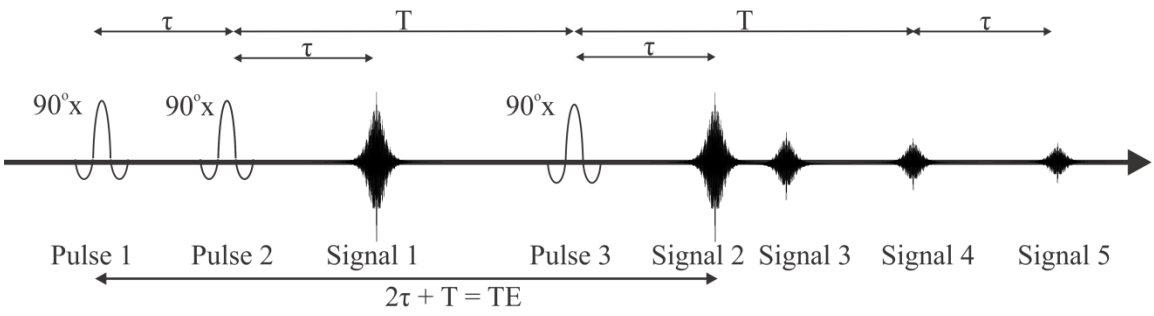

Figure 1.12: Stimulated echo experiment (adapted from Hahn [72]). The first 90°x pulse tips $\overrightarrow{M_o}$ into the transverse plane along the y-axis. During time τ, the transverse magnetization de-phases. A second 90°x pulse tilts the spins about the x-axis into the x-z plane. After time T following the second pulse, a third 90°x pulse tilts the magnetization in the x-z plane back to the transverse x-y plane. A stimulated echo (signal 2) is formed after another period τ.

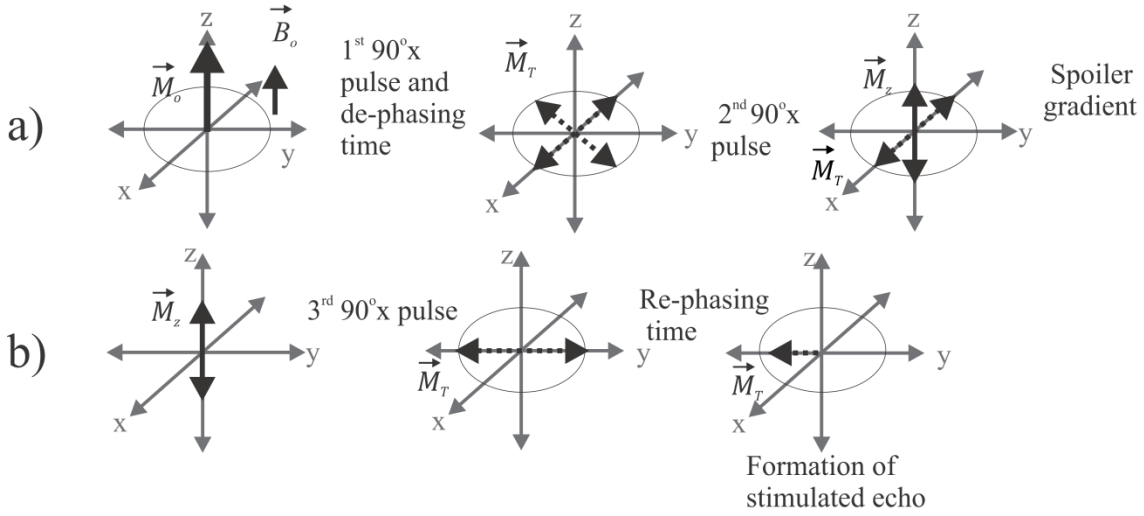

Figure 1.13: Illustration of a stimulated echo which refocuses de-phasing due to time-independent magnetic field variations or chemical shift. a) A 90°x pulse is applied, rotating $\overrightarrow{M_o}$ (solid line) into the transverse plane along the y-axis. The transverse magnetization, denoted as $\overrightarrow{M_T}$ (dotted line) de-phases. A second 90°x pulse is applied, which rotates magnetization that is not along the x-axis into the x-z plane. A spoiler gradient is typically applied here to de-phase transverse components. b) The third 90°x pulse rotates the longitudinal magnetization into the transverse plane. The spins re-phase and form a stimulated echo. Adapted from Elster [69].

1.3.11 Important MRS Parameters

Relevant MRS parameters in this work include the repetition time (TR), and the echo time (TE) [63]. The TR is the time from the initial excitation pulse in one sequence repetition to the initial excitation pulse in the next pulse sequence repetition. TE, as previously described, is the time between excitation and signal acquisition. The mixing time (TM), a parameter in STEAM [30], corresponds to time when the magnetization of interest is stored along the longitudinal axis [63]. Another important parameter is the number of averages. The signal to noise ratio (SNR) increases with the square root of the number of averages (assuming no movement of sample or participant) [69]. The voxel size is also relevant for SNR, as SNR increases with voxel volume. The three orthogonal slice-selective gradients (G_x, G_y, and G_z) can be used to select a 3-D voxel.

1.4 *In-Vivo* MRS Pulse Sequences

1.4.1 Spatial Localization for *In-Vivo* MRS Pulse Sequences

As previously described, the signal for MRS typically must be localized to a specified region. Utilizing slice-selective pulses with magnetic field gradients enables selectively exciting or refocusing spins in a voxel or slice of interest. Figure 1.14 illustrates a sinc-shaped RF pulse, which is used to excite an approximately rectangular slice profile when applied with a magnetic field gradient. Such a shape is used because the rectangle is the Fourier Transform of the sinc.

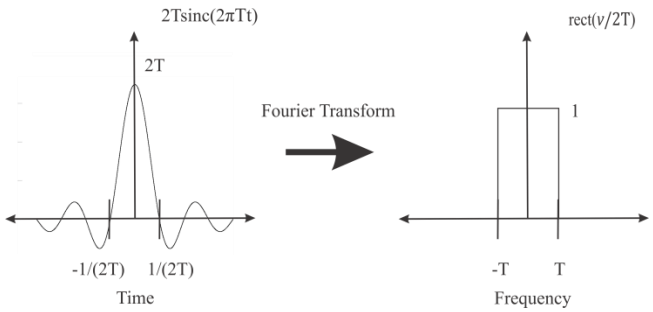

Figure 1.14: Fourier transform of the sinc. A sinc shaped pulse in the time domain is used to excite a rectangular slice in the frequency domain as shown. Gibbs ringing on the rectangle (due to truncation of the sinc) is not shown. Adapted from Luo [73].

Two common *in-vivo* pulse sequences which achieve spatial localization are PRESS and STEAM. Both PRESS and STEAM are single-shot sequences. This characteristic enables shimming (minimizing B_o inhomogeneities) exactly over the voxel of interest itself. Furthermore, single-shot sequences are less susceptible to motion artifacts compared to multi-shot acquisition sequences. Motion can reduce signal-to-noise, broaden line widths, or induce artifacts that affect quantification.

1.4.2 PRESS (Point RESolved Spectroscopy)

Figure 1.15 illustrates the PRESS pulse sequence [74,75]. PRESS acquires signal by using a double spin echo: a 90°-180°-180° RF pulse sequence. During each of the 90° and 180° pulses, gradients in the x, y, and z direction are applied exclusively. Each pulse in conjunction with the applied gradient thus affects spins in mutually orthogonal rectangular slabs. The intersection of the three slabs becomes the cubic voxel from which signal is acquired. The total TE of the sequence is the sum of the first and second TEs (TE_1 and TE_2). The spoiler (or crusher) gradients remove signal from unwanted pathways and signal from imperfect RF pulses [69]. Equation (1.42) describes the signal acquired from the PRESS sequence as a function of TE [76], assuming no J-coupling (to be discussed in Section 1.5.3).

$$\mathrm{S(TE)} = \mathrm{S(0)}\left(1 - 2\mathrm{e}^{\left(-\frac{\mathrm{TR}-\frac{\mathrm{TE}}{2}}{\mathrm{T_1}}\right)} + \mathrm{e}^{\left(\frac{-\mathrm{TR}}{\mathrm{T_1}}\right)}\right)\mathrm{e}^{-\frac{\mathrm{TE}}{\mathrm{T_2}}} \tag{1.42}$$

where $S(TE)$ is the signal at time TE, $S(0)$ is the signal at time TE = 0, and TR is the repetition time. If TE << TR, one can simplify Equation (1.42) to:

$$\mathrm{S(TE)} = \mathrm{S(0)}\left(1 - \mathrm{e}^{\left(\frac{-\mathrm{TR}}{\mathrm{T_1}}\right)}\right)\mathrm{e}^{\frac{-\mathrm{TE}}{\mathrm{T_2}}} \tag{1.43}$$

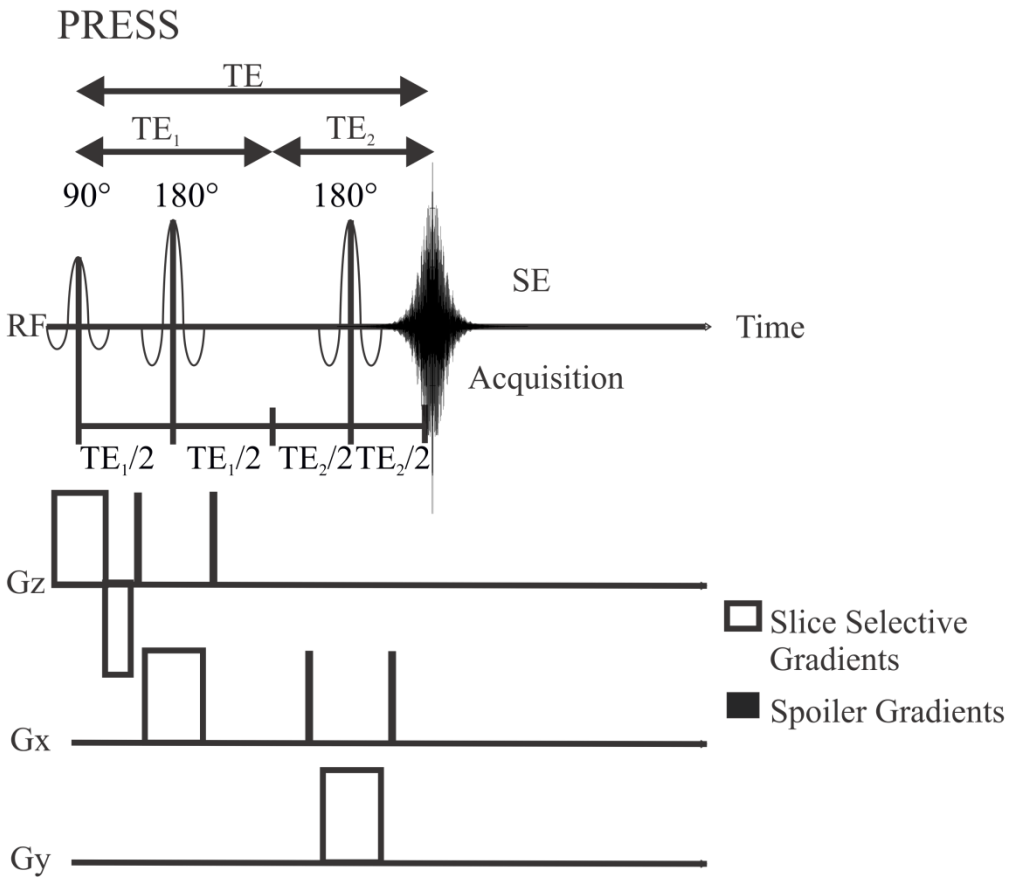

Figure 1.15: The PRESS sequence. PRESS acquires signal by using a double spin echo: a 90°-180°-180° RF pulse sequence [74,75]. During each of the 90° and 180° pulses, gradients in the x, y, and z direction are applied exclusively, resulting in voxel localization. The total TE of the sequence is the sum of the first and second TEs. The signal is acquired from the second half of the spin echo.

1.4.3 STEAM (STimulated Echo Acquisition Mode)

Figure 1.16 illustrates the STEAM pulse sequence [30]. STEAM collects signal by using a stimulated echo from a 90°-90°-90° RF pulse sequence. During each of the 90° pulses, gradients in the x, y, and z directions are applied exclusively. Just as in PRESS, each pulse affects spins in mutually orthogonal rectangular slabs. The intersection of the 3 slabs is the voxel from which signal is obtained. The stimulated echo is formed at time TE + TM (mixing time). During the TM, the desired magnetization is stored as longitudinal magnetization [69], and crusher gradients

are applied to de-phase any undesired signal present in the transverse plane, particularly signal from imperfect pulses and the additional spin-echoes. Since STEAM uses 90° pulses rather than 180° pulses, the minimum TE for STEAM is shorter than that for PRESS [69] as PRESS requires 180° refocusing pulses (which may be longer due to power constraints) and spoiler gradients around the refocusing pulses. The signal collected using STEAM, however, is less than that using PRESS since STEAM utilizes a stimulated echo instead of a spin echo [69].

Equation (1.44) expresses the signal acquired from STEAM as a function of TE, TM, and TR [77] in the absence of J-coupling (to be discussed in Section 1.5.3):

$$\mathrm{S(TE)} = \frac{\mathrm{S(0)}}{2}\left(1 - \mathrm{e}^{-\frac{\mathrm{TR}-\mathrm{TM}-\frac{\mathrm{TE}}{2}}{\mathrm{T_1}}}\right)\mathrm{e}^{-\frac{\mathrm{TM}}{\mathrm{T_1}}}\mathrm{e}^{-\frac{\mathrm{TE}}{\mathrm{T_2}}} \tag{1.44}$$

where $S(TE)$ is the STEAM signal at time TE, and $S(0)$ is the initial STEAM signal. When TE + TM << TR, one can deduce:

$$\mathrm{S(TE)} = \frac{\mathrm{S(0)}}{2}\left(1 - \mathrm{e}^{-\frac{\mathrm{TR}}{\mathrm{T_1}}}\right)\mathrm{e}^{-\frac{\mathrm{TM}}{\mathrm{T_1}}}\mathrm{e}^{-\frac{\mathrm{TE}}{\mathrm{T_2}}} \tag{1.45}$$

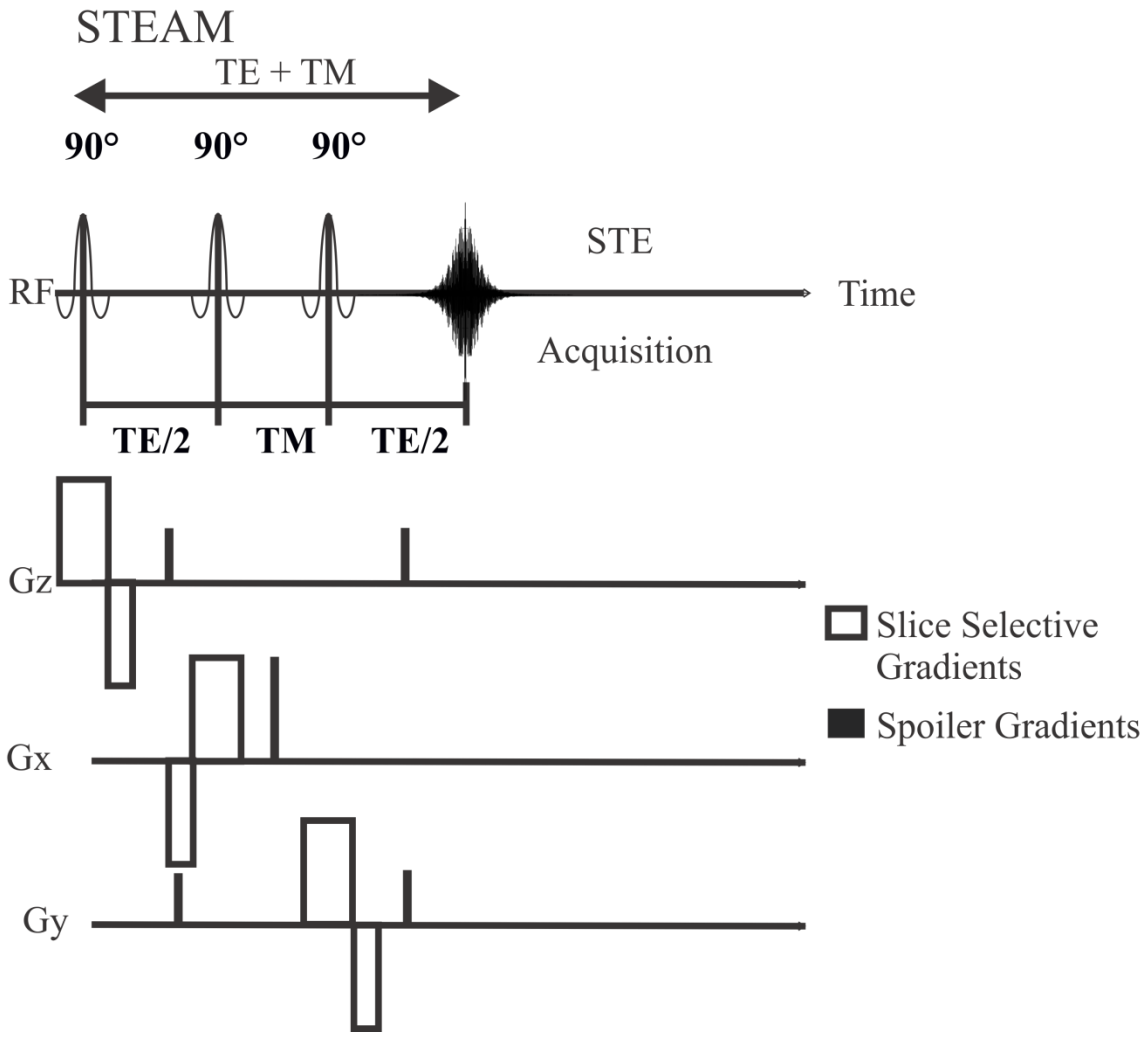

Figure 1.16: The STEAM sequence. STEAM acquires signal by using a stimulated echo utilizing a 90°-90°-90° RF pulse sequence [30]. During each of the 90° pulses, gradients in the x, y, and z directions are executed synchronously, resulting in voxel localization. The stimulated echo is formed at time TE + TM. During the TM, the necessary magnetization is stored as longitudinal magnetization. Crusher gradients are applied to de-phase undesired signal present in the transverse plane, such as the unsought spin-echoes. The signal collected using STEAM is half of that using PRESS (for uncoupled spins) since STEAM utilizes a stimulated echo instead of a spin echo.

1.4.4 Inversion Recovery

Inversion recovery (IR) sequences are typically used to either determine the T_1 relaxation time of different tissues or materials, or to selectively null the signal from a particular tissue or protons resonating at a particular frequency [69]. A regular pulse sequence is preceded by a 180° inversion pulse. This pulse rotates all magnetization (or the selected magnetization if the pulse is selective to a certain frequency) to the negative z-axis. Protons resonating at different frequencies regain their longitudinal magnetization along the positive z-axis at different rates, depending on their T_1 relaxation rate. The T_1 relaxation time of protons resonating at particular frequencies can thus be measured by applying this pulse and waiting different time periods (inversion delay times, TI) before applying the excitation pulse. Varying degrees of magnetization are excited to the transverse plane for each TI depending on how much longitudinal magnetization had recovered to the positive z-axis. The measured signal is plotted as a function of TI and the T_1 relaxation time is estimated by fitting the plot to the following expression [57]:

$$M_z = M_o(1 - 2e^{-\frac{TI}{T_1}}) \tag{1.46}$$

where M_o is the initial magnetization. Equation (1.46) can also be solved for the TI at which $M_z = 0$ for protons resonating at a particular frequency. This TI is the null time for those protons and is equivalent to 0.693 * T_1 [57]. One can apply the spin-echo, PRESS sequence, or any other sequence at the null time of protons that are desired to be suppressed. Figure 1.17 displays the T_1 relaxation recovery curves for protons and their corresponding null times.

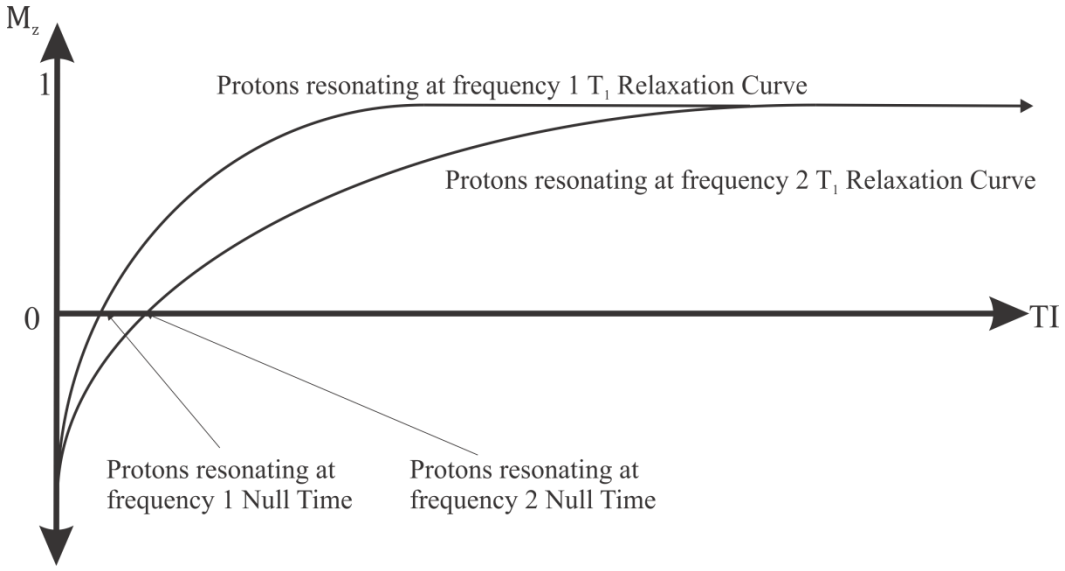

Figure 1.17: T_1 relaxation recovery curves for protons in an IR experiment. The signal from the protons would be suppressed at their respective null times. Protons resonating at resonance frequency 2 have a longer T_1 than protons resonating at frequency 1.

1.5 The MRS Spectrum

1.5.1 Obtaining the MRS Spectrum

As previously described, the time-dependence of the electromotive force is known as the free induction decay, or FID, and through the Fourier Transform yields a frequency spectrum. The FID contains information about the resonance frequencies and the abundance of protons in the experimental sample. Figure 1.18 displays the steps in obtaining a MRS spectrum. As outlined formerly, the Fourier transform of a time-domain signal $(f(t))$ yields the angular frequency domain signal $(F(\omega))$ [57]:

$$F(\omega) = \int_{-\infty}^{\infty} f(t) e^{-2\pi i \omega t} dt \tag{1.47}$$

The Fourier transformation yields both Lorentzian absorption and dispersion lines [63]. The dispersion line has extensive tails which reduce the spectral resolution. The spectrum is thus phased such that only the absorption component remains. The resonant frequency, height, and

area of each peak in the MRS spectrum can be measured. The peak areas signify the relative abundance of the protons which resonate at their corresponding specific frequencies.

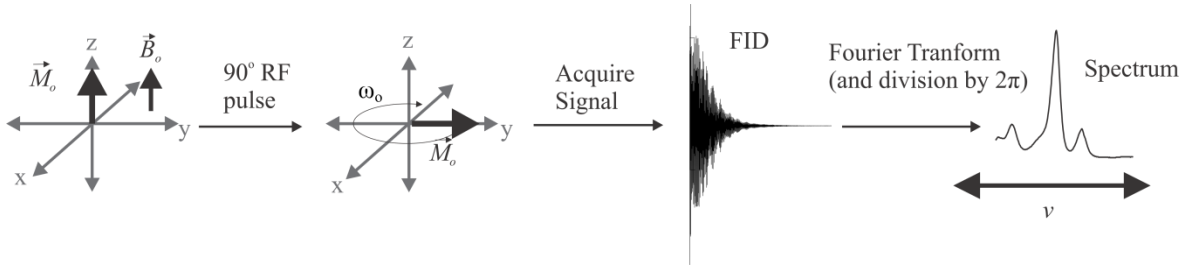

Figure 1.18: Steps in obtaining an MRS spectrum. A 90°x RF pulse is applied to rotate the longitudinal magnetization to the transverse axis. The signal is acquired from the free induction decay (FID). A Fourier Transform is performed to obtain the MRS spectrum. Protons resonate at their corresponding resonant frequencies, v. The area beneath the peak represents the relative abundance of the proton.

Before the Fourier Transform is applied, some FIDs are Gaussian or exponentially multiplied in the time domain. This additional step enhances the SNR and/ or the spectral resolution of the spectrum depending on the chosen parameters [63]. Zero-filling can also be applied to improve the visual appearance of spectra and potentially enable improved quantification [78-80]. Zero-filling involves artificially extending the FID by adding a string of points with no amplitude to the FID before applying the Fourier Transform, resulting in interpolation between acquired points in the spectrum [78,80].

1.5.2 Chemical Shift

Nuclei in different environments will resonate at different frequencies, resulting in a spectrum like the one shown in Figure 1.19. This phenomenon is known as chemical shift. When an atom is in a magnetic field, its electrons circulate and create a small magnetic field that opposes the externally applied field $\overrightarrow{B_o}$. The actual field at the nucleus is therefore different than the applied field [57]:

$$B = B_o(1 - \sigma) \tag{1.48}$$

where σ is the dimensionless shielding constant. The resonance frequency depends on this magnetic field:

$$\omega = \gamma B_o(1 - \sigma) \tag{1.49}$$

The electronic environment around each nucleus depends on the types of nuclei and bonds in the molecule and determines the chemical shift of that nucleus. The separation between peaks increases with increasing B_o. Higher field strengths thus provide a better spectral resolution. The chemical shift value (δ, in ppm) is given as [81]:

$$\delta = \frac{v - v_{ref}}{v_o} \text{x} 10^6 \tag{1.50}$$

where v is the resonance frequency of the nucleus of interest, and v_{ref} is a reference frequency [63]. A common reference frequency is that of tretramethylsilane (TMS, $Si(CH_3)_4$). TMS is assigned a chemical shift value of 0. Chemical shift values are reported using Equation (1.50) to remove dependence on the applied field strength $\overrightarrow{B_o}$. Figure 1.19 illustrates the MRS spectrum for a fatty acid (linoleic acid). Peaks which have a higher chemical shift experience a higher local magnetic field (they are relatively less shielded) whereas peaks that have a lower chemical shift experience a lower local magnetic field (they are relatively more shielded). The chemical shift phenomenon makes it possible to use MRS to discern the molecular composition of subjects of interest, as nuclei in different electronic environments will appear as separate peaks. The calculated area beneath each peak is proportional to the relative abundance of the protons resonating at that frequency. MRS can also be used to deduce structural information about a molecule. For example, in Figure 1.19, the area beneath peak A is ideally 3/2 times the area beneath peak D because 3 A protons contribute to the signal for every 2 D protons in the molecule shown. In reality, with *in-vivo* MRS pulse sequences, differences in T_2 relaxation rates of the protons, as well as effects due to a phenomenon called J-coupling (which will be reviewed in a later section) prevent accurate quantification. Chemical shift evolution is refocused using a spin echo (Section 1.3.9).

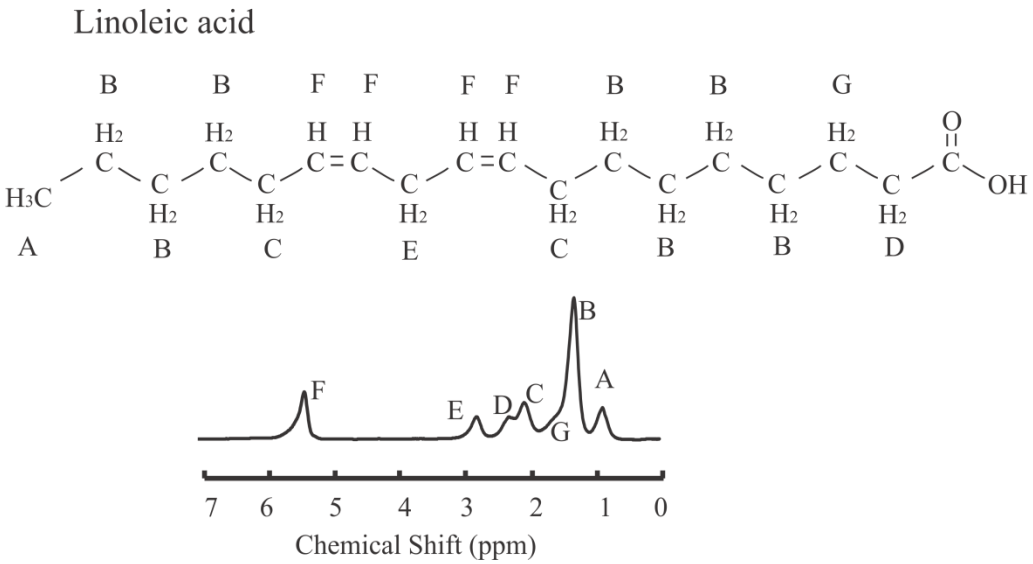

Figure 1.19: The MRS spectrum of the fatty acid linoleic acid at 3 T, indicating the different chemical shifts of each proton.

1.5.3 J- Coupling

J-coupling causes peak splitting and signal amplitude and phase modulations as a function of time [63]. Magnetically equivalent nuclei are chemically equivalent and also have the same magnetic resonance properties [82]. The magnetic field of non—magnetically-equivalent adjacent protons (within 4 bonds) [63] alters the local magnetic field that each proton experiences through hyperfine interactions. This phenomenon is known as J-coupling, scalar coupling, or spin-spin coupling. The symbol J_{AB} denotes the J-coupling constant (Hz) between arbitrary coupled protons A and B, and can be used to determine the strength of the coupling interaction using the ratio [63]:

$$\frac{J_{AB}}{\delta} \tag{1.51}$$

where δ is the frequency difference between the two coupled protons in Hz. If the coupling strength is much greater than 1 then the protons are strongly coupled and their coupling behaviour is difficult to predict. If the coupling strength is much less than 1, then the protons are weakly coupled [83]. The behaviour of weakly coupled spins can be more easily predicted. If a

proton is weakly coupled to n equivalent nuclei, the proton's signal will be split into $n+1$ peaks, with peak intensities given by Pascal's triangle (Figure 1.20). The J-coupling constant is independent of the applied magnetic field magnitude B_o. As seen in Equation (1.51), the coupling interaction becomes weaker as the magnitude B_o increases (because the frequency difference between two protons increases).

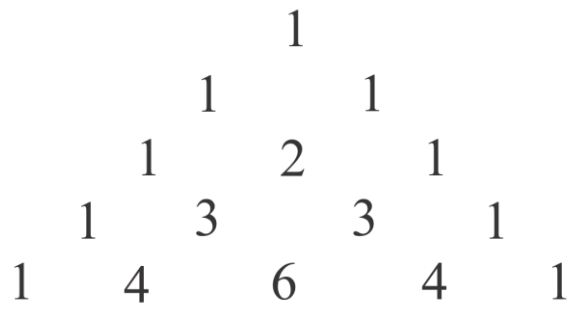

Figure 1.20: Pascal's triangle. When a proton is coupled to n equivalent nuclei, the proton's signal is split into $n+1$ peaks. The peak intensities are given by Pascal's triangle.

Several conventions exist regarding J-coupled spins. To distinguish between weak and strong J-coupling, a lettering system is employed. Letters close together in the alphabet (like A and B) denote strongly coupled nuclei whereas letters far away in the alphabet (such as A and X) denote weakly-coupled nuclei. The frequency or chemical shift is written as decreasing from left to right. Figure 1.21 displays the peak splitting due to J-coupling for several hypothetical scenarios. For reasons that will be explained shortly, the distance between peaks is always J Hz. At different field strengths, J-coupled peaks will therefore be located at different chemical shifts when using conventional spectra with axes in ppm.

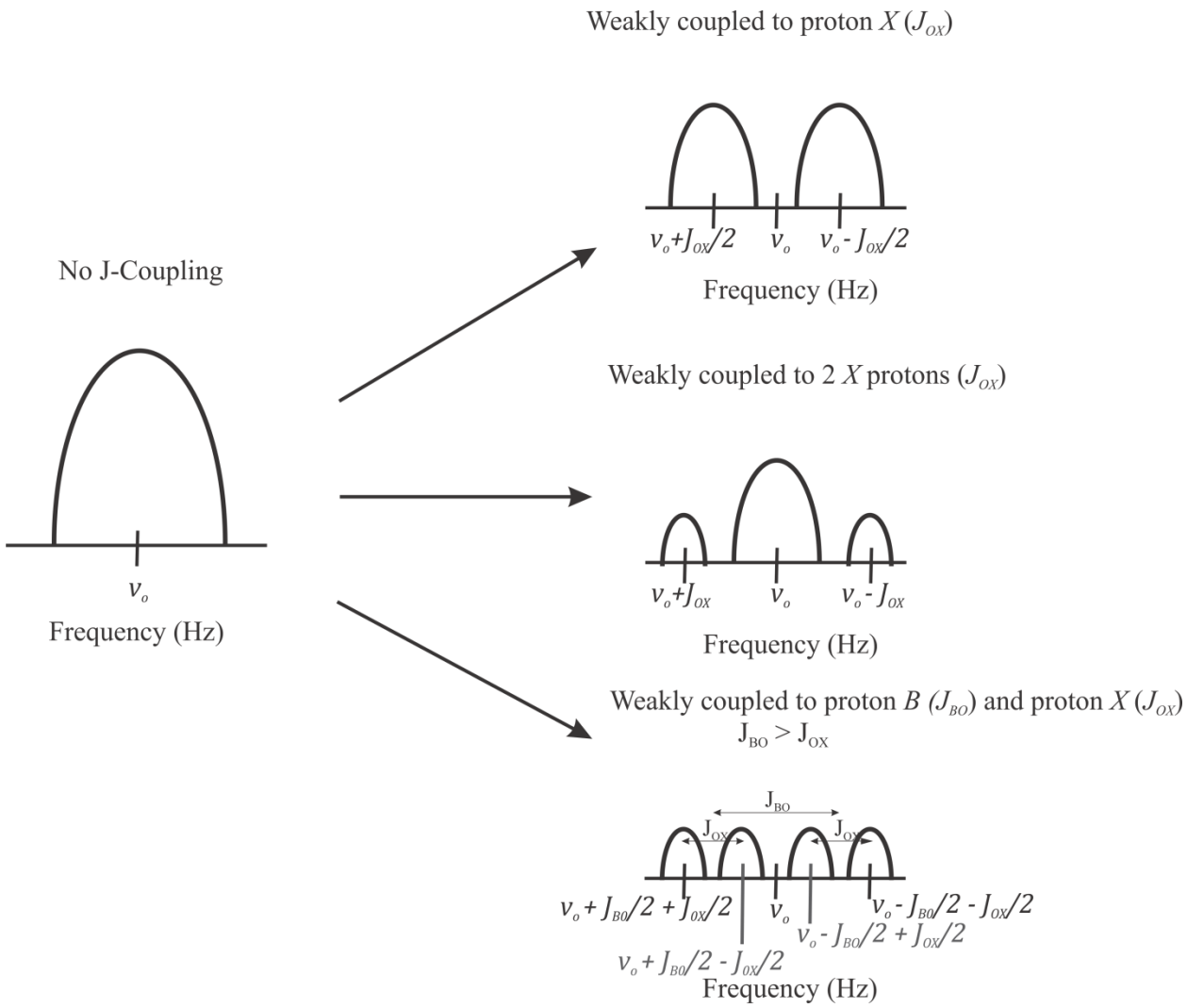

Figure 1.21: Peak splitting for hypothetical coupling scenarios. The proton O (resonant frequency v_O) is not coupled (left), weakly coupled to proton X (top right), weakly coupled to two X protons (middle right), or weakly coupled to protons B and X (bottom right). The relative areas of the peaks are per Figure 1.20. The distance between the peaks in Hz is also denoted using the appropriate J constant. Only the peaks for proton O are shown. Half-sinusoids are used to represent Lorentzian lineshapes for illustration purposes.

As previously mentioned, the peak splitting occurs due to hyperfine interactions between nuclear and electron spins in the s-orbital. These interactions consider Fermi contact and the Pauli Exclusion Principle [63]. Fermi contact refers to the relationship between a nucleus and a bound electron. S-orbital electrons have a non-zero electron density at the nucleus, leading to interactions that change the energy levels of the nucleus. An anti-parallel configuration of the

electron and nuclear spins is energetically favored. In the case of no coupling, only two different resonant frequencies arise (Figure 1.22) because electrons will be anti-parallel to their corresponding nucleus since that is the favorable state. The only energy states possible are thus that of the nucleon (in ^{1}H spectroscopy, the ^{1}H proton) either aligned with $\overrightarrow{B_o}$ (lower energy state) or against $\overrightarrow{B_o}$ (higher energy state). If coupling exists, the two nucleons will share an electron bond. The Pauli Exclusion Principle demands that only one spin-1/2 particle occupy a quantum state at a given time [63], requiring that both electrons in the bond are anti-parallel to each other. Configurations in which the electron is also anti-parallel to its nucleus are energetically favorable over configurations in which the electron is parallel to its nucleus. Figure 1.23 illustrates how J-coupling changes the energy levels of the protons in a weakly coupled AX system, yielding different resonant frequencies. Energy levels wherein the proton and electron spins for A or X are parallel are less favorable and thus gain energy of $hJ_{AX}/4$. The converse also holds. Since the energy of the levels is altered, the resonant frequency also changes, yielding the peak splitting.

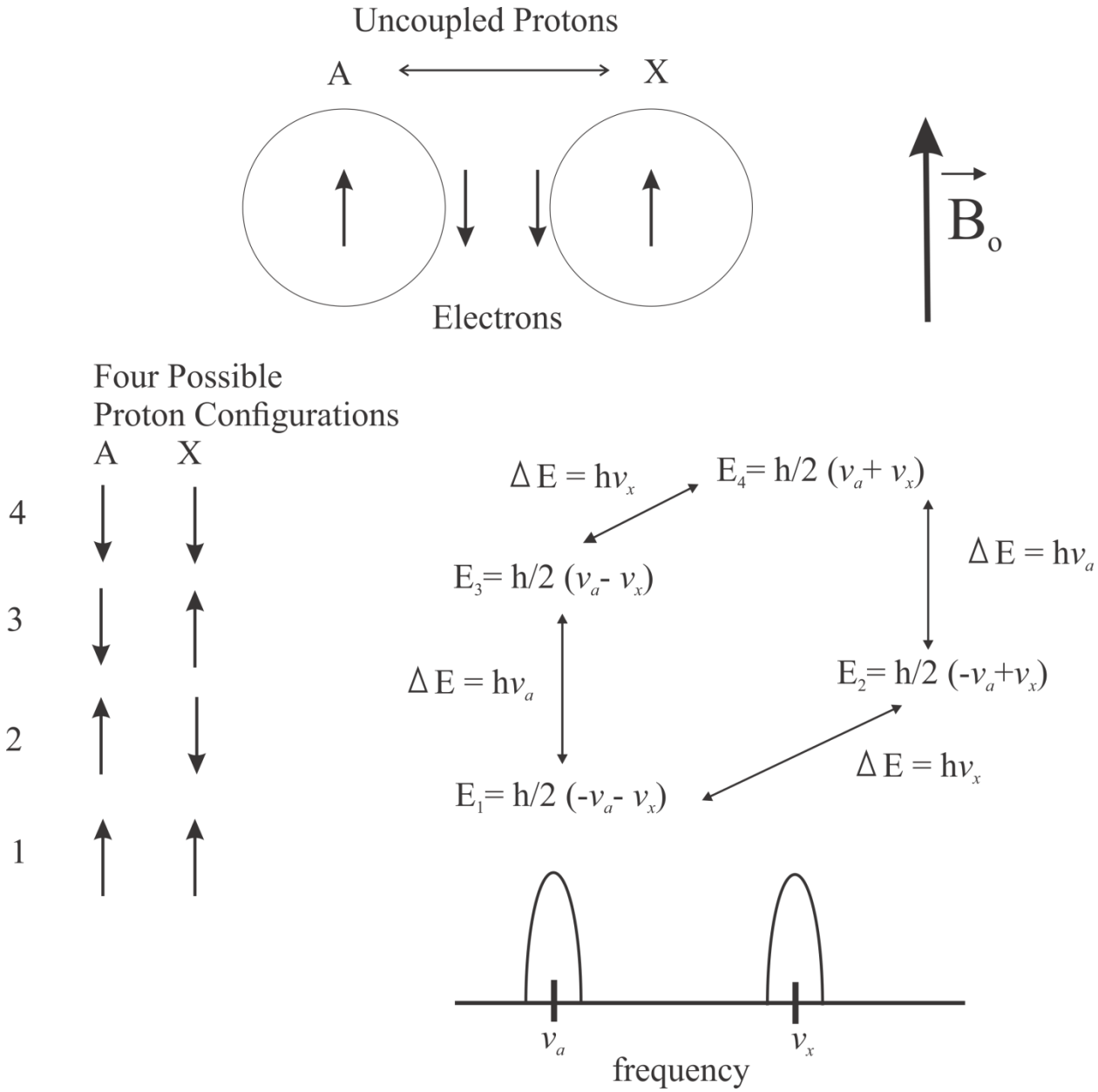

Figure 1.22: Possible energy levels and corresponding resonant frequencies for an AX system with no coupling. The energy state aligned with $\overrightarrow{B_o}$ is the lower energy state. Adapted from de Graaf [63].

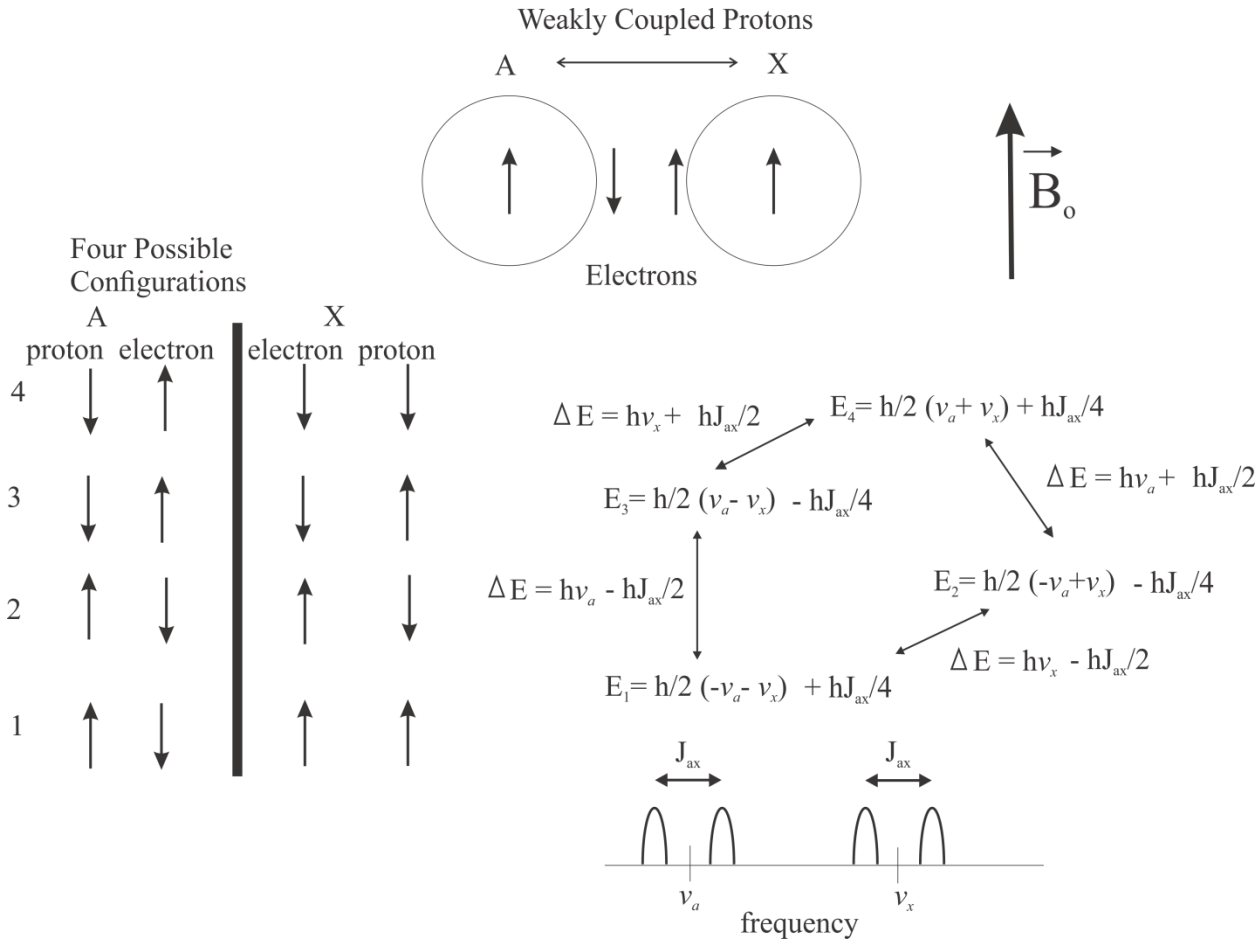

Figure 1.23: Possible energy levels and corresponding resonant frequencies for an *AX* system with coupling. Energy levels where electrons for both *A* and *X* protons are anti-parallel to their corresponding protons have energy decreased by $hJ_{ax}/4$. The converse also holds. Adapted from de Graaf [63].

Figure 1.24 summarizes the energy levels and consequent resonant frequencies for uncoupled, weakly coupled, and strongly coupled 2-spin systems, including the limit where two protons have the same resonant frequency. In the case of strongly coupled systems, the states at the inner energy levels become mixed.

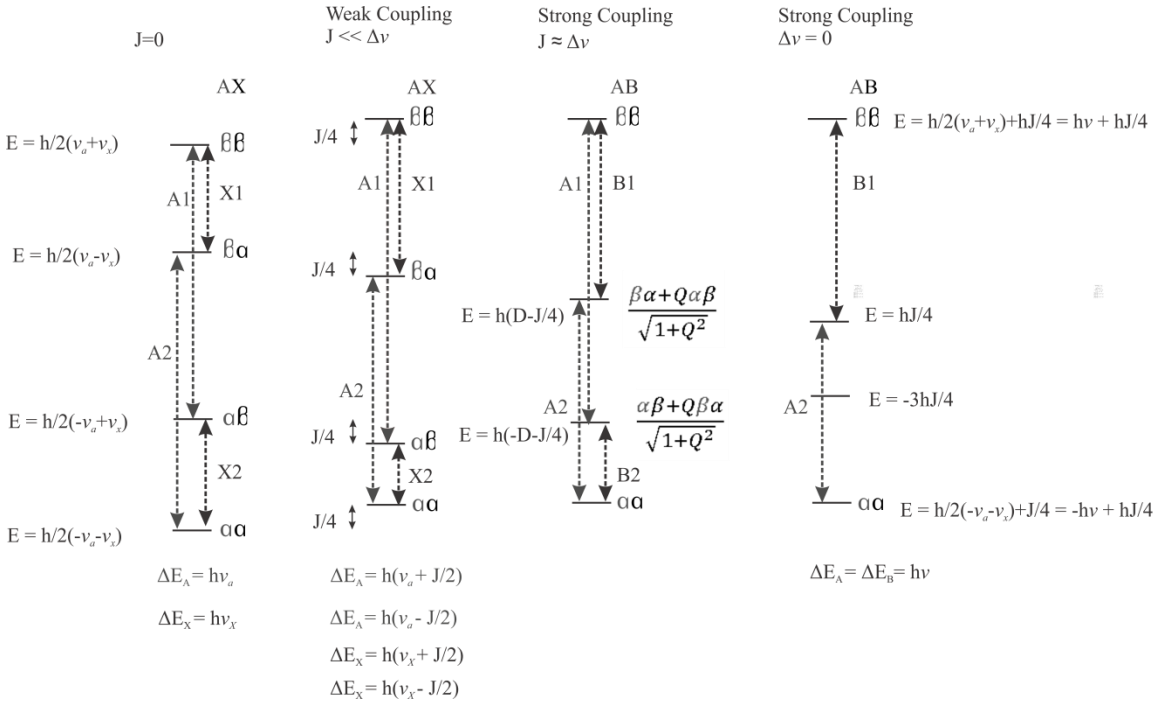

Parameters are defined below, where I is the intensity of the signal [83]

$$2D = \sqrt{\Delta\nu^2 + J^2} \qquad I_{A2} = I_{B1} = \frac{(1+Q)^2}{(1+Q^2)}$$

$$Q = \frac{J}{\Delta\nu + 2D} \qquad I_{A1} = I_{B2} = \frac{(1-Q)^2}{(1+Q^2)}$$

$$Q \to 0, \qquad J \ll \Delta\nu$$

Figure 1.24: Energy levels and resulting resonant frequencies for uncoupled (J = 0, protons A and X), weakly coupled (J << $\Delta\nu$, protons A and X) and strongly coupled (J ≈ $\Delta\nu$, protons A and B) spin systems. The limit is also shown where two protons are equivalent ($\Delta\nu$ = 0). The α energy level is that aligned with $\overrightarrow{B_o}$ (lower energy level) whereas the β energy level is that aligned against $\overrightarrow{B_o}$(higher energy level). For weakly coupled systems (J << $\Delta\nu$) or uncoupled systems (J = 0), simplifications are made (D ≈ $\frac{\Delta\nu}{2}$, Q ≈ 0), yielding the two left energy level diagrams. Adapted from de Graaf [63,83].

Both strong and weak coupling lead to signal modulations as a function of time. This effect occurs because spins that precess with lower or higher frequency will become out of phase

with each other, leading to smaller, and potentially negative peaks. A spin echo sequence does not refocus the effects of J-coupling in a homonuclear spin system, resulting in signal modulations as a function of echo time.

1.6 Product Operator Formalism

1.6.1 The Vector Model

Product operator formalism can be used to assess the behavior of non-coupled and weakly-coupled spins to time or pulse sequences. The Vector Model visualizes the spins as vectors rotating during an MRS experiment. In order to be consistent with vector mathematical convention [63,83], all product operator mathematics will be demonstrated using counter-clockwise rotations. This convention seems to be more popular in the literature when deriving spin behavior. However, the mathematics can be derived using clockwise rotations as well [84,85] and yields the same end-result as long as the scientist is consistent and mindful of his or her chosen convention. In this thesis, the axes shown in Figure 1.25 will be used for demonstrations of product operator formalism.

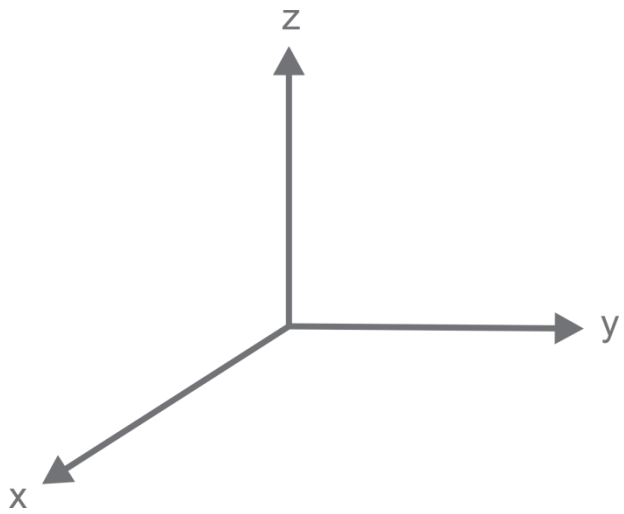

Figure 1.25: Axes used for product operator formalism illustrations.

1.6.2 Operators

In the field of quantum mechanics, operators denote observable quantities, including energy, angular momentum, and magnetization [84,85]. In this demonstration, I_x, I_y, and I_z will represent each corresponding component of the magnetization. The density operator, σ is the sum of the three operators [84]:

$$\sigma(t) = a(t)I_x + b(t)I_y + c(t)I_z \tag{1.52}$$

1.6.3 Hamiltonians and the Equation of Motion

The density operator at time t, $\sigma(t)$ for a spin system is calculated from $\sigma(0)$ using the Liouville Von Neuman Equation, also known as the equation of motion:

$$\frac{\partial\sigma}{\partial t} = -\frac{i}{\hbar}[H, \sigma] \tag{1.53}$$

H is the relevant Hamiltonian and ħ is the constant, h divided by 2π. The solution to Equation (1.53) is:

$$\sigma(t) = exp(-iHt/\hbar)\,\sigma(0)exp\,(iHt/\hbar) \tag{1.54}$$

For pulses about the x and y axes:

$$H_{pulse,x} = -\omega_{RF}I_x\hbar \tag{1.55}$$

$$H_{pulse,y} = -\omega_{RF}I_y\,\hbar \tag{1.56}$$

where $\omega_{RF} = \gamma B_{RF}$. For precession in $\overrightarrow{B_o}$,

$$H_z = -\omega_I I_z\hbar \tag{1.57}$$

where ω_I represents the Larmor frequency of the corresponding spin I in the spin system. Since spins have slightly different precessional frequencies (ω_I) due to chemical shift (Section 1.5.2), the Hamiltonian in Equation (1.57) denotes chemical shift evolution.

Solving the equation of motion for an RF pulse involves using the following identity [84,85]:

$$exp(-i\omega t I_a)\{original\ operator\}\, exp(i\omega t I_a) = \{original\ operator\}cos(\omega t) + \{new\ operator\}sin(\omega t) \tag{1.58}$$

As seen in Equation (1.58), the angular momenta follow regular vector rotations [84,85]. Typically, a shorthand notation is used. For instance,

$$\sigma(t_n) = exp(-i\omega_I t_n I_z)\, \sigma(0) exp\ (i\omega_I t_n I_z) \tag{1.59}$$

would be written as:

$$\sigma(0) \xrightarrow{\omega_I t_n I_z} \sigma(t_n) \tag{1.60}$$

when propagating product operator formalism. Table1.1 and Table 1.2 display the solutions to Equation (1.58) for RF pulses and for chemical shift evolution during free precession in $\overrightarrow{B_o}$, respectively.

Table 1.1: Response of spins to RF pulses (with phase indicated).

Spin	Hamiltonian	Solution
	$-\boldsymbol{\omega_{RF}} \boldsymbol{I_x}$ħ	
I_x	→	I_x
I_y	→	$I_y \cos(\omega_{RF} t) + I_z \sin(\omega_{RF} t)$
I_z	→	$I_z \cos(\omega_{RF} t) - I_y \sin(\omega_{RF} t)$
	$-\boldsymbol{\omega_{RF}} \boldsymbol{I_y}$ħ	
I_x	→	$I_x cos(\omega_{RF} t) - I_z \sin(\omega_{RF} t)$
I_y	→	I_y
I_z	→	$I_z \cos(\omega_{RF} t) + I_x \sin(\omega_{RF} t)$

Table 1.2: Response of spins to chemical shift evolution during free precession in $\overrightarrow{B_o}$ ($\boldsymbol{H} = -\boldsymbol{\omega_I I_z}\hbar$).

Spin	Hamiltonian	Solution
	$-\boldsymbol{\omega_I I_z}\hbar$	
I_x	→	$I_x cos(\omega_I t) + I_y \sin(\omega_I t)$
I_y	→	$I_y \cos(\omega_I t) - I_x \sin(\omega_I t)$
I_z	→	I_z

1.6.4 Product Operator Formalism for Two Spins

The previous parts of this section considered a single proton I, with vector operators $I_x, I_y,$ and I_z. For two spins I and S, the additional operators $S_x, S_y,$ and S_z are also required, as are anti-phase (non-observable magnetization) terms: $2I_xS_z, 2I_yS_z, 2I_zS_x, 2I_zS_y$ [85]. The notation demands that the operator $2I_xS_z$ (for example) is referred to as spin I anti-phase with respect to spin S (i.e. the non z spin is considered anti-phase to the z spin). RF pulses are propagated through the multi-spin system using the same rules described in the previous section. The RF pulse rotations for the anti-phase terms are summarized in Table 1.3.

Table 1.3: Response of anti-phase spins to RF pulses (with phase indicated)**.**

Spin	Hamiltonian	Solution
	$-\boldsymbol{\omega_{RF}I_x}\hbar$	
$2I_xS_z$	→	$2I_xS_z$
$2I_yS_z$	→	$2I_yS_z\cos(\omega t) + 2I_zS_z\sin(\omega t)$
$2I_zS_x$	→	$2I_zS_x\cos(\omega t) - 2I_yS_x\sin(\omega t)$
$2I_zS_y$	→	$2I_zS_y\cos(\omega t) - 2I_yS_y\sin(\omega t)$
	$-\boldsymbol{\omega_{RF}I_y}\hbar$	
$2I_xS_z$	→	$2I_xS_z cos(\omega t) - 2I_zS_z\sin(\omega t)$
$2I_yS_z$	→	$2I_yS_z$
$2I_zS_x$	→	$2I_zS_x\cos(\omega t) + 2I_xS_x\sin(\omega t)$
$2I_zS_y$	→	$2I_zS_y\cos(\omega t) + 2I_xS_y\sin(\omega t)$
	$-\boldsymbol{\omega_{RF}S_x}\hbar$	
$2I_xS_z$	→	$2I_xS_z cos(\omega t) - 2I_xS_y\sin(\omega t)$
$2I_yS_z$	→	$2I_yS_z\cos(\omega t) - 2I_yS_y\sin(\omega t)$
$2I_zS_x$	→	$2I_zS_x$
$2I_zS_y$	→	$2I_zS_y\cos(\omega t) + 2I_zS_z\sin(\omega t)$
	$-\boldsymbol{\omega_{RF}S_y}\hbar$	
$2I_xS_z$	→	$2I_xS_z cos(\omega t) + 2I_xS_x\sin(\omega t)$
$2I_yS_z$	→	$2I_yS_z\cos(\omega t) + 2I_yS_x\sin(\omega t)$
$2I_zS_x$	→	$2I_zS_x\cos(\omega t) - 2I_zS_z\sin(\omega t)$
$2I_zS_y$	→	$2I_zS_y$

Free precession in $\overrightarrow{B_o}$ is more complex in a coupled system; using Equations (1.57) and (1.58) is inadequate. In addition to the standard free precession Hamiltonians that account for chemical shift evolution, the coupling Hamiltonian must also be considered [83]:

$$H_J = 2\pi J_{IS} I \cdot S \tag{1.61}$$

For weakly coupled systems only, Equation (1.61) can be simplified to [83]:

$$H_J = 2\pi J_{IS} I_z S_z \tag{1.62}$$

Similar to the single spin system, the Equation of Motion is solved using the identity:

$$exp(-iH_J t)\{original\ operator\}exp(iH_J t) = \{original\ operator\}cos(\pi J_{IS} t) + \{new\ operator\}sin(\pi J_{IS} t) \quad (1.63)$$

The new operator is determined from commutation relations for spin [84,85]. Table 1.4 displays the solutions to Equation (1.63) for coupling evolution in $\overrightarrow{B_o}$. Figure 1.26 illustrates signal modulation for a 2-spin weakly coupled system. For the *IS* system shown in the figure, in-phase coherence $\pm I_y$ exists at times that are multiples of $\frac{1}{J}$ whereas anti-phase coherences $\pm 2I_x S_z$ exist at timings that are odd multiples of $\frac{1}{2J}$. The small peaks seen when the signal is anti-phase are attributed to some anti-phase coherences evolving into in-phase (observable) coherences during the signal acquisition period [63,83,86].

Table 1.4: Response of coupled spins under J-coupling Hamiltonian.

Spin	Hamiltonian	Solution
	$\boldsymbol{2\pi J_{IS} I_z S_z}$	
I_x	→	$I_x \cos(\pi J_{IS} t) + 2I_y S_z \sin(\pi J_{IS} t)$
I_y	→	$I_y \cos(\pi J_{IS} t) - 2I_x S_z \sin(\pi J_{IS} t)$
I_z	→	I_z
$2I_x S_z$	→	$2I_x S_z \cos(\pi J_{IS} t) + I_y \sin(\pi J_{IS} t)$
$2I_y S_z$	→	$2I_y S_z \cos(\pi J_{IS} t) - I_x \sin(\pi J_{IS} t)$
$2I_z S_x$	→	$2I_z S_x \cos(\pi J_{IS} t) + S_y \sin(\pi J_{IS} t)$
$2I_z S_y$	→	$2I_z S_y \cos(\pi J_{IS} t) - S_x \sin(\pi J_{IS} t)$

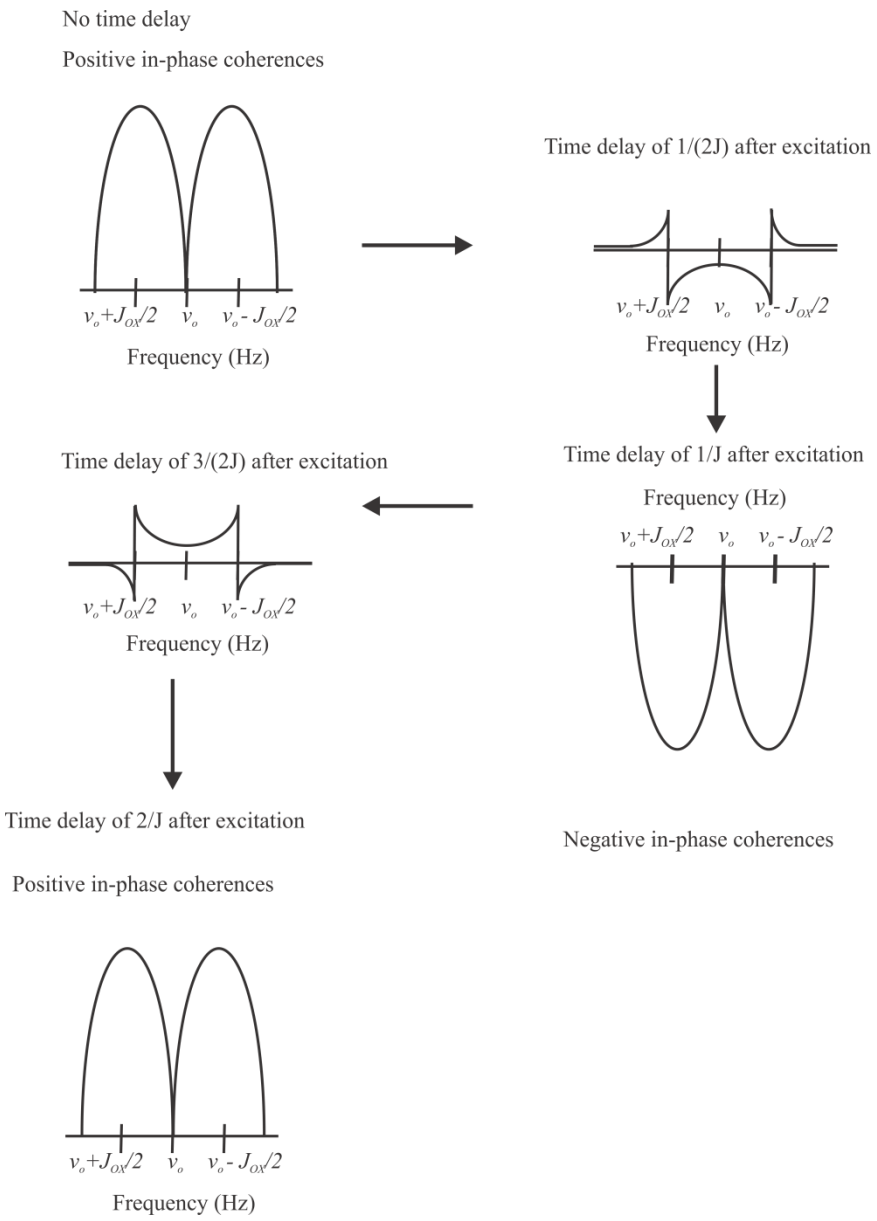

Figure 1.26 Signal modulation for a weakly coupled IS system [83]. In-phase coherence $\pm I_y$ exists at times that are multiples of $\frac{1}{J}$ whereas anti-phase coherences $\pm 2I_xS_z$ exist at timings that are odd multiples of $\frac{1}{2J}$. The small activity seen when the signal is anti-phase is a result of some anti-phase coherences evolving into in-phase (observable) coherences during the signal acquisition period [63,83,86]. These are exaggerated in size in the figure for visibility.

As seen in Table 1.2, multiple quantum coherences also exist, but are not observable: $2I_xS_y, 2I_yS_x, 2I_xS_x, 2I_yS_y$. These correlations evolve among themselves while precessing about $\overrightarrow{B_o}$, but, in the absence of pulses, do not interconvert with other classes of correlations or with observable coherences [85]. Unlike anti-phase coherences which can evolve to observable magnetization with free precession, the multiple quantum coherences do not evolve to observable magnetization with free precession about $\overrightarrow{B_o}$. The term $2I_zS_z$ corresponds to a non-equilibrium population distribution and is also not observable [84,85]. It is relevant that a factor of two is present in the terms for anti-phase terms and multiple quantum coherences. For example, I_x is converted to $2I_yS_z$ when $t = \frac{1}{2J}$ [85]. This factor is utilized because the magnetization components for individual spins have values of 1/2 or −1/2, whereas the correlations have values of 1/4 or −1/4. The factor of two ensures mathematical consistency in calculations [85].

The evolution of a strongly coupled system is much more difficult to calculate because the full extent of Equation (1.61) must be accounted for and propagated through in the mathematics [87,88]. A density matrix computation is therefore often utilized [85].

1.7 J-Coupling Evolution During PRESS and STEAM Pulse Sequences

J-coupling interactions affect the peak shapes and intensities during PRESS and STEAM pulse sequences [89-92]. As seen in the previous section, the J-coupling evolution for a weakly-coupled system can be described mathematically. For a spin-echo experiment, such as PRESS, the evolution of a weakly coupled AX system is represented by an in-phase coherence (A_x), and an anti-phase coherence ($2A_yX_z$), where the axes were chosen arbitrarily [83]. As previously described, a spin-echo sequence refocuses chemical shift evolution. Thus, only the effects of T_2 relaxation and J-coupling evolution remain for the response of magnetization to a PRESS sequence [83]:

$$A_x = \left(A_x\, cos(\pi J_{AX} TE) + 2A_yX_z\, sin(\pi J_{AX} TE)\right)e^{-\frac{TE}{T_2}} \tag{1.64}$$

J_{AX} is the coupling constant between spins A and X. Equation (1.64) shows that the signal evolution for A during a PRESS sequence follows a standard sinusoidal modulation. In PRESS,

the behavior of weakly coupled spins is only affected by the total TE (sum of TE_1 and TE_2), whereas the expression for strongly coupled spins is impacted by each individual TE [63]. For STEAM, the net observable signal for spin A in a A_nX spin system is given by [83]:

$$S(TE+TM) = \frac{1}{2}(cos^2\left(\frac{\pi J_{AX} TE}{2}\right) - \frac{1}{2}sin^2\left(\frac{\pi J_{AX} TE}{2}\right)\left[1 - cos^{n-1}\left(\frac{\pi J_{AX} TE}{2}\right) cos\left(\frac{\Delta\omega_{AX} TE}{2}\right)\right] cos^{n-1}(\pi J_{AX} TM)\, cos(\Delta\omega_{AX} TM) \quad (1.65)$$

where $\Delta\omega_{AX}$is the frequency difference between spins A and X. The first term represents A magnetization that was along the longitudinal axis during the TM. The second term emerges from zero quantum coherences (a type of multiple quantum coherence) during the TM period [63].

1.8 Other Factors that Affect Signal Response to a PRESS or STEAM Sequence

Section 1.7 described how J-coupling can affect signal response to a PRESS or STEAM sequence, in addition to T_2 relaxation effects. Other factors must also be considered when predicting or analyzing signal response. Imperfect-shaped pulses can impact spin response [89,93]. A perfectly rectangular shape is impossible to create because it would require a temporal sinc pulse that is infinite. Thus, the sinc pulse is truncated, yielding irregularities and an imperfect slice-selection shape, affecting the spin response [89,93]. Furthermore, the chemical shift displacement artifact is also problematic [83,94]. For example, a slice excited using the PRESS pulse sequence has a dimension of [83]:

$$\Delta x = \frac{BW}{G} \quad (1.66)$$

in each direction (cm), where BW is the bandwidth (Hz) and G is the gradient strength (Hz/cm). Consequently, a chemical shift difference of $\Delta\delta$ (Hz) between spins will cause a slice to be shifted away from the central location by ε [83]:

$$\varepsilon = \Delta x \frac{\Delta\delta}{BW} \quad (1.67)$$

The combined PRESS signal, instead of being formed from both spins A and X experiencing all pulses, is now composed from weighted signals from each of the regions. Figure 1.27 illustrates the voxel shift displacement artifact for two 180° pulses during a PRESS sequence.

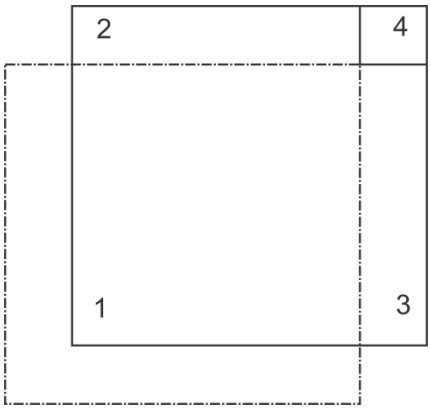

Figure 1.27: The voxel shift displacement artifact in two dimensions for a PRESS sequence. The solid line represents the localized volume of spin A and the dotted line the localized volume of spin X during the 180° refocusing pulses. Adapted from deGraaf [83].

1.9 Spectral Editing

The objective of spectral editing is to differentiate overlapped signal peaks. Many spectral editing methods exploit differences in J-coupling evolution of various spins. For instance, the TE values of PRESS can be chosen in such a manner that the J-coupling modulation of a contaminant proton yields minimal signal in synchronization with the desired proton yielding sufficient signal [95]. Another method is to exploit different T_2 relaxation times of certain protons. For example, using a long TE reveals signals from protons with a long T_2 relaxation time that would otherwise be concealed by peaks with a shorter T_2 using a short TE [18,26,27]. Utilizing a longer TE can also yield improved spectral resolution of some desired peaks [20,44].

1.10 High Field MRS

MRI machines used in the clinic are typically 1.5 T to 3 T; however, studies have used high field strengths to study fat composition in animals [33-37,39] , and some research has been done in humans at 7 T [23,24,38]. Since higher field strength magnets generally require a smaller bore to obtain sufficient homogeneity, they are often only used for small animal experiments. One main advantage of using a higher magnetic field is a higher SNR. The SNR increases about linearly with higher field strength [31,32]. This proportionality can be explained using Faraday's Law [66]. As previously mentioned, the MRS voltage V is proportional to the rate of change of the magnetic field flux Ψ induced by the rotating magnetization [69,96]:

$$V = -\frac{d(\Psi)}{dt} = -\int \frac{d(\frac{B_1}{I} \cdot M_T)}{dt} dV_s \sim \frac{d(M_o e^{-i\omega_o t})}{dt} = -iM_o \omega_o e^{-i\omega_o t} \tag{1.68}$$

where M_T is the magnitude of the magnetization moments per volume in the transverse plane (Ampères/meter), V_s is the volume sample (meters^3), and $\frac{B_1}{I}$ is the magnetic field per unit current of the coil (Tesla/Ampères). For a 90° rotation, the magnitude of the transverse magnetization $M_T = M_o e^{-i\omega_o t}$ [96]. Each of M_o and ω_o, as shown in Section 1.2, are proportional to B_o. For *in-vivo* MRS, the noise is mainly due to the subject as opposed to electronics. Consequently, the noise voltage depends on $\sqrt{R}$, where R is the resistance of the subject that is sensed by the coil [97], and is proportional to B_o^2, yielding a B_o dependency for SNR.

Another advantage of high field MRS is improved spectral resolution. Equation (1.50) in Section 1.5.2 demands that the difference in frequency between protons with different chemical shifts increase with field strength; thus peaks are more separable using a higher field strength. Using higher magnetic field strengths also poses disadvantages. Magnetic field inhomogeneities and susceptibility effects increase with increasing field strength [31], leading to reduced T_2^* relaxation times and consequently larger linewidths as indicated in Figure 1.8 [31].

1.11 Citations

1. Machann J, Stefan N, Schabel C, et al. Fraction of unsaturated fatty acids in visceral adipose tissue (VAT) is lower in subjects with high total VAT volume - a combined ^{1}H MRS and volumetric MRI study in male subjects. NMR Biomed 2013;26:232-236.
2. Cordes C, Baum T, Dieckmeyer M, et al. MR-based assessment of bone marrow fat in osteoporosis, diabetes, and obesity. Front Endocrinol 2016;7:10.3389/fendo.2016.00074 (7 pages).
3. Kumar M, Jagannathan N, Seenu V, Dwivedi S, Julka P, Rath G. Monitoring the therapeutic response of locally advanced breast cancer patients: Sequential *in vivo* proton MR spectroscopy study. J Magn Reson Imaging 2006;24:325-332.
4. Korteweg MA, Veldhuis WB, Mali WPTM, et al. Investigation of lipid composition of dissected sentinel lymph nodes of breast cancer patients by 7T proton MR spectroscopy. J Magn Reson Imaging 2012;35:387-392.
5. He Q, Shkarin P, Hooley RJ, Lannin DR, Weinreb JC, Bossuyt VIJ. *In vivo* MR spectroscopic imaging of polyunsaturated fatty acids (PUFA) in healthy and cancerous breast tissues by selective multiple-quantum coherence transfer (Sel-MQC): A preliminary study. Magn Reson Med 2007;58:1079-1085.
6. Fardanesh R, Marino MA, Avendano D, Leithner D, Pinker K, Thakur SB. Proton MR spectroscopy in the breast: Technical innovations and clinical applications. J Magn Reson Imaging 2019;50:1033-1046.
7. Pollesello P, Eriksson O, Höckerstedt K. Analysis of total lipid extracts from human liver by ^{13}C and ^{1}H Nuclear Magnetic Resonance Spectroscopy. Anal Biochem 1996;236:41-48.
8. Johnson NA, Walton DW, Sachinwalla T, et al. Noninvasive assessment of hepatic lipid composition: Advancing understanding and management of fatty liver disorders. Hepatology 2008;47:1513-1523.
9. Patsch JM, Li X, Baum T, et al. Bone marrow fat composition as a novel imaging biomarker in postmenopausal women with prevalent fragility fractures. J Bone Miner Res 2013;28:1721-1728.
10. Yeung DKW, Griffith JF, Antonio GE, Lee FKH, Woo J, Leung PC. Osteoporosis is associated with increased marrow fat content and decreased marrow fat unsaturation: A proton MR spectroscopy study. J Magn Reson Imaging 2005;22:279-285.
11. Karampinos DC, Ruschke S, Dieckmeyer M, et al. Quantitative MRI and spectroscopy of bone marrow. J Magn Reson Imaging 2018;47:332-353.
12. Oriol A, Valverde D, Capellades J, Cabañas ME, Ribera JM, Arús C. *In vivo* quantification of response to treatment in patients with multiple myeloma by ^{1}H magnetic resonance spectroscopy of bone marrow. Magn Reson Mater Phy 2007;20:93-101.
13. Hodson L, Skeaff CM, Fielding BA. Fatty acid composition of adipose tissue and blood in humans and its use as a biomarker of dietary intake. Prog Lipid Res 2008;47:348-380.
14. Yeung DKW, Lam SL, Griffith JF, et al. Analysis of bone marrow fatty acid composition using high-resolution proton NMR spectroscopy. Chem Phys Lipids 2008;151:103-109.
15. Griffith JF, Yeung DKW, Ahuja AT, et al. A study of bone marrow and subcutaneous fatty acid composition in subjects of varying bone mineral density. Bone 2009;44:1092-1096.

16. Ren J, Dimitrov I, Sherry AD, Malloy CR. Composition of adipose tissue and marrow fat in humans by ^{1}H NMR at 7 Tesla. J Lipid Res 2008;49:2055-2062.
17. Lundbom J, Hakkarainen A, Fielding BA, et al. Characterizing human adipose tissue lipids by long echo time ^{1}H-MRS in vivo at 1.5 Tesla: validation by gas chromatography. NMR Biomed 2010;23:466-472.
18. Lundbom J, Hakkarainen A, Söderlund S, Westerbacka J, Lundbom N, Taskinen M-R. Long-TE ^{1}H MRS suggests that liver fat is more saturated than subcutaneous and visceral fat. NMR Biomed 2011;24:238-245.
19. Lundbom J, Bierwagen A, Bodis K, et al. Deep subcutaneous adipose tissue lipid unsaturation associated with intramyocellular lipid content. Metabolism 2016;65:1230-1237.
20. Lundbom J, Bierwagen A, Bodis K, et al. ^{1}H-MRS of femoral red and yellow bone marrow fat composition and water content in healthy young men and women at 3 T. Magn Reson Mater Phy 2019;32:591-597.
21. Machann J, Stefan N, Schick F. ^{1}H MR spectroscopy of skeletal muscle, liver and bone marrow. Eur J Radiol 2008;67:275-284.
22. Machann J, Stefan N, Wagner R, et al. Intra- and interindividual variability of fatty acid unsaturation in six different human adipose tissue compartments assessed by ^{1}H-MRS *in vivo* at 3 T. NMR Biomed 2017;30:e3744 (10 pages).
23. Gajdošík M, Hingerl L, Škoch A, et al. Ultralong TE *in vivo* ^{1}H NMR spectroscopy of omega-3 fatty acids in subcutaneous adipose tissue at 7 T. J Magn Reson Imaging 2019;50:71-82.
24. Dimitrov IE, Douglas D, Ren J, et al. *In vivo* determination of human breast fat composition by ^{1}H MRS at 7T. Magn Reson Med 2013;67:20-26.
25. Tufts LS, Shet K, Liang F, Majumdar S, Li X. Quantification of bone marrow water and lipid composition in anterior cruciate ligament-injured and osteoarthritic knees using three-dimensional magnetic resonance spectroscopic imaging. Magn Reson Imaging 2016;34:632-637.
26. Bingölbali A, Fallone BG, Yahya A. Comparison of optimized long echo time STEAM and PRESS proton MR spectroscopy of lipid olefinic protons at 3 Tesla. J Magn Reson Imaging 2015;41:481-486.
27. Troitskaia A, Fallone BG, Yahya A. Long echo time proton magnetic resonance spectroscopy for estimating relative measures of lipid unsaturation at 3 T. J Magn Reson Imaging 2013;37:944-949.
28. Oostendorp M, Engelke UFH, Willemsen MAAP, Wevers RA. Diagnosing inborn errors of lipid metabolism with proton nuclear magnetic resonance spectroscopy. Clin Chem 2006;52:1395-1405.
29. Bottomley PA. Spatial localization in NMR spectroscopy *in vivo*. Ann NY Acad Sci 1987;508:333-348.
30. Frahm J, Merboldt K-D, Hänicke W. Localized proton spectroscopy using stimulated echoes. J Magn Reson 1987;72:502-508.
31. Ladd ME. Pros and cons of ultra-high-field MRI/MRS for human application. Prog Nucl Mag Res Sp 2018;109:1-50.
32. Ocali O, Atalar E. Ultimate intrinsic signal-to-noise ratio in MRI. Magn Reson Med 1989;39:462-473.

33. Strobel K, van den Hoff J, Pietzsch J. Localized proton magnetic resonance spectroscopy of lipids in adipose tissue at high spatial resolution in mice *in vivo*. J Lipid Res 2008;49:473-480.
34. He D, Mustafi D, Fan X, et al. Magnetic resonance spectroscopy detects differential lipid composition in mammary glands on low fat, high animal fat versus high fructose diets. PLOS ONE 2018;13:e0190929 (12 pages).
35. Lee Y, Jee H, Noh H, et al. In vivo ^{1}H-MRS hepatic lipid profiling in nonalcoholic fatty liver disease: an animal study at 9.4 T. Magn Reson Med 2013;70:620-629.
36. Yahya A, Tessier AG, Fallone BG. Effect of J-coupling on lipid composition determination with localized proton magnetic resonance spectroscopy at 9.4 T. J Magn Reson Imaging 2011;34:1388-1396.
37. Yaligar J, Gopalan V, Wee Kiat O, et al. Evaluation of dietary effects on hepatic lipids in high fat and placebo diet fed rats by *in vivo* MRS and LC-MS techniques. PLOS ONE 2014:0091436 (10 pages).
38. de Graaf RA, Klomp DWJ, Luijten PR, Boer VO. Intramolecular zero-quantum-coherence 2D NMR spectroscopy of lipids in the human breast at 7 T. Magn Reson Med 2014;71:451-457.
39. Ramamonjisoa N, Ratiney H, Mutel E, et al. *In vivo* hepatic lipid quantification using MRS at 7 Tesla in a mouse model of glycogen storage disease type 1a. J Lipid Res 2013;54:2010-2022.
40. Bougnoux P, Koscielny S, Chajès V, Descamps P, Couet C, Calais G. α- Linolenic acid content of adipose breast tissue: a host determinant of the risk of early metastasis in breast cancer. Br J Cancer 1994;70:330-334.
41. Lundbom J, Heikkinen S, Fielding B, Hakkarainen A, Taskinen M-R, Lundbom N. PRESS echo time behavior of triglyceride resonances at 1.5 T: Detecting ω-3 fatty acids in adipose tissue *in vivo*. J Magn Reson 2009;201:39-47.
42. Škoch A, Tošner Z, Hájek M. The *in vivo* J-difference editing MEGA-PRESS technique for the detection of n-3 fatty acids. NMR Biomed 2014;27:1293-1299.
43. Wang J, Wang M-Y, Kuo W-H, Chen K-L, Shih TT-F. Proton MR spectroscopy of normal breasts: Association of risk factors for breast cancer with water and lipid composition of the breast. Magn Reson Imaging 2016;34:524-528.
44. Škoch A, Jírů F, Dezortová M, et al. Intramyocellular lipid quantification from ^{1}H long echo time spectra at 1.5 and 3 T by means of the LCModel technique. J Magn Reson Imaging 2006;23:728-735.
45. Mosconi E, Fontanella M, Sima DM, et al. Investigation of adipose tissues in Zucker rats using *in vivo* and *ex vivo* magnetic resonance spectroscopy. J Lipid Res 2011;52:330-336.
46. Dimitrov I, Ren J, Sherry D, Malloy C. Fundamental advantages at 7 T allow for fat composition quantification. Medicamundi 2009;53:42-46.
47. Knothe G, Kenar JA. Determination of the fatty acid profile by ^{1}H-NMR spectroscopy. Eur J Lipid Sci Tech 2004;106:88-96.
48. Vlahov G. Application of NMR to the study of olive oils. Prog Nucl Mag Res Sp 1999;35:341-357.
49. Viallon M, Leporq B, Drinda S, et al. Chemical-shift-encoded Magnetic Resonance Imaging and Spectroscopy to reveal immediate and long-term multi-organs composition changes of a 14-days periodic fasting intervention: A technological and case report. Front Nutr 2019;6:1-13.

50. Yahya A, Fallone BG. T_2 determination of the J-coupled methyl protons of lipids: *In vivo* illustration with tibial bone marrow at 3T. J Magn Reson Imaging 2010;31:1514-1521.
51. Osawa CC, Gonçalves LAG, Ragazzi S. Correlation between free fatty acis of vegetable oils evaluated by rapid tests and by the official method. J Food Compos Anal 2007;20:523-528.
52. Mougios V. Exercise biochemistry: Human Kinetics: 2006.
53. Fadzillah NA, Rohman A, Salleh RA, et al. Authentication of butter from lard adulteration using high-resolution of nuclear magnetic resonance spectroscopy and high-performance liquid chromatography. Int J Food Prop 2017;20:2147-2156.
54. Mundi MS, Koutsari C, Jensen MD. Effects of increased fatty acid availablity on adipose tissue fatty acid storage in men. J Clin Endocrinol Metab 2014;99:E635-E2642.
55. Attané C, Estève D, Chaoui K, Schiltz O, Reina N, Muller C. Human bone marrow is comprised of adipocytes with specific lipid metabolism. Cell Reports 2020;30:949-958.
56. Ebbert JO, Jensen MD. Fat depots, free fatty acids, and dysipidemia. Nutr 2013;5:498-508.
57. Bottomley P. Chapter 1: Basics of NMR. Handbook of Magnetic Resonance Spectroscopy *in vivo*: MRS theory, practice and applications: John Wiley & Sons Ltd; 2016.
58. Jensen WB. The origins of the symbols A and Z for atomic weight and number. J Chem Edu 2005;82:1764-1765.
59. Constantinides C. Magnetic Resonance Imaging: The basics: CRC Press Taylor Francis Group: 2014.
60. Singhal A. The Pearson guide to physical chemistry for the IIT JEE: Pearson India: 2014.
61. Pochapsky T, Pochapsky S. NMR for physical and biological scientists: Garland Science Taylor & Francis Group: 2006.
62. Krey U, Owen A. Basic theoretical physics: A concise overview: Springer: 2007.
63. de Graaf RA. *In vivo* NMR spectroscopy: Principles and techniques. West Sussex PO19 8SQ, England: John Wiley & Sons: 2007.
64. Susskind L, Friedman A. Quantum mechanics: the theoretical minimum. New York: Basic Books: 2014.
65. Cowan B. Nuclear magnetic resonance and relaxation: Cambridge University Press: 1997.
66. Griffiths DJ. Introduction to electrodynamics.: Pearson: 2013.
67. Fujita H, T. Z, Yang X, Finnerty MJ, Handa S. RF surface receive array coils: The art of an LC circuit. J Magn Reson Imaging 2013;38:12-25.
68. De Zanche N. Birdcage volume coil design. eMagRes 2011: 10.1002/9780470034590/emrstm.1288 (11 pages).
69. Elster AD. Questions and Answers in MRI http://mriquestions.com/index.html. 2019.
70. Park S-H. MRI Fundamentals. Volume 2021. Department of Bio and Brain Engineering: Korea Advanced Institute of Science and Technology.
71. Collins CM. Electromagnetics in magnetic resonance imaging: Physical principles, related applications, and ongoing developments: Morgan & Claypoll Publishers: 2016.
72. Hahn EL. Spin echoes. Phys Rev 1950;80:580-602.
73. Luo H. Physics-based data analysis for wind turbine condition monitoring. Clean Energy 2017;1:4-22.

74. Ordidge RJ, Bendall MR, Gordon RE, Connelly A. Volume selection for *in-vivo* spectroscopy. Magnetic Resonance in Biology and Medicine: Tata McGraw-Hill; 1985.
75. Bottomley P. Selective volume method for performing localized NMR spectroscopy. USA; 1984.
76. Traber F, Block R, Lamerichs J. ^{1}H metabolite ralxation times at 3.0 Tesla: Measurements of T_1 and T_2 values in normal brain and determination of regional differences in transverse relaxation. J Magn Reson Imaging 2004;19:537-545.
77. Helms G. Analysis of 1.5 Tesla proton MR spectra of human brain using LCmodel and an imported basis set. Magn Reson Imaging 1999;17:1211-1218.
78. Zhu X, Tomanek B, Sharp J. A pixel is an artifact: On the necessity of zero-filling in fourier imaging. Concepts Magn Reson 2013;42A:32-44.
79. Lindon JC, Ferrige AG. Digitisation and data processing in Fourier transform NMR. Prog Nuc Magn Reson Sp 1980;14:27-66.
80. Barthold E, Ernst RR. Fourier spectroscopy and causality principle. J Magn Reson 1973;11:9-19.
81. Balci M. Basic ^{1}H- and ^{13}C- NMR spectroscopy: Elsevier: 2005.
82. Harris RK, Lynden-Bell RM. Nuclear magnetic resonance spectoscopy: A physicochemical view: Pitman Publishing: 1983.
83. de Graaf R, Rothman D. *In vivo* detection and quantification of scalar coupled ^{1}H NMR resonances. Concepts Magn Reson 2001;13:32-76.
84. Keeler J. Chapter 6: Product Operators (from course "Understanding NMR spectroscopy"). University of Cambridge, Department of Chemistry; 2004.
85. Goldenberg DP. The Product Operator Formalism: A Physical and Graphical Interpretation. Concepts Magn Reson 2010;36A:49-83.
86. Sørensen OW, Eich GW, Levitt MH, Bodenhausen G, Ernst RR. Product operator formalism for the description of NMR pulse experiments. Prog Nucl Mag Res Sp 1983;16:163-192.
87. Kay LE, McClung RED. A product operator description of AB and ABX spin systems. J Magn Reson 1988;77:258-273.
88. Wilman A, Allen P. The response of the strongly coupled AB system of citrate to typical ^{1}H MRS localization sequences. J Magn Reson B 1995;107:25-33.
89. Thompson RB, Allen PS. Response of metabolites with coupled spins to the STEAM sequence. Magn Reson Med 2001;45:955-965.
90. Wilman A, Allen P. Observing N-acetyl aspartate via both its N-acetyl and its strongly coupled aspartate groups in *in-vivo* proton Magnetic Resonance Spectroscopy. J Magn Reson B 1996;113:203-213.
91. Hamilton G, Middleton MS, Bydder M, et al. Effect of PRESS and STEAM sequences on magnetic resonance spectroscopic liver fat quantification. J Magn Reson Imaging 2009;30:145-152.
92. Stables L, Kenna R, Anderson A, Constable R, Gore J. Analysis of J coupling-induced fat suppression in DIET imaging. J Magn Reson 1999;136:143-151.
93. Thompson RB, Allen PS. Sources of variability in the response of coupled spins to the PRESS sequence and their potential impact on metabolite quantification. Magn Reson Med 1999;41:1162-1169.

94. Yablonskiy DA, Neil JJ, Raichle ME, Ackerman JJ. Homonuclear J coupling effects in volume localized NMR spectroscopy: pitfalls and solutions. Magn Reson Med 1998;39:169-178.
95. Snyder J, Wilman A. Field strength dependence of PRESS timings for simultaneous detection of glutamate and glutamine from 1.5 to 7 T. J Magn Reson 2010;203:66-72.
96. Hoult DI, Richards RE. The signal-to-noise ratio of the nuclear magnetic resonance experiment. J Magn Reson Imaging 1976;24:71-85.
97. Hoult D, Lauterbur PC. The sensitivity of the zeugmatographic experiment involving human samples. J Magn Reson 1979;34:341-344.

Chapter 2

Background Information, Methods, and Procedures

2.1 Fatty Acids

2.1.1 Fatty Acid Structures

Fatty acids comprise fats, oils, and waxes [1]. These structures are mostly insoluble in water, but soluble in non-polar organic solvents. Fatty acids are mainly used in the body to store energy as either fat deposits, adipose tissue or cell membranes. Fatty acids are mainly composed of carbon (C), hydrogen (H), and oxygen (O) Figure 2.1 depicts a fatty acid (linoleic acid) [1]. The fatty acid comprises of a carboxyl group (COOH) at one end and a methyl (CH_3) group at the other end. In the body, three fatty acids are attached to a glycerol backbone to form a triglyceride [2], as depicted in Figure 2.2, where R denotes the attached fatty acids.

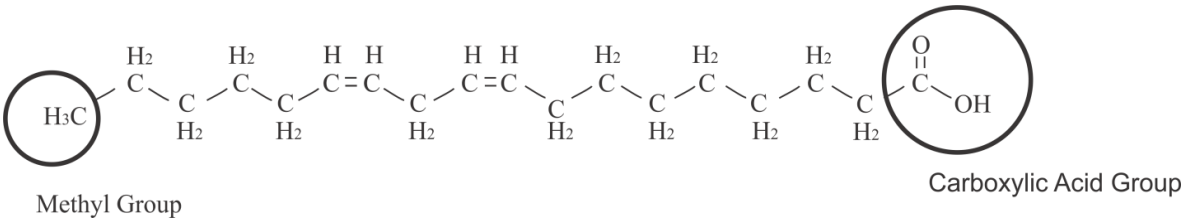

Figure 2.1: Molecular structure of linoleic acid, a di-unsaturated fatty acid

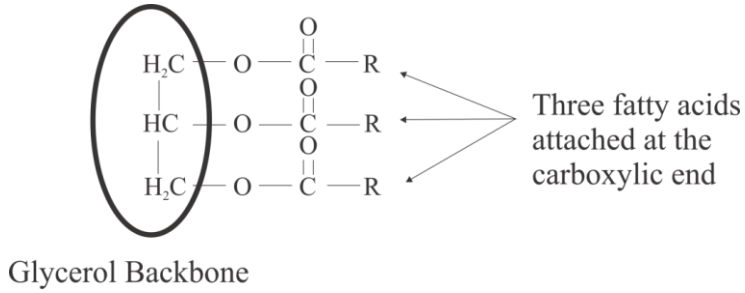

Figure 2.2: Molecular structure of a triglyceride, where 'R' denotes the attached fatty acids.

2.1.2 Saturated Fatty Acids

Figure 2.3 displays examples of the fatty acids found in adipose tissue. Saturated fatty acids (SFA) have no double bonds between carbon atoms. In the body, the saturated fatty acids consist primarily of palmitic acid [3-5]. Palmitic acid is displayed as the first fatty acid in Figure 2.3. Saturated fatty acids make up about 28% of fatty acid content in human adipose tissue [3-5].

2.1.3 Unsaturated fatty acids

Unsaturated fatty acids have at least 1 double bond between carbon atoms. Mono-unsaturated fatty acids (MUFA) have one double bond and constitute about 51% of human adipose tissue [3-5]. The second structure shown in Figure 2.3 is oleic acid, which is the primary mono-unsaturated fatty acid in humans [3-5]. If unsaturated fatty acids have more than one double bond, they are referred to as poly-unsaturated fatty acids (PUFA). Di-unsaturated fatty acids have two double bonds and form about 14% of human adipose fat content [3-5]. Di-unsaturated fatty acids are mostly linoleic acid in adipose tissue [3-5]. The latter is depicted in Figure 2.3. Tri-unsaturated fatty acids have three double bonds and are about 1% of human fat content [3-5]. Oleic acid is an omega-9 fatty acid because the 1st carbon-to-carbon double bond is at the 9th carbon from the methyl [1]. Likewise, linoleic acid is an omega-6 fatty acid and linolenic acid is an as omega-3 fatty acid due to the positions of their 1st double bond. Other ω-3 fatty acids of higher degree of un-saturation (docosahexaenoic acid and eicosapentaenoic acid) make up less than 0.5 % of the total fatty acid content [3].

Palmitic acid (saturated fatty acid)

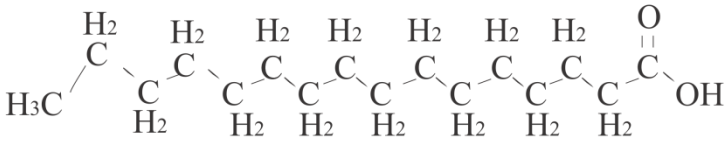

Oleic acid (mono-unsaturated fatty acid)

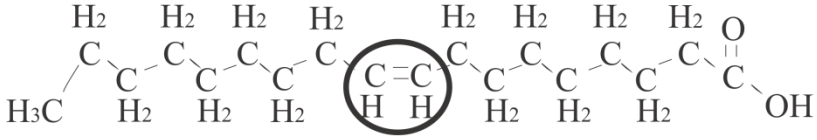

Linoleic acid (di-unsaturated fatty acid)

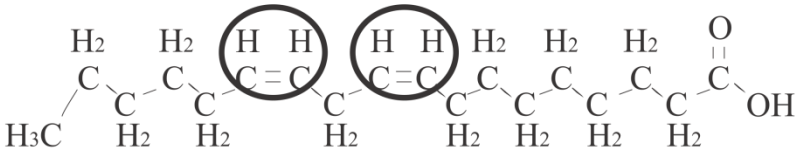

Linolenic acid (tri-unsaturated fatty acid)

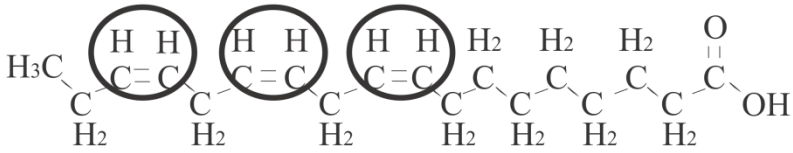

Figure 2.3: Molecular structure of several fatty acids. Palmitic acid is saturated, oleic acid is mono-unsaturated, linoleic acid is di-unsaturated, and linolenic acid is tri- unsaturated. Oleic acid is an ω-9 fatty acid, whereas linoleic acid and linolenic acid are ω-6 and ω-3 fatty acids, respectively. The double bonds are denoted in circles.

2.2 MRS of Fatty Acids

2.2.1 Chemical Shift of Relevant Protons

The concept of chemical shift was introduced in Chapter 1 and is exploited in fat composition quantification with MRS. Figure 2.4 displays the spectrum obtained from linoleic acid using STEAM (STimulated Echo Acquisition Mode) with a TE (echo time) of 20 ms and a TM (mixing time) of 20 ms at 3 T. The bulk methylene (CH_2) protons resonate at approximately 1.3 ppm. The allylic methylene (CH=CH-C**H**$_2$-) protons resonate at ≈ 2.0 ppm and the diallylic methylene (CH=CH-C**H**2-CH=CH) protons resonate at ≈ 2.8 ppm. The olefinic protons (C**H**=C**H**) resonate at ≈ 5.4 ppm. The methyl groups of saturated fatty acids, oleic acid and linoleic acids resonate at 0.823 ppm, 0.823 ppm and 0.839 ppm, respectively [6]. The methyl groups of all three fatty acids have J-coupling interactions with their 1.3 ppm methylene neighbours [7]. In contrast, the methyl protons of ω-3 fatty acids resonate at about 0.925 ppm [6] and are coupled to their ≈ 2.0 ppm allylic protons [7]. At 9.4 T, both methyl groups are weakly-coupled to their corresponding neighbors. At 3 T, the ω-3 methyl protons undergo a weaker coupling interaction compared to the non-ω-3 methyl protons, leading to differences in J-coupling behaviour between ω-3 and non-ω-3 methyl protons. All unsaturated fatty acids will contribute to the olefinic peak. Each di-unsaturated fatty acid and tri-unsaturated fatty acid will contribute twice and three times as much signal, respectively, as a mono-unsaturated fatty acid to the olefinic peak. Di-unsaturated and tri-unsaturated fatty acids will also contribute to the diallylic peak. Each tri-unsaturated fatty acid will contribute twice as much area than each di-unsaturated fatty acid. The area of the bulk methylene peak will be proportional to the average chain length of all the fatty acids in a given sample. All fatty acids should contribute the same signal to the methyl peak, regardless of saturation level or chain length, making the methyl proton an effective normalization factor [8]. The various fat peaks are utilized in several different ways for fat composition assessment. The protons of the glycerol backbone also yield characteristic peaks and have been utilized to study relative free fatty acid (versus triglyceride) levels [9]. The protons of the central carbons resonate at ≈ 5.2 ppm [10] and those of the outer carbons resonate at 4.1 ppm and 4.3 ppm [10]. Chapter 3 of this thesis is focused on sequence optimization involving the methyl protons at 9.4 T. Chapters 4 pertains to sequence optimization based on signal from the methyl and olefinic protons at 3 T. In Chapter 5, measurements of the

methyl, olefinic, diallylic, and methylene protons are obtained at 3 T. Chapter 6 optimizes sequences for olefinic quantification and minimizing glycerol (middle carbon) proton signal.

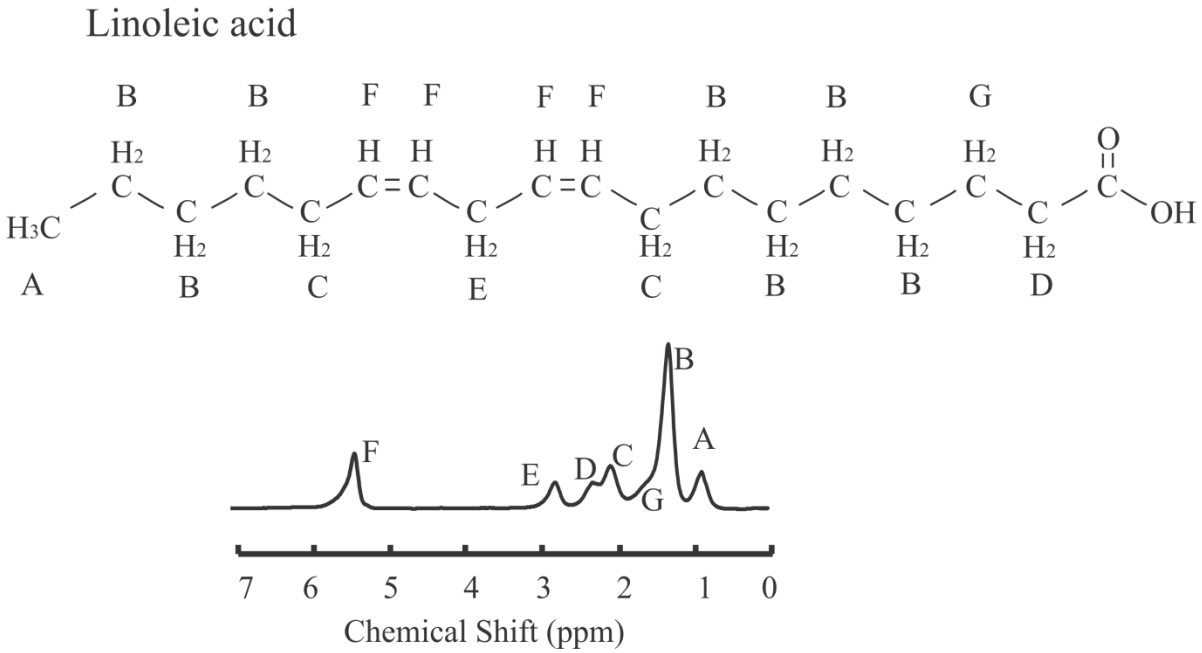

Figure 2.4: MRS spectrum of linoleic acid acquired using STEAM TE= 20 ms (TM= 20 ms) at 3 T. The bulk methylene (CH_2) protons resonate at 1.3 ppm. The allylic methylene (CH=CH-C**H**$_2$-) protons resonate at ≈ 2.0 ppm and the diallylic methylene (CH=CH-C**H**$_2$-CH=CH) protons resonate at ≈ 2.8 ppm. The olefinic protons (C**H**=C**H**) resonate at ≈ 5.4 ppm.

2.2.2 Signal Evolution of the Fat Protons

All protons in fatty acids are involved in J-coupling interactions [11-14]. Figure 2.5 illustrates the J coupling interactions in the fatty acid chains at 3 T. At 9.4 T, coupling strengths are weaker accordingly as described in Chapter 1. The most relevant proton interactions in this thesis are those of the methylene, olefinic, and methyl protons. The 1.3 ppm methylene protons are coupled to the 0.9 ppm methyl protons (J = 6.9 Hz [11], J/δ ≈ 0.04 at 9.4 T, J/δ ≈ 0.1 at 3 T) in non-ω-3 fatty acids, and the 2.0 ppm allylic protons (J = 7.1 Hz [14], J/δ ≈ 0.03 at 9.4 T, J/δ ≈ 0.08 at 3 T). The 1.3 ppm methylene protons are also coupled to the 1.6 ppm methylene protons (J = 7.1 Hz [14], J/δ ≈ 0.06 at 9.4 T, J/δ ≈ 0.2 at 3 T). The 5.4 ppm olefinic protons are coupled to each

other (J ≈ 16.3 Hz [15], J/δ ≈ 0.08 at 9.4 T, J/δ ≈ 0.3 at 3 T) and coupled to their neighboring 2.0 ppm and 2.8 ppm protons (J = 7 Hz [15], J/δ ≈ 0.005 at 9.4 T, J/δ ≈ 0.02 at 3 T). As previously described, the methyl groups of saturated fatty acids, oleic acid, and linoleic acid are involved in J-coupling interactions with their 1.3 ppm methylene neighbours [7] whereas the methyl protons of ω-3 fatty acids are coupled to their neighbouring ≈ 2.0 ppm allylic protons (J = 7.5 Hz [13], J/δ ≈ 0.02 at 9.4 T, J/δ ≈ 0.05 at 3 T). The glycerol CH protons (≈ 5.2 ppm) on triglyceride backbones also undergo J-coupling interactions. They are coupled to the methylene glycerol protons that resonate at 4.1 ppm an 4.3 ppm [10]. This coupling interaction will be explored further in Chapter 6.

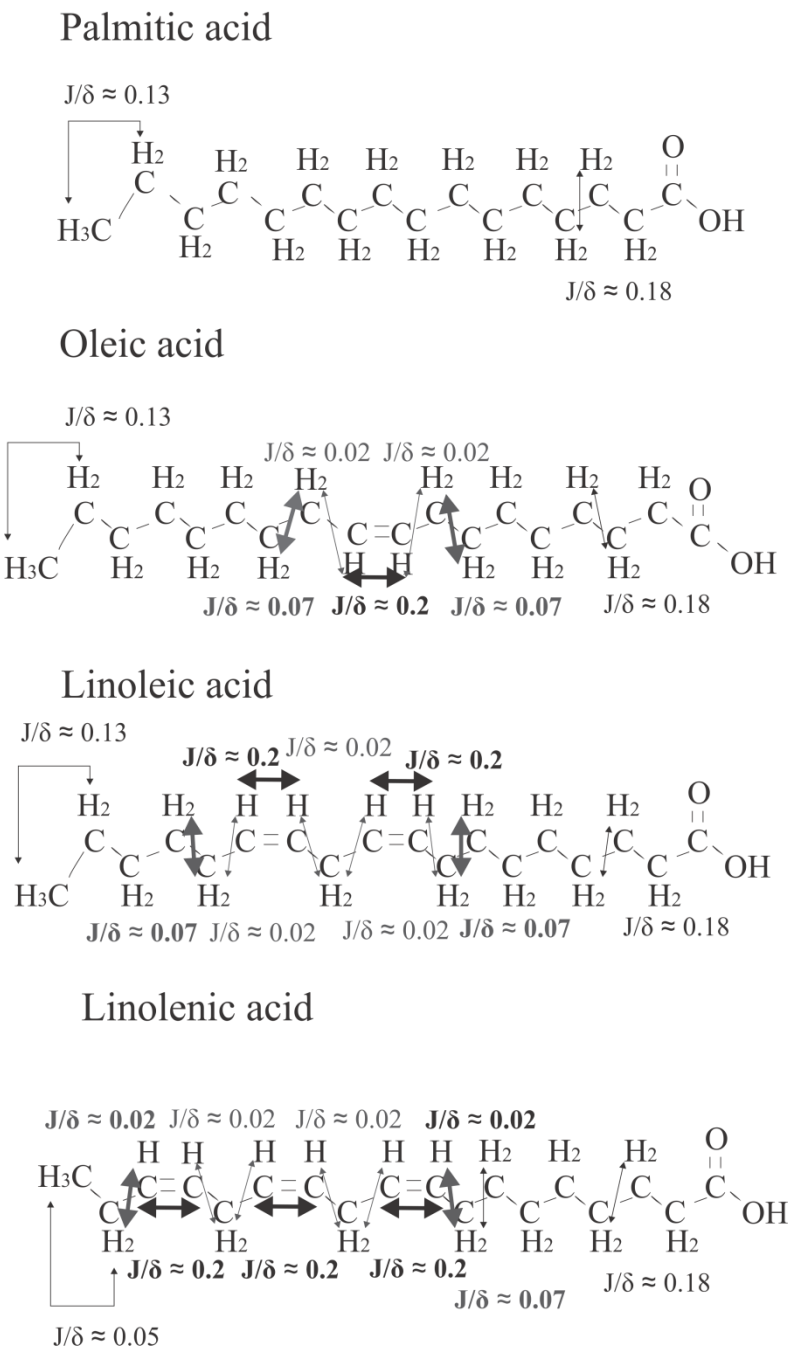

Figure 2.5: J-coupling interactions in adipose fatty acids. Values of $\frac{J}{\delta}$ are shown for 3 T.

2.3 General MRI Hardware

2.3.1 Basic MR Scanner

Figure 2.6 displays the cross-section of a cylindrical MRI scanner. These scanners use a super-conducting solenoid magnet which yields a horizontal $\overrightarrow{B_o}$ field. A cylindrical cryostat is used to maintain superconductivity. The coils are submerged in helium. A nitrogen outer shell reduces helium boil-off for the 9.4 T magnet in this work. For the 3 T magnet, a cold head re-condenses helium gas to liquid to prevent it from burning off. Gradient coils are multi-faceted inside the cylindrical magnet. As mentioned in Chapter 1, the gradient field alters the main magnetic field in a predictable way and can be used for selecting 3D voxels in spectroscopy. A current is delivered to the gradient coils to form a secondary magnetic field. In standard cylindrical magnets, gradients are produced by coils winded on a coaxial cylindrical surface. Figure 2.7 displays a Maxwell pair, which is used to create a gradient in the z direction. Shim coils are also layered within the cylindrical magnet. The shim coils are used for correcting field inhomogeneities. Passive shims consist of magnetic materials strategically placed in appropriate locations at the set-up of the magnet. Active shims are coil windings that deliver a current to create additional magnetic fields that compensate for the inhomogeneities of the original field. The RF coil is closest to the MRI subject and transmits and receives the MR signal, unless a different coil (such as a surface coil or birdcage head coil) is used instead (Section 1.3.4). The MRI scanner is shielded from its surroundings through either passive shielding, such as a steel RF shield, or active shielding. The latter consists of constructing electrical windings that create their own magnetic field to negate the main magnetic field where it is not needed.

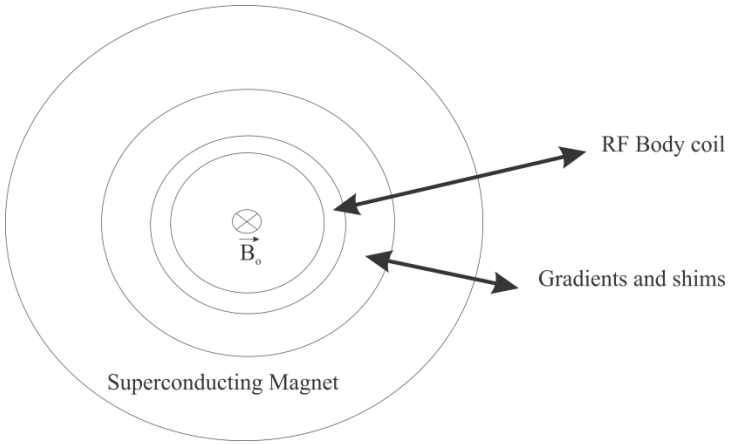

Figure 2.6: Cross-section of a standard cylindrical MRI scanner, indicating the positions of the RF body coil, shim and gradients coils, and the superconducting magnet.

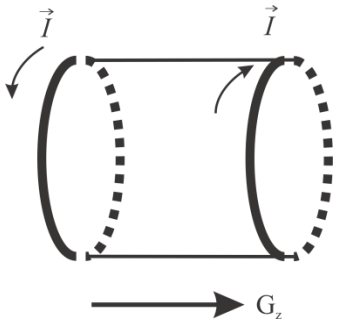

Figure 2.7: A Maxwell Pair used to create a gradient in the z-direction.

2.3.2 The RF Transmit Chain

The transmit chain amplifies the RF signal created by the spectrometer and guides it to the RF coil (Figure 2.8) [16]. A power monitoring unit accounts for patient safety by sampling forward and reflected power at the amplifier's output to supervise the specific absorption rate (SAR) [16]. A transmit/receive switch is used to isolate one of the modes if a coil can be used for both transmission and reception [17]. Impedance matching is performed at either end of a transmission line for highest energy transfer between the coil and subject [17].

Figure 2.8: Steps in the RF Transmit Chain.

2.3.3 Quadrature Mode

Quadrature mode or transmission is used to reduce power waste or ameliorate coil sensitivity. It is formed using two independent linearly-polarized coils at two connections with a 90° phase shift in the sinusoidal electrical current delivered [17]. Driving equal powers to each connection yields double the $\overrightarrow{B_1}$ field magnitude compared to only using the original linearly-polarized coil. This change yields a $\sqrt{2}$ increase in sensitivity [17,18]. Volume coils can be driven in quadrature mode but surface coils can only be driven linearly; thus quadrature mode is an added advantage of using a volume coil.

2.3.4 The RF Receive Chain

As described in Chapter 1, MR signal detection requires an RF coil tuned to the Larmor frequency of the spins system. A voltage is induced by Faraday's Law of Induction from the precessing magnetization. The Signal to Noise Ratio (SNR) was described in Chapter 1, and can be calculated in experiments as the average signal intensity over the standard deviation of the noise [19]. Equation 1.16 in Chapter 1 describes the magnetization vector for a spin ½ system as [20]:

$$M_o = \frac{\gamma^2 \hbar^2 N B_o}{4kT} \tag{2.1}$$

Equation 1.68 in Chapter 1 also indicates that the voltage signal,V, depends on this magnetization:

$$V \sim \frac{d(M_o e^{-i\omega_o t})}{dt} = -iM_o \omega_o e^{-i\omega_o t} \tag{2.2}$$

Chapter 1 specified that signal increases with voxel volume [17]. The signal also relies on the reception quality of the coil, or its ability to induce EMF from the magnetic flux in the coil, B_T [21]. Acquiring more averages in MRS also yields increasing signal, linearly with the number of averages N_{AVE} [17]. The factors described above affect signal. The other important parameter for SNR is the noise. The dominant noise in MRI arises from ions within the subject. The ions constitute shifting magnetic fields that are sensed by the reception coil [22]. This ionic motion is arbitrary and yields a frequency spectrum that includes all frequencies within the bandwidth (BW) of the MRI study. The standard deviation of this noise (V_N) indicates how the signal changes due to noise (Equation (2.3)) [17]. Since the ionic movement is random, the standard deviation of the noise is effected by temperature (Equation (2.3)) [23,24]:

$$V_N \sim (BW)^{1/2}(4kT)^{1/2} \tag{2.3}$$

In Equation (2.3), k is the Boltzmann constant and T is the temperature. Section 1.10 described that the noise standard deviation is also proportional to $\sqrt{R}$ [22] (R is resistance) and R is proportional to B_o^2 in *in-vivo* MR systems [22]. This relationship differs in experiments where coil noise dominates, like with NMR of small chemical samples [22]. The noise also increases with the number of averages but it is not correlated between measurements. Aggregating the random noise yields a $N_{AVE}^{1/2}$ increase in the standard deviation of the noise [17]. Considering all these factors, the SNR can be written as [17,20,22-24]:

$$SNR = \frac{V}{V_N} \sim \frac{M_o \omega_o (voxel\ volume) B_T N_{AVE}^{1/2}}{\sqrt{4kT(BW)R}} \tag{2.4}$$

where B_T is the coil's capacity to produce EMF from the magnetic flux in the coil. Due to reciprocity [21], maximizing B_T is equivalent to maximizing it's transmit sensitivity.

In addition to the coil, the NMR signal is processed through several other devices (including amplification devices) in the receive chain before it is digitized and used [17]. Each of these devices can potentially add noise and reduce the SNR.

2.3.5 Eddy Current Compensation

Eddy currents are induced in conductors by a changing magnetic field (such as gradients turning on and off) [25]. The eddy currents themselves create magnetic fields that oppose the initial generating field, yielding artifacts and distortions. Compensation involves modifying the input current to the gradients to pre-distort the pulse shapes, accounting for anticipated eddy-current biases as effectively as possible [25]. Figure 2.9 displays how eddy current compensation systems (also known as a pre-emphasis systems) pre-distort the waveform to correct for eddy currents.

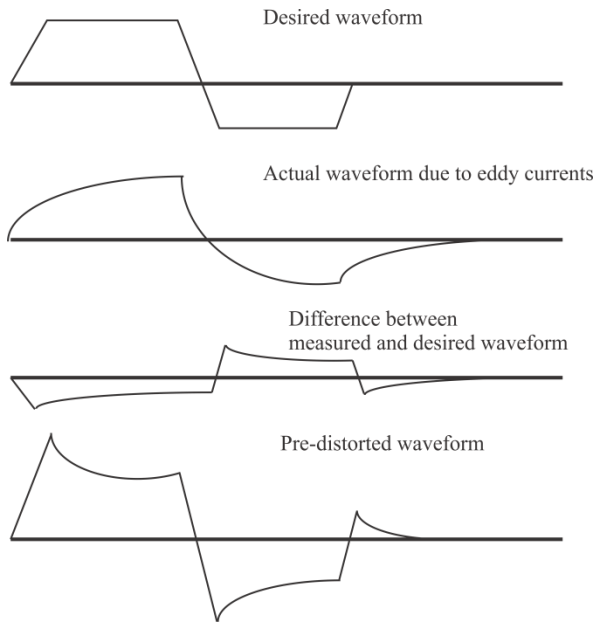

Figure 2.9: Eddy current compensation. The top waveform is the desired waveform. The actual waveform is distorted because of eddy currents. The pre-emphasis system computes the difference between the two waveforms and adjusts the input waveform (bottom) to compensate for the biases. Adapted from Burl [26].

2.4 Using Product Operator Formalism to Predict Methyl Spin Behavior

Chapter 1 introduced product operator formalism as a means to predict uncoupled and weakly coupled spin response to pulse sequences. At 9.4 T, both ω-3 and non-ω-3 methyl groups are weakly coupled and their theoretical behaviour can be modelled [13,27-30] and exploited to resolve ω-3 methyl resonances from non-ω-3 methyl resonances. This section describes the product operator derivation of the response of weakly coupled methyl protons to a spin echo sequence [13], using counter-clockwise rotations and the axes shown in Figure 1.25. The derivation was used to optimize the PRESS sequence at 9.4 T to resolve the weakly coupled ω-3 and non-ω-3 proton signals.

The ω-3 and non-ω-3 methyl protons were modeled as A_2X systems. X is one of three methyl protons and A_1 and A_2 are each of the neighboring allylic protons (for ω-3 fats) or methylene protons (for non-ω-3 fats) [13]. The derivation is equivalent for the ω-3 and non-ω-3 methyl protons. As mentioned in Chapter 1, a spin-echo sequence refocuses chemical shift evolution. In the following description, the J-coupling evolution for the spins after they are excited by a 90° pulse is described as per Table 1.4. The coupling Hamiltonians required are:

$$H_{J1} = 2\pi J_{A_1X} X_z A_{1z} \tag{2.5}$$

$$H_{J2} = 2\pi J_{A_2X} X_z A_{2z} \tag{2.6}$$

The impact of coupling with A_1 during free precession for time t is calculated using Table 1.4:

$$X_x \xrightarrow{2\pi J_{A_1X} X_z A_{1z}} X_x \cos\left(\pi J_{A_1X} t\right) + 2X_y A_{1Z} \sin\left(\pi J_{A_1X} t\right) \tag{2.7}$$

The impact of coupling with A_2 during the free precession is then quantified (also using Table 1.4):

$$X_x \cos\left(\pi J_{A_1X} t\right) + 2X_y A_{1Z} \sin\left(\pi J_{A_1X} t\right) \xrightarrow{2\pi J_{A_2X} X_z A_{2z}} \cos\left(\pi J_{A_1X} t\right) [X_x \cos\left(\pi J_{A_2X} t\right) + 2X_y A_{2Z} \sin\left(\pi J_{A_2X} t\right)] + \sin\left(\pi J_{A_1X} t\right) [2X_y A_{1Z} \cos\left(\pi J_{A_2X} t\right) - 4X_x A_{1Z} A_{2Z} \sin\left(\pi J_{A_2X} t\right)] \tag{2.8}$$

The ω-3 methyl protons share the same coupling constant with both their neighboring allylic protons (7.5 Hz) [13] and the non-ω-3 methyl protons share the same coupling constant with both their neighboring methylene protons (6.9 Hz) [11]; thus, the expression above can be simplified:

$$J_{A_1X} = J_{A_2X} = J_{AX} \tag{2.9}$$

$$X_x \xrightarrow{2\pi J_{A_1X} X_z A_{1z}} \xrightarrow{2\pi J_{A_2X} X_z A_{2z}} X_x cos^2(\pi J_{AX} t) + 2X_y A_{2Z} \sin(\pi J_{AX} t) \cos(\pi J_{AX} t) + 2X_y A_{1Z} \sin(\pi J_{AX} t) \cos(\pi J_{AX} t) - 4X_x A_{1Z} A_{2Z}\, sin^2(\pi J_{AX} t) \tag{2.10}$$

The above can be re-arranged to yield the following:

$$X_x \xrightarrow{2\pi J_{A_1X} X_z A_{1z}} \xrightarrow{2\pi J_{A_2X} X_z A_{2z}} X_x[\tfrac{1}{2} + \tfrac{\cos(2\pi J_{AX} t)}{2}] + 2X_y A_{2Z} \sin(\pi J_{AX} t) \cos(\pi J_{AX} t) + 2X_y A_{1Z} \sin(\pi J_{AX} t) \cos(\pi J_{AX} t) - 4X_x A_{1Z} A_{2Z}\, sin^2(\pi J_{AX} t) \tag{2.11}$$

The only term leading to methyl proton observable magnetization is:

$$X_x \left[\frac{1}{2} + \frac{\cos(2\pi J t)}{2}\right] \tag{2.12}$$

All other terms correspond to anti-phase coherences. The methyl protons form a triplet signal, with a constant central peak ($\frac{X_x}{2}$) and sinusoidally varying side multiplets ($\frac{X_x cos(2\pi JTE)}{2}$). Timings where the in-phase side peak signals sum to 0 minimize overlap between the two peaks and occur for total TE values of:

$$\frac{(2n+1)}{4J} \tag{2.13}$$

where n is an integer. Timings where the side multiplets are positive in-phase occur for total TEs of:

$$\frac{n}{J} \tag{2.14}$$

Timings where the side multiplets are negative in-phase occur for total TE values of:

$$\frac{2n+1}{2J} \tag{2.15}$$

Since the J constants are slightly different for ω-3 and non-ω-3 methyls, these timings are different for the two protons and don't overlap perfectly. Figure 2.10 displays the expected theoretical behaviour of weakly-coupled methyl peaks.

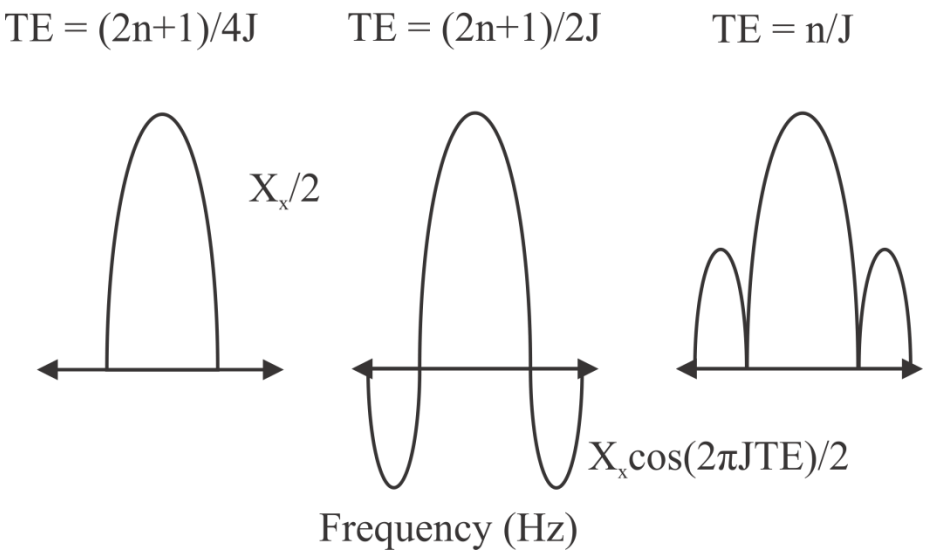

Figure 2.10: Expected J-evolution of weakly coupled methyl protons. The central peak is constant (outside of T_2 decay) while the outer triplet peaks vary sinusoidally with TE.

2.5 Experiments at 9.4 T

2.5.1 9.4 T Magnet

The 9.4 T MR system consists of a 9.4 T, 21.5 cm diameter MRI scanner from Magnex Scientific, Oxford, UK. It is operated with a TMX console from the National Research Council of Canada Institute for Biodiagnostics, West, Calgary, AB, Canada. The magnet is displayed in Figure 2.11. The waveguide through which animal monitoring equipment is passed through is also shown in the photo. The steel RF cage provides passive shielding of surroundings from the 9.4 T magnet.

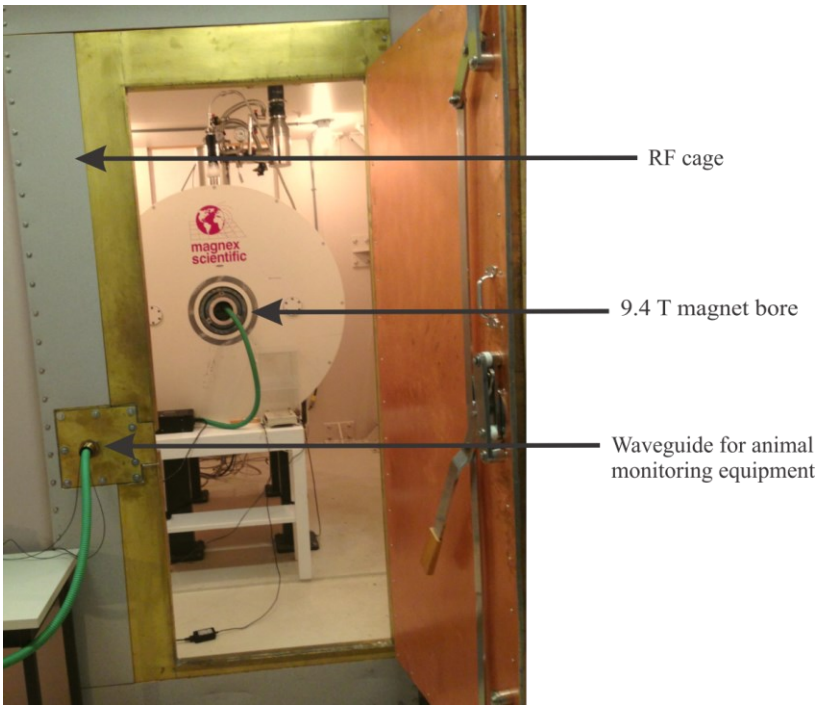

Figure 2.11: 9.4 T MRI scanner with RF cage, bore, and waveguide through which the animal monitoring equipment is passed.

The animal monitoring equipment consists of several inter-connected parts. A temperature monitor (Figure 2.12) is located outside the RF cage. The temperature monitor is connected to a black rectal probe in the animal. Based on its temperature feedback and adjustments made by the animal technician, a heating module (Figure 2.13) inside the RF cage warms the animal through a green tube that goes into the magnet bore. The heating module is connected to a fan module (Figure 2.14) that is outside the RF cage through another green tube. Both the green tube connecting the heating module to the fan and the black probe for the temperature monitor are passed through the waveguide in the RF cage. Within the RF cage, a respiratory gating machine (Figure 2.15) monitors the animal's breathing through a gating pillow on the animal (connected through the blue wire). Feedback from this machine is also wired through the waveguide in the RF cage. The temperature monitor, fan and heat system, and respiration monitor are all connected to a console that is used for animal monitoring. The complete small animal gating and temperature monitoring system used was model 1025 from Small Animal Instruments Inc. (Stony Brook, New York, USA).

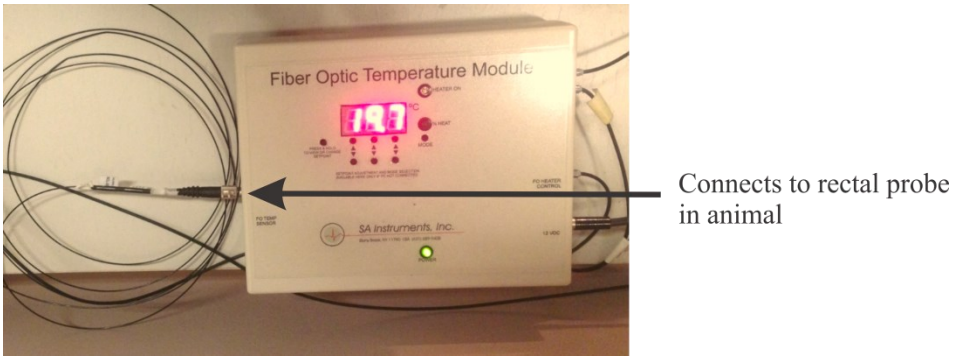

Figure 2.12: 9.4 T temperature monitor outside of RF cage. The black wire is connected to a rectal probe in the animal.

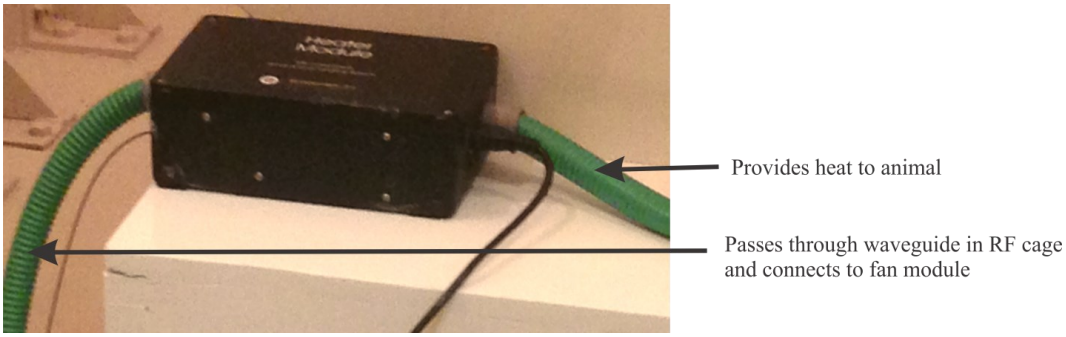

Figure 2.13: 9.4 T heating module inside the RF cage. One green tube is configured to go into the bore, delivering heat to the animal. The other green tube passes through the waveguide in the RF cage and connects the module to the fan.

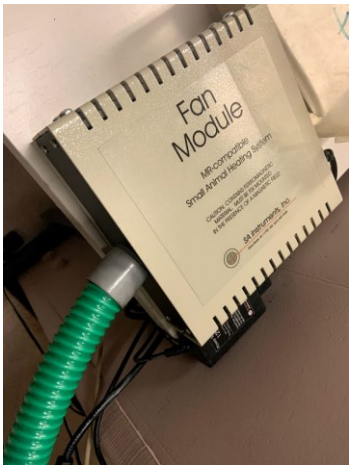

Figure 2.14: 9.4 T fan module outside the RF cage.

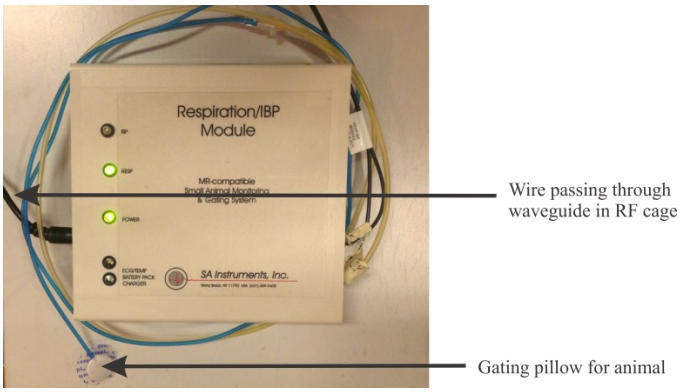

Figure 2.15: Respiratory gating machine within the RF cage. One wire (blue) is connected to a gating pillow on the animal in the bore. The other wire (black) is passed through the waveguide in the RF cage to connect to the animal monitoring console.

The 9.4 T MR scanner consists of a 1.47 m long superconducting magnet. It utilizes 12.0 cm diameter gradient coils. The superconductivity is maintained using nitrogen that surrounds the helium, maintaining its temperature. The gradient coils are cooled with circulating water and are connected to an external set of amplifiers. The maximum achievable gradient strength is 180 mT/m. Superconducting shim coils are constructed within the structure to compensate for magnetic field inhomogeneities. At commissioning, the magnet homogeneity was 4.56 ppm peak to peak over a 10 cm diameter spherical volume. Resistive shim coils are also used, and are connected to an external power supply. The currents through these coils are tuned by the user. Like the gradient coils, they are also temperature-controlled using circulating water. Figure 2.16 displays the hardware panel used for the shim, gradient, and RF cables, and the water cooling lines, located inside the RF shield. Figure 2.17 displays the hardware panel (outside the RF shield) which houses the RF power supply and amplifier, the primary and secondary gradient amplifiers, the shim power supply, and the pre-emphasis (eddy current compensation, Section 2.3.5) computer.

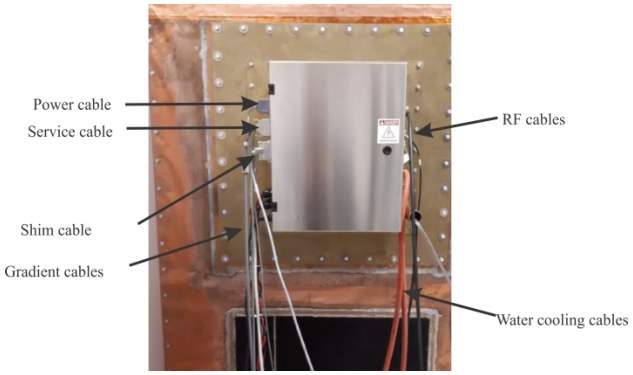

Figure 2.16: Panel used for shim, gradient (black and red wires), and RF cables. The water cooling lines are also attached. The service cable is used to ramp the magnet down for service.

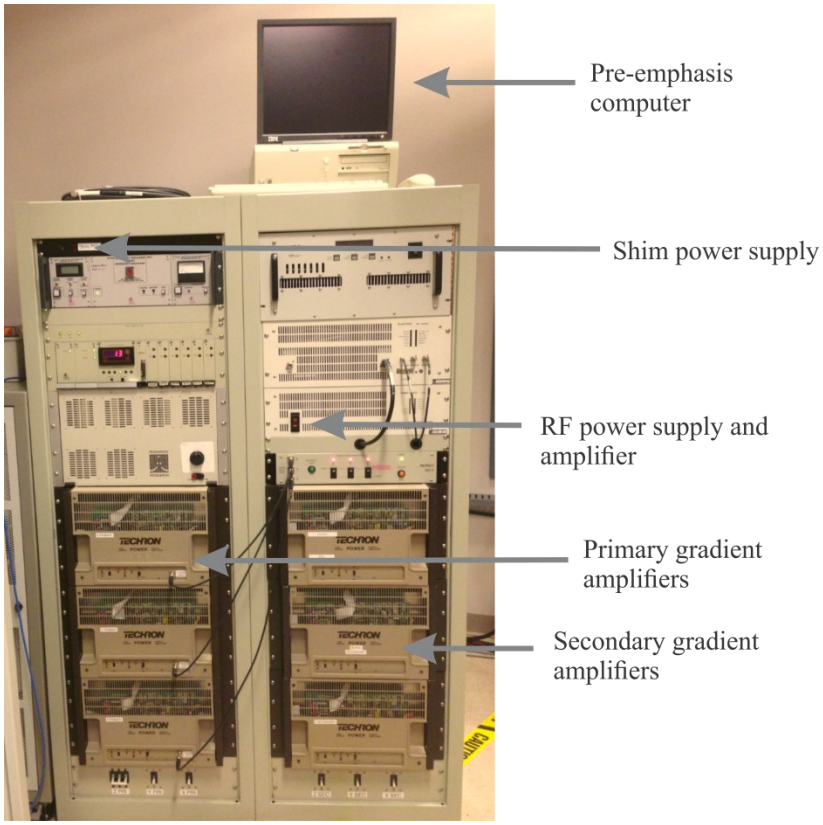

Figure 2.17: Panel that includes the RF power supply and amplifier, primary and secondary gradient amplifiers, and the pre-emphasis computer.

The TMX console at the operating station permits designing or adjusting pulse sequences, sequence parameters, shims, and RF transmit/receive amplification (Sections 2.3.2

and 2.3.4). It also includes graphics which indicate the location of voxel placements in an image. Figure 2.18 is a screenshot of the TMX console during a mouse spectroscopy scan.

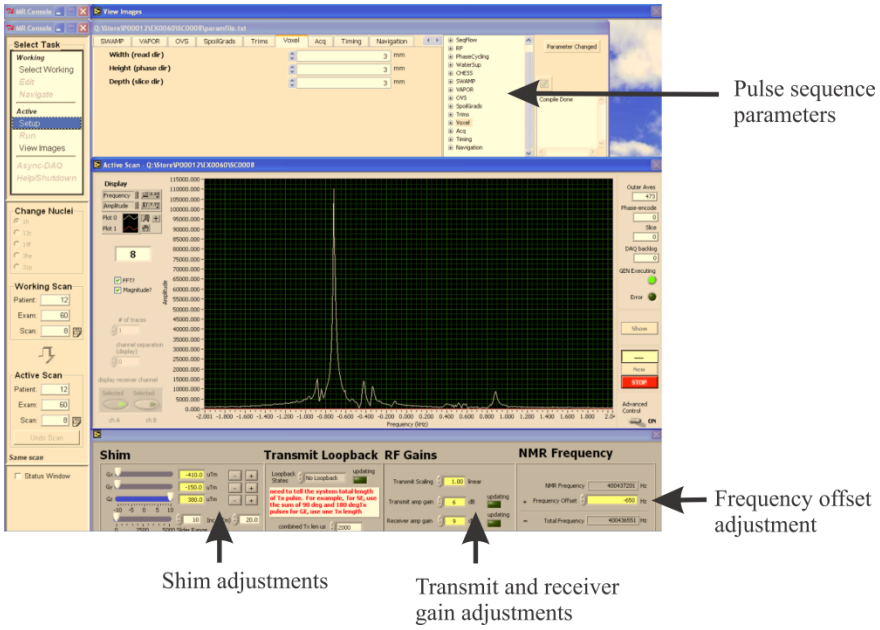

Figure 2.18: Screenshot of TMX console during a mouse scan, indicating controls for shim adjustments, transmit and receiver gain adjustment, frequency offset adjustment, and pulse sequence parameters.

2.5.2 9.4 T Phantom Experiments

Spherical glass phantoms (30 mm diameter, ≈ 10 mL volume) were filled with one of peanut oil (JVF Canada, Toronto, ON, Canada), canola oil (No name Loblaws, Canada), walnut oil (M. Graham, West Linn, OR), cod liver oil (Pharmetics, Laval, QC, Canada), or linseed oil (Sigma-Aldrich Canada, Oakville, ON, Canada). Figure 2.19 displays an example of a phantom.

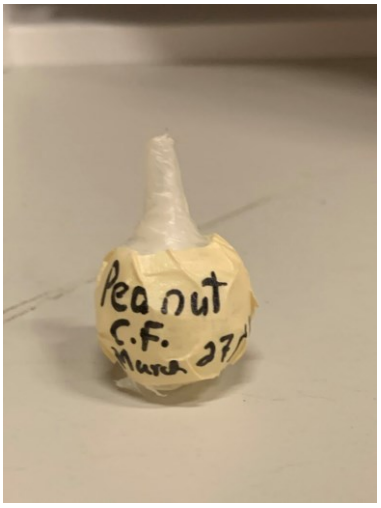

Figure 2.19: Oil phantom used for 9.4 T experiments.

Phantoms were positioned in the center of a 4.3 cm diameter birdcage RF coil from the National Research Council of Canada Institute for Biodiagnostics, West. The birdcage coil was used for both transmission and reception. The coil is pictured in Figure 2.20, with a phantom secured before being pushed to the center of the coil. An acrylic cylinder surrounds the coil and is designed such that the coil center coincides with the magnet isocenter. The yellow and red screws are used to tune and match the coil to the load. Figure 2.21 displays the frequency sweeper.

Figure 2.20: 9.4 T Birdcage RF coil with secured phantom. The yellow and red screws are used to tune and match the coil to the load.

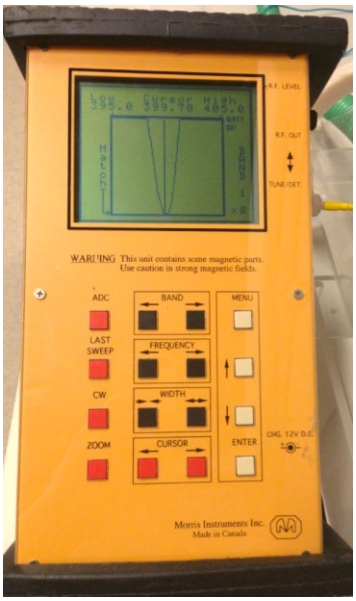

Figure 2.21: Frequency sweeper.

Phantom MRS spectra were acquired as detailed below. Localizer images were obtained, followed by spin echo images in two orthogonal directions. For the imaging, a TE of 16.3 ms and TR (repetition time) of 900 ms were used, with 20 slices of 2 mm width. A 5 x 5 x 5 mm^3 voxel was centered in the middle of the phantom. The chemical shift displacement artifact was accounted for by localizing a 8 x 8 x 8 mm^3 voxel, and then only using the 5 x 5 x 5 mm^3 voxel in the experiment. The larger voxel size ensures that any spins which are affected by chemical shift displacement (as calculated using Equation (1.67)) are still within the region of interest. PRESS spectra were acquired from this voxel. The PRESS pulses were 2 ms 5-lobed sinc RF pulses with 3000 Hz bandwidth. The TR was 5 s and the TE was varied from 25 to 399 ms, depending on the experiment being performed. TE_1 was 15 ms and TE_2 was varied accordingly. The spectra were acquired with 32 averages using 8192 complex data points at a sampling frequency of 10,000 Hz. An 8-step phase cycling scheme was used. Shimming was manually performed on the methylene signal until the peak amplitude was maximized, yielding a methylene linewidth of ≈ 25 Hz. The transmit gain was manually optimized for each experiment to ensure a 90° excitation pulse and 180° refocusing pulse were achievable. The receiver gain, which amplifies the received signal, was optimized and kept constant for all spectral acquisitions.

The spectra were processed with software provided by the National Research Council of Canada Institute for Biodiagnostics, West, Calgary, AB, Canada (Spectrum Viewer v. 2.00.02). All spectra were zero-filled, filtered by 3 Hz (exponential multiplication), Fourier Transformed, automatically corrected for baseline, and manually corrected for phase.

2.5.3 9.4 T Animal Experiments

Animal feeding, sedation, handling, anesthesia, and sacrifice were performed by a qualified animal care technician. The MRS experiments were performed on female CD1 IGS mice. The mice were fed a particular diet (depending on the experiment being performed) for a set period of time. For the MRS experiments, the mice were sedated with isoflurane using a plastic tube and a nose cone secured to the mice's airways. This set-up is depicted in Figure 2.22. A gating pillow was secured to the upper abdomen to provide respiratory feedback. Also shown in Figure 2.22, a rectal probe was inserted for temperature monitoring. Figure 2.23 displays the mouse wrapped and secured with gauge and tape onto the coil bed on her back. The lower abdomen of each mouse was positioned in the middle of the birdcage coil described above for the phantoms. Figure 2.24 illustrates the birdcage coil set-up (with the mouse at the coil center), including connection to the frequency sweeper. The rectal probe in combination with the temperature monitoring module, heating module, and fan module described in Section 2.5.1 were used to maintain the temperature of the mice at 37° C and the breathing steady at between 600 – 1000 ms per breath for the duration of the MRS scans. The animal care technician was responsible for monitoring the animal's breathing and temperature and for maintaining the appropriate sedation during the scan.

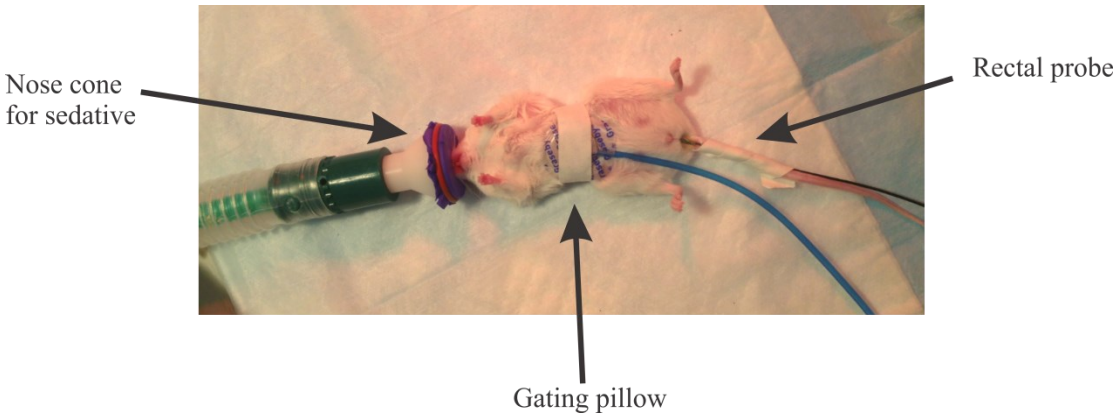

Figure 2.22: Mouse sedation, indicating nose cone, gating pillow and rectal probe.

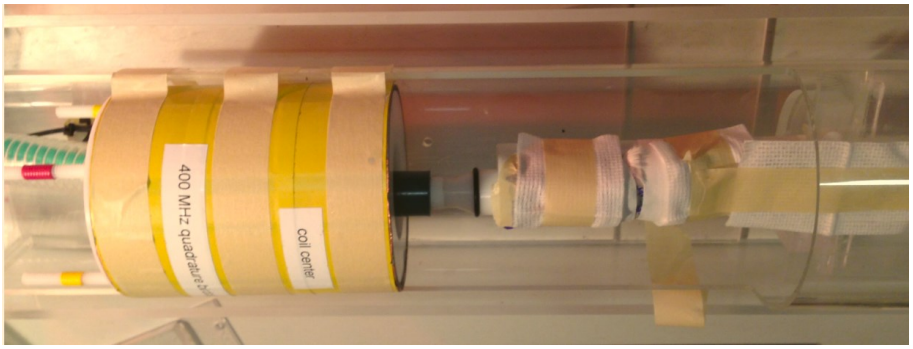

Figure 2.23: Mouse wrapped and secured onto birdcage coil bed.

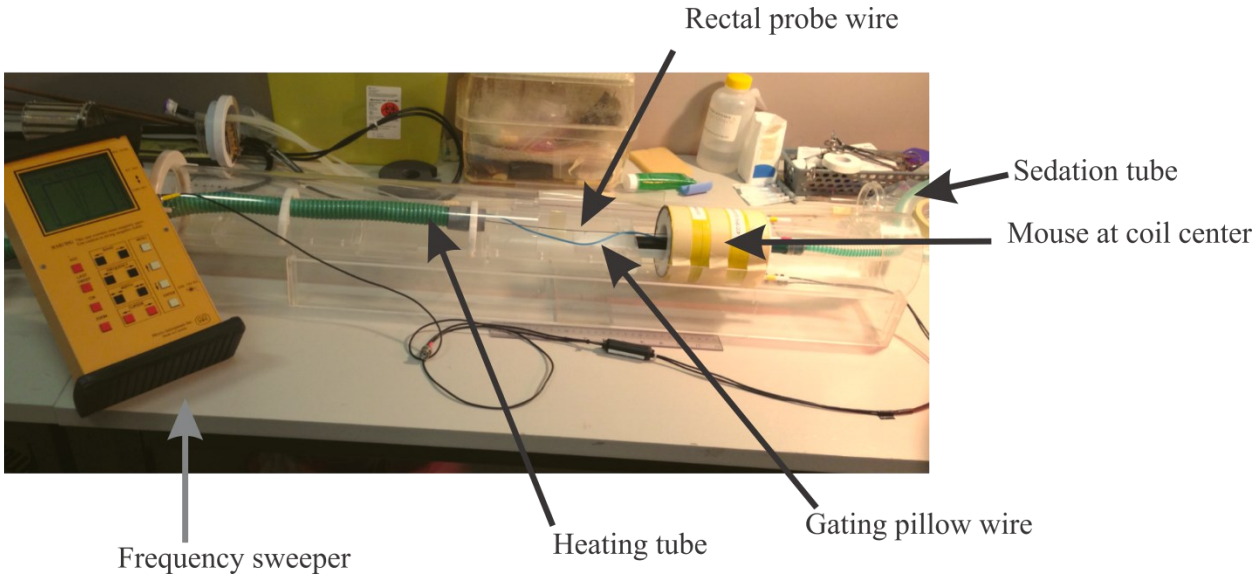

Figure 2.24: Mouse set-up, including sedation and heating tubes, gating pillow and rectal probe wires, and frequency sweeper.

MRS spectra were acquired from the mouse abdominal adipose tissue using the following procedure. Spin echo images were obtained in two orthogonal directions using 30 slices of 1 mm width with TR of 900 ms and TE of 16.3 ms. Gated PRESS spectra were obtained from the mouse with short TE and the appropriate long TEs depending on the experiment (TE_1 = 15 ms, TE_2 altered accordingly) from a 3 x 3 x 3 mm^3 or 4 x 4 x 4mm^3 voxel in the visceral fat of the mouse abdomen. Figure 2.25 displays the axial and coronal images for the placement of a voxel in a mouse, with accompanying anatomy in the surrounding region. Chemical shift displacement artifact was considered by using larger voxels (that include displaced volumes, as described in Section 2.5.2) for localization. Manual zero order shimming was performed to maximize the methylene peak height, until the methylene linewidth was less than 45 Hz. The same experimental parameters described for the oil spectra were employed, except 2048 points were acquired for the animal spectra.

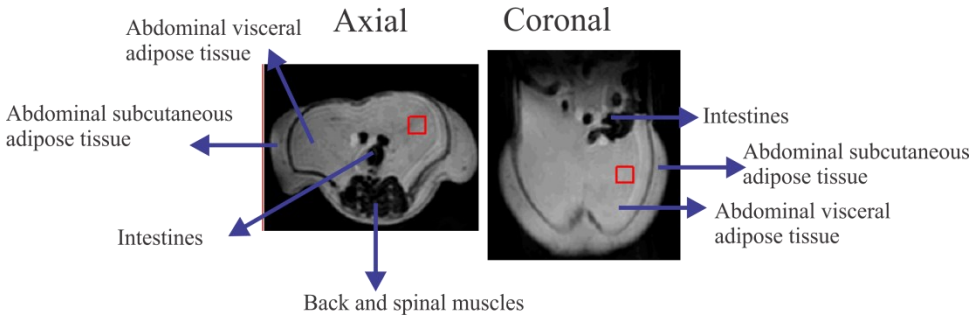

Figure 2.25: Axial and coronal images of voxel placement in a mouse, with surrounding anatomical regions.

Data from the mice were processed as described for the phantoms in Section 2.5.2, except a 5 Hz line broadening was utilized. The SNR was again measured using peak heights and the standard deviation of the noise for a fixed range of chemical shifts, utilizing the MATLAB program. Some of the short TE spectra were fit in LCModel (Linear Combination Model), which will be further described in Section 2.7.

At the end of the experiments, the mice were euthanized using carbon dioxide inhalation with a flow rate of 25 % of the chamber. These procedures are per current Canadian Council on Animal Care guidelines [31]. The mice abdominal visceral tissue was collected for gas chromatography. Fat samples were stored in the -80°C freezer. A modified Folch technique was

employed to extract lipids from the adipose tissue [32,33]. Boron trifluoride (BF_3) was utilized to saponify and methylate the lipid fraction [33]. Gas liquid chromatography was used to separate, classify, and quantify the fatty acids in the samples [34]. The gas chromatography column was an Agilent GC model 7890a (Agilent Technologies, Mississauga, ON, Canada) and consisted of a 100 x 0.25 m column with hydrogen as the carrier gas. All fatty acid extraction and analysis was performed by Dr. Catherine Field's laboratory.

2.6 Experiments at 3 T

2.6.1 3 T Magnet

Experiments were performed with a 3 T Philips whole-body 35 cm diameter superconductive scanner from Intera, Philips Heathcare, Best, Netherlands (Figure 2.26). The magnet has a homogeneity specification of 0.8 ppm peak to peak (after linear gradient shimming) over a 10 cm diameter spherical volume. The maximum gradient strength is 80 mT/m and the power requirement is 400 V. A cold head maintains the helium temperature and thus the superconductivity. For the oil phantoms, a transmit/receive RF birdcage head coil (Philips Healthcare) operating in quadrature mode was used (Figure 2.27). For *in-vivo* tibial bone marrow experiments, one element of the Flex-L surface coil (Philips Healthcare) was utilized for signal reception. Figure 2.28 displays the Flex-L coil. Velcro straps were employed to secure the coil in place. The body birdcage coil (quadrature mode) was used for transmission. For breast scans, both elements of the Flex-L surface coil were used for reception, and the body birdcage coil was employed for transmission. A specially-designed board was used for the breast scans, with built-in grooves for the Flex-L coil elements (Figure 2.29). The body birdcage coil was used for both signal transmission and reception for the abdominal scans, along with a gating pillow (Philips Healthcare) pictured in Figure 2.30, to track breathing.

Figure 2.26: Philips whole body 3 T MRI.

Figure 2.27: Philips transmit/receive birdcage head coil.

Figure 2.28: Philips Flex-L surface coil.

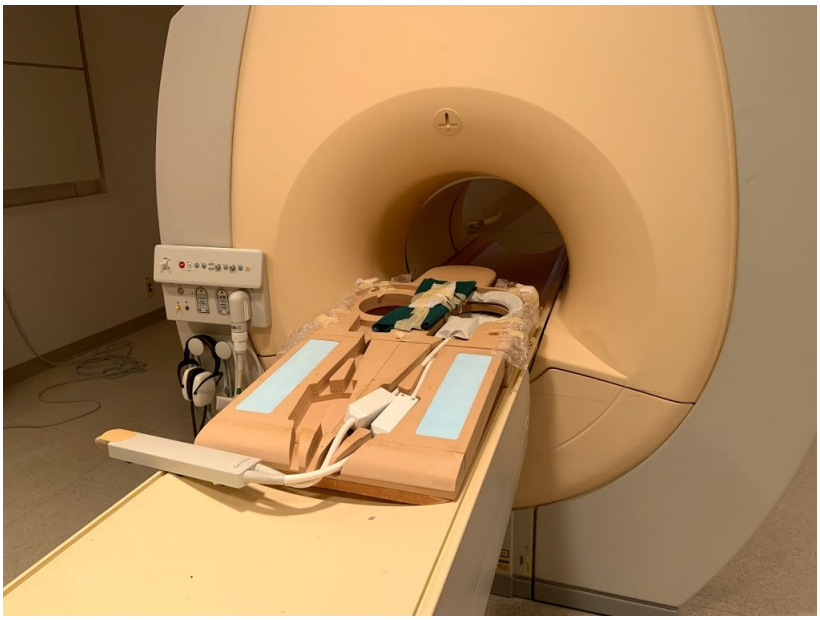

Figure 2.29: Specially designed breast board with Philips Flex-L surface coil.

Figure 2.30: Philips gating pillow.

2.6.2 3 T Phantom Experiments

Phantom experiments were performed on nine edible oils: almond oil (Gagan Foods International, Delta, BC, Canada), canola oil (No name Loblaws, Canada), cod liver oil (Pharmetics, Laval, QC, Canada), corn oil (Canada Safeway, Calgary, AB, Canada), linseed oil (Sigma-Aldrich Canada, Oakville, ON, Canada), peanut oil (JVF Canada, Toronto, ON, Canada), sesame oil (Flavor Full Foods, Taipei Hsien, Taiwan), sunflower oil (Canada Safeway), and walnut oil (M. Graham, West Linn, OR). Experiments were also performed on tricaprylin (Sigma-Aldrich) and oleic acid (Sigma-Aldrich). The oils were in their respective bottles as purchased. Each phantom was placed in the center of the Philips birdcage head coil (transmit/receive), and the coil was centered in the bore using the Philips laser centering system.

MRS spectra were prepared for acquisition from a voxel of interest as follows. Images in two orthogonal directions were acquired using a Turbo Field Echo (TFE). The field echo is similar to the IR (inversion recovery) in that a preparatory 180° pulse rotates all magnetization to the negative z-axis. The image is acquired after a delay, yielding T_1 contrast. Using a turbo

sequence facilitates acquiring multiple phase encoded echoes during each TR, reducing imaging time. The multi-shot TFE sequences used for phantom imaging consisted of a 800 ms delay, a TE of 4.6 ms, a TR of 11 ms, and a TFE factor of 64 (i.e. 64 echoes with different phase encodes are included in each TR). Three 10 mm slices were acquired in each direction. Voxels were localized as 20 x 20 x 20 mm^3 volumes centered in the middle of the phantoms. The oleic acid bottle was relatively small and thus 10 x 10 x 10 mm^3 voxels were used for oleic acid and tricaprylin (Chapter 6). Shimming was completed using the scanner's second-order shimming pencil beam auto procedure based on FASTERMAP [35] on the same voxel of interest. With FASTERMAP [35], several pencil beam excitations are assessed through the selected volume to map regional inhomogeneities [36]. FASTERMAP calculates the coefficients of spherical harmonics for the $\overrightarrow{B_o}$ field to yield the required shim corrections. The electrical current necessary for minimizing undesirable gradients in the voxel is also computed.

During the spectral acquisition, the following parameters and procedures were utilized. Employing a setting on the Philips console that displays the voxel displacement for a chemical shift verified that the chemical shift displacement did not extend outside the region of interest. Water suppression was not necessary and a 16 step phase cycling scheme was utilized. Depending on the experiment being completed, the TE was varied from 20 ms to 300 ms for STEAM, and 40 ms to 300 ms for PRESS. For PRESS, TE_1 was set to 17 ms or 15 ms and TE_2 was adjusted accordingly. For STEAM, a TM of 20 ms was consistently used as this had been previously optimized [37] to yield high olefinic signal, which is an important peak for fat composition assessment. PRESS and STEAM (mixing time, TM = 20 ms) spectra were acquired with the following parameters: 3 s repetition time (TR), 32 signal averages, 2048 points, and a 2000 Hz spectral bandwidth. The PRESS sequence consisted of a 90° excitation pulse followed by two 180° refocusing pulses. The STEAM sequence included three 90° pulses. Figure 2.31 displays the Philips console for an example oil.

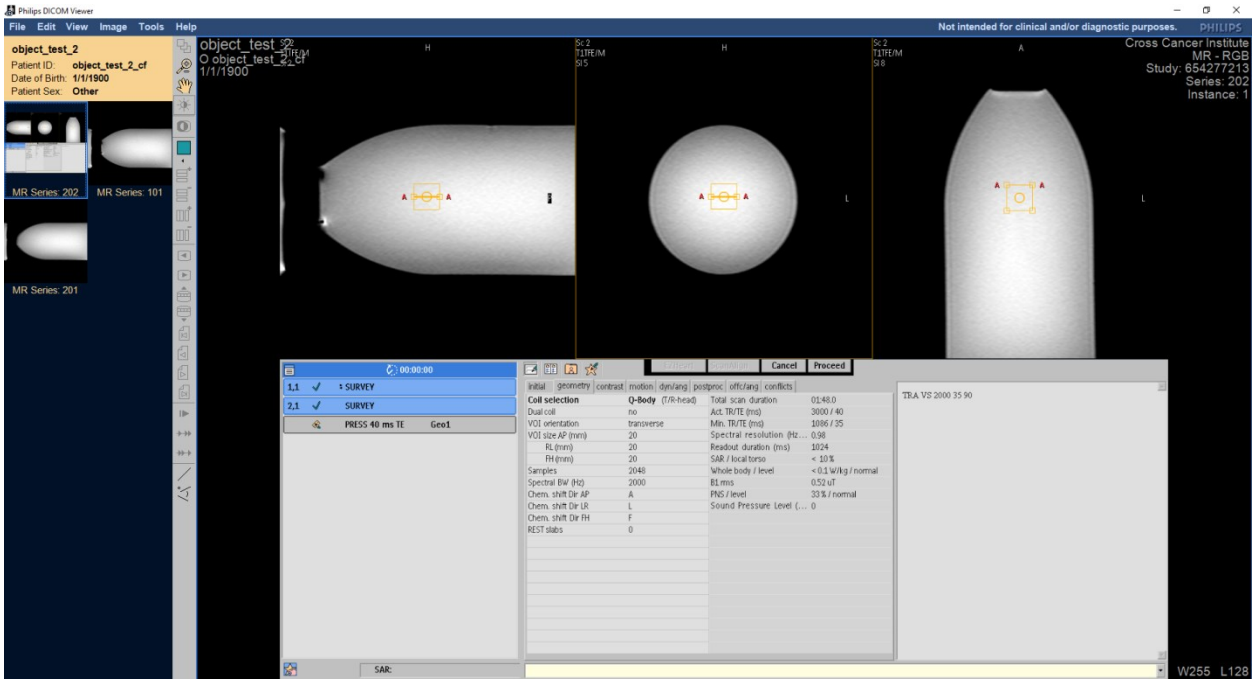

Figure 2.31: Philips console for an example oil bottle. Parameters can be adjusted using the controls shown.

The spectra were analyzed using the Philips integration program. Oil spectra were Gaussian filtered by 3 Hz, then Fourier transformed and manually corrected for phase and baseline. Manual peak area integration in the Philips program was employed. For the experiment that correlated methyl linewidth with ω-3 fat content, oil spectra were Gaussian filtered to ensure that the methylene linewidths were 15.2 ± 0.78 Hz for all the oils in the study and to mimic *in-vivo* linewidths. SNR for peaks of interest was measured by dividing peak height by the standard deviation of the noise between a set chemical shift range measured with the Philips software.

2.6.3 3 T Human Experiments

Human spectra were acquired from adipose tissue in regions of interest. Informed consent was obtained from all volunteers through a protocol approved through the local ethics board. For tibial bone marrow scans, volunteers lay supine on the MRI table and one element of the Philips Flex-L coil was centered on the tibial bone marrow below the knee. It was secured using Velcro straps and the center of the Flex-L coil was positioned in the center of the bore using the Philips

laser system. Multi-shot turbo spin echo (TSE) scout images were obtained in two orthogonal directions in 3 mm slices using a TSE factor of 3, a TE of 8 ms, and TR of 800 ms. A 7 x 7 x 7 mm^3 to 8 x 8 x 8 mm^3 voxel was centered in the tibial bone marrow below the knee. The TSE is similar to the TFE; several spin echoes are acquired for each TR. Shimming was performed as described for the phantoms. STEAM and PRESS spectra were acquired with short TE (STEAM TE = 20 ms and PRESS TE = 40 ms) and the TEs relevant for the particular experiment being performed. All other parameters were as detailed for the phantom scans. For subcutaneous abdominal scans, patients also lay supine on the MRI table. The Philips gating pillow was secured to centre of the abdominal region using a Velcro blanket. The abdominal centre was positioned in the center of the bore using the Philips laser system and the body coil was used for both signal reception and transmission. Multi-shot TSE images were obtained in two orthogonal directions in 3 mm slices with a TSE factor of 20, a TE of 40 ms, and TR of 1294 ms. Depending on the size of the volunteer, a 10 x 10 x 10 mm^3 to 20 x 20 x 20 mm^3 voxel was positioned in the subcutaneous abdominal fat, on the right gluteus side. Shimming was performed using the pencil beam volume method in the Philips console, as the regular pencil beam auto method is more sensitive to motion and thus not optimal for gated scans [36]. A voxel volume about 1.5 times larger than the voxel selected for spectroscopy (but still within the homogeneous region) was aligned to the voxel of interest and shimming was performed on this larger volume. Gated spectra were obtained using PRESS and STEAM and the same parameters described for the phantoms, with the relevant TEs for the particular experiment. For the breast scans, volunteers lay prone on a specially designed breast board with the right breast hanging into the two Flex-L surface coils (for signal reception). The body coil was used for transmission. T_2- weighted orthogonal images were obtained for scouting to maximize contrast between fat and water. The images were collected in 5 mm slices using a multi-shot TSE with TSE factor of 15, TE of 60 ms, and TR of 4 s. Depending on the size of the volunteer, a 10 x 10 x 10 mm^3 to 20 x 20 x 20 mm^3 voxel was positioned in a fat portion of the breast, a fat-water portion of the breast, or a water portion of the breast, contingent on the experiment being performed. The shimming was completed as described for the phantoms, with pencil beam auto. PRESS and STEAM spectra were acquired using the same parameters as detailed for the phantoms, with the relevant TEs for the experiment desired. For the IR experiments in the breast, an IR pulse of 100 Hz bandwidth was set to the water frequency before the PRESS sequence, with appropriate inversion delay

time for the experiment being performed. The chemical shift displacement was verified in all experiments as previously outlined.

For all human experiments other than those in Chapter 5, spectra were analyzed as described for the phantoms using the Philips analysis console. A 4 Hz filter was used instead of a 3 Hz filter. LCModel was used to peak-fit the data in Chapter 5 because of peak overlap in the breast and abdominal spectra.

2.7 LCModel Analysis

LCModel [38] software was utilized to analyze the short TE animal spectra acquired at 9.4 T in Chapter 3. It was also employed to fit the *in-vivo* PRESS spectra from the tibial bone marrow, breast, and subcutaneous adipose tissue in Chapter 5. LCModel is a useful tool for peak fitting when there is peak overlap and peaks cannot be directly integrated. LCModel employs acquired *in-vitro* spectra or simulated spectra to compose a model basis spectrum. The user must input time-domain *in-vivo* data. LCModel accounts for the baseline, coupling interactions, and sequence-specific complications. The objective of the model is to solve numerous problems associated with the quantification of *in-vivo* spectra. One issue is that the baseline is difficult to characterize. Furthermore, not including enough parameters in a model results in biases, but including too many parameters yields distortions, potentially making the solution more difficult to converge to. LCModel exploits mathematical methods [39] to find the best solution to these issues.

Input *in vivo* data is processed as a linear combination of model spectra from *in-vitro* metabolite solutions or a simulated basis set. LCModel first zero-fills both the *in-vivo* data and the *in-vitro* data set. The data is then Fourier Transformed [38]. Line broadening and shifting along the ppm axis of the basis set are completed. The line broadening compensates for the shorter T_2 relaxation times *in vivo*, and the shifting is completed for referencing. The baseline is accounted for with cubic B-splines that have knots separated by equivalent spaces. A cubic B-spline is a piece-wise polynomial function of order 2 [40]. Zero order (and first order when appropriate) phase corrections are also performed.

The LCModel basis sets used for all the experiments were independent of pulse sequence and TE because singlet peaks were modelled to obtain areas [41]. At 9.4 T, lipid peaks were simulated at 0.9, 1.3, 1.6, 2.1, 2.3, 2.8, 4.2, 4.3, 4.7, 5.2, and 5.3 ppm. An additional ω-3 peak around 0.95 ppm was also included. Allowed standard deviations of the chemical shifts were set to 0 for all peaks except for the ω-3 peak which was permitted a standard deviation of ± 0.01ppm. All peaks were simulated because the ω-3 peak is not included in any pre-existing LCModel setting tailored to fats and could not be added. The simulated peak linewidths were specified. At 3 T, an existing setting provided by the manufacturer tailored to fat peaks was utilized (no ω-3 peak). The default parameters for the simulated peaks in this setting were employed. For each spectrum at both field strengths, specific parameters were optimized manually to achieve the most representative fit. These included the spectrum shift, spectrum start and end, and spectrum center, to assist with referencing, and, if necessary, the zero degree phasing parameters. For all LCModel analyzed data, fitted spectra were obtained as well as tables of Cramér- Rao lower bound (CRLB) values for each lipid [42]. CRLBs represent the lowest possible standard deviation of a parameter [43].They are a useful tool for judging the effectiveness of quantification; a CRLB < 20 % is considered effective quantification [44] and twice the absolute CRLB defines the 95 % confidence interval of the data [41]. Figure 2.32 is an example of a short-TE PRESS spectrum from the breast fat at 3 T analyzed with LCModel. The table of peak areas, concentrations, and CRLBs are shown on the right. In this example, the concentrations are the raw areas under the peaks.

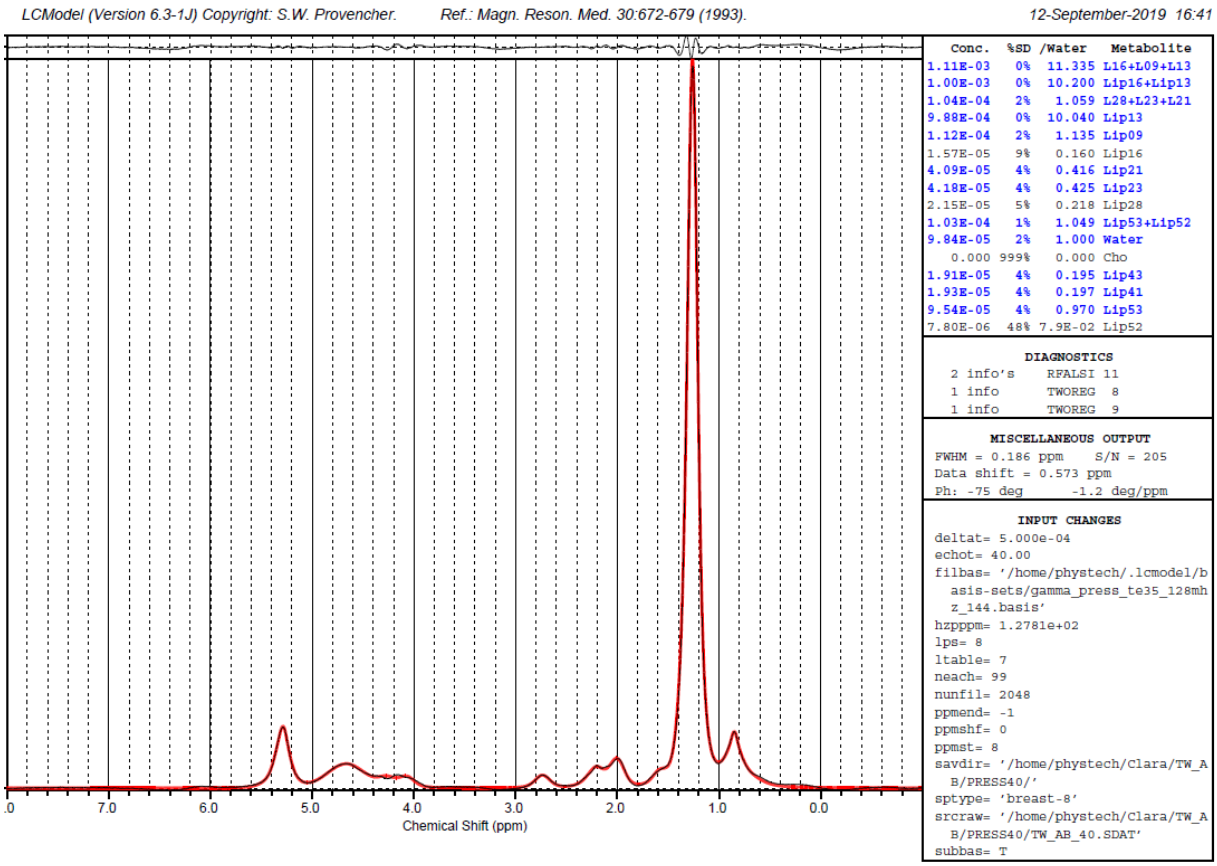

Figure 2.32: LCModel output for a breast spectrum using PRESS with TE of 40 ms at 3 T. The peak areas, concentrations, and CRLB are shown in a column on the right.

2.8 16.5 T NMR Experiments

High resolution NMR spectra were obtained for each of the nine oils used throughout this thesis from a 700 MHz (16.5 T) Varian/Agilent (Palo Alto, California, USA) VNMRS spectrometer by Dr. Ryan McKay and his team at the Chemistry Department. Oil preparation consisted of dissolving 50 µL of pure oil into 550 µL of deuterated chloroform. The following parameters were used for spectra acquisitions: 8389.26 Hz spectral bandwidth, 5 s repetition time, 42000 samples, 30° flip angle, and 16 averages.

The oil spectra at 16.5 T were processed on VNMRJ version 4.2 (the software interface for Varian spectrometers). The measured areas were used as a gold standard assessment of oil

phantom composition. At 16.5 T, the glycerol peak area does not contaminate the olefinic peak area as it does at 3 T and 9.4 T. The 16.5 T NMR data was therefore also used to evaluate the error introduced by glycerol in the oils (Chapter 6).

2.9 Citations

1. National Academic Press (US). Fats and other lipids. Diet and health: Implications for reducing chronic disease risk; 1989.
2. IUPAC-IUB Commission on Biochemical Nomenclature (CBN). The nomenclature of lipids. Eur J Biochem 1977;79:11-21.
3. Yeung DKW, Lam SL, Griffith JF, et al. Analysis of bone marrow fatty acid composition using high-resolution proton NMR spectroscopy. Chem Phys Lipids 2008;151:103-109.
4. Griffith JF, Yeung DKW, Ahuja AT, et al. A study of bone marrow and subcutaneous fatty acid composition in subjects of varying bone mineral density. Bone 2009;44:1092-1096.
5. Ren J, Dimitrov I, Sherry AD, Malloy CR. Composition of adipose tissue and marrow fat in humans by ^{1}H NMR at 7 Tesla. J Lipid Res 2008;49:2055-2062.
6. Guillén MD, Ruiz A. High resolution ^{1}H nuclear magnetic resonance in the study of edible oils and fats. Trends Food Sci Technol 2001;12:328-338.
7. Lundbom J, Heikkinen S, Fielding B, Hakkarainen A, Taskinen M-R, Lundbom N. PRESS echo time behavior of triglyceride resonances at 1.5 T: Detecting ω-3 fatty acids in adipose tissue *in vivo*. J Magn Reson 2009;201:39-47.
8. Machann J, Stefan N, Schabel C, et al. Fraction of unsaturated fatty acids in visceral adipose tissue (VAT) is lower in subjects with high total VAT volume - a combined ^{1}H MRS and volumetric MRI study in male subjects. NMR Biomed 2013;26:232-236.
9. Fairgrieve-Park L, Fallone CJ, Yahya A. Long TE PRESS and STEAM for measuring the triglyceride glycerol CH_2 protons at 3 T NMR Biomed 2018;32:e4021 (8 pages).
10. Kosugi Y, Matsubara K. Conformational analysis of triacylglycerols by means of Nuclear Magnetic Resonance and Molecular Mechanics. J Jpn Oil Chem Soc 1989;38:415-420.
11. Oostendorp M, Engelke UFH, Willemsen MAAP, Wevers RA. Diagnosing inborn errors of lipid metabolism with proton nuclear magnetic resonance spectroscopy. Clin Chem 2006;52:1395-1405.
12. Hamilton G, Middleton MS, Bydder M, et al. Effect of PRESS and STEAM sequences on magnetic resonance spectroscopic liver fat quantification. J Magn Reson Imaging 2009;30:145-152.
13. Škoch A, Tošner Z, Hájek M. The *in vivo* J-difference editing MEGA-PRESS technique for the detection of n-3 fatty acids. NMR Biomed 2014;27:1293-1299.
14. Stokes A, Feng Y, Mitropoulos T, Warren W. Enhanced refocusing of fat signals using optimized multipulse echo sequences. Magn Reson Med 2013;69:1044-1055.
15. Purcell JM, Morris SG, Susi H. Proton magnetic resonance spectra of unsaturated fatty acids. Anal Chem 1966;38:588-592.
16. Ansorge R, Graves M. The physics and mathematics of MRI: Morgan & Claypool Publishers: 2016.
17. Elster AD. Questions and Answers in MRI http://mriquestions.com/index.html. 2019.
18. Glover GH, Hayes CE, Pelc NJ, et al. Comparison of linear and circular polarization for Magnetic Resonance Imaging. J Magn Reson 1985;64:225-270.
19. Dietrich O, Raya JG, Reeder SB, Reiser MF, Schoenberg S. Measurement of signal-to-noise ratios in MR images: Influence of multichannel coils, parallel imaging, and reconstruction filters. J Magn Reson Imaging 2007;26:375-385.

20. Cowan B. Nuclear magnetic resonance and relaxation: Cambridge University Press: 1997.
21. Hoult D. The principle of reciprocity in signal strength calculations: A mathematical guide. Concepts Magn Reson 2000;12:173-187.
22. Gruber B, Froeling M, Leiner T, Klomp DWJ. RF coils: a practical guide for nonphysicists. J Magn Reson Imaging 2018;48:590-604.
23. Johnson JB. Thermal agitation of electricity in conductors. Nature 1927;119:50-51.
24. Nyquist H. Thermal agitation of electric charge in conductors. Phys Rev 1928;32:110-113.
25. Niederländer B, Blümler P. Simple eddy current compensation by additional gradient pulses. Concepts Magn Reson 2018;47A:e21469 (7 pages).
26. Burl M, Young IR. Eddy currents and their control. eMagRes 2007: https://doi.org/10.1002/9780470034590.emrstm0147.
27. Sørensen OW, Eich GW, Levitt MH, Bodenhausen G, Ernst RR. Product operator formalism for the description of NMR pulse experiments. Prog Nucl Mag Res Sp 1983;16:163-192.
28. Goldenberg DP. The Product Operator Formalism: A Physical and Graphical Interpretation. Concepts Magn Reson 2010;36A:49-83.
29. Keeler J. Chapter 6: Product Operators (from course "Understanding NMR spectroscopy"). University of Cambridge, Department of Chemistry; 2004.
30. de Graaf R, Rothman D. *In vivo* detection and quantification of scalar coupled ^{1}H NMR resonances. Concepts Magn Reson 2001;13:32-76.
31. Canadian Council on Animal Care. Guidelines. https://www.ccac.ca/en/standards/guidelines/. Accessed March 2020.
32. Folch J, Lees M, Stanley GHS. A simple method for the isolation and purification of total lipides from animal tissues. J Biol Chem 1957;226:497-509.
33. Field CJ, Ryan EA, Thomson ABR, Clandinin MT. Dietary fat and and the diabetic state alter insulin binding and the fatty acyl composition of the adipocyte plasma membrane. Biochem J 1988;253:417-424.
34. Cruz-Hernandez C, Goeuriot S, Giuffrida F, Thakkar SK, Destaillats F. Direct quantification of fatty acids in human milk by gas chromatography. J Chromatogr A 2013;1284:174-179.
35. Shen J, Rycyna RE, Rothman DL. Improvements on an *in vivo* automatic shimming method [FASTERMAP]. Magn Reson Med 1997;38:834-839.
36. Philips. Application Guide Spectroscopy. Volume 4: Achieva Release 3.2 Series.
37. Bingölbali A, Fallone BG, Yahya A. Comparison of optimized long echo time STEAM and PRESS proton MR spectroscopy of lipid olefinic protons at 3 Tesla. J Magn Reson Imaging 2015;41:481-486.
38. Provencher SW. Estimation of metabolite concentrations from localized *in vivo* proton NMR spectra. Magn Reson Med 1993;30:672-679.
39. Provencher SW. A constrained regularization method for inverting data represented by linear algebraic or integral equations. Comput Phys Commun 1982;27:213-227.
40. Prautzsch H, Boehm W, Paluszny M. Bézier and B-spline techniques: Springer-Verlag 2002.
41. Provencher S. LCModel & LCMgui User's Manual. 2018.

42. Cavassila S, Deval S, Huegen C, Van Ormondt D, Graveron-Demilly D. Cramér- Rao bounds: an evaluation tool for quantitation. NMR Biomed 2001;14:278-283.
43. Kreis R. The trouble with quality filtering based on relative Cramér-Rao lower bounds Magn Reson Med 2016;75:15-18.
44. Heo H, S. K, Lee HH, et al. On the utility of short echo time (TE) single voxel ^{1}H–MRS in non–invasive detection of 2–hydroxyglutarate (2HG); Challenges and potential improvement illustrated with animal models using MRUI and LCModel. PLOS ONE 2016;11:e0147794 (18 pages).

Chapter 3

Resolving the ω-3 Methyl Resonance with Long Echo Time Magnetic Resonance Spectroscopy in Mouse Adipose Tissue at 9.4 T

A version of this chapter has been published:

Fallone, C.J., Tessier, A.G., Field, C.J., and Yahya, A. (2021). Resolving the ω-3 methyl resonance with long echo time magnetic resonance spectroscopy in mouse adipose tissue at 9.4 T. *NMR in Biomedicine* 34: e4455 (11 pages).

3.1 Abstract

Tissue omega-3 (ω-3) content is biologically important to disease; however, its quantification with Magnetic Resonance Spectroscopy (MRS) *in vivo* is challenging due to its low concentration. In addition, the ω-3 methyl resonance (≈ 0.98 ppm) overlaps that of the non-ω-3 (≈ 0.90 ppm), even at 9.4 T. We demonstrate that a PRESS (Point RESolved Spectroscopy) sequence with an echo time (TE) of 109 ms resolves the ω-3 and non-ω-3 methyl peaks at 9.4 T. Sequence efficacy was verified on five oils of differing ω-3 fat content; the ω-3 content obtained correlated with that measured using 16.5 T NMR (R^2 = 0.97). The PRESS sequence was also applied to measure ω-3 content in visceral adipose tissue of three different groups of mice with n = 3, each fed a different 20 % w/w fat diet. The fat portion of the diet consisted of low (1.4 %), medium (9.0 %), or high (16.4 %) ω-3 fat. The sequence was also applied to a control mouse fed a standard chow diet (5.6 % w/w fat which was 5.9 % ω-3). Gas chromatography (GC) analysis of excised tissue was performed for each mouse. The ω-3 fat content obtained with the PRESS sequence correlated with the GC measures (R^2 = 0.96).

Apparent T_2 times of methyl protons were assessed by obtaining spectra from the oils and another group of four mice (fed the high ω-3 diet) with TE values of 109 ms and 399 ms. Peak areas were fit to a mono-exponentially decaying function and apparent T_2 values of the ω-3 and non-ω-3 methyl protons were 906 ± 148 ms and 398 ± 78 ms, respectively, in the oils. In mice, the values were 410 ± 68 ms and 283 ± 57 ms for ω-3 and non- ω-3 fats, respectively.

3.2 Introduction

Tissue fat composition has shown relevance to disease [1-7]. For example, lower levels of unsaturated fat in abdominal adipose tissue have been associated with obesity in humans [1,8,9] and in rodents [10,11]. Fat unsaturation levels have also been found altered in other diseases in various tissues in humans and in animals [2-7,12-19], including breast cancer [4,5,19], bone disease [2,6,7,15,18], and diabetes [6,16]. Omega-3 (ω-3) dietary fat intake in humans is related inversely with disease, including obesity [20,21], diabetes [20,21], osteoporosis [22,23], and breast cancer [24,25]. Dietary ω-3 fat also promotes muscular health [26], and ω-3 supplements were found to enhance tumor cell death when used with chemotherapy, while reducing toxic side effects [27]. Lower levels of α-linolenic acid (an ω-3 fat) in breast [28] and low ω-3 to ω-6 fat ratios in buttocks [29] were reported to predict breast cancer metastases in humans. In addition, low ω-3 fat in human abdominal adipose tissue was associated with obesity [8,9]. Studies also indicate that ω-3 levels in human blood serum correspond with bone health [30], and improved insulin sensitivity and metabolic profile in overweight men [31]. Rodent studies illustrate that ω-3 levels change with diet and are reflected in tissue fat composition such as the liver [32], retrioperitoneal adipose tissue [32], gonadal adipose tissue [32], abdominal adipose tissue [33], and femur [34]. In humans, dietary fatty acid intake is the dominant determinant of fat composition in adipose tissue, whereas age, sex, and genetics have a minor impact [35].

Magnetic Resonance Spectroscopy (MRS) has been used to assess fat composition *in vivo* [1,2,5,11,12,36-42]; however, ω-3 fat quantification is challenging due to the low abundance of ω-3 fats (≈ 1%) in adipose tissue [43] and the close proximity of the ω-3 methyl resonance (≈ 0.98 ppm) to that of the non-ω-3 methyl (≈ 0.9 ppm) [44]. The closeness of the chemical shifts of the two methyl groups makes it difficult to resolve their resonances with standard short echo time (TE) *in-vivo* proton MRS techniques [45]. However, since levels of ω-3 fat can be altered in disease [8,9,27-29]; there is motivation to assess levels of ω-3 non-invasively with MRS. Different spectral editing techniques have been employed to resolve the ω-3 methyl resonance from that of the non-ω-3 resonance. At 1.5 T, an MRS technique based on a long TE [46] of 540 ms was used to quantify ω-3 fat. At 3 T, J-difference editing [47] and the methyl linewidth [48] have been investigated for

quantifying ω-3. Both latter methods exploited that the ω-3 methyl protons are more weakly coupled than the non-ω-3 methyl protons at 3 T.

Higher magnetic field strengths such as 7 T or 9.4 T have been employed to assess fat composition in animal [12,37,38,49,50] and human [45] studies, providing the benefits of enhanced spectral resolution and signal to noise ratio (SNR). Equations incorporating the areas of various fat peaks have been used to quantify saturated, mono-unsaturated and di-unsaturated fatty acid [12,37,38,49] composition; however, ω-3 fatty acids were not included, likely because of the low concentration of ω-3 fatty acids [43], and because it is challenging to resolve the ω-3 resonance even at high field strengths [45]. A study at 7 T utilized Point RESolved Spectroscopy (PRESS) with an ultra-long TE (1000 ms) to resolve the ω-3 methyl peak from that of the non ω-3 [45]. The ultra-long TE permitted the methylene and non-ω-3 methyl peaks to lose significant signal compared to the ω-3 methyl peak due to differences in transverse (T_2) relaxation [45]. The timing was also optimized such that the J-coupling evolution of the methyl protons, which are weakly-coupled at 7 T, resulted in improved resolution of the two methyl resonances [45].

The objective of this work is to determine an optimal PRESS echo time to quantify relative ω-3 fat content at 9.4 T, a commonly employed high field strength for animal MRS studies [12,37,49]. The higher spectral resolution at 9.4 T yields better separation of the 1.3 ppm methylene resonance from that of the methyl protons, enabling using a shorter TE than 1000 ms, thereby reducing losses due to T_2 relaxation. The efficacy of the timing was verified on oil samples and *in vivo* on abdominal fat of mice fed different fat diets. MRS quantification was compared to gas chromatography (GC) results from excised tissue from the animals. In addition, relative decay rates of ω-3 and non-ω-3 methyl protons in mice were measured to investigate if differences in T_2 times between the two methyl protons exist which could have an effect on quantification of ω-3 content.

3.3 Materials and Methods

Theoretical:

A detailed description of product operator formalism for the methyl protons can be found in the supporting materials of Škoch *et al.* [47]. Details relevant to the presented work are provided here. Omega-3 and non-ω-3 fatty acids differ in their structure where the first carbon to carbon double bond of ω-3 fatty acids is located on the third carbon from the end-chain fatty acid methyl (Figure 3.1). Omega-3 methyl protons neighbor the allylic methylene protons (≈ 2.0 ppm) and have a higher chemical shift (≈ 0.98 ppm) compared to that of the non-ω-3 methyl protons (≈ 0.9 ppm) which neighbor the 1.3 ppm methylene protons [44,46]. Both the ω-3 and non-ω-3 methyl protons are weakly-coupled to their corresponding neighbors at 9.4 T with a coupling constant of about 7 Hz [14,47]. Product operator formalism was utilized to describe their J-coupling evolution as a function of TE [47,51] (PRESS is a double spin echo sequence). The ω-3 and non-ω-3 methyl protons were modeled as A_2X systems, with X as one of three methyl protons and A as the neighboring allylic protons (for ω-3 fats) or methylene protons (for non-ω-3 fats) [47]. The term that yields methyl proton observable magnetization is $X_x\left[\frac{1}{2}+\frac{\cos(2\pi JTE)}{2}\right]$, where J denotes the coupling constant between the methyl and methylene protons. The methyl protons form a triplet signal, including a constant central peak ($\frac{X_x}{2}$) and sinusoidally varying side multiplets ($\frac{X_x\cos(2\pi JTE)}{2}$). Timings when the in-phase signal of the side multiplets of the ω-3 and non-ω-3 methyl triplets are 0 minimize the overlap between the two peaks. These timings occur for TE values of $\frac{(2n+1)}{4J}$, where n is an integer. Assuming a coupling constant of 6.9 Hz [14] yields a TE of 36 ms when n = 0, a TE of 109 ms when n = 1 and so forth.

Experimental:

All phantom and *in-vivo* experiments were carried out using a 21.5 cm diameter bore horizontal 9.4 T MRI scanner (Magnex Scientific, Oxford, UK) with a TMX console (National Research Council of Canada Institute for Biodiagnostics, West, Calgary, AB, Canada). A 4.3 cm diameter birdcage radiofrequency (RF) coil (National Research Council of Canada Institute for Biodiagnostics, West, Calgary, AB, Canada) was employed for transmission and reception. A

PRESS sequence with 2 ms sinc pulses and 3000 Hz bandwidth was employed with the first echo time, TE_1, set to 15 ms. The following experimental parameters were used: 5000 ms repetition time (TR), 8-step phase cycling, 10,000 Hz sampling frequency, and 32 averages. Manual shimming was performed to maximize the methylene peak height. Spectra were processed and analyzed with Spectrum Viewer version 2.00.002, from the National Research Institute of Canada for Biodiagnostics, West. They were zero-filled, filtered (3 Hz and 5 Hz exponential filter, for phantom and *in-vivo* spectra, respectively), Fourier transformed, baseline and phase corrected. Peak areas were integrated using the software with integration bounds for the two methyl resonances provided in the sections below. Integration for each resonance was performed such that only the area of the central peak of the methyl triplet was measured; any signal from the two side peaks was excluded.

Phantom scans:

Phantom spectra were acquired as 8192 complex data points with the PRESS sequence from 5 x 5 x 5 mm^3 voxels placed in the centre of the phantoms. Shimming yielded a methylene linewidth of about 25 Hz. Experiments were performed on five oils of varying ω-3 fat content, namely, peanut oil (0 % ω-3), canola oil (≈ 10 % ω-3), walnut oil (≈ 17 % ω-3), cod liver oil (≈ 24 % ω-3) and linseed oil (≈ 57 % ω-3). The expected ω-3 content of the oils was determined from high-resolution spectra (5 s acquisition time, 8389.26 Hz sweep width, 30° flip angle and 16 averages) acquired from the oil samples (50 µL dissolved in 550 µL of deuterated chloroform) with a 700 MHz (16.5 T) Varian/AgilentVNMRS spectrometer. The ω-3 methyl peak areas and the sum of the ω-3 (0.94 ppm – 1.0 ppm) and non- ω-3 methyl peak (0.84 ppm – 0.9 ppm) areas were obtained using VNMRJ software. 9.4 T spectra were acquired from the oils using TE values that theoretically yield zero in-phase signal for the resonance side multiplets. All the oils were in 30 mm diameter glass spheres. The shortest TE that best resolved the two methyl resonances was used to measure relative ω-3 fat levels (% ω-3 fat content) in each oil by dividing the ω-3 methyl resonance area by the sum of the ω-3 (0.95 ppm – 1.0 ppm) and non-ω-3 methyl resonance (0.89 ppm – 0.93 ppm) areas. The coefficient of determination (R^2) between the % ω-3 fat content determined using 9.4 T MRS and 16.5 T NMR was calculated in MATLAB.

To assess the relative T_2 relaxation decay of the ω-3 and non-ω-3 methyl protons, another long TE suitable for resolving the two resonances was selected. The TE value was chosen such that it resolved the two methyl resonances well (using an n value described in the prior theoretical section) and was less than 500 ms so that adequate signal could be obtained *in vivo*. This latter TE was used along with the first TE determined above to assess differences in relaxation decay between the ω-3 and non-ω-3 methyl protons in the oils and in mice *in vivo*. The ω-3 and non-ω-3 methyl peak values acquired with the two long TE values were fitted to a mono-exponential function in MATLAB using a least-squares algorithm. The average and standard deviation of the ω-3 and non- ω-3 methyl proton apparent T_2 times were calculated for the oils.

In-Vivo animal scans:

The efficacy of the determined PRESS TE for resolving the methyl resonances was verified *in vivo* on mice fed different diets. Nine female CD1 mice were separated into 3 *ad libitium* diet groups: high ω-3 (≈ 16 % ω-3), medium ω-3 (≈ 9 % ω-3), and low ω-3 (≈ 1 % ω-3). All three diets were 20 % w/w fat. Details of the diet fat composition (obtained by GC) are given in Table 3.1. The non-fat portion of the diets consisted of a semi-purified macro-nutrient and micro-nutrient blend as previously described in detail [52]. Mice were scanned when they reached 40 g in weight (about 3 months of age), and then again at approximately 5 months of age. Sedation was achieved using isoflurane through a plastic tube and a nose cone fastened to the animal's airways. Mice were placed in a supine position and a gating pillow was attached to their upper abdomen to provide respiratory response. The lower abdomen of each mouse was positioned in the middle of the birdcage coil. Temperature was maintained at 37° using a rectal probe connected to a heating module. Spin echo images were obtained using thirty 1 mm slices, with a TE of 16.3 ms and a TR of 900 ms. Gated PRESS spectra were obtained using PRESS with a TE of 25 ms (short-TE, TE_1 =15 ms, TE_2 = 10 ms) and PRESS with the TE determined to resolve the two methyl resonances from a 3 x 3 x 3 mm^3 voxel in the visceral fat of the abdomen (Figure 3.2). Spectra were acquired as 2048 points. Shimming yielded a methylene linewidth of about 35 Hz. Each mouse was euthanized by carbon dioxide inhalation (in accordance with current Canadian Council on Animal Care guidelines [53], using a flow rate of 25 % of the chamber) after its second scan and a sample of visceral abdominal fat tissue was excised for GC

analysis. The relative ω-3 fat levels were determined using the spectra acquired with the TE chosen to resolve the methyl resonances, by dividing the ω-3 methyl resonance areas by the sum of the ω-3 (0.94 ppm – 1.0 ppm) and non-ω-3 methyl peak (0.86 ppm – 0.93 ppm) areas. The averages and standard deviations of the MRS measures of ω-3 content over the three mice in each diet group were calculated for each of the two time points and the latter time point values were plotted against the corresponding average estimates obtained by GC. Scans were also performed with the two TE values on a female CD1 control mouse (about 4 months of age) that was fed a standard chow diet and excised tissue was also analyzed with GC. The control chow diet (PicoLab Rodent Diet 20 [54]) was 5.6 % w/w fat, and the fat portion consisted of ≈ 5.9 % ω-3 fat. Correlation of GC ω-3 tissue composition with that of the corresponding diet was also assessed. Error bars on plots are ± standard deviation of values over the three mice in each group. Coefficients of determination for linear correlations were calculated in MATLAB.

Differences in T_2 relaxation decay between ω-3 and non-ω-3 methyl protons were also investigated *in vivo* on four other female CD1 mice fed the high ω-3 fat diet for 5 ± 2 months. The mice were scanned after they reached a weight of about 45 g and PRESS spectra were acquired with the short TE and the two long TE values for T_2 estimation. Two of the mice were larger so a 4 x 4 x 4 mm^3 voxel was employed. Apparent (as J-coupling effects are included) T_2 times were obtained from the ω-3 and non-ω-3 methyl peak areas acquired with the two long TE values by fitting the normalized peak areas to a mono-exponentially decaying function in MATLAB. Average ω-3 and non- ω-3 methyl resonance apparent T_2 times were calculated for the mice, along with their standard deviations.

Signal to noise ratios (SNR) of peaks were calculated by dividing peak height by the standard deviation of the noise between 7-8 ppm.

Short-TE spectra were fit using LCModel [55] using a simulated basis set which included resonances at 0.9, 1.3, 1.6, 2.1, 2.3, 2.8, 4.2, 4.3, 4.7, 5.2 and 5.3 ppm in addition to an ω-3 resonance at 0.95 ppm.

Gas Chromatography:

Abdominal visceral tissue was extracted for GC from each mouse post euthanasia and the tissue samples were frozen in a -80°C freezer. Lipids were extracted from adipose tissue using a modified Folch technique [56,57]. The lipid fraction was saponified and methylated using boron trifluoride (BF_3) [56]. Fatty acids were separated, identified and quantified by automated gas liquid chromatography (Agilent GC model 7890a, Agilent Technologies, Mississauga, ON, Canada) using a 100 x 0.25 column (Agilent) as previously described [58].

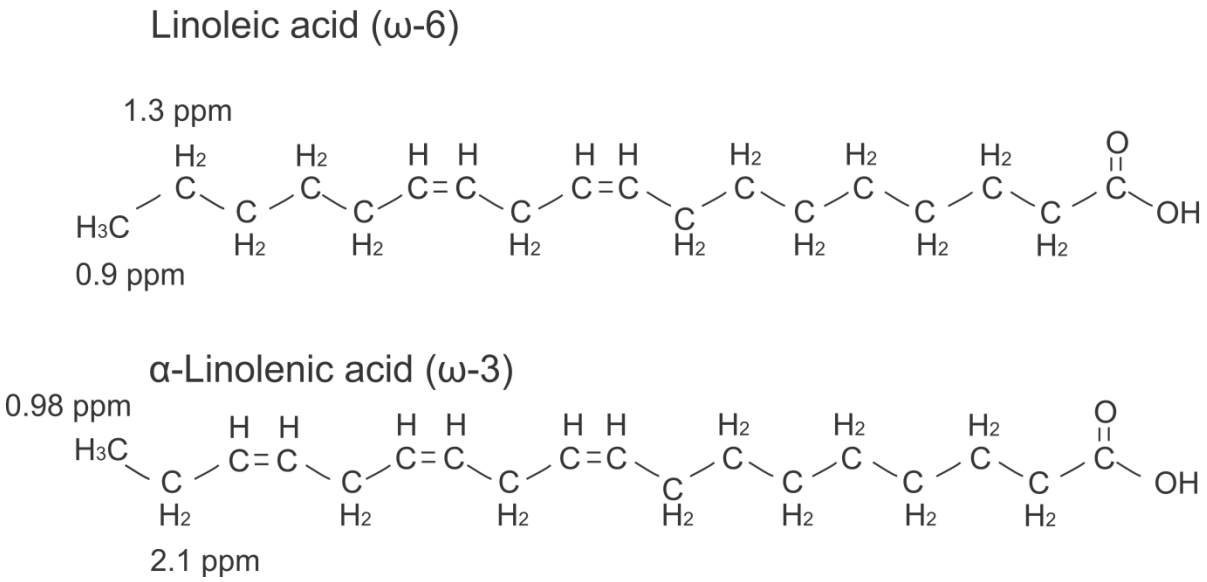

Figure 3.1: Molecular structures of linoleic acid (an ω-6 fatty acid) and α-linolenic acid (an ω-3 fatty acid). The first carbon-to-carbon double bond occurs on the 6th and 3rd carbons from the end-chain methyl (CH_3) groups for ω-6 and ω-3 fats, respectively.

Table 3.1: Fat composition of the 20 % w/w fat high, medium, and low ω-3 diets. The percentage of the ω-3 components shown are of the total fat content in the diet.

High ω-3 Diet	**% of total**	**% ω-3**
Flax	22.0	11.5
Lard	30.0	0.4
Olive	38.0	0.3
Docosahexaenoic acid (DHA)	10.0	4.2
Total	100.0	16.4
Medium ω-3 Diet	**% of total**	**% ω-3**
Flax	10.0	5.2
Lard	73.0	1.1
Olive	7.0	0.05
DHA	5.0	2.1
Canola	5.0	0.5
Total	100.0	9.0
Low ω-3 Diet	**% of total**	**% ω-3**
Lard	86.0	1.3
Olive	14.0	0.1
Total	100.0	1.4

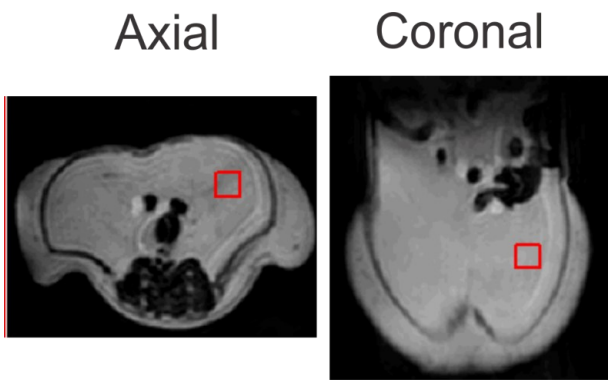

Figure 3.2: Axial and coronal abdominal images of one of the mice showing the location of the 3 x 3 x 3 mm^3 MRS voxel.

3.4 Results

The shortest optimal total PRESS echo time for resolving the ω-3 and non-ω-3 methyl resonances was 109 ms, corresponding to n = 1 in the theoretical section of the Materials and Methods. A TE of 36 ms, corresponding to n = 0, did not adequately resolve the two resonances. Figure 3.3 displays the oil spectra acquired from PRESS using a short TE (25 ms) and the optimized long TE (109 ms) at 9.4 T. In addition, Figure 3.3 presents the ω-3 methyl peak to total methyl peak area ratio (% ω-3 content) obtained at 9.4 T (with a TE of 109 ms) versus that measured at 16.5 T for the five oils; an R^2 value of 0.97 is obtained. A TE of 399 ms (corresponding to n = 5 in the theoretical Methods section) was selected as the second echo time for estimating apparent T_2 relaxation times in the oils and in the mice. Spectra acquired from linseed oil using TE of 25 ms (short TE) and the optimized timings of 109 ms and 399 ms are displayed in Figure 3.4. Calculated average apparent T_2 relaxation times and the associated standard deviations for the oil ω-3 and non- ω-3 methyl protons were 906 ms ± 148 ms and 398 ms ± 78 ms, respectively.

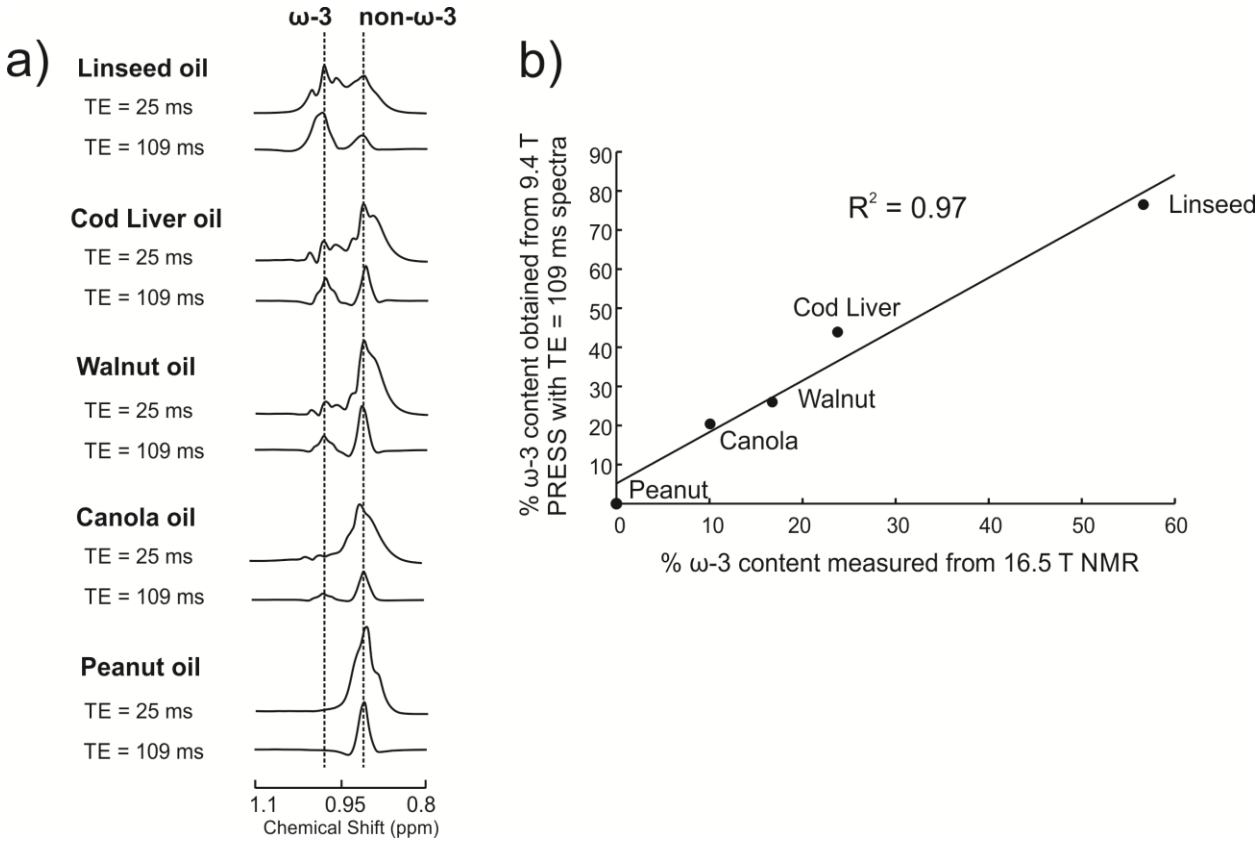

Figure 3.3: Oil spectra acquired using PRESS with a TE of 25 ms and 109 ms at 9.4 T (a). The ω-3 and non-ω-3 methyl peaks are better resolved using the TE of 109 ms. The ω-3 methyl peak to total methyl peak area ratio (% ω-3 content obtained at 9.4 T (with TE of 109 ms)) versus 16.5 T (b) for the five oils.

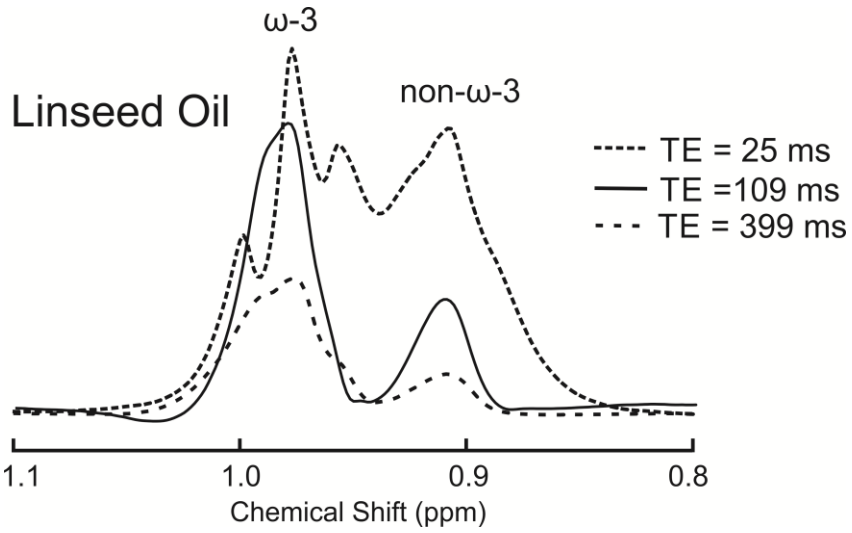

Figure 3.4: Methyl spectra acquired from linseed oil, using TE values of 25 ms, 109 ms, and 399 ms. The ω-3 and non- ω-3 methyl signals are resolved using the optimized TE values of 109 ms and 399 ms, enabling apparent T_2 quantification.

Table 3.2 indicates the average MRS measures of ω-3 fat content obtained from each diet group (standard deviations are also indicated) at the two time points. For the low ω-3 diet mice, a ω-3 peak was not visible; therefore, a value of zero was assigned. Figure 3.5 displays *in-vivo* spectra obtained from the second time point scans. Spectra acquired with TE values of 25 ms and 109 ms are shown for a mouse from the high ω-3 diet group. The methyl spectral range acquired with a TE of 109 ms is shown for a mouse from each of the diet groups and also for the control mouse. The control mouse yielded ω-3 content of 4.20 % using 9.4 T MRS and 2.43 % using GC analysis; the SNR of the ω-3 methyl peak from the 3 x 3 x 3 mm^3 voxel spectrum obtained with TE = 109 ms (in 32 averages) was ≈ 26. Figure 3.6 (a) presents the average adipose tissue ω-3 content in each diet group measured from GC against the average ω-3 fat content in each diet, including that of the control. The coefficient of determination (R^2) was 1.00. Figure 3.6 (b) presents the MRS measures of ω-3 fat against corresponding GC measures, including the control diet. The R^2 value was 0.96. The standard deviations for MRS measurements and GC measurements in each diet group are presented as error bars. The low ω-3 diet has no error bars because the signal was not detectable.

Table 3.2: Averages and standard deviations (for each of the three diet groups) of percentages of ω-3 MRS measures obtained at the two time points.

	1st time point (≈ 3 months of age)	**2nd time point (≈ 5 months of age)**
Diet	**% ω-3 Content**	**% ω-3 Content**
High ω-3	13.3 ± 1.9	12.1 ± 1.5
Medium ω-3	9.0 ± 1.1	7.9 ± 0.6
Low ω-3	0.0	0.0

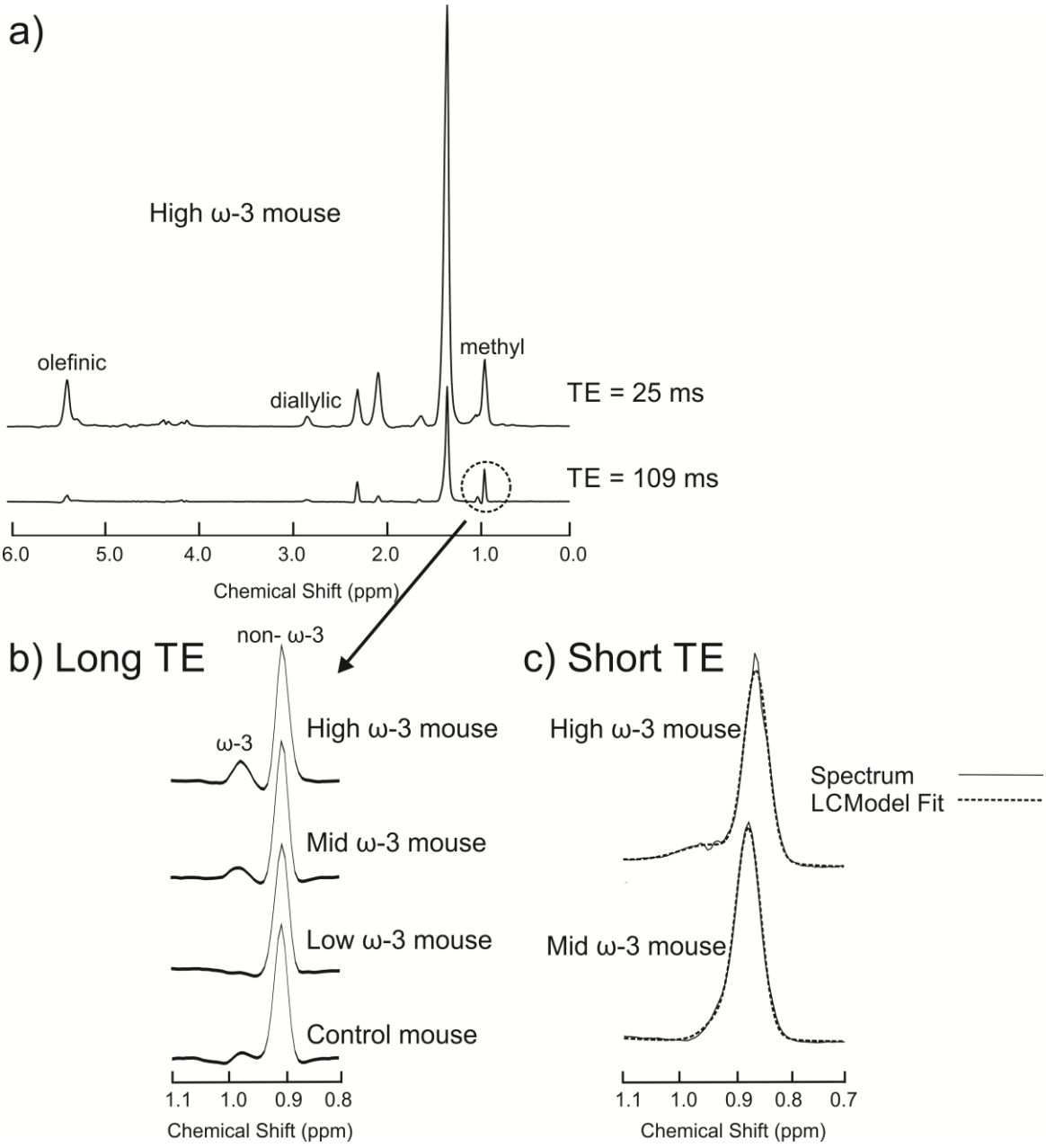

Figure 3.5: Spectra obtained from the second time points from a mouse in the high-ω-3 diet group with the highest ω-3 content with a PRESS TE of 25 ms and a PRESS TE of 109 ms (a). Spectral range showing methyl spectra acquired with a TE of 109 ms from a mouse from each diet group, and from the control mouse (b). Panel (c) shows LCModel fits for the short-TE spectrum shown in (a) and the short-TE spectrum from the mouse with the highest ω-3 content in the mid ω-3 group.

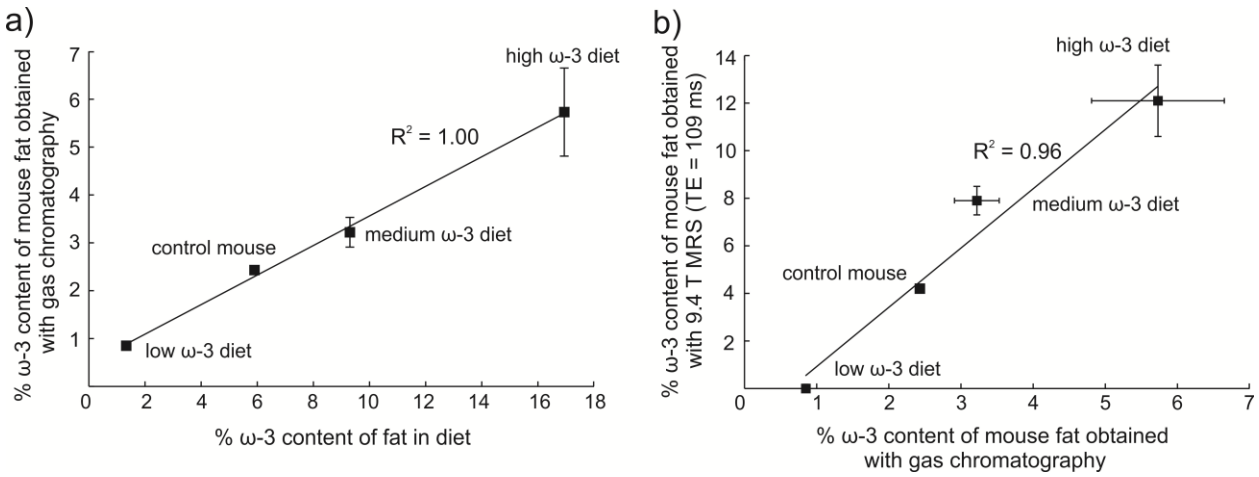

Figure 3.6: Correlation between average ω-3 fat content (for each of the three diet groups) measured using GC versus dietary content (a). Averages and standard deviations (for each of the three diet groups) of ω-3 content acquired from the second time point PRESS spectra (TE of 109 ms) compared to the measures obtained from GC of the excised adipose tissue (b). Standard deviations are shown as error bars. Data for the control mouse is also included.

The short-TE spectrum shown in Figure 3.5 from the high ω-3 diet mouse (had highest ω-3 content) is the only one that showed visible signal for the ω-3 resonance. All remaining mice (in all three groups) showed a single methyl resonance in their short-TE spectra with no visible ω-3 shoulder. LCModel fitting of the short-TE spectrum shown in Figure 3.5(a) is displayed in 3.5(c) along with fitting of the short-TE spectrum from the mouse in the mid ω-3 group that had the highest ω-3 content. The control mouse short-TE spectrum (not shown) was also fitted. The % ω-3 obtained from LCModel analysis of the short-TE spectra are 33.5 %, 12.3 % and 0 %, for the high ω-3, mid ω-3 and control mouse, respectively. The % ω-3 content obtained with GC from the three mice is 6.6 %, 3.4 % and 2.4 %, respectively. The % ω-3 content obtained with long-TE MRS from the three mice are 13.6 %, 7.0 % and 4.2 %, respectively.

Figure 3.7 shows mouse methyl spectra acquired with TE values of 25 ms, 109 ms, and 399 ms from one of the mice used for apparent T_2 estimation. The average apparent T_2 relaxation times in the mice were 410 ± 68 ms and 283 ± 57 ms for ω-3 and non- ω-3 methyl protons,

respectively. The SNR of the ω-3 methyl resonance peak from a 3 x 3 x 3 mm^3 voxel in the mouse abdominal fat was ≈ 40 and ≈ 17, in the TE = 109 ms and TE = 399 ms spectra, respectively.

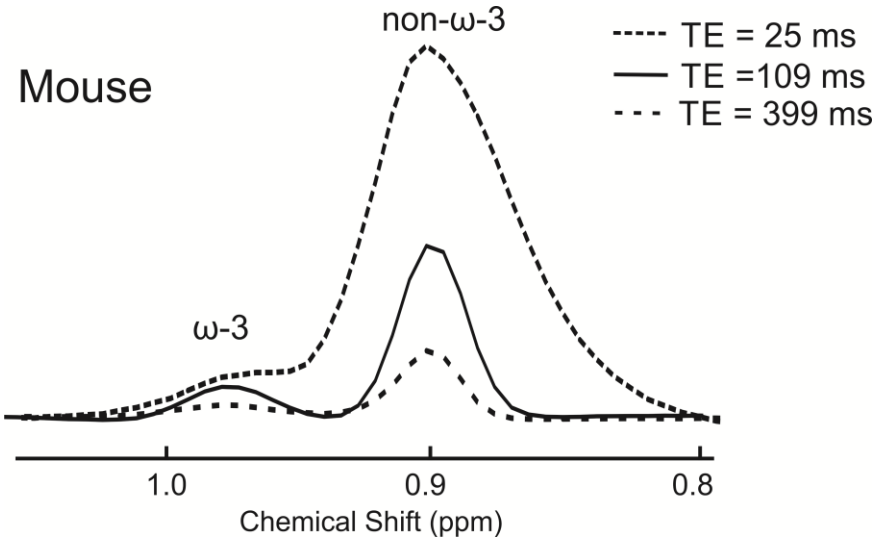

Figure 3.7: Methyl spectra acquired from a mouse fed the high ω-3 fat diet, using TE values of 25 ms, 109 ms, and 399 ms. The ω-3 and non- ω-3 methyl signals are resolved using the optimized TE values of 109 ms and 399 ms, enabling apparent T_2 quantification.

3.5 Discussion

Levels of fat unsaturation in body tissues have shown relevance in disease [1-19]. Including ω-3 fatty acid contributions to fat composition analysis is worthwhile because ω-3 dietary fat intake in humans has been demonstrated to correlate inversely with disease [20-25] as have levels of adipose tissue ω-3 content [8,9,28,29]. Measuring ω-3 fatty acid content with *in vivo* MRS even at high field is challenging because of its low concentration in adipose tissue [43] and because of spectral overlap between the ω-3 and non-ω-3 methyl resonances [44] using standard short-TE techniques. We demonstrate this by attempting to fit three short-TE spectra with LCModel, one obtained from the high ω-3 group, one from the mid-ω-3 group and, the third, from the control mouse. The fitting did not yield accurate relative % ω-3 measures; the relative ω-3 fraction of the mid-ω-3 mouse to the high ω-3 was 0.37 compared to 0.51 obtained with both GC and long

TE MRS. No ω-3 was detected in the control mouse from the short-TE spectrum, whereas the long-TE spectrum yielded a separate resonance for the ω-3 protons.

The issue of resolving the methyl resonances was previously addressed at 7 T [45] by using an optimized ultra-long TE of 1000 ms in oils and in human adipose tissue *in vivo*. The timing was selected to invert the triplet side peaks and to exploit the shorter T_2 of the methylene and non-ω-3 methyl protons compared to that of the ω-3 protons. However, a TE of 1000 ms also results in significant signal loss from the ω-3 protons due to T_2 relaxation. The improved spectral resolution at 9.4 T renders a much shorter TE than 1000 ms to resolve the two methyl resonances. We demonstrate that PRESS with a TE of 109 ms (TE_1=15ms) at 9.4 T achieves the objective and its efficacy is verified in oils and *in vivo* in mice fed different fat diets. In a previous study tailored for ω-3 measurement, differences in ω-3 fat content due to dietary intake were not investigated [45].

Measures of ω-3 fat content in the oils using PRESS with a TE of 109 ms correlated with the expected ω-3 fat content obtained using high resolution 16.5 T NMR (R^2 = 0.97), which is essentially a pulse-acquire experiment (measures not affected by J-coupling or T_2 relaxation effects). The ω-3 fat content was overestimated using 9.4 T MRS compared to 16.5 T NMR; this is likely due to the longer apparent T_2 relaxation time of the ω-3 protons compared to the non-ω-3 protons at 9.4 T. Differences in apparent T_2 relaxation rates of the ω-3 and non-ω-3 methyl protons were investigated in the oils using echo times of 109 and 399 ms. We employ the term apparent because the values obtained only provide a measure of whether differences exist in T_2 relaxation of the two sets of methyl protons. They do not provide an accurate T_2 value because of inclusion of effects of J-coupling modulation. The accuracy is also limited because only two TE values were employed and using an additional longer TE may have improved the measures [59]. Calculated apparent T_2 relaxation times of the oil ω-3 and non-ω-3 methyl protons were 906 ms ± 148 ms and 398 ms ± 78 ms on average, respectively, indicating a higher T_2 for the ω-3 protons by approximately a factor of 2.3. The result is comparable to that reported at 7 T, which found that ω-3 methyl protons in oils (fish, soybean and corn) had on average an apparent T_2 relaxation time 1.9 times that of non-ω-3 methyl protons (average T_2 values for the ω-3 and non-ω-3 methyl protons were 623 ms ± 34 ms and 325 ms ± 7, respectively) [45]. The values obtained

with the previous work at 7 T are lower than what was found in this work; the differences may be in part due to the different oils utilized but are likely due to the TE values used for fitting; the ω-3 and non-ω-3 methyl central peak areas acquired using echo time intervals of 20 ms were fit to a mono-exponential function [45]. J-modulation of the outer triplet signals were acknowledged to have had an effect on the T_2 estimates [45]. The latter likely also affects our estimates despite selecting two TE values which in theory should yield net zero area for the triplet side peaks. Although both TE values of 109 ms and 399 ms resolve the two methyl resonances as seen for linseed oil in Figure 3.4, it is clear that the lineshapes of the ω-3 signal differ for the two TE values. Whereas with a TE of 109 ms, the side peaks of the triplet are minimized, they can be observed in the spectrum obtained with a TE of 399 ms. Deviations from theory can present themselves due to imperfect RF pulses [45,51]. In particular, the PRESS sequence has been shown to potentially have significant effects on metabolite quantification for coupled spins [60]. Furthermore, evolution of anti-phase coherences during the signal acquisition period affects the lineshape [51]. Deviations would also occur if the coupling constants differ from what was assumed; coupling interactions in fats are complex [61]. The deviation of the behavior of the side peaks from what is theoretically expected affects the measured apparent T_2 relaxation time, since their signal either adds or subtracts from the central methyl peak.

In the mice, the ω-3 fat content measured using GC correlated with that in the diets with an R^2 value of 1.00, consistent with the assumption that dietary fat composition is reflected in adipose tissue composition [35]. Other rodent studies also observed that ω-3 levels are affected by diet and that changes can be measured in tissue fat composition [32-34], including abdominal adipose tissue [33]. Ouldamer et al. correlated ω-3 fat content from dietary intake in rats with that quantified from GC and high resolution NMR (11.7 T) of excised tissue [62]. PRESS with a TE of 109 ms clearly resolved the ω-3 and non-ω-3 methyl protons in the mice fed diets that are similar to those consumed habitually by people or prescribed for reducing or preventing diseases [20-25,27,35,52]. The ω-3 fat content measured with MRS over the two time points are similar, suggesting that the mice reached a plateau for ω-3 fat storage before the first MRS scan (when the mice weighed about 40 g). The measured ω-3 fat content from the second time point spectra correlated with that calculated from GC with an R^2 value of 0.96, demonstrating that the sequence enabled relative quantification of ω-3 fatty acid content. As shown in Figure 3.7, a TE

of 399 ms also effectively resolved the two methyl peaks. Estimated ω-3 and non-ω-3 methyl proton apparent T_2 relaxation times were on average 410 ± 68 ms and 283 ± 57 ms, respectively. Like in the oils, the ω-3 protons have a larger T_2 than that of the non-ω-3 protons, but the difference is not as large. The apparent T_2 relaxation times *in vivo* were also likely affected by deviations of the behavior of the side peaks from theory. The larger apparent T_2 relaxation time of the ω-3 methyl protons may contribute to the overestimation of ω-3 content (Figure 3.6(b)). As with MRS studies in general it is challenging to obtain accurate measures due to J-coupling and T_2 relaxation effects[49].

A SNR of 26 was obtained for the ω-3 resonance in the control mouse from the TE = 109 ms spectrum obtained from a 3 x 3 x 3 mm^3 voxel. It appears that the adipose tissue ω-3 concentration limit for detection in this work is ≈ 2 % since this content was detectable in the control mouse fed 5.9 % ω-3 fat content whereas the < 1 % adipose ω-3 concentration was not detectable in the mice fed the low (1.4 %) ω-3 diet. A SNR of ≈ 9 would be expected for the mice fed the low ω-3 fat diet (average ω-3 content of 0.85 % measured with GC); however, no quantifiable resonance was detected in the low ω-3 diet group. Negative signal modulation from the side peaks could potentially be subtracting signal from the central peak. A larger voxel size or a higher number of averages (128 as opposed to 32, which were employed in this work) would likely render the ω-3 resonance visible in the low ω-3 diet group. It has been determined that the SNR limit for quantification of some coupled metabolites in brain MRS studies is SNR > 10 [63]. Peak integration was performed over the spectral region of the central resonance of the methyl triplets, with care being taken to avoid inclusion of any signal from the side peaks (negative signal) which if included could cause a drop in ω-3 measured signal by as much as 30 % depending on ω-3 content.

The presented work at 9.4 T enables resolving the ω-3 methyl resonance from that of the non ω-3 in mice and correlating measures with dietary intake. The non-invasive methodology can be used to investigate the impact of different dietary components on adipose tissue composition in long-term studies and their relation to other measurable factors in disease (such as bone strength, digestibility, or insulin sensitivity) [31-35]. Furthermore, since levels of ω-3 fat can be altered in disease and in feeding trials [8,9,27-29,50,62], the method can potentially be used to assess serial levels of ω-3 non-invasively with MRS in disease and diet models.

3.6 Citations

1. Machann J, Stefan N, Schabel C, et al. Fraction of unsaturated fatty acids in visceral adipose tissue (VAT) is lower in subjects with high total VAT volume - a combined ^{1}H MRS and volumetric MRI study in male subjects. NMR Biomed 2013;26:232-236.
2. Tufts LS, Shet K, Liang F, Majumdar S, Li X. Quantification of bone marrow water and lipid composition in anterior cruciate ligament-injured and osteoarthritic knees using three-dimensional magnetic resonance spectroscopic imaging. Magn Reson Imaging 2016;34:632-637.
3. Pollesello P, Eriksson O, Höckerstedt K. Analysis of total lipid extracts from human liver by ^{13}C and ^{1}H Nuclear Magnetic Resonance Spectroscopy. Anal Biochem 1996;236:41-48.
4. He Q, Shkarin P, Hooley RJ, Lannin DR, Weinreb JC, Bossuyt VIJ. *In vivo* MR spectroscopic imaging of polyunsaturated fatty acids (PUFA) in healthy and cancerous breast tissues by selective multiple-quantum coherence transfer (Sel-MQC): A preliminary study. Magn Reson Med 2007;58:1079-1085.
5. Fardanesh R, Marino MA, Avendano D, Leithner D, Pinker K, Thakur SB. Proton MR spectroscopy in the breast: Technical innovations and clinical applications. J Magn Reson Imaging 2019;50:1033-1046.
6. Patsch JM, Li X, Baum T, et al. Bone marrow fat composition as a novel imaging biomarker in postmenopausal women with prevalent fragility fractures. J Bone Miner Res 2013;28:1721-1728.
7. Karampinos DC, Ruschke S, Dieckmeyer M, et al. Quantitative MRI and spectroscopy of bone marrow. J Magn Reson Imaging 2018;47:332-353.
8. Garaulet M, Hernandez-Morante JJ, Lujan J, Tebar FJ, Zamora S. Relationship between fat cell size and number and fatty acid composition in adipose tissue from different fat depots in overweight/obese humans. Int J Obes 2006;30:899-905.
9. Garaulet M, Pérez-Llamas F, Pérez-Ayala M, et al. Site-specific differences in the fatty acid composition of abdominal adipose tissue in an obese population from a Mediterranean area: relation with dietary fatty acids, plasma lipid profile, serum insulin, and central obesity. Am J Clin Nutr 2001;74:585-591.
10. Calderan L, Marzola P, Nicolato E, et al. *In vivo* phenotyping of the ob/ob mouse by magnetic resonance imaging and ^{1}H-magnetic resonance spectroscopy. Obesity 2006;14:405-414.
11. Mosconi E, Fontanella M, Sima DM, et al. Investigation of adipose tissues in Zucker rats using *in vivo* and *ex vivo* magnetic resonance spectroscopy. J Lipid Res 2011;52:330-336.
12. Lee Y, Jee H, Noh H, et al. In vivo ^{1}H-MRS hepatic lipid profiling in nonalcoholic fatty liver disease: an animal study at 9.4 T. Magn Reson Med 2013;70:620-629.
13. Chen Y, Jiang Z, Long L, et al. Magnetic Resonance Imaging: Proton density fat fraction for assessment of pancreatic fatty infiltration during progression of T2DM Bama Minipigs. J Magn Reson Imaging 2019;50:1905-1913.
14. Oostendorp M, Engelke UFH, Willemsen MAAP, Wevers RA. Diagnosing inborn errors of lipid metabolism with proton nuclear magnetic resonance spectroscopy. Clin Chem 2006;52:1395-1405.

15. Hu HH, Branca RT, Hernando D, et al. Magnetic resonance imaging of obesity and metabolic disorders: Summary from the 2019 ISMRM Workshop. Magn Reson Med 2020;83:1565-1576.
16. Cordes C, Baum T, Dieckmeyer M, et al. MR-based assessment of bone marrow fat in osteoporosis, diabetes, and obesity. Front Endocrinol 2016;7:10.3389/fendo.2016.00074 (7 pages).
17. Wang L, Salibi N, Chang G, et al. Assessment of subchondral bone marrow lipids in healthy controls and mild osteoarthritis patients at 3T. NMR Biomed 2011;25:545-555.
18. Yeung DKW, Griffith JF, Antonio GE, Lee FKH, Woo J, Leung PC. Osteoporosis is associated with increased marrow fat content and decreased marrow fat unsaturation: A proton MR spectroscopy study. J Magn Reson Imaging 2005;22:279-285.
19. Korteweg MA, Veldhuis WB, Mali WPTM, et al. Investigation of lipid composition of dissected sentinel lymph nodes of breast cancer patients by 7T proton MR spectroscopy. J Magn Reson Imaging 2012;35:387-392.
20. Coelho DF, Pereira-Lancha LO, Chaves DS, et al. Effect of high-fat diets on body composition, lipid metabolism and insulin sensitivity, and the role of exercise on these parameters. Braz J Med Biol Res 2011;44:966-972.
21. Hammad SS, Jones PJ. Dietary fatty acid composition modulates obesity and interacts with obesity-related genes. Lipids 2017;52:803-822.
22. Orchard TS, Pan X, Cheek F, Ing SW, Jackson RD. A systematic review of omega-3 fatty acids and osteoporosis. Br J Nutr 2012;107:10.1017/S0007114512001638 (14 pages).
23. Elbahnasawy AS, Valeeva ER, El-Sayed EM, Stepanova NV. Protective effect of dietary oils containing omega-3 fatty acids against glucocorticoid-induced osteoporosis. J Nutr Health 2019;52:323-331.
24. Kaizer LB, N.F., Kriukov V, Tritchler D. Fish consumption and breast cancer risk: an ecological study. Nutr Cancer 1989;12:61-68.
25. Kim J, Lim SY, Shin A, et al. Fatty fish and fish omega-3 fatty acid intakes decrease the breast cancer risk: a case control study. BMC Cancer 2009;9:10.11 186/1471-2407-1479-1216 (11 pages).
26. McGlory C, Calder PC, Nunes EA. The influence of omega-3 fatty acids on skeletal muscle protein turnover in health, disuse, and disease. Front Nutr 2019;6:10.3389/fnut.2019.00144 (13 pages).
27. Baracos VE, Mazurak VC, Ma DWL. *n*-3 Polyunsaturated fatty acids throughout the cancer trajectory: influence on disease incidence, progression, response to therapy and cancer-associated cachexia. Nut Res Rev 2004;17:177-192.
28. Bougnoux P, Koscielny S, Chajès V, Descamps P, Couet C, Calais G. α- Linolenic acid content of adipose breast tissue: a host determinant of the risk of early metastasis in breast cancer. Br J Cancer 1994;70:330-334.
29. Simonsen N, van't Veer P, Strain JJ, et al. Adipose tissue omega-3 and omega-6 fatty acid content and breast cancer in the EURAMIC study. Am J Epidemiol 1998;147:342-352.
30. Högström M, Nordström P, Nordström A. n-3 Fatty acids are positively associated with peak bone mineral density and bone accrual in healthy men: the NO_2 study. Am J Clin Nutr 2007;85:803-807.
31. Albert BB, Derraik JGB, Brennan CM, et al. Higher omega-3 index is associated with increased insulin sensitivity and more favourable metabolic profile in middle-aged overweight men. Sci Rep 2014;4:10.1038/srep06697 (7 pages).

32. Tou JC, Altman SN, Gigliotti JC, Benedito VA, Cordonier EL. Different sources of omega-3 polyunsaturated fatty acids affects apparent digestibility, tissue deposition, and tissue oxidative stability in growing female rats. Lipids Health Dis 2011;10:179-193.
33. Jurešić GC, Percan K, Broznić D. Effect of dietary fatty acid variation on mice adipose tissue lipid content and phospholipid composition. Croat J Food Technol Biotech Nutr 2016;11:128-137.
34. Lau BY, Fajardo VA, McMeekin L, et al. Influence of high-fat diet from differential dietary sources on bone mineral density, bone strength, and bone fatty acid composition in rats. Appl Physiol Nutr Metab 2010;35:598-606.
35. Field CJ, Clandinin MT. Modulation of adipose tissue fat composition by diet: A review. Nutr Res 1984;4:743-755.
36. Lindeboom L, de Graaf RA. Measurement of lipid composition in human skeletal muscle and adipose tissue with ^{1}H-MRS homonuclear spectral editing. Magn Reson Med 2018;79:619-627.
37. He D, Mustafi D, Fan X, et al. Magnetic resonance spectroscopy detects differential lipid composition in mammary glands on low fat, high animal fat versus high fructose diets. PLOS ONE 2018;13:e0190929 (12 pages).
38. Strobel K, van den Hoff J, Pietzsch J. Localized proton magnetic resonance spectroscopy of lipids in adipose tissue at high spatial resolution in mice *in vivo*. J Lipid Res 2008;49:473-480.
39. Coum A, Ouldamer L, Noury F, et al. *In vivo* MR spectroscopy of human breast tissue: quantification of fatty acid composition at a clinical field strength (3 T). Magn Reson Mater Phy 2016;29:1-4.
40. Hamilton G, Schlein AN, Middleton MS, et al. *In vivo* triglyceride composition of abdominal aipose tissue measured by ^{1}H MRS at 3T. J Magn Reson Imaging 2017;45:1455-1463.
41. Peterson P, Trinh L, Må nsson S. Quantitative ^{1}H MRI and MRS of fatty acid composition. Magn Reson Med 2020;85:49-67.
42. Ren J, Dimitrov I, Sherry AD, Malloy CR. Composition of adipose tissue and marrow fat in humans by ^{1}H NMR at 7 Tesla. J Lipid Res 2008;49:2055-2062.
43. Hodson L, Skeaff CM, Fielding BA. Fatty acid composition of adipose tissue and blood in humans and its use as a biomarker of dietary intake. Prog Lipid Res 2008;47:348-380.
44. Guillén MD, Ruiz A. High resolution ^{1}H nuclear magnetic resonance in the study of edible oils and fats. Trends Food Sci Technol 2001;12:328-338.
45. Gajdošík M, Hingerl L, Škoch A, et al. Ultralong TE *in vivo* ^{1}H NMR spectroscopy of omega-3 fatty acids in subcutaneous adipose tissue at 7 T. J Magn Reson Imaging 2019;50:71-82.
46. Lundbom J, Heikkinen S, Fielding B, Hakkarainen A, Taskinen M-R, Lundbom N. PRESS echo time behavior of triglyceride resonances at 1.5 T: Detecting ω-3 fatty acids in adipose tissue *in vivo*. J Magn Reson 2009;201:39-47.
47. Škoch A, Tošner Z, Hájek M. The *in vivo* J-difference editing MEGA-PRESS technique for the detection of n-3 fatty acids. NMR Biomed 2014;27:1293-1299.
48. Fallone CJ, McKay RT, Yahya A. Long TE STEAM and PRESS for estimating fat olefinic/methyl ratios and relative ω-3 fat content at 3T. J Magn Reson Imaging 2018;48:169-177.

49. Yahya A, Tessier AG, Fallone BG. Effect of J-coupling on lipid composition determination with localized proton magnetic resonance spectroscopy at 9.4 T. J Magn Reson Imaging 2011;34:1388-1396.
50. Ramamonjisoa N, Ratiney H, Mutel E, et al. *In vivo* hepatic lipid quantification using MRS at 7 Tesla in a mouse model of glycogen storage disease type 1a. J Lipid Res 2013;54:2010-2022.
51. Sørensen OW, Eich GW, Levitt MH, Bodenhausen G, Ernst RR. Product operator formalism for the description of NMR pulse experiments. Prog Nucl Mag Res Sp 1983;16:163-192.
52. Robinson LE, Field CJ. Dietary long chain (n-3) fatty acids facilitate immune cell activation in sedentary, but not exercise-trained rats. J Nutr 1998;128:498-504.
53. Canadian Council on Animal Care. Guidelines. https://www.ccac.ca/en/standards/guidelines/. Accessed March 2020.
54. Lab Supply. Picolab Rodent Diet 20. Accessed March 1 2020. https://www.labsupplytx.com/labdiet/picolab-rodent-diet-20/.
55. Provencher SW. Estimation of metabolite concentrations from localized *in vivo* proton NMR spectra. Magn Reson Med 1993;30:672-679.
56. Field CJ, Ryan EA, Thomson ABR, Clandinin MT. Dietary fat and and the diabetic state alter insulin binding and the fatty acyl composition of the adipocyte plasma membrane. Biochem J 1988;253:417-424.
57. Folch J, Lees M, Stanley GHS. A simple method for the isolation and purification of total lipides from animal tissues. J Biol Chem 1957;226:497-509.
58. Cruz-Hernandez C, Goeuriot S, Giuffrida F, Thakkar SK, Destaillats F. Direct quantification of fatty acids in human milk by gas chromatography. J Chromatogr A 2013;1284:174-179.
59. Brief EE, Whittall KP, Li DKB, MacKay AL. Proton T_2 relaxation of cerebral metabolites of normal human brain over large TE range. NMR Biomed 2005;18:14-18.
60. Thompson RB, Allen PS. Sources of variability in the response of coupled spins to the PRESS sequence and their potential impact on metabolite quantification. Magn Reson Med 1999;41:1162-1169.
61. Hamilton G, Middleton MS, Bydder M, et al. Effect of PRESS and STEAM sequences on magnetic resonance spectroscopic liver fat quantification. J Magn Reson Imaging 2009;30:145-152.
62. Ouldamer L, Nadal-Desbarats L, Chevalier S, Body G, Goupille C, Bougnoux P. NMR-based lipodomic approach to evaluate controlled dietary intake of lipids in adipose tissue of rat mammary tumor model. J Proteome Res 2016;15:868-878.
63. Crémillieux Y, Dumont U, Mazuel L, et al. Online quantification of lactate concentration in microdialysate during cerebral activation using ^{1}H-MRS and sensitive NMR microcoil. Front Cell Neurosci 2019;13:10.3389/fncel.2019.00089 (8 pages).

Chapter 4

Long TE STEAM and PRESS for Estimating Fat Olefinic/Methyl Ratios and Relative ω-3 Fat Content at 3 T

A version of this chapter has been published:

Fallone, C.J., McKay, R.T., and Yahya, A. (2018). Long TE STEAM and PRESS for estimating fat olefinic/methyl ratios and relative ω-3 fat content at 3T. *Journal of Magnetic Resonance Imaging* 48: 169-177.

4.1 Abstract

Fat olefinic/methyl ratios provide a measure of fat unsaturation. The methyl resonance linewidth is altered with the presence of ω-3fat. The purpose of this research was to optimize Stimulated Echo Acquisition Mode (STEAM) and Point RESolved Spectroscopy (PRESS) echo times (TE) at 3 T to 1) improve olefinic/methyl ratio quantification and 2) enable relative ω-3 fat content assessment. Experiments were completed on nine edible oils and four healthy volunteers (tibial bone marrow). STEAM (mixing time = 20 ms) and PRESS olefinic/methyl ratios as a function of TE at 3 T were compared to high-resolution 16.5 T NMR measures for the oils, and to a literature deduced value for tibial bone marrow. Percent differences were calculated between oil olefinic/methyl ratios obtained at 3 T and 16.5 T. Oil methyl linewidths were calculated at each TE to investigate the correlation with expected ω-3 fatty acid content (calculated from 16.5 T NMR). Linear regression R^2 values measured the correlation of methyl linewidth to ω-3 content. The results revealed that STEAM, TE = 120 ms, yielded average oil olefinic/methyl ratios that differ by about - 4.8 % compared to high resolution ratios. Tibial bone marrow olefinic/methyl ratios differ by -1.8 % compared with literature obtained ratios. PRESS, TE = 180 ms, resulted in oil ratios that differ by 7.8 % and tibial bone marrow ratios that differ by 0.2 %. A TE of 160 ms for both STEAM and PRESS enabled relative levels of oil ω-3 fatty acid content to be estimated (R^2 values ≥ 0.9). In conclusion, STEAM, TE = 120 ms (mixing time = 20 ms), and PRESS, TE = 180 ms, optimally estimated olefinic/methyl ratios. STEAM and PRESS, TE = 160 ms, enable relative oil ω-3 fatty acid estimation from methyl linewidths.

4.2 Introduction

Proton Magnetic Resonance Spectroscopy (MRS) has been used to assess fat unsaturation levels in a number of diseases *in vivo* [1-9]. Adipose tissue, including that of bone marrow, *in vivo* is composed of ≈ 28 % saturated (primarily palmitic acid), ≈ 51 % monounsaturated (primarily oleic acid), ≈ 14 % di-unsaturated (primarily linoleic acid), and ≈ 1 % tri-unsaturated fatty acids [10-13]. Tri-unsaturated fatty acid content is primarily (≈ 80 %) composed of the ω-3 fatty acid linolenic acid [10]. Fat unsaturation can be estimated *in vivo* from the olefinic resonance (≈ 5.4 ppm) and optimized long echo time (TE) Stimulated Echo Acquisition Mode (STEAM) and Point RESolved Spectroscopy (PRESS) sequences have been employed for situations where the water resonance (≈ 4.8 ppm) obscures its signal, such as in spinal bone marrow and in the liver [1,14,15]. A long TE also offers better spectral resolution of methyl and methylene resonances [16]. While it has been demonstrated that olefinic to methylene (≈ 1.3 ppm) ratios obtained with optimized long-TE methods [14,15] correlate with relative levels of fat unsaturation at 3 T, short-TE olefinic to methyl (≈ 0.9 ppm) peak areas have also been used to obtain a measure of fat unsaturation in humans *in vivo* at 1.5 T [4] and in rats at 4.7 T [2]. The methyl resonance serves as an appropriate reference given that every fatty acid has one methyl group [4]. Furthermore, the methyl resonance can potentially provide an indication of linolenic acid levels, which are relevant to breast cancer [17]. The methyl resonance may correlate with the linolenic acid content because of the different chemical shift and coupling interactions of the ω-3 methyl protons. The ω-3 methyl protons neighbour the ≈ 2.0 ppm allylic protons leading to a chemical shift of ≈ 0.93 ppm [18] compared to ≈ 0.83 ppm for the methyl protons of saturated fatty acids, oleic acid, and linoleic acid, which neighbour the 1.3 ppm methylene protons [18]. The difference in neighbouring proton chemical shift (2.0 ppm compared to 1.3 ppm) yields a more weakly-coupled J-coupling interaction at 3 T for the ω-3 methyl protons [19]. The differences between the two methyl groups can lead to variations in the collective lipid methyl linewidth as function of linolenic acid content.

Measurements of fat unsaturation in tibial bone marrow have been shown to be relevant in the study of disease, bone health and dietary treatment. For example, higher fat unsaturation in tibial bone marrow was found to be inversely correlated with insulin sensitivity [20]. A negative

correlation has also been associated between tibial bone marrow fat unsaturation and fasting glucose, a diabetes marker [21]. In addition, it has been demonstrated that dietary fatty acid intake affects tibial bone marrow fat composition [22-24], bone metabolism cellular processes [23] and tibial bone mineral content and histological cortical thickness [25]. A dietary treatment study in rats showed that serum protein levels that affect bone formation were higher in rats with more tibial bone marrow ω-3 fat content [26].

The first objective of the presented work was to optimize long TE STEAM and PRESS sequences (considering J-coupling evolution and transverse (T_2) relaxation effects) to yield olefinic/methyl oil and tibial bone marrow ratios that match closely to those obtained using high resolution Nuclear Magnetic Resonance (NMR) for the oils, and to a literature deduced value for tibial bone marrow. The second objective of the presented work is to investigate the correlation of methyl linewidth and ω-3 fatty acid content as a function of STEAM and PRESS TE to determine TE values that enable relative levels of fat linolenic acid content to be determined.

4.3 Materials and Methods

Data Acquisition: Experiments were performed with a 3 T Philips whole body Magnetic Resonance Imaging (MRI) scanner (Intera, Philips Healthcare, Best, Netherlands). A transmit/receive radiofrequency (RF) birdcage head coil (Philips Healthcare) was used on nine oils of varying unsaturation content: peanut, cod liver, almond, canola, sesame, linseed, sunflower, corn, and walnut oil. *In vivo,* one element of the Flex-L surface coil (Philips Healthcare) was employed for signal reception (body coil for transmission), and motion was minimized using Velcro straps to hold the coil in place. STEAM (TE = 20 to 300 ms in steps of 20 ms, mixing time [TM] = 20 ms) and PRESS (TE = 40 to 300 ms in steps of 20 ms) spectra were acquired with the following parameters: 3 sec repetition time (TR), 32 signal averages, 2048 samples, and a 2000-Hz spectral bandwidth. For PRESS, the first echo time was fixed at 15 ms, and the second echo time was altered to change the total echo time. The scanner's automatic second order shimming procedure based on FASTERMAP [27] was employed on a shim voxel identical to that of the voxel of interest and the RF transmitter frequency was centered between the methyl and olefinic resonances (≈ 3.15 ppm). Water suppression was not required and a 16-

step phase cycling scheme was used. A 20 x 20 x 20 mm^3 voxel was centered in the oil phantoms and an 8 x 8 x 8 mm^3 voxel was positioned in tibial bone marrow ≈ 10 cm below the knee in four healthy volunteers (two males and two females, age range 23 - 31 years). Informed consent was obtained from all volunteers through a protocol approved by our local ethics board. In order to ensure data repeatability, four spectra were acquired for each TE value for the oils. For the tibial bone marrow, one spectrum was acquired at each TE for each volunteer. One of the four volunteers was scanned in a separate session where four spectra were acquired with the short echo times (STEAM TE = 20 ms and PRESS TE = 40 ms) and with the determined long echo times to evaluate repeatability.

For comparison, oil spectra were also acquired using a high resolution 700 MHz (16.5 T) Varian/Agilent (Palo Alto, CA) VNMRS spectrometer. Samples were prepared by dissolving ~ 50 µL of pure oil into 550 µL of deuterated chloroform. The following parameters were used: 8389.26 Hz sweep width, 5 s acquisition time, 100 ms delay between excitation and acquisition, 42000 samples, 30° flip angle and 16 averages. As a validation of the 16.5 T measurements, a spectrum from a sample of pure linoleic acid was also acquired.

Data Processing: Spectra acquired at 3 T were filtered, phase-corrected, and peak areas of the olefinic (5.1 ppm – 5.6 ppm) and methyl (0.7 ppm – 1.1 ppm) resonances were calculated using Philips spectroscopy software. The olefinic/methyl area ratios were calculated as a function of TE from the mean of the four areas acquired for each peak. In addition, for each oil the mean of the four methyl linewidths (full width half maxima) was calculated for each STEAM and PRESS TE at 3 T. To ensure a fair comparison of linewidths across all oils, the filtering was slightly adjusted to ensure that all methylene linewidths were similar (15.2 Hz ± 0.8 Hz).

The spectra acquired at 16.5 T were processed on VNMRJ. The olefinic areas (5.25 ppm – 5.50 ppm), and the sum of the methyl areas (0.84 ppm – 0.90 ppm, and 0.94 ppm – 1.0 ppm for the ω-3 resonance) were calculated to determine olefinic/methyl ratios. The diallylic (2.6 ppm – 3.0 ppm) and the 2.3 ppm peak areas (2.2 ppm – 2.4 ppm) were also calculated for sunflower and canola oil to assess poly-unsaturation and di-unsaturation levels.

Data Analysis: To assess repeatability of the oil scans, a coefficient of variation (COV) was calculated (mean/standard deviation) for the olefinic peak from the four spectra at each TE. To

assess repeatability *in vivo*, a COV was calculated for the olefinic peak from the four spectra acquired at each of STEAM with TE = 20 ms, PRESS with TE = 40 ms and STEAM and PRESS with the optimal long TE values. For the oils, optimal TE values for STEAM and PRESS were determined by comparing the measured olefinic to methyl ratios at 3 T to those obtained at 16.5 T. A percent (%) difference between 3 T and 16.5 T measurements, averaged over all the oils, was calculated for each TE and the result was used to determine the optimal TE values. At the optimal echo times, a linear regression was computed between the measured olefinic/methyl ratios at 3 T and 16.5 T for the oils, and the coefficient of determination (R^2) was calculated. *In vivo*, optimal echo times for STEAM and PRESS were determined by comparing ratios acquired at 3 T to those calculated from literature composition for tibial bone marrow. The literature composition values were derived from gas chromatography [12,15]. A percent difference between 3 T measurements and the literature, averaged over the volunteers, was determined for each TE. Signal-to-noise ratios (SNR) was determined by measuring peak height and dividing it by the standard deviation of the noise in the 10 – 12 ppm spectral region.

Oil methyl linewidths were plotted for each TE value versus the literature ω-3 fatty acid content [15], and STEAM and PRESS echo times which yielded the highest R^2 values were selected as optimal timings for relative ω-3 fatty acid quantification. A more accurate estimate of actual ω-3 fatty acid content was calculated from the 16.5 T NMR data by dividing the ω-3 methyl peak area at ≈ 0.97 ppm by the sum of the ω-3 methyl peak area and the dominant methyl peak area (≈ 0.88 ppm) [18]. The ω-3 methyl peak was only observable for the four oils with highest ω-3 fatty acid content: linseed, cod liver, walnut, and canola oil. The measured methyl linewidths at the optimal TE values were plotted versus the 16.5 T measured ω-3 fatty acid composition for the four oils and a linear coefficient of determination, R^2, was calculated. Diallylic-to-methyl ratios were calculated for sunflower oil and canola oil from the 16.5 T NMR spectra to assess poly-unsaturation. Di-unsaturated linoleic acid content was calculated from the diallylic and 2.3 ppm peak areas and the ω-3 fatty acid content [28]. To validate the high resolution NMR measurements, olefinic to methyl and diallylic to methyl ratios were calculated for the linoleic acid sample.

4.4 Results

Figure 4.1 displays spectra acquired for canola oil at 3 T and at 16.5 T, and for tibial bone marrow at 3 T. The methyl signal from ω-3 fatty acids (0.94 ppm – 1.0 ppm) is resolved from the methyl signal of the other fatty acids (0.84 ppm – 0.90 ppm) at 16.5 T, but not at 3 T. Both phantom and *in-vivo* COV values for repeatability assessment were under 5 %. High resolution NMR linoleic acid olefinic-to-methyl and diallylic-to-methyl ratios were found to be 1.28 and 0.65, respectively, agreeing within 5 % with the expected ratios of 1.33 and 0.67, respectively. STEAM with a TE of 120 ms and PRESS with a TE of 180 ms were found to yield olefinic/methyl ratios that match most closely with the 16.5 T NMR ratios for the oils and to a literature composition deduced value *in vivo*. Table 4.1 displays the average % differences for short- TE techniques (STEAM TE = 20 ms and PRESS TE = 40 ms), and optimized long-TE techniques. The linear coefficients of determinations (R^2) for the olefinic/methyl ratios measured at 3 T versus 16.5 T at the optimal timings were 0.89 and 0.79 for STEAM TE = 120 ms and PRESS TE = 180 ms, respectively. Figure 4.2 shows normalized peak areas for the olefinic and methyl resonances of canola oil and tibial bone marrow as a function of STEAM and PRESS TE, as well as the spectral lineshapes for olefinic and methyl resonances of tibial bone marrow obtained with the optimal timings. The SNR of each peak is also displayed.

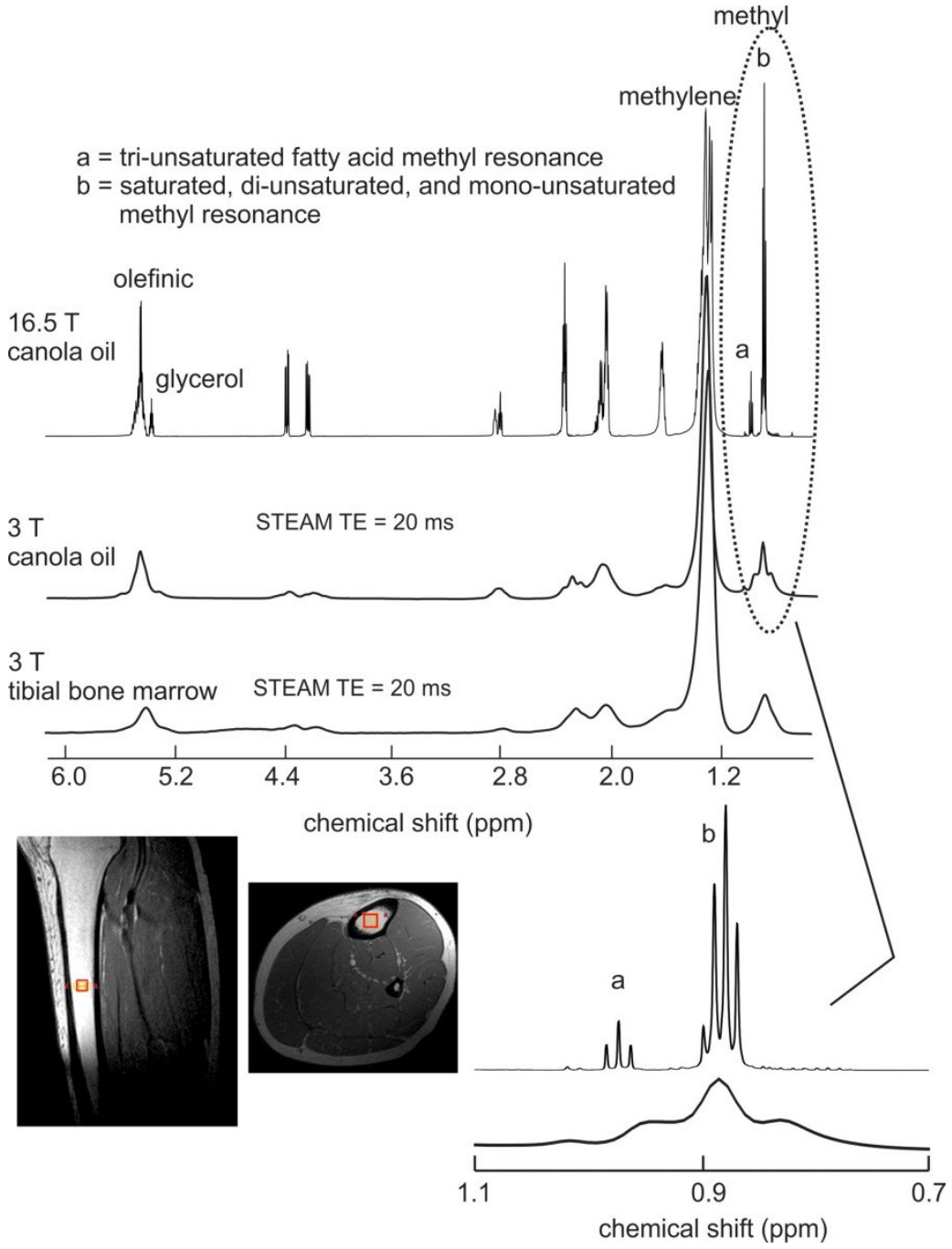

Figure 4.1: Canola oil spectra acquired at 3 T and at 16.5 T, and a tibial bone marrow spectrum (obtained from one volunteer) acquired at 3 T. The methyl signal from ω-3 fatty acids (0.94 ppm – 1.0 ppm) can be resolved from the methyl signal of other fatty acids (0.84 ppm – 0.90 ppm) at 16.5 T, but not at 3 T. The voxel location for one of the volunteers is shown on axial and sagittal images.

Table 4.1: Percent differences between measured olefinic/methyl ratios at 3 T and 16.5 T for the oils.

Technique	% difference (average over all oils)	% difference (average over all volunteers)
STEAM TE = 20 ms	5.4	9.3
PRESS TE = 40 ms	63.7	53.5
STEAM TE = 120 ms	-4.8	-1.8
PRESS TE = 180 ms	7.8	0.2

* For tibial bone marrow, % differences were based on literature composition.

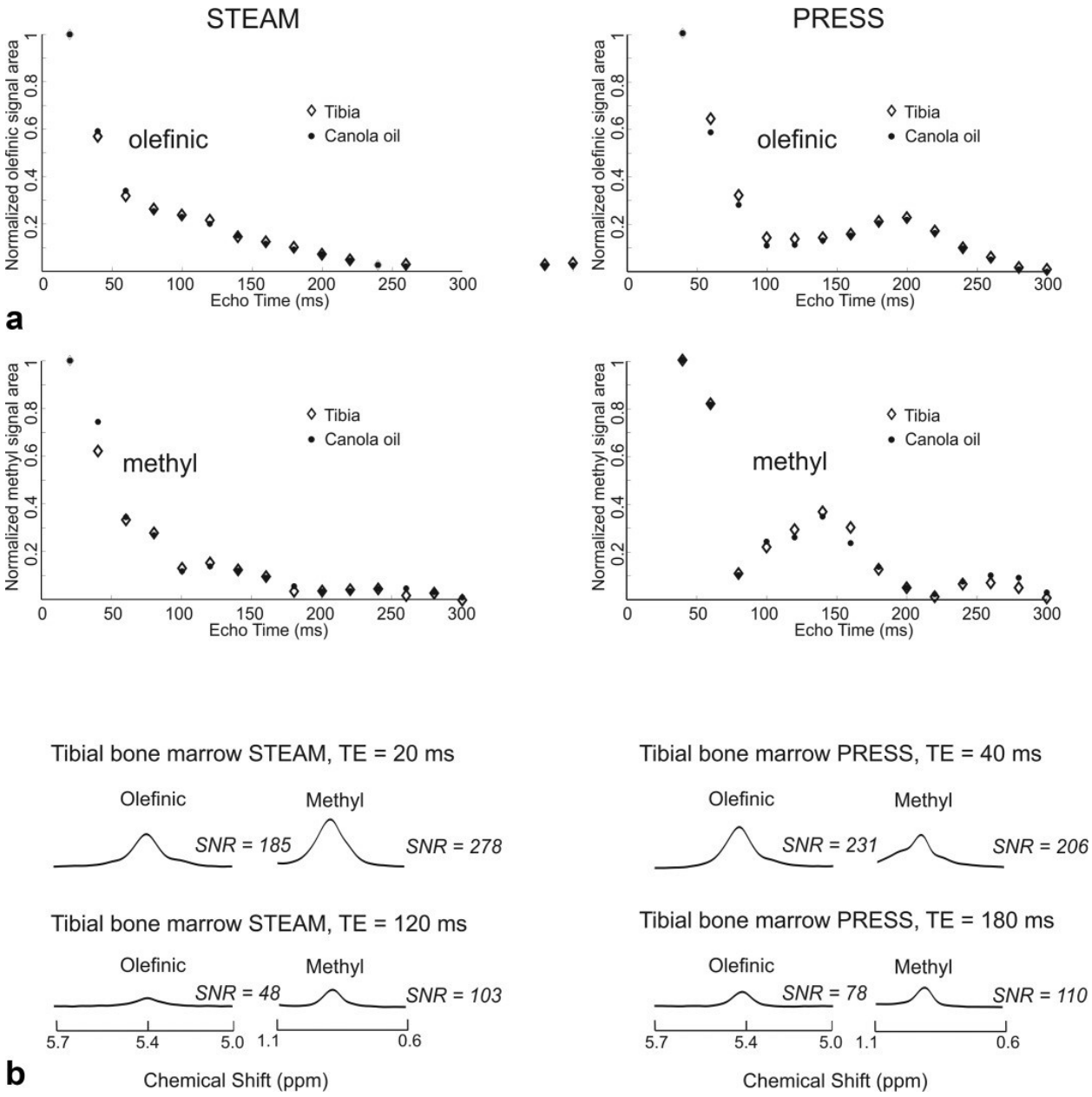

Figure 4.2: Normalized (to maximum) olefinic and methyl resonance areas (a) for canola oil and tibial bone marrow as a function of echo time using STEAM (left) and PRESS (right). Olefinic and methyl lineshapes from tibial bone marrow are shown (b) on the same scale for short TE (STEAM TE = 20 ms and PRESS TE = 40 ms), and optimized long-TE methods (STEAM TE = 120 ms and PRESS TE = 180 ms). For all STEAM spectra, TM = 20 ms. The SNR values for each peak are displayed to the right of each spectrum.

The left side of Figure 4.3 displays the methyl linewidth as a function of STEAM and PRESS TE for all nine oils. STEAM and PRESS with a TE of 160 ms were deduced to be optimal techniques for assessing relative ω-3 fatty acid content of the oils, with R^2 values of 0.94 and 0.95, respectively, for measured methyl linewidths plotted against literature ω-3 fatty acid content. The right side of Figure 4.3 shows the linear correlation between ω-3 fatty acid content (determined from 16.5 T NMR) and the measured methyl resonance linewidth using optimal techniques, with associated R^2 values of 0.90 and 0.97 for STEAM and PRESS respectively. Figure 4.4 displays the methyl line shapes of peanut, walnut and linseed oils as examples obtained with a non-optimal technique (PRESS, TE = 80 ms) and with the optimal methods.

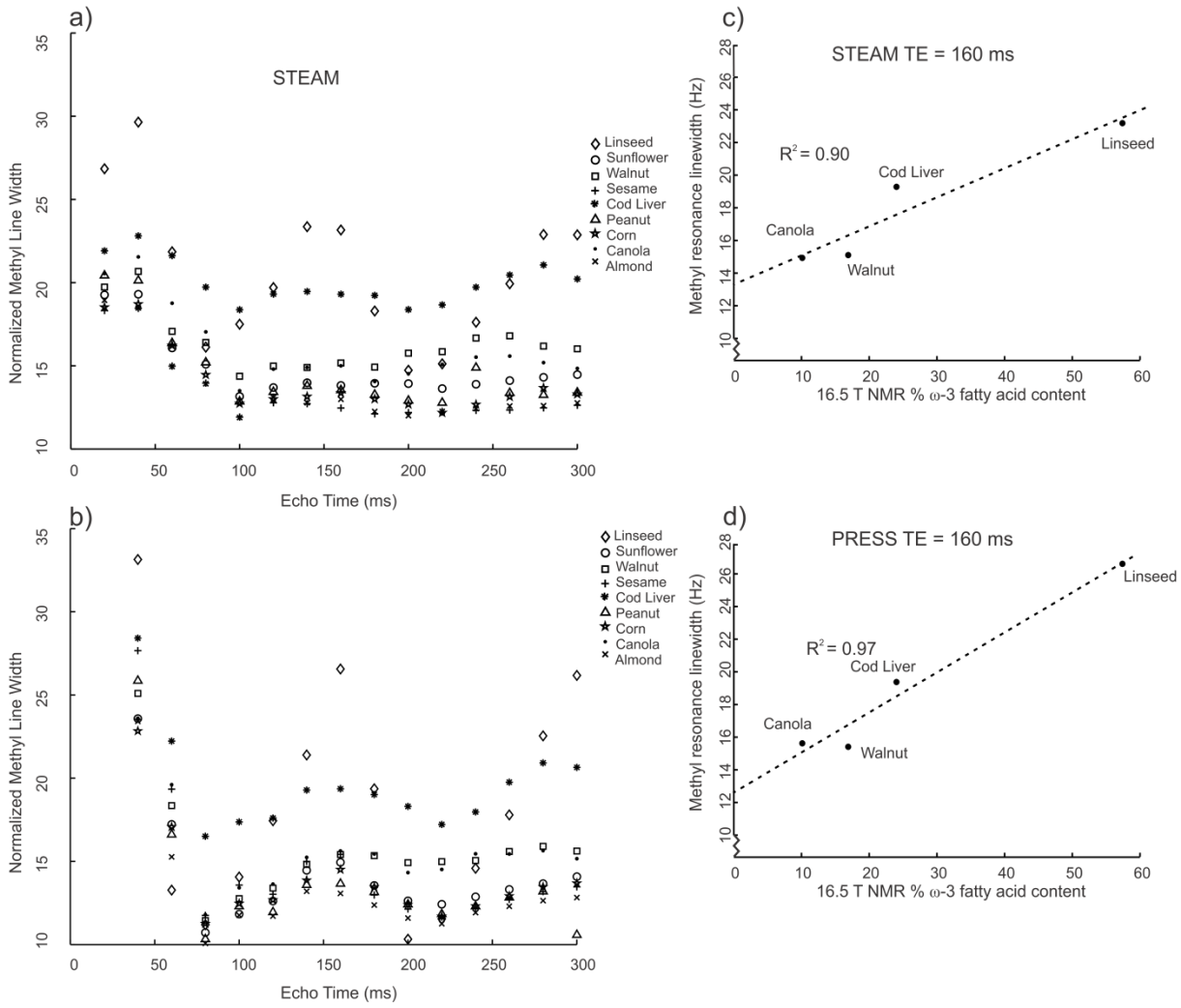

Figure 4.3: Methyl linewidths of nine oils as a function of echo time for STEAM (a) and PRESS (c). STEAM with TE = 160 ms and PRESS with TE = 160 ms were determined to be optimal echo times for characterizing the oils based on relative ω-3 fatty acid content. The figure also displays the linear regression of the methyl linewidth versus ω-3 fatty acid content (obtained from 16.5 T NMR) for STEAM TE = 160 ms (b) and PRESS TE = 160 ms (d). For STEAM, TM = 20 ms.

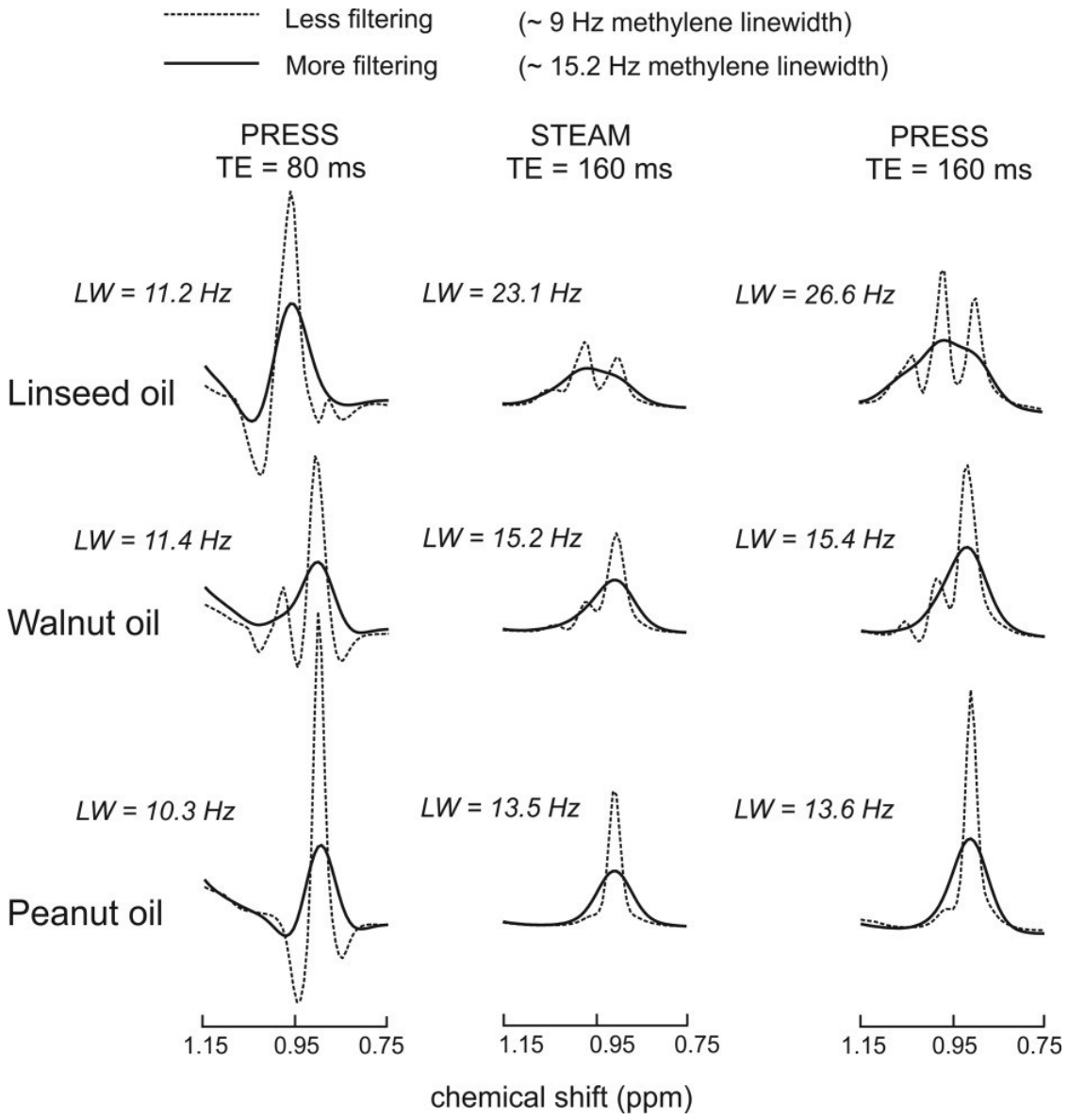

Figure 4.4: Methyl line shapes for linseed oil, walnut oil, and peanut oil obtained with a non-optimal timing (PRESS TE = 80 ms) and with the optimal timings (STEAM TE = 160 ms and PRESS TE = 160 ms) determined in the presented work. Line shapes are shown with less filtering (≈ 9 Hz methylene linewidth) and more filtering (≈ 15.2 Hz methylene linewidth), the latter more representative of *in-vivo* spectra. For STEAM, TM = 20 ms.

The diallylic to methyl ratios determined from the high resolution NMR spectra were found to be 0.37 and 0.26 for sunflower and canola oil, respectively. Di-unsaturated linoleic acid content was found to be 55 % and 18 % for sunflower and canola oil, respectively.

4.5 Discussion

Long-TE MRS techniques are advantageous for suppressing the water signal to better quantify the olefinic lipid resonance [1,14,15] or for improving the resolution of lipid methyl and methylene peaks [16]. In the presented work, long-TE STEAM and PRESS techniques that yield olefinic/methyl ratios that match most closely to ratios determined from high resolution NMR spectra for the oils and to ratios determined from the literature for tibial bone marrow were investigated at 3 T. In addition, a correlation between methyl linewidths and relative ω-3 fatty acid content was demonstrated for certain STEAM and PRESS TE values.

Timings were optimized to measure olefinic to methyl ratios that matched most closely to ratios obtained with 16.5 T NMR (for the oils) or to literature (for tibial bone marrow). Methyl and olefinic protons in the oils and *in vivo* exhibit similar T_2 relaxation decays leading to the same suitable echo times (STEAM with a TE of 120 ms and PRESS with a TE of 180 ms). PRESS with a TE of 180 ms yields more representative olefinic/methyl ratios compared to those provided from PRESS with a TE of 40 ms, likely because J-coupling effects result in a smaller olefinic resonance area compared to the methyl resonance area at the optimized echo time. In contrast, the olefinic resonance area is larger in comparison to the methyl resonance area at the short echo time, yielding an overestimation of the olefinic to methyl ratio. A limitation of our methodology is that the 3 T olefinic areas included contributions from the ≈ 5.21 ppm glycerol proton, whereas the glycerol contribution was excluded from the high resolution oil and tibial bone marrow literature compositions to have an estimate of the true olefinic to methyl ratio. In addition, the glycerol proton is involved in J-coupling interactions [29] which causes its signal to modulate as a function of TE. Since its modulation is unknown, its actual contribution to the olefinic area at different TE values is uncertain.

Methyl linewidths were investigated as a tool for assessing relative ω-3 fatty acid content. Admittedly, the linewidth increases with larger magnetic field inhomogeneities and susceptibility differences (increase with higher field strength). A consistent voxel size and shimming procedure was employed for all the oil experiments to yield a similar magnetic field environment. The methylene resonance linewidth was used as a reference. Small variations in the linewidth were addressed by adjusting the amount of filtering such that all the oil methylene

linewidths were similar (15.2 Hz ± 0.8 Hz) ensuring that any methyl linewidth differences are primarily due to J-coupling evolution effects. We found that techniques of STEAM with a TE of 160 ms (TM = 20 ms) and PRESS with a TE of 160 ms can be used to determine relative ω-3 fatty acid content of oils from the methyl linewidth. Using a non-optimal echo time yields relatively similar linewidths despite differences in ω-3 fatty acid content (linseed oil ≈ 50 %, walnut oil ≈ 12 %, and peanut oil ≈ 0 %), whereas using the optimal TE values yields linewidths that broaden for oils with higher ω-3 fatty acid content. The methyl groups of saturated fatty acids, oleic acid and linoleic acids resonate at ≈ 0.84 – 0.90 ppm, and are involved in J-coupling interactions with their 1.3 ppm methylene neighbours [19]. The methyl protons of ω-3 fatty acids resonate at ≈ 0.94 – 1.0 ppm and exhibit a more weakly-coupled interaction at 3 T with their neighbouring ≈ 2.0 ppm allylic protons, leading to differences in J-coupling evolution [19] compared to the other methyl protons. Figure 4.4 shows that the outer left peak of the ω-3 multiplet is in-phase at the optimal echo times as a result of J-coupling evolution rewinding, whereas it is out of phase at a non-optimal timing. When the ω-3 resonances are in-phase, their linewidths add to the collective methyl linewidth. Furthermore, the centre of the methyl resonance peak shifts to a slightly higher ppm. The combined effects yield broader linewidths for higher ω-3 fatty acid content. The ω-3 content of cod liver oil is dominated by eicosapentaenoic acid (EPA) and docosahexanoic acid; however, for the other oils, the ω-3 fatty acid content is primarily linolenic acid [15]. Linolenic acid is the most significant ω-3 component of human adipose tissue [10]. A limitation of the study is that the technique was used to assess oils with high linolenic acid content, specifically linseed oil (≈ 50 %), walnut oil (≈ 12 %), and canola oil (≈ 10 %), whereas linolenic acid only makes up about 1 % of fatty acid content in human adipose tissue [10-13]. However, a recent *in vivo* study at 1.5 T reported narrower methyl linewidths in subjects with higher risk of breast cancer and proposed that the observation may be due to different fat composition [30]. In proton MRS, the methyl resonance is the key source for extracting information about ω-3 content. The 2.8 ppm diallylic resonance increases with increased levels of poly-unsaturation; however, there is no indication of whether the signal is originating from di-unsaturated linoleic acid or tri-unsaturated ω-3 linolenic acid. For example, we estimated from the high resolution spectra that the sunflower oil contains ≈ 55 % linoleic acid and negligible linolenic acid, while the canola oil contains ≈ 18 % linoleic acid and ≈ 10 %

linolenic acid. The diallylic to methyl ratio was found to be about 1.4 times larger for sunflower oil (0.37 compared to 0.26 for canola oil), despite the absence of linolenic acid, due to the higher linoleic acid fat content.

Long-TE for both PRESS and STEAM were explored in this work. Overall, both the long-TE PRESS (TE = 180 ms) and STEAM (TE = 120 ms) sequences yield olefinic/methyl measures that agree within 10 % of ratios determined from high resolution NMR and from the literature, for the oils and *in vivo*, respectively. An advantage of the PRESS sequence is that the obtained tibial bone marrow olefinic SNR is ~ 1.6 times larger compared to what was acquired with STEAM. However, it should be cautioned that SNR differences are dependent on tissue specific T_2 relaxation constants; it was previously shown that a higher olefinic SNR was obtained with STEAM with a TE of 100 ms compared to what was measured with PRESS with a TE of 200 ms in spinal bone marrow [14]. Another advantage of the PRESS timing is that the longer TE of 180 ms provides more opportunity for water T_2 relaxation decay should a large water signal be present [14]. However, a disadvantage of the PRESS sequence is that it did not perform as well as STEAM for estimating relative levels of oil unsaturation based on olefinic to methyl ratios (R^2 of 0.79 for PRESS compared to 0.89 for STEAM). For the optimized PRESS and STEAM sequences (both with TE = 160 ms) for methyl linewidth measurements, PRESS has advantages over STEAM, namely, providing a higher SNR and a better measure of relative levels of oil ω-3 content (R^2 of 0.97 compared to R^2 of 0.90 for STEAM).

In addition to the already mentioned study shortcomings (inclusion of glycerol signal in the olefinic peak area at 3 T and using oils high in linolenic acid content for the methyl linewidth assessment), there are a few other limitations of the study. The long TE values yield lower SNR values for both the olefinic and methyl resonances compared to the SNR obtained with short echo times. The largest reduction occurs for the olefinic signal with STEAM with a TE of 120 ms (SNR is ≈ 26 % of that obtained with STEAM TE = 20 ms). However, the SNR is still relatively high (≈ 48) and adequate for obtaining measures of fat unsaturation. Another limitation is that the optimal TE values were determined for tibial bone marrow and may be different for other anatomical tissue depending on the T_2 relaxation constants of both the olefinic and methyl protons. Also, the optimal timings *in vivo* were determined based on literature composition of tibial bone marrow and not on the actual bone marrow composition of the study

volunteers. In addition, a small number of volunteers were scanned and a patient study measuring differences in fat unsaturation with disease was not performed.

In addition to bone marrow, the work of the presented study can find application in the study of fat unsaturation in other anatomical tissue. For example, hepatic fat unsaturation has been shown to negatively correlate with obesity and hepatic steatosis [7]; studies have also shown that patients with non-alcoholic fatty liver disease (NAFLD) have lower levels of hepatic ω-3 fatty acids compared to healthy subjects [31,32]. Lower levels of unsaturated fat were found in visceral adipose tissue of obese males that had higher visceral adipose tissue volume [4], while elevated levels of saturated fats in visceral adipose tissue of obese women have been correlated with gene and protein expressions that regulate visceral fat volume, which is associated with metabolic disease [33]. The amount of fat unsaturation in skeletal muscle has been shown to be negatively correlated with lipid metabolic defects associated with obesity [34]. It has also been demonstrated that the fatty acid content of skeletal muscle correlated with dietary fat composition [35] and that increasing the ω-3 fatty acid content in skeletal muscle improves muscle function and metabolism [36,37].

In conclusion, STEAM with a TE of 120 ms (TM = 20 ms) and PRESS with a TE of 180 ms yield representative olefinic to methyl ratios in tibial bone marrow *in vivo*. In addition, STEAM and PRESS sequences with a TE of 160 ms (TM = 20 ms for STEAM) can assess relative levels of ω-3 fatty acid content based on relative methyl peak linewidths.

4.6 Citations

1. Lundbom J, Hakkarainen A, Söderlund S, Westerbacka J, Lundbom N, Taskinen M-R. Long-TE ^{1}H MRS suggests that liver fat is more saturated than subcutaneous and visceral fat. NMR Biomed 2011;24:238-245.
2. Mosconi E, Fontanella M, Sima DM, et al. Investigation of adipose tissues in Zucker rats using *in vivo* and *ex vivo* magnetic resonance spectroscopy. J Lipid Res 2011;52:330-336.
3. Yeung DKW, Griffith JF, Antonio GE, Lee FKH, Woo J, Leung PC. Osteoporosis is associated with increased marrow fat content and decreased marrow fat unsaturation: A proton MR spectroscopy study. J Magn Reson Imaging 2005;22:279-285.
4. Machann J, Stefan N, Schabel C, et al. Fraction of unsaturated fatty acids in visceral adipose tissue (VAT) is lower in subjects with high total VAT volume - a combined ^{1}H MRS and volumetric MRI study in male subjects. NMR Biomed 2013;26:232-236.
5. Pollesello P, Eriksson O, Höckerstedt K. Analysis of total lipid extracts from human liver by ^{13}C and ^{1}H Nuclear Magnetic Resonance Spectroscopy. Anal Biochem 1996;236:41-48.
6. He Q, Shkarin P, Hooley RJ, Lannin DR, Weinreb JC, Bossuyt VIJ. *In vivo* MR spectroscopic imaging of polyunsaturated fatty acids (PUFA) in healthy and cancerous breast tissues by selective multiple-quantum coherence transfer (Sel-MQC): A preliminary study. Magn Reson Med 2007;58:1079-1085.
7. Johnson NA, Walton DW, Sachinwalla T, et al. Noninvasive assessment of hepatic lipid composition: Advancing understanding and management of fatty liver disorders. Hepatology 2008;47:1513-1523.
8. Patsch JM, Li X, Baum T, et al. Bone marrow fat composition as a novel imaging biomarker in postmenopausal women with prevalent fragility fractures. J Bone Miner Res 2013;28:1721-1728.
9. Korteweg MA, Veldhuis WB, Mali WPTM, et al. Investigation of lipid composition of dissected sentinel lymph nodes of breast cancer patients by 7T proton MR spectroscopy. J Magn Reson Imaging 2012;35:387-392.
10. Hodson L, Skeaff CM, Fielding BA. Fatty acid composition of adipose tissue and blood in humans and its use as a biomarker of dietary intake. Prog Lipid Res 2008;47:348-380.
11. Yeung DKW, Lam SL, Griffith JF, et al. Analysis of bone marrow fatty acid composition using high-resolution proton NMR spectroscopy. Chem Phys Lipids 2008;151:103-109.
12. Griffith JF, Yeung DKW, Ahuja AT, et al. A study of bone marrow and subcutaneous fatty acid composition in subjects of varying bone mineral density. Bone 2009;44:1092-1096.
13. Ren J, Dimitrov I, Sherry AD, Malloy CR. Composition of adipose tissue and marrow fat in humans by ^{1}H NMR at 7 Tesla. J Lipid Res 2008;49:2055-2062.
14. Bingölbali A, Fallone BG, Yahya A. Comparison of optimized long echo time STEAM and PRESS proton MR spectroscopy of lipid olefinic protons at 3 Tesla. J Magn Reson Imaging 2015;41:481-486.
15. Troitskaia A, Fallone BG, Yahya A. Long echo time proton magnetic resonance spectroscopy for estimating relative measures of lipid unsaturation at 3 T. J Magn Reson Imaging 2013;37:944-949.

16. Škoch A, Jírů F, Dezortová M, et al. Intramyocellular lipid quantification from ^{1}H long echo time spectra at 1.5 and 3 T by means of the LCModel technique. J Magn Reson Imaging 2006;23:728-735.
17. Bougnoux P, Koscielny S, Chajès V, Descamps P, Couet C, Calais G. α- Linolenic acid content of adipose breast tissue: a host determinant of the risk of early metastasis in breast cancer. Br J Cancer 1994;70:330-334.
18. Guillén MD, Ruiz A. High resolution ^{1}H nuclear magnetic resonance in the study of edible oils and fats. Trends Food Sci Technol 2001;12:328-338.
19. Lundbom J, Heikkinen S, Fielding B, Hakkarainen A, Taskinen M-R, Lundbom N. PRESS echo time behavior of triglyceride resonances at 1.5 T: Detecting ω-3 fatty acids in adipose tissue *in vivo*. J Magn Reson 2009;201:39-47.
20. Machann J, Stefan N, Wagner R, et al. Intra- and interindividual variability of fatty acid unsaturation in six different human adipose tissue compartments assessed by ^{1}H-MRS *in vivo* at 3 T. NMR Biomed 2017;30:e3744 (10 pages).
21. Huovinen V, Viljakainen H, Hakkarainen A, et al. Bone marrow fat unsaturation in young adults is not affected by present or childhood obesity, but increases with age: A pilot study. Metabolism 2015;64:1574-1581.
22. Al-Nouri DM, Al-Khalifa AS, Shahidi F. Long-term supplementation of dietary omega-6/omega-3 ratios alters bone marrow fatty acid and biomarkers of bone metabolism in growing rabbits. J Funct Foods 2012;4:584-593.
23. Lau BYY, Cohen DJA, Ward WE, Ma DWL. Investigating the role of polyunsaturated fatty acids in bone development using animal models. Molecules 2013;18:14203-14227.
24. Li Y, Seifert MF, Lim SY, Salem NJ, Watkins BA. Bone mineral content is positively correlated to *n-3* fatty acids in the femur of growing rats. Br J Nutr 2010;104:674-685.
25. Liu D, Veit HP, Wilson JH, Denbow DM. Long-term supplementation of various dietary lipids alters bone mineral content, mechanical properties, and histological characteristics of Japanese quail. Poult Sci 2003;82:831-839.
26. Li Y, Seifert MF, Ney DM, et al. Dietary conjugated linoleic acids alter serum IGF-I and IGF binding protein concentrations and reduce bone formation in rats fed (n-6) or (n-3) fatty acids. J Bone Miner Res 1999;14:1153-1162.
27. Shen J, Rycyna RE, Rothman DL. Improvements on an in vivo automatic shimming method (FASTERMAP). Magn Reson Med 1997;38:834-839.
28. Guillén MD, Ruiz A. Rapid simultaneous determination by proton NMR of unsaturation and composition of acyl groups in vegetable oils. Eur J Lipid Sci Technol 2003;105:688-696.
29. Ramadan S, Ratai E-M, Wald LL, Mountford CE. *In vivo* 1D and 2D correlation MR spectroscopy of the soleus muscle at 7 T. J Magn Reson 2010;204:91-98.
30. Wang J, Wang M-Y, Kuo W-H, Chen K-L, Shih TT-F. Proton MR spectroscopy of normal breasts: Association of risk factors for breast cancer with water and lipid composition of the breast. Magn Reson Imaging 2016;34:524-528.
31. Elizondo A, Araya J, Rodrigo R, et al. Polyunsaturated fatty acid pattern in liver and erythrocyte phospholipids from obese patients. Obesity 2007;15:24-31.
32. Parker HM, Johnson NA, Burdon CA, Cohn JS, O'Connor HT, George J. Omega-3 supplementation and non-alcoholic fatty liver disease: A systematic review and meta-analysis. J Hepatol 2012;56:944-951.

33. Petrus P, Rosqvist F, Edholm D, et al. Saturated fatty acids in human visceral adipose tissue are associated with increased 11-β-hydroxysteroid-dehydrogenase type 1 expression. Lipids Health Dis 2015;14:42-46.
34. Velan SS, Said N, Durst C, et al. Distinct patterns of fat metabolism in skeletal muscle of normal-weight, overweight, and obese humans. Am J Physiol Regul Integr Comp Physiol 2008;295:R1060-R1065.
35. Andersson A, Nälsén C, Tengblad S, Vessby B. Fatty acid composition of skeletal muscle reflects dietary fat composition in humans. Am J Clin Nutr 2002;76:1222-1229.
36. Rodacki CLN, Rodacki ALF, Pereira G, et al. Fish-oil supplementation enhances the effects of strength training in elderly women. Am J Clin Nutr 2012;95:428-436.
37. Smith GI, Julliand S, Reeds DN, Sinacore DR, Klein S, Mittendorfer B. Fish oil-derived *n-3* PUFA therapy increases muscle mass and function in healthy older adults. Am J Clin Nutr 2015;102:115-122.

Chapter 5

Apparent T_2 Relaxation Times and Fat Unsaturation Measurements in Breast, Tibial, and Subcutaneous Adipose Tissue at 3 T

A version of this chapter has been submitted for publication.

Authors: **Fallone, C.J**., Tessier, A.G., and Yahya, A.

Title: Apparent T_2 relaxation times and fat unsaturation measurements in breast, tibial, and subcutaneous adipose tissue at 3 T

5.1 Abstract

Measures of fat unsaturation, relevant to disease, can be obtained *in vivo* with magnetic resonance spectroscopy (MRS) by measuring the olefinic resonance (≈ 5.4 ppm), which provides an indication of the total number of double bonds. Long echo time (TE) Point RESolved Spectroscopy (PRESS) has been previously optimized for obtaining olefinic to methylene (1.3 ppm) or methyl (≈ 0.9 ppm) ratios at 3 T in tibial bone marrow. This work measures apparent (includes J-coupling evolution) T_2 relaxation times for the olefinic, methylene, and methyl protons in tibial bone marrow, subcutaneous and breast adipose tissue in healthy volunteers (11 males and 7 females) to investigate if intra-individual fat unsaturation comparisons can be made without T_2 corrections. PRESS with varying TE was employed. Statistical significance was found between breast and tibial bone marrow olefinic apparent T_2 values ($p = 0.005$ from two-tailed paired t-test). Olefinic/methylene measures using PRESS with a TE of 40 ms and the previously optimized long TE of 200 ms were obtained for the three regions (not measured previously in breast) to investigate intra-individual differences. No significant differences were found. Diallylic (≈ 2.8 ppm) to methylene ratios for poly-unsaturation assessment were calculated from the TE = 40 ms PRESS spectra. Poly-unsaturation measures were significantly different for tibial bone marrow compared to subcutaneous ($p = 0.001$) and breast ($p = 0.05$) adipose tissues, with average values of 1.7 ± 0.4, 2.2 ± 0.4, and 2.3 ± 0.8%, respectively.

Inversion recovery was investigated for minimizing water signal in breast using an inversion delay time of 613 ms preceding PRESS (TE = 40 ms). The olefinic signal to noise ratio was about six times greater than that obtained using PRESS with a TE of 200 ms, providing an alternative to long-TE for fat unsaturation measurements in breast.

5.2 Introduction

Levels of fat unsaturation have been demonstrated to correlate inversely with disease [1-14]. For example, unsaturated fat content in humans has been found to be lower in visceral adipose tissue [1], liver [2], breast tissue [5,6], and bone marrow [7-13] in diseases such as obesity [1,2], breast cancer [5,6], osteoporosis [7,9-11,13], bone lesions [12], and diabetes [9,11]. Magnetic Resonance Spectroscopy (MRS) has been utilized to quantify the olefinic resonance (≈ 5.4 ppm) to assess total fat unsaturation *in vivo* [2,3,12,15-17]. The water resonance (≈ 4.8 ppm) overlaps the olefinic resonance in short echo time (TE) spectra in tissues such as breast, red bone marrow, and liver, making its quantification challenging [15-19]. Long-TE STimulated Echo Acquisition Mode (STEAM) and Point RESolved Spectroscopy (PRESS) sequences have been shown to better resolve the olefinic peak from that of water by exploiting the relatively shorter transverse (T_2) relaxation time of water [15-20]. In addition, it takes advantage of improved spectral resolution of the 1.3 ppm methylene resonance from that of the 0.9 ppm methyl at longer TE values [20,21], enabling normalization to either resonance. A longer TE sequence may also yield more consistent results; in bone marrow studies of disease and age, using a short TE has been implicated as potentially causing contradicting results from different MRS studies [19]. Long-TE STEAM with a TE of 100 ms [16] and PRESS with a TE of 200 ms [17] were optimized for measuring olefinic to methylene ratios in tibial [17] and spinal bone marrow [16,17] at 3 T. In addition, since the methyl resonance arises from the same number of protons per triglyceride, it is a useful normalization factor [1]. Long-TE STEAM (TE =120 ms) and PRESS (TE = 180 ms) timings were optimized for olefinic to methyl measures in tibial bone marrow [22]. The techniques examined the J-coupling evolution of the different lipid proton groups, which are expected to be similar in bone marrow and other adipose tissue. Water is prevalent in breast tissue, and although less so in subcutaneous adipose tissue, it has been shown to increase with weight loss in studies of obesity [23], rendering a long-TE sequence advantageous. Moreover, measures of fat unsaturation acquired with long TE spectra in subcutaneous abdominal adipose tissue were in better agreement with results from gas chromatography than those acquired from short TE, likely due to decay of the water resonance signal and intense methylene peaks [20]. Quantification based on long-TE spectra benefit from corrections for T_2 losses. The T_2 times of the protons groups, which differ from each other [24-26], may vary in different adipose tissues [27]. T_2 times are longer for more unsaturated

fats due to increased fluidity from double bonds [28]. Furthermore, within a fat molecule, protons closer to the methyl end of the fatty acid tend to have longer T_2 due to greater fluidity in the methyl end of the molecule compared to the carboxylic acid end [28]. The presented work compares apparent (to indicate inclusion of J-coupling effects) T_2 relaxation times of olefinic, methyl, and methylene resonances in breast, subcutaneous, and tibial bone marrow adipose tissue at 3 T to determine if olefinic/methylene or olefinic/methyl ratios obtained in those regions with the optimized long-TE values for tibial bone marrow [16,17,22] can be directly compared to each other without correcting for differences in T_2. The olefinic apparent T_2 relaxation time in thigh adipose tissue [29] and subcutaneous adipose tissue in the abdominal region [30] have been estimated at 3 T; however, to our knowledge, estimates have not been determined for tibial bone marrow and breast adipose tissue. We also employ our measures from long-TE spectra to estimate olefinic/methylene ratios in the different adipose tissues. This metric has been previously employed using PRESS with a TE of 200 ms in tibial bone marrow [17] and subcutaneous adipose tissue in the abdominal region [15,20,31], but not in breast tissue. A more complex multiple quantum coherence sequence has been used to map poly-unsaturation content in breast tissue at 2.1 T [32]. A 7 T study determined breast poly- and mono-unsaturation composition using resonances (not easily resolvable at 3 T) other than the olefinic resonance with a TE-averaged STEAM sequence [33]. Another study at 3 T acquired short TE STEAM spectra and used spectral fitting to quantify the same resonances used in the 7 T study and obtained similar results for composition [34]. It is difficult to compare the measures in the latter two references to those obtained from previous studies in other adipose tissue. Intra-individual differences in total fat unsaturation [15,31,35,36] have been investigated in different adipose sites, including abdominal adipose tissue and tibial bone marrow [36], to gain insights about fat storage in different depots and their potential role in pathology [19,36]. The presented work explores intra-individual variability in fat unsaturation measures determined between previously examined adipose tissue, namely subcutaneous and tibial bone marrow, in addition to that of breast in a group of healthy volunteers. We also demonstrate the efficacy of using an inversion recovery (IR) sequence to resolve the olefinic signal from that of water in breast tissue with a short-TE sequence, providing an alternative to long-TE in situations where signal loss due to T_2 relaxation would be of concern.

5.3 Methods

All experimental data were acquired using a 3 T Philips whole body Magnetic Resonance Imaging (MRI) scanner (Intera, Philips Healthcare, Best, Netherlands) in accordance with our local ethics review board. Seven women (ages 22 to 41) and 11 men (ages 20 to 57) participated in the study. Two women elected not to participate in the abdominal scans. For all three anatomic regions, spectra were acquired using a PRESS sequence with TR of 3 s and TE values of 40, 60, 80, 140, 200 and 240 ms. The first TE of PRESS was set to 17 ms and the second TE was altered accordingly. The following parameters were applied: 32 signal averages, 2048 samples, and a 2000 Hz spectral bandwidth. Shimming was performed using the scanner's automatic 2nd order pencil beam shimming module. For tibial bone marrow and breast, shimming was performed over the voxel of interest, but for the abdominal region shimming was performed over a larger volume centered on the voxel of interest to mitigate effects of respiratory motion. The RF pulse frequency was set to 3 ppm, the center of the fat spectrum. The built in Philips body coil was used for signal transmission in all cases.

For the tibial bone marrow scans, volunteers lay supine and one element of the Flex-L Philips surface coil (Philips Healthcare) secured with VELCRO straps was used for signal reception. A 7 x 7 x 7 mm^3 to 8 x 8 x 8 mm^3 voxel was positioned in the right tibial bone marrow (a few cm below the knee as shown in Figure 5.1 a). Images were acquired as 3 mm slices using a multishot turbo spin echo (TSE) sequence with TSE factor of 3, a TE of 8 ms, and a TR of 800 ms.

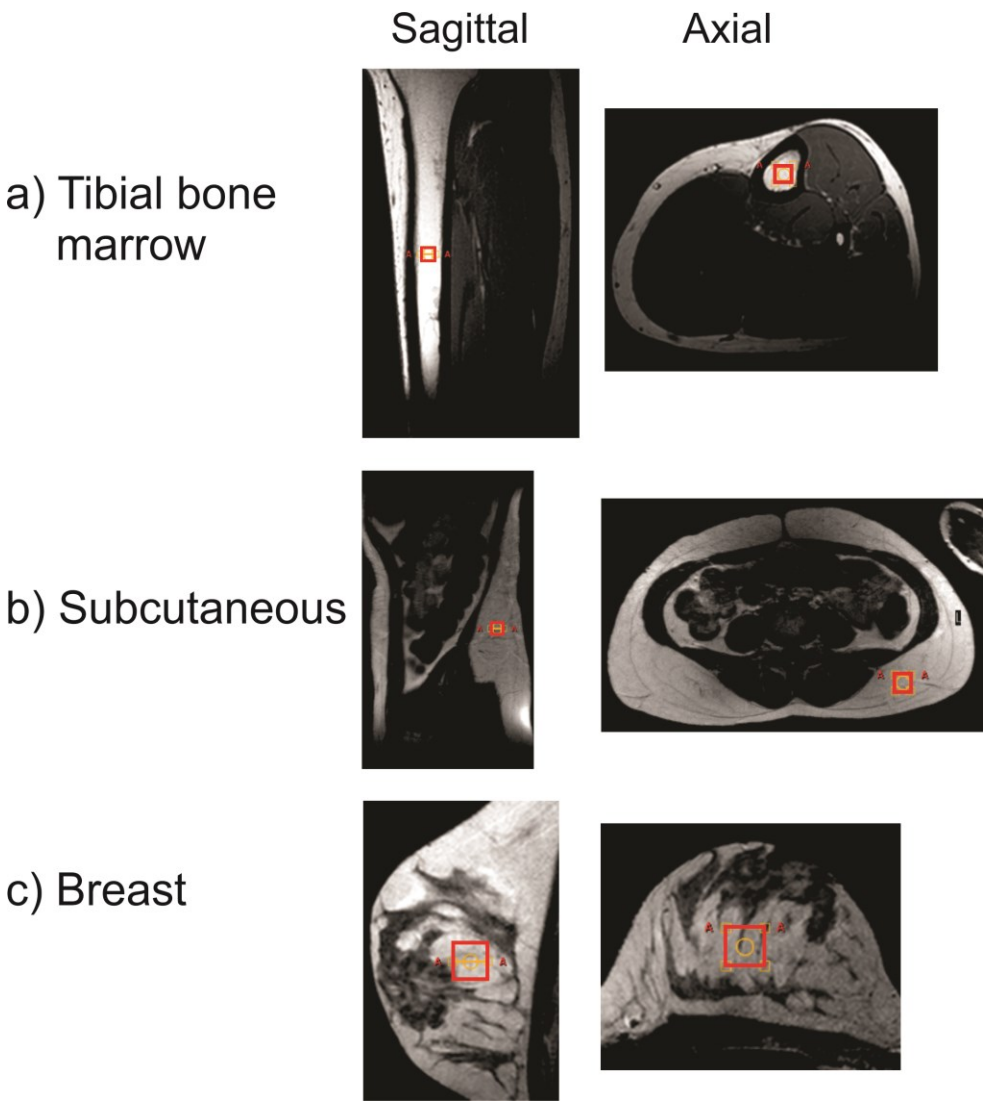

Figure 5.1: Voxel (8 x 8 x 8 mm^3) location in tibial bone marrow (a), in subcutaneous adipose tissue in the abdominal region (15 x 15 x 15 mm^3, b), and in breast adipose tissue (15 x 15 x 15 mm^3, c) for apparent T_2 measurements in one of the female volunteers.

For the abdominal subcutaneous adipose tissue scans, volunteers lay supine with a gating sensor placed above the abdominal region using a VELCRO wrap. The body coil was used for signal reception. A 10 x 10 x 30 mm^3 to 20 x 20 x 20 mm^3 voxel was situated in the deep subcutaneous adipose tissue located near the L3-L5 spinal region (Figure 5.1 b). Images were acquired in 3 mm slices using a multishot TSE sequence, with a TSE factor of 20, a TE of 40 ms and a TR of 1924 ms. Spectra were acquired using respiratory gating.

For the breast scans, females lay prone on an in-house built breast board. The body coil was used for signal transmission and both elements of the Flex-L surface coil were employed for signal reception from the volunteer's right breast. A 10 x 10 x 10 mm^3 to 15 x 15 x 15 mm^3 voxel was placed in an adipose region of the breast (Figure 5.1 c). Images were acquired in 5 mm slices using a multishot turbo spin echo (TSE) with TSE factor of 15, echo time (TE) of 60 ms and repetition time (TR) of 4 s. To investigate the use of inversion recovery to resolve the olefinic resonance from that of water, one of the volunteers was scanned in a separate session and water spectra from a 10 x 10 x 10 mm^3 voxel located in a non-adipose region were obtained to estimate a water longitudinal (T_1) relaxation time. A PRESS sequence preceded by an inversion recovery pulse of 100 Hz bandwidth were acquired with inversion times (TI) of 250, 450, 550, 650, 750, 850, and 1000 ms, with a TR of 3 s and a TE of 40 ms. Water resonance areas (determined by integrating the peak using Philips spectroscopy analysis software) for each TI were plotted as a function of TI and the curve was fit using a non-least squares fit in MATLAB to a function of the form $M = M_o(1 - 2\exp\left(-\frac{TI}{T_1}\right))$. The null time was deduced by solving the expression above for zero signal ($null\ time = \ln(2)\, T_1$). The same volunteer was then scanned in a separate session and PRESS spectra were acquired from a 20 x 20 x 20 mm^3 voxel containing both fat and water. Three spectra were acquired, namely, one with a TE of 40 ms and no inversion pulse, one with a TE of 40 ms and a preceding inversion pulse with the calculated inversion delay (null time), and one with TE of 200 ms with no inversion pulse. Olefinic peak areas and heights for the latter two spectra were determined by analyzing the spectral region of 5.1 – 5.5 ppm using the Philips spectroscopy analysis software. The signal to noise ratio (SNR) of the olefinic resonance was determined by the peak height divided by the standard deviation of the noise between 7-8 ppm.

Aside from the breast IR spectra, all spectra from the three anatomic regions were analyzed using Linear Combination Model (LCModel, Version 6.31 – 1P) [37]. The basis set used was 'breast-8' and individual parameters were manually optimized for each spectrum. Olefinic (5.1 – 5.5 ppm), methyl (0.8 – 1.1 ppm), and methylene (1.2-1.7 ppm) peak areas were provided by LCModel. Olefinic, methyl, and methylene areas were plotted as a function of TE and fit to the function $M = M_o \exp\left(-\frac{\mathrm{TE}}{\mathrm{T_2}}\right)$, using a least-squares analysis in MATLAB. Apparent methylene, methyl, and olefinic proton T_2 relaxation times were computed. For the methylene

protons, the relaxation times were calculated using all TE data points. However, only the peak areas obtained with TE values of 40, 60 and 80 ms were utilized for the olefinic and methyl resonances, because the J-coupling modulation at longer TE values does not result in a continuously decaying function. The average apparent T_2 relaxation times and corresponding standard deviations were calculated for the three proton groups in the different tissues, for all the volunteers. Statistical differences between T_2 times of the different proton groups in subcutaneous tissue and tibial bone marrow were evaluated using a two-tailed paired t-test (a p value <= 0.05 was considered significant) for all volunteers (16 volunteers) performed in Excel. The same was carried out to evaluate differences between values obtained in breast adipose tissue and tibial bone marrow (7 female volunteers), and breast and abdominal subcutaneous adipose tissue (5 female volunteers).

Olefinic to methylene ratios were calculated from the PRESS spectra with TE = 40 ms and TE = 200 ms. Diallylic (2.7 – 2.9 ppm) areas obtained from LCModel from TE = 40 ms PRESS spectra enables a relative measure of poly-unsaturation to be estimated by calculating diallylic to methylene area ratios. The same statistical analysis was performed for the olefinic/methylene and diallylic/methylene ratios as described above for the apparent T_2 values.

5.4 Results

Figure 5.2 displays spectra acquired from tibial bone marrow, subcutaneous adipose tissue and breast tissue of a female volunteer. Over all the volunteers, full-width-at-half-maxima (FWHM) of methylene peaks ranged from 8 Hz to 16 Hz in tibial bone marrow, 11 Hz to 32 Hz in the subcutaneous adipose tissue, and 21 Hz to 32 Hz in breast adipose tissue. Figure 5.3 shows LCModel fits overlaid on spectra acquired from a female volunteer using PRESS with a TE of 40 ms. Figure 5.4 displays the normalized olefinic, methyl, and methylene resonance areas from the subcutaneous adipose tissue of a volunteer with the corresponding apparent T_2 exponential fits overlaid. Average apparent T_2 relaxation times and their standard deviations are indicated in Table 5.1 for the olefinic, methyl, and methylene protons measured in each anatomical site. Table 5.2 displays the p-values obtained from the t-tests performed to assess differences between apparent T_2 relaxation times of the proton groups in subcutaneous and tibial bone marrow

adipose tissue and between breast and tibial bone marrow adipose tissue. P-values obtained for comparisons between breast and subcutaneous adipose tissue T_2 relaxation times in the female volunteers are also included. Table 5.3 presents the averages and standard deviations of olefinic/methylene ratios obtained using PRESS with a TE of 40 ms and 200 ms in the different tissues. Diallylic/methylene ratios obtained from the TE = 40 ms spectra are also listed. Table 5.4 displays p-values obtained from t-tests performed to assess differences between the ratios obtained from subcutaneous adipose tissue and tibial bone marrow and between those from breast adipose tissue and tibial bone marrow. P-values obtained for comparisons of the ratios between breast and subcutaneous adipose in the female volunteers are also included.

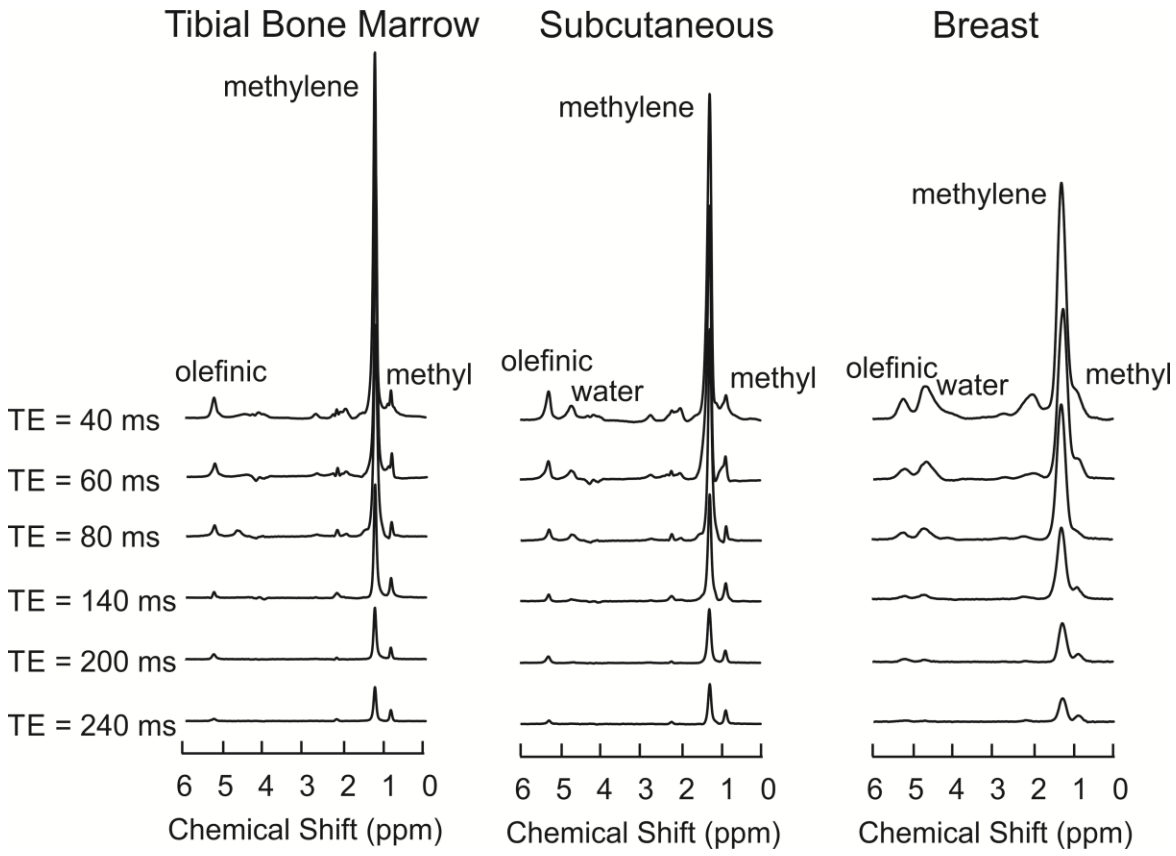

Figure 5.2: Spectra acquired from the tibial bone marrow, subcutaneous adipose tissue, and breast from a female volunteer for apparent T_2 calculations.

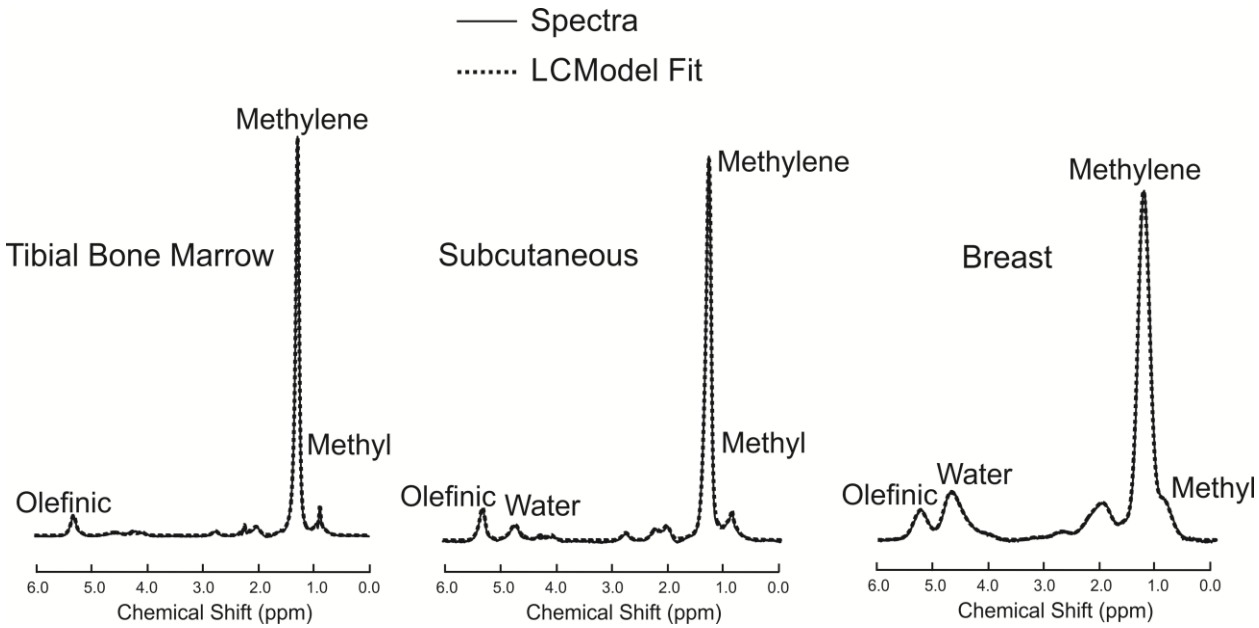

Figure 5.3: Spectra acquired with PRESS with a TE of 40 ms with their corresponding LCModel fits overlaid.

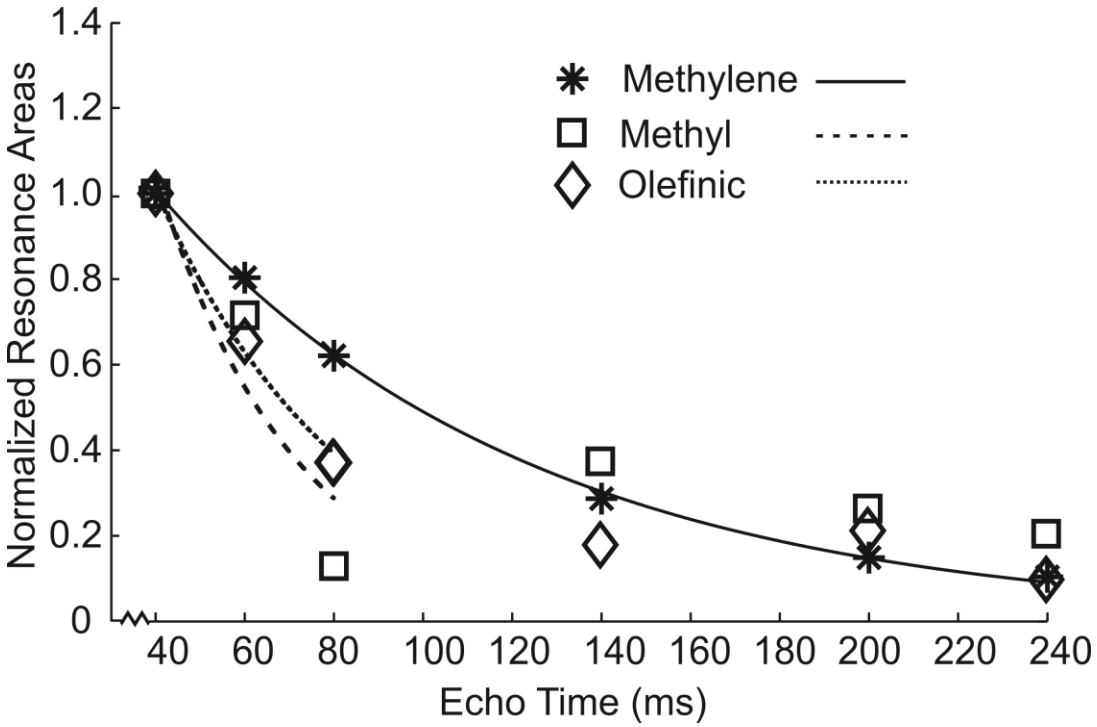

Figure 5.4: Normalized olefinic, methyl, and methylene resonance areas from subcutaneous tissue of one of the volunteers plotted as a function of TE with corresponding exponential fits overlaid.

Table 5.1: Average apparent T_2 relaxation times (ms) over all volunteers (female only for breast) and their standard deviations for olefinic, methyl, and methylene protons in the three anatomic regions.

Tibial bone marrow			**Subcutaneous tissue**			**Breast adipose tissue**		
olefinic	methyl	methylene	olefinic	methyl	methylene	olefinic	methyl	methylene
47.8 ± 3.0 ms	41.0 ± 6.5 ms	83.3± 2.1 ms	44.8 ± 6.0 ms	39.2 ± 9.1 ms	84.2 ± 4.1 ms	36.1 ± 7.1 ms	37.4 ± 8.9 ms	71.8 ± 16.5 ms *77.7 ± 6.3 ms

*Excluding one outlier value

Table 5.2: P-values obtained from two-tailed paired t-tests to determine statistical significance of differences in apparent T_2 values of olefinic, methyl and methylene protons between the tissues.

	p-values (subcutaneous and tibial bone marrow)	**p-values (breast and tibial bone marrow)**	**p-values (breast and subcutaneous)**
Olefinic	0.11	0.005	0.26
Methyl	0.27	0.25	0.48
Methylene	0.42	0.13	0.21

Table 5.3: Olefinic/methylene ratios averaged over all volunteers (females only for breast) are calculated from PRESS TE = 40 ms spectra and PRESS TE = 200 ms spectra from tibial bone marrow, subcutaneous, and breast adipose tissue. Diallylic/methylene ratios calculated from PRESS TE = 40 ms spectra are also shown. Standard deviations are included.

Olefinic/methylene (PRESS TE = 40 ms)			Olefinic/methylene (PRESS TE = 200 ms)			Diallylic/methylene (PRESS TE = 40 ms)		
tibia	subcutaneous	breast	tibia	subcutaneous	breast	tibia	subcutaneous	breast
9.2 ± 0.9%	9.9 ± 1.1%	9.8 ± 2.2%	13.5 ± 1.8%	13.3 ± 2.2%	11.5 ± 2.7%	1.7 ± 0.4%	2.2 ± 0.4%	2.3 ± 0.8%

Table 5.4: P-values obtained from two-tailed paired t-tests to determine statistical significance of differences in olefinic/methylene and diallylic/methylene ratios between the tissues.

	p-values (subcutaneous and tibial bone marrow)	**p-values (breast and tibial bone marrow)**	**p-values (breast and subcutaneous)**
Olefinic/methylene (PRESS TE = 40 ms)	0.06	0.34	0.66
Olefinic/methylene (PRESS TE = 200 ms)	0.71	0.22	0.16
Diallylic/methylene (PRESS TE = 40 ms)	0.001	0.05	0.67

Figure 5.5(b) illustrates the T_1 relaxation curve for water protons obtained from a non-adipose region of the breast (Figure 5.5(a)). A T_1 relaxation time of 883 ms was estimated with a resulting null time of about 613 ms. Figure 5.6(a) displays the voxel localization in a region containing some adipose and non-adipose tissue. Spectra acquired with PRESS with a TE of 40 ms and no IR delay, PRESS with a TE of 40 ms and an IR delay of 613 ms, and PRESS with a TE of 200 ms and no IR delay, are also displayed in Figure 5.6(b). The SNR values of the olefinic resonance using PRESS with a TE of 40 ms and IR was 329 compared to 56, which was obtained with PRESS with a TE of 200 ms. The olefinic area is about 7.5 times higher using PRESS with a TE of 40 ms and IR. The FWHM of the methylene peak in the voxel containing a mixture of tissues was 27 Hz (TE = 40 ms, no IR).

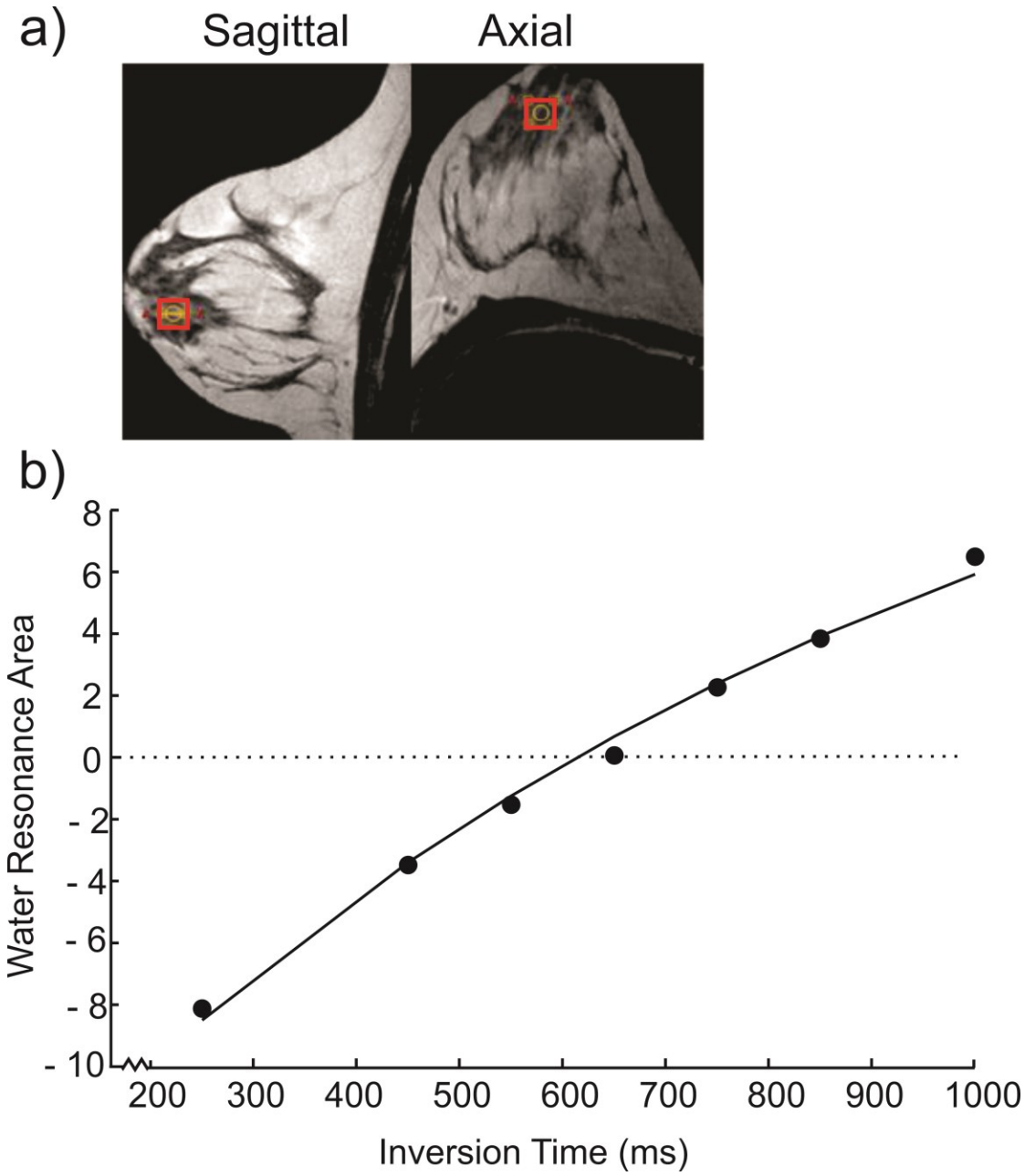

Figure 5.5: Voxel positioning of a 10 x 10 x 10 mm^3 voxel in a non-adipose breast region (a). T_1 curve of water signal area plotted as a function of inversion time delay (b).

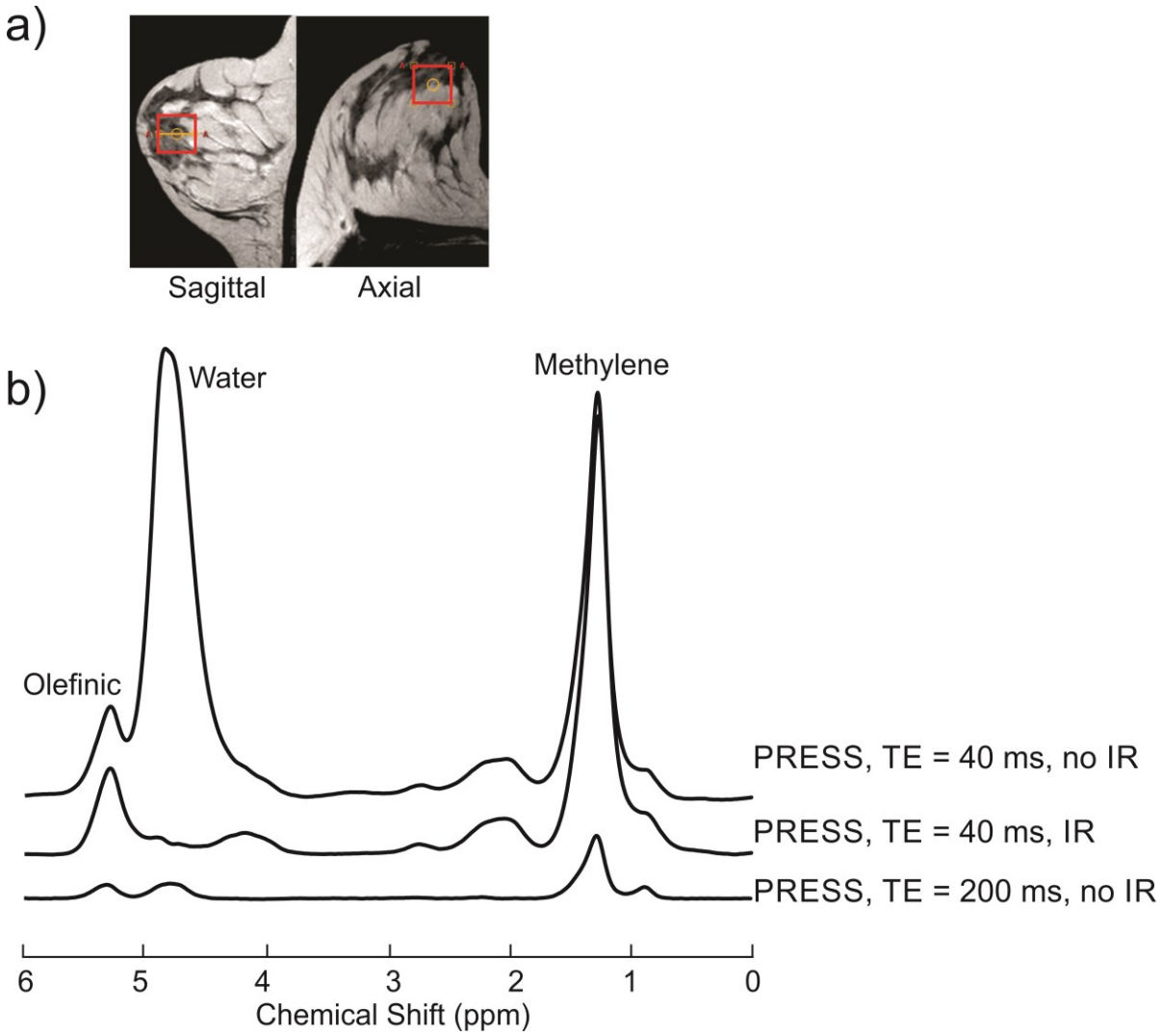

Figure 5.6: Spectra acquired from a 20 x 20 x 20 mm^3 voxel containing a mixture of adipose and non-adipose tissue (a) are shown in (b) using PRESS with a TE of 40 ms and no IR, PRESS with a TE of 40 ms and a 613 ms IR delay, and PRESS with a TE of 200 ms and no IR.

5.5 Discussion

Fat unsaturation measures *in vivo* are important to pathology [1-14]. Magnetic Resonance Spectroscopy (MRS) enables non-invasive measurements of total fat unsaturation *in vivo* by quantifying the olefinic resonance (≈ 5.4 ppm) [2,3,12,15-17]. In tissues where water signal (≈ 4.8 ppm) overlaps that of the olefinic, long TE sequences have been optimized and applied to resolve

the olefinic peak from the water peak, exploiting the shorter T_2 relaxation time of water compared to the olefinic [15-20]. Other anatomical regions could also benefit from the decay of water signal; breast tissue contains high water content that can obscure the olefinic resonance peak [32] and water content in abdominal adipose tissue can increase in some situations [23]. Employing a long TE also enables better resolution of the methyl (≈ 0.9 ppm) and methylene (1.3 ppm) resonances [20,21] and has been reported to offer more representative results in bone marrow [19] and abdominal adipose tissue [20]. In this work, apparent T_2 times of olefinic, methyl and methylene resonance in tibial bone marrow, subcutaneous and breast adipose tissue are compared at 3 T to determine if measures obtained from long TE spectra in the different anatomic regions can be compared to each other without corrections for differences in T_2. Average apparent T_2 values (±standard deviations) of 47.8 (±3.0) ms, 44.8 (± 6.0) ms, and 36.1 (± 7.1) ms were obtained for the olefinic protons in tibial bone marrow, subcutaneous and breast adipose tissues, respectively. For the methyl protons, average apparent T_2 values (±standard deviations) of 41.0 (± 6.5) ms, 39.2 (± 9.1) ms, and 37.4 (± 8.9) ms were obtained in tibial bone marrow, subcutaneous and breast adipose tissues, respectively while average values of 83.3 (± 2.1) ms, 84.2(± 4.1) ms and 71.8 (± 16.5) ms were calculated for the methylene protons, in the different tissues, respectively. Note that excluding one outlier low value (36.8 ms) for methylene protons in breast tissue resulted in an average of 77.7 ± 6.3 ms. A significant statistical difference ($p = 0.005$) was only found between apparent T_2 values of olefinic protons in breast and tibial bone marrow (≈ 25 % lower) indicating that if comparisons of olefinic measures in those tissues are being made, corrections for T_2 should be considered. It should be emphasized that all values obtained in this work are apparent T_2 values because the effects of J-coupling evolution are included which affects T_2 quantification [20,26,33,38,39], particularly for the olefinic and methyl protons and to a lesser extent the methylene protons [40], which display a monoexponential decay. Therefore, corrections for T_2 for the olefinic and methyl protons cannot generally be made based on the values presented; however, they indicate relative differences in signal decay. The methodology employed in this work could explain the discrepancy when comparing our estimates to that of others in the literature. The T_2 relaxation time of methyl protons in tibial bone marrow at 3 T have been estimated using a narrow bandwidth PRESS sequence, that rewinded the J-coupling evolution, to be 132.6 ms [26], a much higher value than that obtained here. In subcutaneous abdominal adipose tissue, olefinic, methyl, and methylene T_2 relaxation

times (which include the effects of J-coupling) at 3 T were estimated to be 54 ms, 70 ms, and 82 ms, respectively [30] using a STEAM sequence with TE values of 15, 20, 25, and 30 ms. Although the olefinic and methylene apparent T_2 relaxation times are somewhat comparable to ours (44.8 ms and 84.2 ms, respectively), the methyl T_2 relaxation is approximately twice what was measured in this work (39.2 ms). Measured differences are likely due to the difference in response of coupled spins to PRESS and STEAM sequences [16,22,41]. More specifically, a study previously showed that T_2 measurements computed using PRESS were 25 to 50 % shorter than those calculated using STEAM in liver fat [41]. Breast fat T_2 measurements in the literature have been limited to using imaging at 3 T (primarily the methylene signal); magnitude MRI images using Hahn echoes with TE values of 20 and 100 ms were used to estimate fat T_2 (primarily methylene signal) in breast to be 52.96 ms [42], about 25 % lower than our estimate. The deviation may be due to signal contributions from the other fat resonances.

We also estimated, from short-TE PRESS spectra, average olefinic/methylene ratios of 9.2, 9.9 and 9.8% in tibial bone marrow, subcutaneous and breast adipose tissues, respectively. No statistical significance was found between the three average values. In addition, we calculated the ratios from spectra acquired with TE = 200 ms (previously optimized to measure olefinic/methylene ratios in tibial bone marrow [17]), namely, 13.5 %, 13.3 % and 11.5 % , respectively. The values are a few percent higher with the long TE, likely due to differences in T_2 relaxation between the olefinic and methylene protons and J-coupling behavior [22]; poorer spectral resolution using short TE [19,21] may contribute a source of error. We estimated diallylic/methylene ratios of 1.7 %, 2.2 % and 2.3 % in tibia, subcutaneous and breast adipose tissue, respectively, using the short-TE spectra. The mean tibial bone marrow value was statistically different from those found in the other two tissues. Levels of total fat unsaturation [15,17,20,24,31,33,36] and poly-unsaturation [15,17,20,24,31-33,36] in tibial bone marrow [17,24,36], subcutaneous adipose tissue [15,20,31,36], and breast adipose tissue [32,33] have been previously reported. Of the studies that provide quantitative metrics comparable to ours, measurements at 7 T in tibial bone marrow reported olefinic/methylene and diallylic/methylene ratios of 0.06 and 0.02, respectively, using STEAM with a TE of 20 ms [24]. In tibial bone marrow we obtained average olefinic/methylene and diallylic/methylene values of 0.092 and 0.017 using PRESS with a TE of 40 ms. The diallylic/methylene ratios are comparable; however, our olefinic/methylene ratio is approximately 53 % higher. Deviations could be explained by differences in T_2 relaxation and J-

coupling evolution at the different field strengths. In addition, a limitation of our olefinic quantification is that contributions from the ≈ 5.3 ppm glycerol resonance were included, which can cause overestimations of about 13 % using PRESS with a TE of 40 ms [43]. The higher field strength of 7 T better resolves the glycerol and the olefinic resonance, improving olefinic resonance quantification.

In subcutaneous adipose tissue measurements at 1.5 T, it was reported that olefinic/methylene measures calculated from PRESS with a TE of 200 ms agreed better with gas chromatography analysis of the same tissue [20] than short-TE results did. The authors cite difficulties in obtaining a proper fit with shorter TE spectra partly due to the influence of the intense methylene signal, which decays at the longer TE. This effect is likely less pronounced at 3 T because of better separation of methylene and methyl peaks. PRESS with a TE of 200 ms was used at 1.5 T [31] to estimate olefinic/methylene ratios of about 11 % in deep subcutaneous tissues, in close agreement with our value of about 13 %. Intra-subject variability of olefinic/methyl and diallylic/methyl ratios were reported for tibial bone marrow and deep subcutaneous adipose tissue at 3 T using a short-TE (TE = 20 ms) STEAM sequence [36]. It was found that for both metrics, values in tibial bone marrow were approximately 93-96 % of those found in deep subcutaneous adipose tissue. While our short-TE measures for olefinic/methylene yielded similar differences between the two tissues, diallylic/methylene values in tibial bone marrow are about 77 % of those in subcutaneous tissue in this study. Differences may be due to the subjects; we performed measurements on healthy volunteers, whereas Machann et al. [36] obtained measurements from volunteers with a range of BMI and insulin sensitivity.

To our knowledge, olefinic/methylene and diallylic/methylene ratios have not been previously quantified in breast tissue. Fat unsaturation measurements in breast tissue are limited, likely due to the challenges posed from the water contamination of the olefinic resonance and the poor methyl and methylene spectral resolution. In the few studies reported, olefinic/methylene ratios were not provided; different metrics were employed. A selective multiple quantum coherence transfer sequence was designed at 2.1 T to detect olefinic protons coupled to diallylic protons (2.8 ppm) as a means of mapping total poly-unsaturation fat throughout breast tissue [32]; however, total fat unsaturation was not quantifiable using this method. At 7 T, a TE-averaged STEAM sequence was used to estimate the unsaturation fat content as 72.2 % , using the allylic

and diallylic peaks, and the 2.3 ppm methylene peaks in a fat composition model [33]. A similar result for total fat unsaturation (76.2 %) was obtained from a study at 3 T which made use of the same peaks and employed peak fitting [34]. Another study at 7 T used zero-quantum-coherence 2D NMR spectroscopy and STEAM with a TE of 5 ms to investigate lipids in breast [44]. The total unsaturation content was 73 % using the former technique and 62.7 % using the latter. The STEAM technique exploited peaks not completely resolvable at 3 T.

The lower number of studies on fat unsaturation measurement in breast tissue may be due to the poorer field homogeneity [45,46] obtained in breast tissue reflected by the broader methylene linewidths and overlap of methyl and methylene resonance (Figure 5.2). In this work, we explore the feasibility of using an IR sequence to suppress the water resonance from that of the olefinic in breast tissue containing water. Inversion recovery has been employed to remove the fat signal from the water signal in brain diffusion MRI [47], and in MRI of calf [48] and the musculoskeletal system [49]. IR has also been used to remove both fat and water signals to view short T_2 molecules, enabling imaging of cortical bone [50,51], patellar tendon [50], Achilles tendon [50,51], and deep radial and calcified layers of articular cartilage [51]. MR-IDEAL (iterative decomposition of water and fat with echo asymmetry and least-squares estimation) scans were also explored as a means to separate olefinic sigal from that of water in the knee, ankle, spine, breast and abdomen [52]. To our knowledge, the inversion recovery method has not been explored to minimize water signal to reveal the olefinic fat signal. Figure 5.6 displays that the olefinic and water resonances are not resolved using PRESS with a short TE of 40 ms. The IR method with an inversion delay of 613 ms was successful at suppressing the water signal, revealing the olefinic resonance. The suppression is superior to that obtained by water T_2 relaxation with long-TE PRESS and the olefinic resonance SNR is 5.9 times higher.

In conclusion, the presented work investigates intra-subject variability of apparent T_2 relaxation times of fat Olefinic, methylene and methyl protons in tibial bone marrow, subcutaneous and breast adipose tissue. No significant differences were found with the exception of the T_2 of breast olefinic protons compared to that of tibial bone marrow. Therefore, olefinic measures obtained with previously optimized long-TE techniques in breast should be corrected for T_2 differences. Intra-subject variability of total unsaturation and poly-unsaturation measures was also assessed. No significant differences in total unsaturation was found; however, tibial

bone marrow poly-unsaturation levels were found to be lower than in subcutaneous and breast adipose tissue. While long-TE methods offer advantages, loss of signal due to T_2 relaxation can be of concern; we demonstrate that using an IR method with a short-TE sequence successfully suppresses water overlapping the olefinic resonance in breast tissue.

5.6 Citations

1. Machann J, Stefan N, Schabel C, et al. Fraction of unsaturated fatty acids in visceral adipose tissue (VAT) is lower in subjects with high total VAT volume - a combined ^{1}H MRS and volumetric MRI study in male subjects. NMR Biomed 2013;26:232-236.
2. Johnson NA, Walton DW, Sachinwalla T, et al. Noninvasive assessment of hepatic lipid composition: Advancing understanding and management of fatty liver disorders. Hepatology 2008;47:1513-1523.
3. Mosconi E, Fontanella M, Sima DM, et al. Investigation of adipose tissues in Zucker rats using *in vivo* and *ex vivo* magnetic resonance spectroscopy. J Lipid Res 2011;52:330-336.
4. Strobel K, van den Hoff J, Pietzsch J. Localized proton magnetic resonance spectroscopy of lipids in adipose tissue at high spatial resolution in mice *in vivo*. J Lipid Res 2008;49:473-480.
5. Korteweg MA, Veldhuis WB, Mali WPTM, et al. Investigation of lipid composition of dissected sentinel lymph nodes of breast cancer patients by 7T proton MR spectroscopy. J Magn Reson Imaging 2012;35:387-392.
6. Fardanesh R, Marino MA, Avendano D, Leithner D, Pinker K, Thakur SB. Proton MR spectroscopy in the breast: Technical innovations and clinical applications. J Magn Reson Imaging 2019;50:1033-1046.
7. Yeung DKW, Griffith JF, Antonio GE, Lee FKH, Woo J, Leung PC. Osteoporosis is associated with increased marrow fat content and decreased marrow fat unsaturation: A proton MR spectroscopy study. J Magn Reson Imaging 2005;22:279-285.
8. Patsch JM, Li X, Baum T, et al. Bone marrow fat composition as a novel imaging biomarker in postmenopausal women with prevalent fragility fractures. J Bone Miner Res 2013;28:1721-1728.
9. Karampinos DC, Ruschke S, Dieckmeyer M, et al. Quantitative MRI and spectroscopy of bone marrow. J Magn Reson Imaging 2018;47:332-353.
10. Hu HH, Branca RT, Hernando D, et al. Magnetic resonance imaging of obesity and metabolic disorders: Summary from the 2019 ISMRM Workshop. Magn Reson Med 2020;83:1565-1576.
11. Cordes C, Baum T, Dieckmeyer M, et al. MR-based assessment of bone marrow fat in osteoporosis, diabetes, and obesity. Front Endocrinol 2016;7:10.3389/fendo.2016.00074 (7 pages).
12. Tufts LS, Shet K, Liang F, Majumdar S, Li X. Quantification of bone marrow water and lipid composition in anterior cruciate ligament-injured and osteoarthritic knees using three-dimensional magnetic resonance spectroscopic imaging. Magn Reson Imaging 2016;34:632-637.
13. Wang L, Salibi N, Chang G, et al. Assessment of subchondral bone marrow lipids in healthy controls and mild osteoarthritis patients at 3T. NMR Biomed 2011;25:545-555.
14. Gajdošík M, Chadzynski GL, Hangel G, et al. Ultrashort-TE stimulated echo acquisition mode (STEAM) improves the quantification of lipids and fatty acid chain unsaturation in the human liver at 7 T. NMR Biomed 2015;28:1283-1293.
15. Lundbom J, Hakkarainen A, Söderlund S, Westerbacka J, Lundbom N, Taskinen M-R. Long-TE ^{1}H MRS suggests that liver fat is more saturated than subcutaneous and visceral fat. NMR Biomed 2011;24:238-245.

16. Bingölbali A, Fallone BG, Yahya A. Comparison of optimized long echo time STEAM and PRESS proton MR spectroscopy of lipid olefinic protons at 3 Tesla. J Magn Reson Imaging 2015;41:481-486.
17. Troitskaia A, Fallone BG, Yahya A. Long echo time proton magnetic resonance spectroscopy for estimating relative measures of lipid unsaturation at 3 T. J Magn Reson Imaging 2013;37:944-949.
18. Huovinen V, Viljakainen H, Hakkarainen A, et al. Bone marrow fat unsaturation in young adults is not affected by present or childhood obesity, but increases with age: A pilot study. Metabolism 2015;64:1574-1581.
19. Lundbom J, Bierwagen A, Bodis K, et al. ^{1}H-MRS of femoral red and yellow bone marrow fat composition and water content in healthy young men and women at 3 T. Magn Reson Mater Phy 2019;32:591-597.
20. Lundbom J, Hakkarainen A, Fielding BA, et al. Characterizing human adipose tissue lipids by long echo time ^{1}H-MRS in vivo at 1.5 Tesla: validation by gas chromatography. NMR Biomed 2010;23:466-472.
21. Škoch A, Jírů F, Dezortová M, et al. Intramyocellular lipid quantification from ^{1}H long echo time spectra at 1.5 and 3 T by means of the LCModel technique. J Magn Reson Imaging 2006;23:728-735.
22. Fallone CJ, McKay RT, Yahya A. Long TE STEAM and PRESS for estimating fat olefinic/methyl ratios and relative ω-3 fat content at 3T. J Magn Reson Imaging 2018;48:169-177.
23. Laaksonen DE, Nuutinen J, Lahtinen T, Rissanen A, Niskanen LK. Changes in abdominal subcutaneous fat water content with rapid weight loss and long-term weight maintenance in abdominally obese men and women. Int J Obes 2003;27:677-683.
24. Ren J, Dimitrov I, Sherry AD, Malloy CR. Composition of adipose tissue and marrow fat in humans by ^{1}H NMR at 7 Tesla. J Lipid Res 2008;49:2055-2062.
25. Querleux B, Cornillon C, Jolivet O, Bittoun J. Anatomy and physiology of subcutaneous adipose tissue by in vivo magnetic resonance imaging and spectroscopy: Relationships with sex and presence of cellulite. Skin Res Technol 2002;8:118-124.
26. Yahya A, Fallone BG. T_2 determination of the J-coupled methyl protons of lipids: *In vivo* illustration with tibial bone marrow at 3T. J Magn Reson Imaging 2010;31:1514-1521.
27. de Bazelaire CMJ, Duhamel GD, Rofsky NM, Alsop DC. MR imaging relaxation times of abdominal and pelvic tissues measured *in vivo* at 3.0 T: Preliminary results Radiology 2004;230:652-659.
28. Robinson MD, Cistola DP. Nanofluidity of fatty acid hydrocarbons as monitored by benchtop time-domain nuclear magnetic resonance. Biochem 2014;53:7515-7522.
29. Peterson P, Månsson S. Simultaneous quantification of fat content and fatty acid composition using MR imaging. Magn Reson Med 2013;69:688-697.

30. Hamilton G, Schlein AN, Middleton MS, et al. *In vivo* triglyceride composition of abdominal aipose tissue measured by ^{1}H MRS at 3T. J Magn Reson Imaging 2017;45:1455-1463.
31. Lundbom J, Bierwagen A, Bodis K, et al. Deep subcutaneous adipose tissue lipid unsaturation associated with intramyocellular lipid content. Metabolism 2016;65:1230-1237.
32. He Q, Shkarin P, Hooley RJ, Lannin DR, Weinreb JC, Bossuyt VIJ. *In vivo* MR spectroscopic imaging of polyunsaturated fatty acids (PUFA) in healthy and cancerous breast tissues by selective multiple-quantum coherence transfer (Sel-MQC): A preliminary study. Magn Reson Med 2007;58:1079-1085.
33. Dimitrov IE, Douglas D, Ren J, et al. *In vivo* determination of human breast fat composition by ^{1}H MRS at 7T. Magn Reson Med 2013;67:20-26.
34. Coum A, Ouldamer L, Noury F, et al. *In vivo* MR spectroscopy of human breast tissue: quantification of fatty acid composition at a clinical field strength (3 T). Magn Reson Mater Phy 2016;29:1-4.
35. Viallon M, Leporq B, Drinda S, et al. Chemical-shift-encoded Magnetic Resonance Imaging and Spectroscopy to reveal immediate and long-term multi-organs composition changes of a 14-days periodic fasting intervention: A technological and case report. Front Nutr 2019;6:1-13.
36. Machann J, Stefan N, Wagner R, et al. Intra- and interindividual variability of fatty acid unsaturation in six different human adipose tissue compartments assessed by ^{1}H-MRS *in vivo* at 3 T. NMR Biomed 2017;30:e3744 (10 pages).
37. Provencher SW. Estimation of metabolite concentrations from localized *in vivo* proton NMR spectra. Magn Reson Med 1993;30:672-679.
38. Yahya A, Tessier AG, Fallone BG. Effect of J-coupling on lipid composition determination with localized proton magnetic resonance spectroscopy at 9.4 T. J Magn Reson Imaging 2011;34:1388-1396.
39. Lundbom J, Heikkinen S, Fielding B, Hakkarainen A, Taskinen M-R, Lundbom N. PRESS echo time behavior of triglyceride resonances at 1.5 T: Detecting ω-3 fatty acids in adipose tissue *in vivo*. J Magn Reson 2009;201:39-47.
40. Breitkreutz DY, Fallone BG, Yahya A. Effect of *J* coupling on 1.3-ppm lipid methylene signal acquired with localised proton MRS at 3T. NMR Biomed 2015;28:1324-1331.
41. Hamilton G, Middleton MS, Bydder M, et al. Effect of PRESS and STEAM sequences on magnetic resonance spectroscopic liver fat quantification. J Magn Reson Imaging 2009;30:145-152.
42. Rakow-Penner R, Daniel B, Yu H, Sawyer-Glover A, Glover GH. Relaxation times of breast tissue at 1.5T and 3T measured using IDEAL. J Magn Reson Imaging 2006;23:87-91.
43. Fallone CJ, Yahya A. Effect of triglyceride glycerol CH signal on olefinic resonance quantification with proton magnetic resonance spectroscopy at 3 T. Biomed Phys Eng Express 2019;5:027004 (10 pages).
44. de Graaf RA, Klomp DWJ, Luijten PR, Boer VO. Intramolecular zero-quantum-coherence 2D NMR spectroscopy of lipids in the human breast at 7 T. Magn Reson Med 2014;71:451-457.
45. Hancu I, Govenkar A, Lenkinski RE, Lee S-K. On shimming approaches in 3T breast MRI. Magn Reson Med 2013;69:862-867.

46. Maril N, Collins CM, Greenman RL, Lenkinski RE. Strategies for shimming the breast. Magn Reson Med 2005;54:1139-1145.
47. Hernando D, Karampinos DC, King KF, et al. Removal of olefinic fat chemical shift artifact in diffusion MRI. Magn Reson Med 2011;65:692-701.
48. Ohno N, Miyati T, Suzuki S, et al. Hybrid quantitative MRI using chemical shift displacement and recovery-based simultaneous water and lipid imaging: A preliminary study. Magn Reson Imaging 2018;50:61-67.
49. Del Grande F, Santini F, Herzka DA, et al. Fat-suppression techniques for 3-T MR imaging of the musculoskeletal system. Radiographics 2014;34:217-233.
50. Ma Y-J, Zhu Y, Lu X, Carl M, Chang EY, Du J. Short T_2 imaging using a 3D double adiabatic inversion recovery prepared ultrashort echo time cones (3D DIR-UTE-Cones) sequence. Magn Reson Med 2018;79:2555-2563.
51. Du J, Takahashi AM, Bae WC, Chung CB, Bydder GM. Dual Inversion Recovery, Ultrashort Echo Time (DIR UTE) imaging: Creating high contrast for short-T_2 species. Magn Reson Med 2010;63:447-455.
52. Yu H, Shimakawa A, McKenzie CA, Brodsky E, Brittain JH, Reeder SB. Multiecho water-fat separation and simultaneous R2* estimation with multifrequency fat spectrum modeling. Magn Reson Med 2008;60:1122-1134.

Chapter 6

Effect of Triglyceride Glycerol CH Signal on Olefinic Resonance Quantification with Proton Magnetic Resonance Spectroscopy at 3 T

A version of this chapter has been published:

Fallone, C.J., and Yahya, A. (2019). Effect of triglyceride glycerol CH signal on olefinic resonance quantification with proton magnetic resonance spectroscopy at 3 T. *Biomedical Physics and Engineering Express* 5: 027004 (10 pages).

6.1 Abstract

The *in-vivo* Magnetic Resonance Spectroscopy (MRS) techniques STimulated Echo Acquisition Mode (STEAM) and Point Resolved Spectroscopy (PRESS) are used to assess fat unsaturation levels in human adipose tissue by measuring the olefinic proton resonance at ≈ 5.4 ppm. At clinical field strengths, the resonance is overlapped by that of the triglyceride glycerol CH proton at ≈ 5.2 ppm. In the presented work, olefinic resonance contamination by that of the glycerol CH proton for STEAM and PRESS as a function of echo time (TE) is assessed at 3 T. MRS spectra were acquired from the triglyceride tricaprylin (contains glycerol but no olefinic protons), and from free oleic acid (contains olefinic but no glycerol protons) using STEAM (TE of 20 to 300 ms, mixing time of 20 ms) and PRESS (TE of 40 to 300 ms), with TE increments of 10 ms. Estimated olefinic signal contamination by the glycerol CH resonance was evaluated for short-TE (STEAM with TE of 20 ms and PRESS with TE of 40 ms) for human adipose tissue based on a literature composition and using the spectra acquired for tricaprylin and oleic acid. Contaminations of ≈ 20 % for STEAM with a TE = 20 ms and ≈ 13 % for PRESS with a TE = 40 ms were obtained. Glycerol CH contributions to the olefinic resonance was also estimated for eight oils in a similar manner. High-resolution *in-vitro* 16.5 T Nuclear Magnetic Resonance (NMR) spectra of the oils suggest that in the absence of significant T_2 relaxation and J-coupling effects, 9 to 17 % (depending on unsaturated fatty acid content) of the olefinic signal is attributable to the glycerol CH proton. The signal yield responses of the glycerol CH and the olefinic protons as a function of TE indicate that a TE of 90 ms for STEAM and a TE of 200 ms for PRESS are suitable for quantification of the olefinic resonance with minimal impact from the glycerol CH resonance. Signal area yields relative to those obtained with short-TE were 30 % and 29 % for the olefinic resonance and 4 % and 5 % for the glycerol resonance for STEAM with a TE of 90 ms and PRESS with a TE of 200 ms, respectively. The efficacy of the timings was verified *in vivo* on tibial bone marrow.

6.2 Introduction

Proton Magnetic Resonance Spectroscopy (MRS) has been utilized to measure levels of fat unsaturation in several diseases *in vivo* [1-10]. Adipose tissue is composed of saturated (≈ 35 %) and unsaturated fatty acids (≈ 65 %) [11]. The olefinic resonance (≈ 5.4 ppm) provides a measure of fat unsaturation *in vivo* and has been quantified by short echo time (TE) [2-4,12,13] and optimized long TE Stimulated Echo Acquisition Mode (STEAM) [14] and Point RESolved Spectroscopy (PRESS) [15] sequences [1,16-18]. Long TE techniques were applied to spinal bone marrow [16] and liver [1] to effectively suppress overlapping water signal. However, adipose tissue fatty acids in the body are primarily stored in the form of triglycerides [19] and the olefinic signal is unavoidably also contaminated by the triglyceride glycerol CH proton (≈ 5.2 ppm) at clinical field strengths [20-23]. It has been suggested that increases in glycerol signal with disease can influence the detection of changes in olefinic levels due to the overlap of peaks [24], affecting fat unsaturation quantification. As shown in Figure 6.1, the 5.2 ppm glycerol proton is bonded to the middle carbon of the triglyceride glycerol backbone. The glycerol CH proton is weakly coupled to the methylene glycerol protons that resonate at ≈ 4.2 ppm at 3 T [25]. The olefinic protons on the other hand are weakly coupled to the neighboring 2.1 ppm and 2.8 ppm protons, and strongly coupled to each other [26]. To our knowledge, the impact of the glycerol resonance on quantification of the olefinic resonance has not been previously assessed.

The objective of the presented work is to investigate potential levels of olefinic signal contamination by the glycerol CH signal when using standard short-TE STEAM and PRESS sequences. In addition, we characterize the T_2 decay and J-coupling response of the glycerol CH proton as a function of TE at 3 T to determine TE values for STEAM and PRESS which minimize the glycerol signal while maintaining relatively high olefinic signal. The glycerol proton response is investigated using tricaprylin, which is a saturated triglyceride fatty acid and therefore contains no olefinic protons, rendering the glycerol CH signal un-obscured. Free oleic acid (no glycerol protons), a mono-unsaturated fatty acid, is used to study the response of the olefinic protons. The proton responses were also employed to estimate olefinic signal contamination by the glycerol CH proton for adipose tissue when employing short TE PRESS and STEAM techniques.

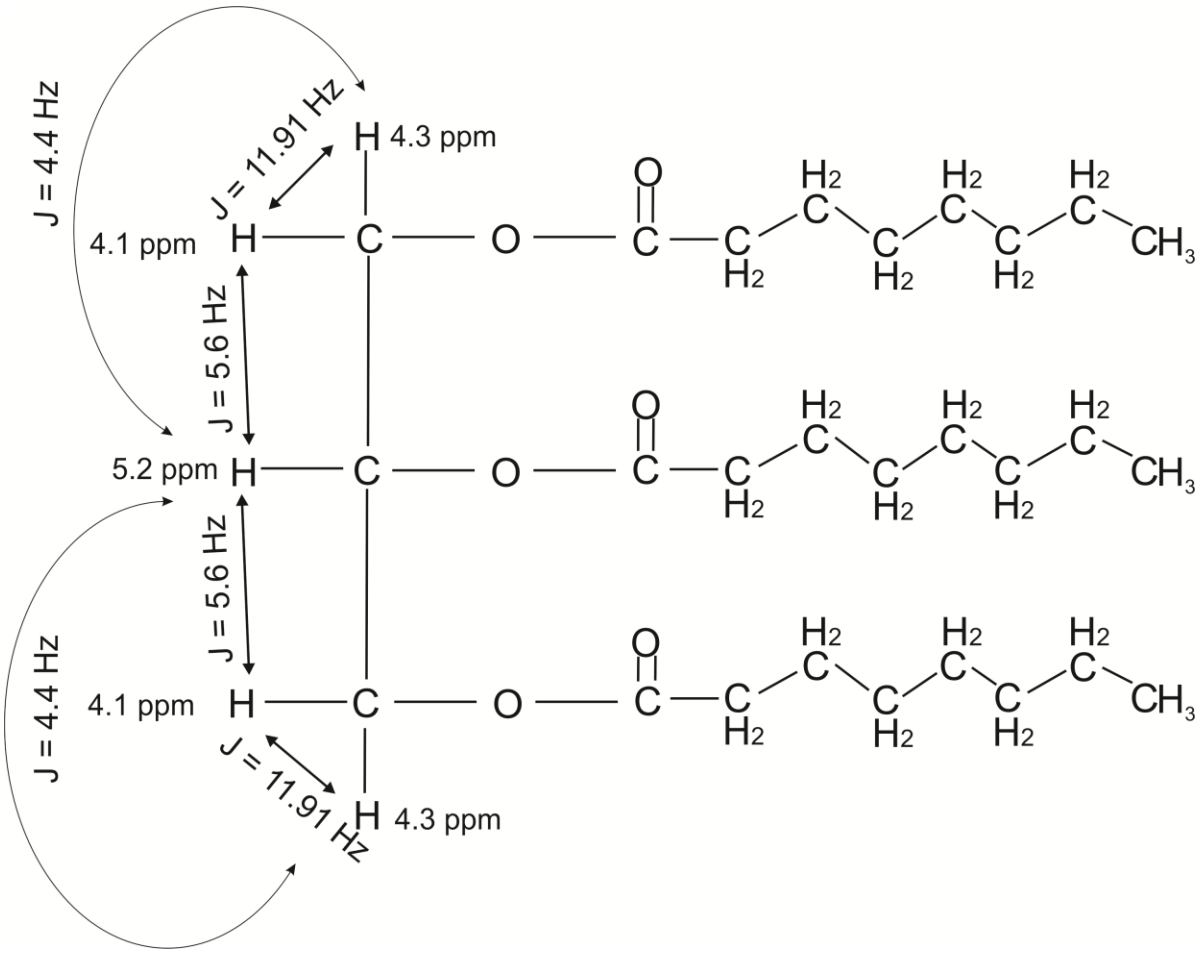

Figure 6.1**:** Molecular structure of tricaprylin, a saturated triglyceride. The glycerol CH proton which resonates at 5.2 ppm is coupled to the 4.3 ppm and 4.1 ppm glycerol protons [25].

6.3 Materials and Methods

Data Acquisition:

Phantom:

A 3 T Philips whole body Magnetic Resonance Imaging (MRI) scanner (Intera, Philips Healthcare, Best, Netherlands) with a transmit/receive radiofrequency (RF) birdcage head coil (Philips Healthcare) was employed for all scans. Spectra were obtained from free fatty acid oleic acid (olefinic resonance, no glycerol resonance), and the triglyceride tricaprylin (glycerol resonance, no olefinic resonance) with STEAM (TE = 20 to 300 ms in steps of 10 ms, mixing

time TM = 20 ms) and PRESS (TE = 40 to 300 ms in steps of 10 ms). A PRESS TE of 35 ms was achievable; however, to minimize eddy current effects a short TE of 40 ms was selected. The following parameters were employed: 3 s repetition time (TR), 32 signal averages, 2048 samples, and a 2000 Hz spectral bandwidth. For all PRESS sequences, the first part of the asymmetric total echo time (first echo time) was set to 17 ms, and the second part (second echo time) was adjusted to set the total echo time. The study utilized the Philips scanner's automatic second order shimming procedure (based on FASTERMAP [27]) on the voxel of interest. The RF transmitter frequency was set to ≈ 3.15 ppm, the midpoint between the methyl (≈ 0.9 ppm) and olefinic (≈ 5.4 ppm) resonances. Water suppression was not required, and a 16 step phase cycling scheme was employed. Signal was obtained from 10 x 10 x 10 mm^3 voxels centered within the two phantoms.

To quantify the contamination of the glycerol resonance on the olefinic resonance in the absence of T_2 relaxation and J-coupling effects, spectra of eight common edible oils (peanut, walnut, sunflower, linseed, almond, corn, canola, sesame) were acquired using a high resolution 700 MHz (16.5 T) Varian/Agilent VNMRS spectrometer. About 50 µL of each oil was dissolved in 550 µL of deuterated chloroform and the following parameters were employed: 8389.26 Hz sweep width, 5.1 s repetition time, 42000 samples, 30° flip angle and 16 averages.

***In vivo*:**

To estimate olefinic T_2 *in vivo* relative to that in oleic acid, *in-vivo* spectra were acquired from the tibial bone marrow of a healthy volunteer (female, age 34) from an 8 x 8 x 8 mm^3 voxel positioned about 10 cm below the left knee using a PRESS sequence with TE = 40 ms, 80 ms, 140 ms, 200 ms and 240 ms; sequence parameters were consistent with those of phantom scans. To verify the efficacy of the determined long-TE values for suppression of glycerol CH signal, spectra were acquired in another session from tibial bone marrow of another volunteer (female, age 28) from a 7 x 7 x 10 mm^3 voxel with both PRESS and STEAM (short-TE and determined long-TE values). For *in-vivo* scans the body coil was used for RF transmission and one surface coil element of the Philips Flex-L coil was employed for signal reception.

Data Analysis:

Phantom:

Spectra acquired at 3 T were filtered with a 2 Hz Gaussian filter and phase-corrected. Olefinic peak areas of oleic acid (5.1 ppm – 5.6 ppm) and glycerol CH areas of tricaprylin (5.0 to 5.4 ppm) were measured using Philips spectroscopy software (Version 3.2.3.1) from the filtered spectra. The glycerol and olefinic resonance areas acquired with STEAM and PRESS were normalized to their corresponding signals acquired with STEAM with TE = 20 ms and PRESS with TE = 40 ms, respectively. Normalized peak areas were plotted as a function of TE. Appropriate long TE values for measuring olefinic signal with minimal contamination from glycerol CH signal were selected such that the TE yielded normalized absolute olefinic signal areas ≥ 25 %, normalized absolute glycerol CH signal areas ≤ 5 % and the largest difference between the normalized olefinic and glycerol resonance areas. The latter condition was imposed because there was no timing which resulted in simultaneous minimal glycerol signal and maximal olefinic signal.

Glycerol CH contamination of the olefinic resonance in adipose tissue at 3 T obtained with short TE techniques (STEAM TE = 20 ms and PRESS TE = 40 ms) was estimated from corresponding spectra acquired from tricaprylin and oleic acid. Human adipose tissue was assumed to be 34 % saturated (no olefinic protons, assumed to be primarily palmitic acid), 51 % mono-unsaturated (oleic acid), 14 % di-unsaturated (linoleic acid), and 1 % tri-unsaturated (linolenic acid) [11]. Triglycerides *in vivo* can include a variety of fatty acids attached to the glycerol backbone [28]. However, to simplify calculations without affecting the outcome, it was assumed that the composition is 34 % tripalmitin (glycerol with three palmitic acid molecules), 51 % triolein (glycerol with three oleic acid molecules), 14 % trilinolein (glycerol with three linoleic acid molecules), and 1 % trilinolenin (glycerol with three linolenic acid molecules), respectively. Table 6.1 lists the densities, molecular weights [29-32], the ratio of the two properties (mol/unit volume) and the number of olefinic protons present in each molecule.

Table 6.1: Densities and molecular weights for tricaprylin [29,30], oleic acid [31], tripalmatin [30], triolein [29,30], trilinolein [29] and trilinolenin [32].

Molecule	Density (g/mL)	Molecular Weight (g/mol)	Number of Olefinic Protons	mol/L
Tricaprylin	0.953	470.70	0	2.02
Oleic Acid	0.890	282.47	2	3.15
Tripalmitin	0.875	807.35	0	1.08
Triolein	0.913	885.47	6	1.03
Trilinolein	0.927	879.38	12	1.05
Trilinolenin	0.940	873.34	18	1.08

Olefinic peak areas measured from oleic acid short-TE spectra were used to calculate the total estimated olefinic peak area expected from a unit volume of adipose tissue by using the assumed triglyceride composition and compensating for differences in density, molecular weight and number of olefinic protons between oleic acid and each triglyceride. Equation 6.1 was used where triglyceride represents one of tripalmitin, triolein, trilinolein, and trilinolenin. The estimated theoretical peak area for each triglyceride contribution was calculated and the sum yielded the total expected olefinic peak area from a unit volume of adipose tissue.

$$(olefinic\ peak\ area)_{triglyceride} = (olefinic\ peak\ area)_{oleic\ acid} * \frac{(\frac{mol}{unit\ volume})_{triglyceride}}{(\frac{mol}{unit\ volume})_{oleic\ acid}} * \frac{number\ of\ olefinic\ protons\ in\ triglyceride}{number\ of\ olefinic\ protons\ in\ oleic\ acid} * \%\ of\ triglyceride\ present \quad (6.1)$$

Similarly, the total estimated glycerol peak area for a unit volume of adipose tissue was calculated (based on the short-TE glycerol area of tricaprylin) as the sum of the following for each of tripalmitin, triolein, trilinolein, and trilinolenin.

$$(glycerol\ peak\ area)_{triglyceride} = (glycerol\ peak\ area)_{tricaprylin} * \frac{(\frac{mol}{unit\ volume})_{triglyceride}}{(\frac{mol}{unit\ volume})_{tricaprylin}} * \frac{number\ of\ glycerol\ protons\ in\ triglyceride}{number\ of\ glycerol\ protons\ in\ tricaprylin} * \%\ of\ triglyceride\ present \quad (6.2)$$

The expected glycerol contamination of the olefinic resonance was calculated by taking the ratio of the total estimated glycerol area to the total estimated olefinic area (glycerol CH peak area/olefinic peak area). Using the above equations, the expected glycerol contamination of the olefinic resonance was also calculated for the eight oils for short-TE STEAM and PRESS at 3 T, based on compositions obtained from literature [17]. The saturated fatty acid portion was assumed to be tripalmitin [33-37]. The estimated contaminations were compared to values measured using 16.5 T NMR.

VNMRJ (the software interface for Varian NMR spectrometers) was used to process the 16.5 T spectra acquired from the eight oils. Olefinic (5.25 ppm – 5.50 ppm), glycerol CH (5.20 – 5.25 ppm), and methyl peak areas (0.84 ppm – 1.0 ppm) were measured. Glycerol CH to olefinic resonance area ratios provide a measure of olefinic signal contamination in the absence of T_2 and J-coupling signal losses and were correlated with levels of oil unsaturation obtained from measured olefinic to methyl peak area ratios.

In vivo:

In-vivo spectra acquired were filtered with a 4 Hz Gaussian filter and phase-corrected. Olefinic peak areas (5.1 ppm – 5.6 ppm) were measured using Philips spectroscopy software (Version 3.2.3.1) from the filtered spectra. The PRESS olefinic resonance areas acquired were normalized to their corresponding signals acquired with PRESS with TE = 40 ms, respectively. Normalized peak areas were plotted as a function of TE.

6.4 Results

Figure 6.2 shows the olefinic spectral region obtained for canola oil at 3 T and at 16.5 T where it can be seen that the olefinic and glycerol resonances can be differentiated from each other at 16.5 T, but not at 3 T.

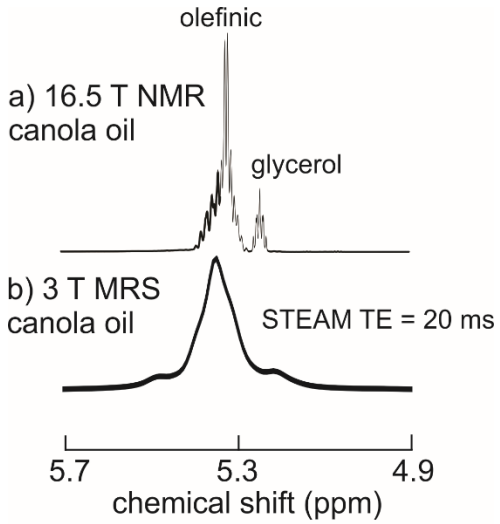

Figure 6.2: Glycerol and olefinic spectra obtained from canola oil using 16.5 T NMR (a) and 3 T MRS (b). The glycerol and olefinic resonances are clearly resolved at 16.5 T but not at 3 T.

Figure 6.3 presents the molecular structures and corresponding 3 T spectra acquired for oleic acid and tricaprylin with STEAM with a TE of 20 ms. As seen in the figure, the oleic acid spectrum has an olefinic resonance (J) at ≈ 5.4 ppm and no glycerol resonance, whereas the

tricaprylin spectrum has a glycerol CH resonance (K) at ≈ 5.2 ppm and no olefinic resonance. Oleic acid olefinic linewidths (no filtering applied) were 10.5 Hz and 8.8 Hz for short-TE STEAM and PRESS, respectively. Using the assumed adipose tissue composition and the acquired 3 T spectra, it is estimated that glycerol CH would contaminate the olefinic resonance by ≈ 20 % for STEAM with a TE = 20 ms (TM = 20 ms) and ≈ 13 % for PRESS with a TE = 40 ms in human adipose tissue.

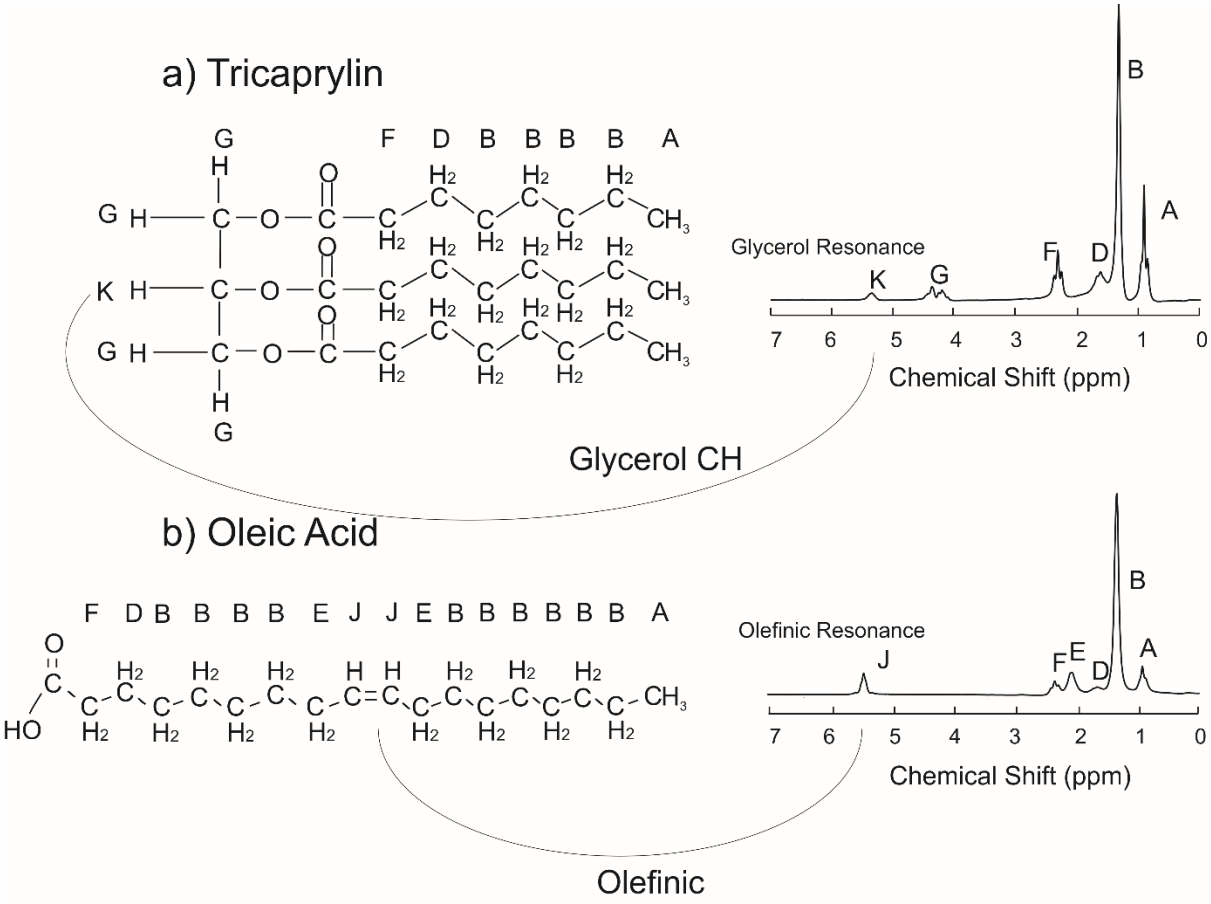

Figure 6.3: Molecular structures and corresponding 3 T STEAM (TE = 20 ms, TM = 20 ms) spectra for (a) tricaprylin and (b) oleic acid. The tricaprylin spectrum exhibits the glycerol CH resonance at ≈ 5.2 ppm, and the oleic acid demonstrates the olefinic resonance at ≈ 5.4 ppm.

Figure 6.4 shows the normalized resonance areas for the glycerol CH proton (tricaprylin) and olefinic protons (oleic acid) as a function of STEAM and PRESS TE. STEAM with a TE of

90 ms and PRESS with a TE of 200 ms were determined to be suitable echo times for olefinic quantification as per the criteria described in the Methods Section. Figure 6.4 illustrates that normalized glycerol CH signal levels relative to those of olefinic are quite low at the selected long TE values. Figure 6.5 displays the glycerol CH (tricaprylin) and olefinic (oleic acid) resonances obtained with short-TE and with the selected long-TE values. STEAM with a TE of 90 ms resulted in olefinic and glycerol CH areas that are 30 % and 4 %, respectively, of those obtained with a short TE of 20 ms. PRESS with a TE of 200 ms provided olefinic and glycerol CH areas that are 29 % and 5 %, respectively, of those obtained with a short TE of 40 ms.

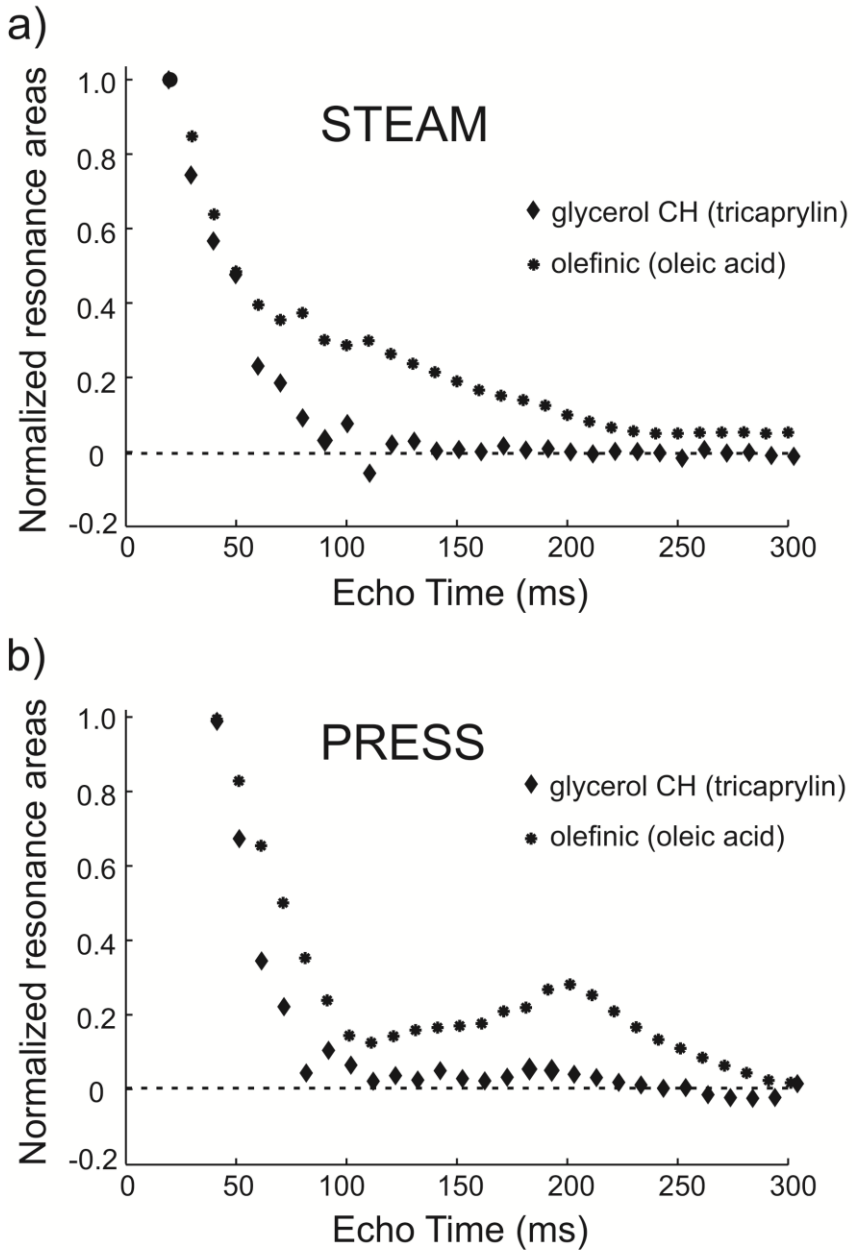

Figure 6.4: Normalized resonance signal areas for tricaprylin and oleic acid. Signal areas at each TE for (a) STEAM and (b) PRESS are normalized to signal acquired for STEAM with TE = 20 ms and PRESS with TE = 40 ms, respectively.

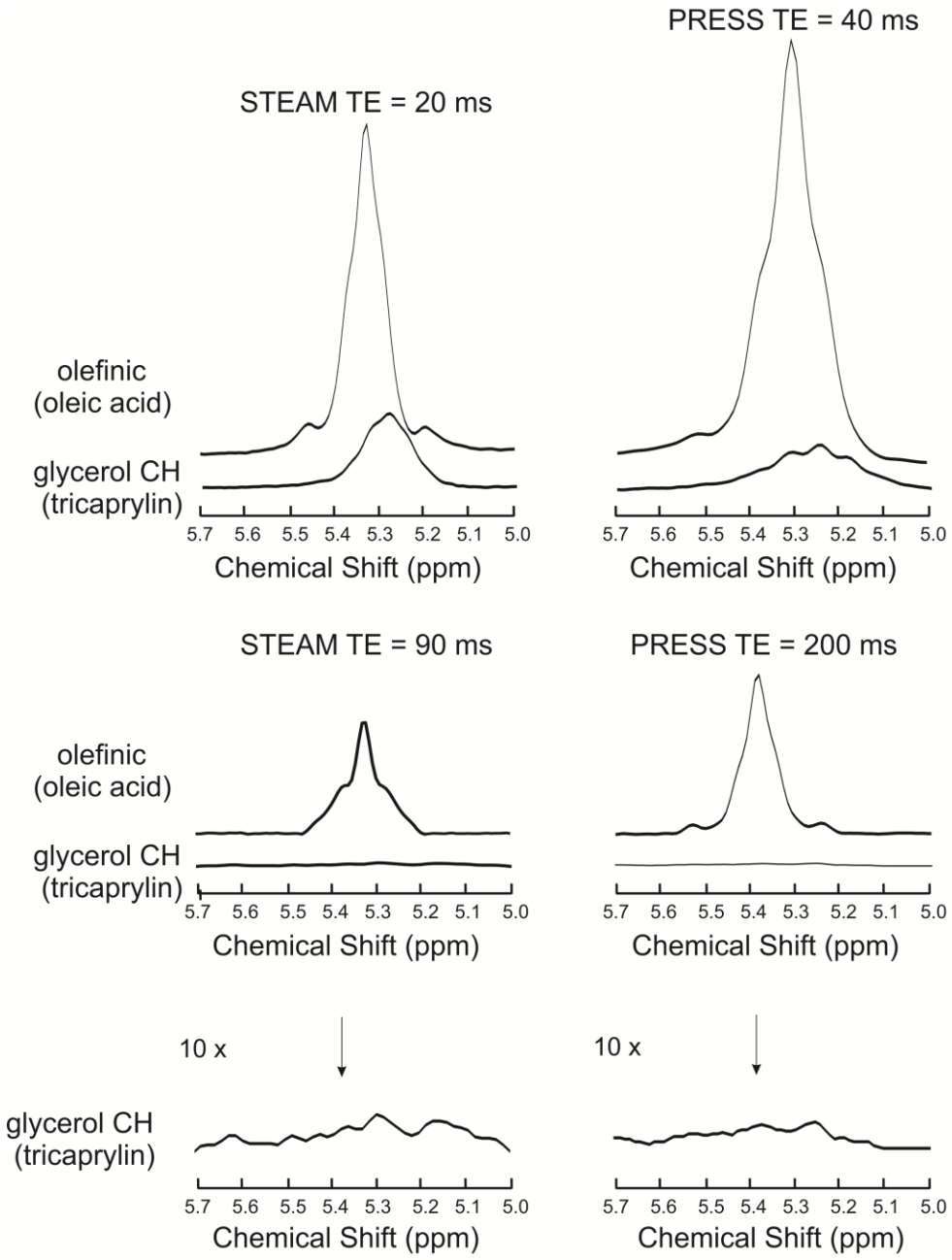

Figure 6.5: Olefinic and glycerol resonances obtained from oleic acid and tricaprylin, respectively, for short echo time (TE) (STEAM TE = 20 ms, PRESS TE = 40 ms) and optimized echo times (STEAM TE = 90 ms and PRESS TE = 200 ms). The glycerol signals have decayed significantly at the optimal TE values, whereas the olefinic signals are still relatively strong compared to their corresponding short-TE signals.

Table 6.2 demonstrates the estimated % contamination of the olefinic peak by the glycerol CH proton that would be obtained at 3 T with short-TE STEAM and PRESS techniques for the eight oils. The table also reports the % contamination obtained with 16.5 T high-resolution NMR (minimal T_2 and J-coupling evolution effects); contaminations of 9 – 17 % were obtained. Also included in Table 6.2 are 16.5 T NMR measured olefinic to methyl area ratios providing a measure of relative fat unsaturation of the oils.

Table 6.2: Estimated levels of olefinic resonance contamination by the glycerol CH resonance for eight edible oils using short-TE techniques at 3 T are calculated as described in the Methods Section (glycerol CH peak area/olefinic peak area). Percent contaminations of olefinic resonance calculated from16.5 T NMR spectra are also displayed. Olefinic to methyl ratios obtained from 16.5 T NMR are provided as an estimate of relative levels of fat unsaturation.

Oil	Estimated % Contamination with STEAM TE = 20 ms	Estimated % Contamination with PRESS TE = 40 ms	% Contamination (16.5 T NMR)	Olefinic to Methyl Ratio (16.5 T NMR)
Linseed	7.4	5.0	9.9	1.19
Walnut	7.8	5.3	9.1	1.14
Corn	11.1	7.5	11.5	0.961
Sunflower	10.7	7.3	12.3	0.924
Canola	11.9	8.1	12.6	0.848
Sesame	12.5	8.5	13.8	0.755
Almond	13.1	8.9	15.0	0.719
Peanut	13.8	9.4	16.6	0.641

Panel (a) of Figure 6.6 displays plots of olefinic peak area for oleic acid and *in-vivo* tibial bone marrow as a function of PRESS TE. Panel (b) presents the tibial bone marrow spectra acquired with STEAM and PRESS with both short-TE and with the determined long TE values suitable for glycerol CH signal suppression.

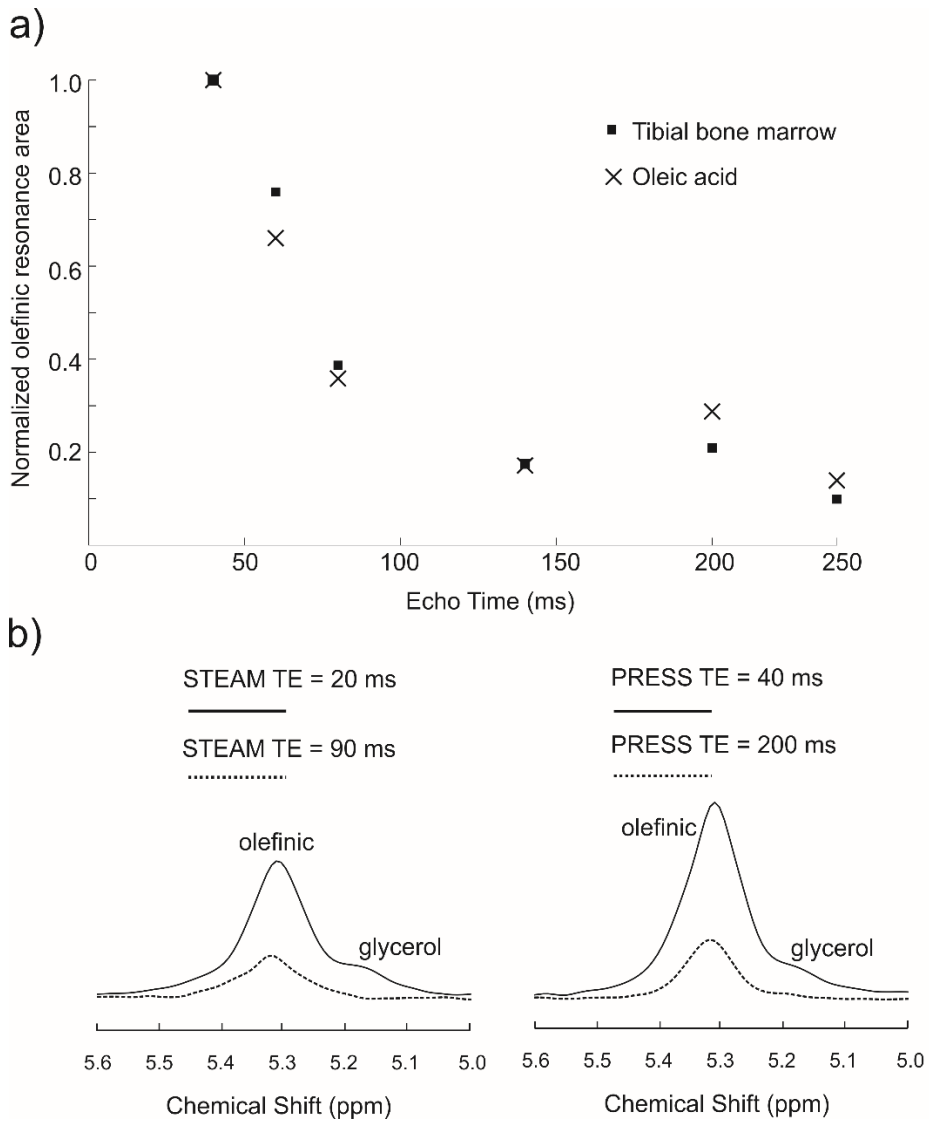

Figure 6.6: Normalized olefinic signal as a function of PRESS TE for oleic acid and for tibial bone marrow *in vivo* (a). Short-TE and optimal long TE STEAM and PRESS spectra acquired *in vivo* from tibial bone marrow are shown in (b). Glycerol CH signal is visible in the short-TE spectra but not in the long-TE ones.

6.5 Discussion

The olefinic proton at ≈ 5.4 ppm has been employed to assess fat unsaturation *in vivo* using short-TE STEAM [4] and PRESS [3,13,38] MRS techniques at clinical field strengths of 1.5 T and 3 T. The olefinic resonance includes contributions from the triglyceride glycerol CH proton (≈ 5.2 ppm) [20-23], which complicates quantification of the olefinic signal [24]. We estimated the % contamination of the olefinic resonance by the glycerol CH resonance in human adipose tissue to be of consequence, namely, ≈ 20 % for STEAM with a TE = 20 ms (TM = 20 ms) and ≈ 13 % for PRESS with a TE = 40 ms, using an assumed literature composition of adipose tissue [11]. The values were calculated based on the spectra acquired from oleic acid and tricaprylin and assumes similar T_2 behaviour *in vivo* (to those in phantom) for both the olefinic and glycerol CH protons. The lower contamination with PRESS is due to the more rapid decay of the glycerol CH signal with increasing TE (Figure 6.4) as a result of J-coupling evolution and T_2 relaxation. The % contamination of the olefinic resonance by that of glycerol CH was also estimated for the eight oils for STEAM TE = 20 ms (TM = 20 ms) and PRESS TE = 40 ms, and compared to the ratio of glycerol to olefinic resonance measured using 16.5 T NMR (minimal J-coupling and T_2 relaxation effects). The STEAM values match closely to those obtained from the high resolution spectra due to less signal loss (from J-coupling and T_2) with the relatively short TE. The longer TE used with short-TE PRESS and the more rapid decay of the glycerol CH proton signal compared to that of the olefinic protons renders lower contamination values. In general, the olefinic signal contamination by the glycerol CH signal increases as the oil unsaturation decreases due to the reduced presence of olefinic protons. The estimated contaminations obtained for sunflower oil with PRESS and STEAM deviate from the trend by a small amount; the inconsistency may be a result of the actual sunflower oil composition differing from the assumed composition.

Our work suggests that for minimal contribution of glycerol CH signal to that of the olefinic protons, STEAM with a TE of 90 ms and PRESS with a TE of 200 ms are suitable choices at 3 T. Both the olefinic and glycerol CH protons undergo T_2 relaxation and J-coupling interactions. The normalized glycerol CH signal levels relative to those of olefinic are quite low at the selected long TE values due to a combination of the difference in J-coupling evolution and lower T_2 value of the glycerol CH protons. The *in-vivo* spectra acquired with the determined

long-TE values show minimal signal in the glycerol CH spectral region compared to the short-TE spectra in which glycerol CH signal can be observed.

A limitation of the work is that the T_2 relaxation rate of the tricaprylin glycerol CH proton is likely to be different from the corresponding T_2 value *in vivo*, rendering a different signal yield *in vivo.* However, in this work we demonstrate that the oleic acid olefinic T_2 decay is similar to that tibial bone marrow. In addition, previous work has shown that olefinic and methyl T_2 relaxation values in tibia bone marrow are comparable to those of canola oil [18]. In addition, methylene T_2 relaxation times of tibial and spinal bone marrow were found to be in the range of those of common edible oils [17]. Therefore, the timings presented are likely applicable to human adipose tissue *in vivo* at 3 T as demonstrated by our long TE *in-vivo* spectra.

Previous long-TE optimizations for measuring olefinic to methylene and olefinic to methyl ratios at 3 T, namely, STEAM TE = 100 ms [16], STEAM TE = 120 ms [18], PRESS TE = 200 ms [17], and PRESS TE = 180 ms [18], resulted in TE values in the vicinity of our determined long-TE values for minimizing glycerol CH signal (STEAM TE = 90 ms and PRESS TE = 200 ms). The glycerol CH signal relative to that of olefinic is significantly lower at the listed TE values; thereby indicating that previously long-TE optimizations performed to suppress water and improve spectral resolution also inherently minimize glycerol CH contamination of the olefinic resonance.

6.6 Citations

1. Lundbom J, Hakkarainen A, Söderlund S, Westerbacka J, Lundbom N, Taskinen M-R. Long-TE ^{1}H MRS suggests that liver fat is more saturated than subcutaneous and visceral fat. NMR Biomed 2011;24:238-245.
2. Mosconi E, Fontanella M, Sima DM, et al. Investigation of adipose tissues in Zucker rats using *in vivo* and *ex vivo* magnetic resonance spectroscopy. J Lipid Res 2011;52:330-336.
3. Yeung DKW, Griffith JF, Antonio GE, Lee FKH, Woo J, Leung PC. Osteoporosis is associated with increased marrow fat content and decreased marrow fat unsaturation: A proton MR spectroscopy study. J Magn Reson Imaging 2005;22:279-285.
4. Machann J, Stefan N, Schabel C, et al. Fraction of unsaturated fatty acids in visceral adipose tissue (VAT) is lower in subjects with high total VAT volume - a combined ^{1}H MRS and volumetric MRI study in male subjects. NMR Biomed 2013;26:232-236.
5. Pollesello P, Eriksson O, Höckerstedt K. Analysis of total lipid extracts from human liver by ^{13}C and ^{1}H Nuclear Magnetic Resonance Spectroscopy. Anal Biochem 1996;236:41-48.
6. He Q, Shkarin P, Hooley RJ, Lannin DR, Weinreb JC, Bossuyt VIJ. *In vivo* MR spectroscopic imaging of polyunsaturated fatty acids (PUFA) in healthy and cancerous breast tissues by selective multiple-quantum coherence transfer (Sel-MQC): A preliminary study. Magn Reson Med 2007;58:1079-1085.
7. Johnson NA, Walton DW, Sachinwalla T, et al. Noninvasive assessment of hepatic lipid composition: Advancing understanding and management of fatty liver disorders. Hepatology 2008;47:1513-1523.
8. Patsch JM, Li X, Baum T, et al. Bone marrow fat composition as a novel imaging biomarker in postmenopausal women with prevalent fragility fractures. J Bone Miner Res 2013;28:1721-1728.
9. Korteweg MA, Veldhuis WB, Mali WPTM, et al. Investigation of lipid composition of dissected sentinel lymph nodes of breast cancer patients by 7T proton MR spectroscopy. J Magn Reson Imaging 2012;35:387-392.
10. Gajdošík M, Chadzynski GL, Hangel G, et al. Ultrashort-TE stimulated echo acquisition mode (STEAM) improves the quantification of lipids and fatty acid chain unsaturation in the human liver at 7 T. NMR Biomed 2015;28:1283-1293.
11. Hodson L, Skeaff CM, Fielding BA. Fatty acid composition of adipose tissue and blood in humans and its use as a biomarker of dietary intake. Prog Lipid Res 2008;47:348-380.
12. Machann J, Stefan N, Wagner R, et al. Intra- and interindividual variability of fatty acid unsaturation in six different human adipose tissue compartments assessed by ^{1}H-MRS *in vivo* at 3 T. NMR Biomed 2017;30:e3744 (10 pages).
13. Tufts LS, Shet K, Liang F, Majumdar S, Li X. Quantification of bone marrow water and lipid composition in anterior cruciate ligament-injured and osteoarthritic knees using three-dimensional magnetic resonance spectroscopic imaging. Magn Reson Imaging 2016;34:632-637.
14. Frahm J, Merboldt K-D, Hänicke W. Localized proton spectroscopy using stimulated echoes. J Magn Reson 1987;72:502-508.
15. Bottomley PA. Spatial localization in NMR spectroscopy *in vivo*. Ann NY Acad Sci 1987;508:333-348.

16. Bingölbali A, Fallone BG, Yahya A. Comparison of optimized long echo time STEAM and PRESS proton MR spectroscopy of lipid olefinic protons at 3 Tesla. J Magn Reson Imaging 2015;41:481-486.
17. Troitskaia A, Fallone BG, Yahya A. Long echo time proton magnetic resonance spectroscopy for estimating relative measures of lipid unsaturation at 3 T. J Magn Reson Imaging 2013;37:944-949.
18. Fallone CJ, McKay RT, Yahya A. Long TE STEAM and PRESS for estimating fat olefinic/methyl ratios and relative ω-3 fat content at 3T. J Magn Reson Imaging 2018;48:169-177.
19. Ren J, Dimitrov I, Sherry AD, Malloy CR. Composition of adipose tissue and marrow fat in humans by ^{1}H NMR at 7 Tesla. J Lipid Res 2008;49:2055-2062.
20. Vlahov G. Application of NMR to the study of olive oils. Prog Nucl Mag Res Sp 1999;35:341-357.
21. Knothe G, Kenar JA. Determination of the fatty acid profile by ^{1}H-NMR spectroscopy. Eur J Lipid Sci Tech 2004;106:88-96.
22. Fadzillah NA, Rohman A, Salleh RA, et al. Authentication of butter from lard adulteration using high-resolution of nuclear magnetic resonance spectroscopy and high-performance liquid chromatography. Int J Food Prop 2017;20:2147-2156.
23. Dimitrov I, Ren J, Sherry D, Malloy C. Fundamental advantages at 7 T allow for fat composition quantification. Medicamundi 2009;53:42-46.
24. Di Pietro G, Capuani S, Manenti G, et al. Bone marrow lipid profiles from peripheral skeleton as potential biomarkers for osteoporosis: A ^{1}H-MR spectroscopy study. Acad Radiol 2016;23:273-283.
25. Kosugi Y, Matsubara K. Conformational analysis of triacylglycerols by means of Nuclear Magnetic Resonance and Molecular Mechanics. J Jpn Oil Chem Soc 1989;38:415-420.
26. Purcell JM, Morris SG, Susi H. Proton magnetic resonance spectra of unsaturated fatty acids. Anal Chem 1966;38:588-592.
27. Shen J, Rycyna RE, Rothman DL. Improvements on an *in vivo* automatic shimming method [FASTERMAP]. Magn Reson Med 1997;38:834-839.
28. Eichmann TO, Kumari M, Haas JT, et al. Studies on the substrate and stereo/regioselectivity of adipose triglyceride lipase, hormone-sensitive lipase, and diacylglycerol-*O*-acyltransferases. J Biol Chem 2012;287:41446-41457.
29. Gouw TH, Vlugter JC. Physical properties of triglycerides. I. Density and refractive index. Fett Wiss Technol 1966;7:544-549.
30. Johnson WJ, Cosmetic Ingredient Review Expert Panel. Final report on the safety assessment of trilaurin, triarachidin, tribehenin, tricaprin, tricaprylin, trierucin, triheptanoin, triheptylundecanoin, triisononanoin, triisopalmitin, triisostearin, trilinolein, trimyristin, trioctanoin, triolein, tripalmitin, tripalmitolein, triricinolein, tristearin, triundecanoin, glyceryl triacetyl hydroxystearate, glyceryl triacetyl ricinoleate, and glyceryl stearate diacetate. Int J Toxicol 2001;20:61-94.
31. Bernardo-Gil G, Esquível M, Ribeiro A. Densities and refractive indices of pure organic acids as a function of temperature. J Chem Eng Data 1990;35:202-204.
32. Sales-Cruz M, Aca-Aca G, Sánchez-Daza O, López-Arenas T. Predicting critical properties, density and viscosity of fatty acids, triacylglycerols and methyl esters by group contribution methods. In: Pierucci S, Buzzi Ferraris G, editors. 20th European Symposium on Computer Aided Process Engineering; 2010.

33. Kostik V, Memeti S, Bauer B. Fatty acid composition of edible oils and fats. J Hyg Eng Des 2013;4:112-116.
34. Orsavova J, Misurcova L, Ambrozova JV, Vicha R, Mlcek J. Fatty acids composition of vegetable oils and its contribution to dietary energy intake and dependence of cardiovascular mortality on dietary intake of fatty acids. Int J Mol Sci 2015;16:12871-12890.
35. Roncero JM, Álvarez-Ortí M, Pardo-Giménez A, Gómez R, Rabadán A, Pardo JE. Virgin almond oil: Extraction methods and composition. Grasas Aceites 2016;67:e143 (10 pages).
36. Bayrak A, Kiralan M, Ipek A, Arslan N, Cosge B, Khawar KM. Fatty acid compositions of linseed (*Linum Usitatissimum* L.) genotypes of different origin cultivated in Turkey. Biotechnol & Biotechnol Eq 2010;24:1836-1842.
37. Tsamouris G, Hatziantoniou S, Demetzos C. Lipid analysis of Greek walnut oil (*Juglans regia* L.). Z Naturforsch 2002;57:51-56.
38. Fairgrieve-Park L, Fallone CJ, Yahya A. Long TE PRESS and STEAM for measuring the triglyceride glycerol CH_2 protons at 3 T NMR Biomed 2018;32:e4021(8 pages).

Chapter 7

Conclusions

7.1 Overview

The study of fat composition is relevant to many diseases, including breast cancer [1,2], bone disease [3-5], obesity [6,7], liver disease [8], and diabetes [9,10]. In animals, ω-3 fat dietary intake has been correlated with bone health [11-13] and anti-cancer biological responses [14,15], among other positive biological changes [16]. In humans, diets high in ω-3 fat were also correlated inversely with diseases such as breast cancer [17,18], bone disease [19,20], obesity [21,22], and diabetes [21,22]. Animal and human studies have shown that dietary fat intake is reflected in adipose tissue composition [16,23-25]. Low ω-3 fat levels in human abdominal adipose tissue [6,7] and in breast [26] and buttocks [27] corresponded to obesity [6,7] and breast cancer [26,27], respectively. Total levels of fat unsaturation are also related inversely to disease in humans, including liver disease [8], obesity [28], breast cancer [1,29], bone disease [3-5,9,10] and diabetes [4,9]. MRS offers a non-invasive method of obtaining such measures. ***The thesis presents optimized MRS techniques to improve relative fat composition quantification in vivo at 9.4 T and at 3 T. The work focused on two aspects of fat composition assessment: enabling relative ω-3 fat quantification, and improving relative measures of total fat unsaturation.***

7.2 Relative ω-3 Fat Quantification

7.2.1 9.4 T MRS

The PRESS sequence was optimized in Chapter 3 to resolve the ω-3 (≈ 1.0 ppm) and non-ω-3 methyl (≈ 0.9 ppm) resonances at 9.4 T, enabling relative % ω-3 content to be estimated Both sets of protons are involved in weak J-coupling interactions at 9.4 T; product operator formalism was used to calculate a theoretical echo time where the methyl multiplets would have 0 in-phase signal from the side peaks, increasing the separation of the two central peaks. PRESS with a TE of 109 ms successfully separated the ω-3 and non-ω-3 methyl resonances, permitting their relative quantification. Mice were fed diets with varying ω-3 fat content (1 %, 9 %, and 16 %) and their fat was collected for GC analysis after MRS scan completion. Comparing the ω-3 fat content obtained with MRS to that obtained using GC yielded an R^2 value of 0.96. An ω-3 fat content of ≈2.4 % was discernible (SNR = 26) using the technique. This was detected in the

control mouse that was fed a standard chow diet. Levels of about 0.9 % ω-3 in the mouse group fed the low ω-3 diet were not detectable with the MRS technique. However, they may have been observable with a higher number of averages or a larger voxel size. The latter is limited by the size of the fat depot in the mouse; a voxel size of 3 x 3 x 3 mm^3 may be largest feasible. The non-invasive methodology can be applied in ω-3 studies of animal models of diet or disease and permits long-term assessments of the models as the animals do not have to be sacrificed to determine their fat composition.

7.2.2 3 T MRS

At 3 T, the two methyl resonances severely overlap; previous spectral editing methods relied on a long TE (540 ms) [30] and difference editing [31] to quantify ω-3 content at 3 T. Chapter 4 demonstrates how optimized PRESS and STEAM sequences at 3 T enable the combined ω-3 (≈ 1.0 ppm) and non-ω-3 methyl (≈ 0.9 ppm) linewidth to correlate to relative ω-3 fatty acid content. The technique exploited the weak coupling evolution of the ω-3 methyl resonance. At the optimized echo times (PRESS and STEAM with a TE of 160 ms), the side multiplets of the ω-3 methyl peak are in-phase and add to the collective methyl linewidth. The efficacy of the technique was verified in oils of varying ω-3 composition. The optimal timings yielded R^2 values ≥ 0.9 when comparing the results obtained using the MRS linewidth at 3 T to the expected composition of the oils obtained from 16.5 T NMR. A limitation of the study is that the technique was illustrated in oils with at least 10 % ω-3 fat content and not in humans, where ω-3 fat content is expected to be about 1 % [32]. However, a study at 1.5 T noted differences in methyl linewidth in breasts of healthy women compared to those with breast cancer [33]. The larger linewidth in healthy breast tissue could potentially be due to a greater amount of ω-3. The research should be extended to determine the limit of ω-3 detectability with the presented linewidth technique.

7.3 Total Fat Unsaturation Measures

7.3.1 Olefinic to Methyl Ratios

Olefinic (≈ 5.4 ppm) to methylene (1.3 ppm) ratios had previously been used for measures of total fat unsaturation [34-39] in tissues where water obstructs the olefinic resonance signal, and also to improve methyl and methylene spectral resolution [31], yielding more consistent and representative results [37,38]. The methyl resonance is present in equivalent amounts in all fatty acids regardless of chain length or degree of unsaturation, rendering it useful for normalization [28]. Chapter 4 describes the technique optimized for measuring relative olefinic to methyl ratios in oils and in tibial bone marrow at 3 T. Using the optimal long echo times (STEAM with a TE of 120 ms and PRESS with a TE of 180 ms) resulted in more representative olefinic to methyl ratios for the oils compared to using short TE (STEAM with a TE of 20 ms and PRESS with a TE of 40 ms). The average percent errors for the short-TE MRS olefinic/methyl measurements versus expected ratios of the oils from 16.5 T NMR were 5.4 % for STEAM and 63.7 % for PRESS. Using the long TEs, the errors were -4.8 % for STEAM and 7.8 % for PRESS. The long TE timings were also optimal in tibial bone marrow *in vivo*, yielding percent errors of -1.8 % (STEAM) and 0.2 % (PRESS) with respect to literature composition of tibial bone marrow. Short TE spectra of tibial bone marrow resulted in sizable larger errors of 9.3 % (STEAM) and 53.5 % (PRESS) compared to the expected values. The optimal long timings yield representative results due to a combination of J-coupling evolution and T_2 relaxation effects. J-coupling evolution is the same in different anatomical regions, but T_2 relaxation values may differ [40]. Chapter 5 determined apparent T_2 relaxation times in tibial bone marrow, subcutaneous, and breast adipose tissue in healthy volunteers. The term apparent is utilized to indicate that measurements include the effects of J-coupling evolution. The objective was to assess if measures of fat unsaturation using the optimized timings in tibial bone marrow could be used for intra-individual comparisons of fat unsaturation with other tissues without correcting for T_2 differences. The research indicated that olefinic, methyl, and methylene proton T_2 relaxation times are not significantly different in the three anatomical regions, with the exception of breast olefinic and tibial bone marrow T_2 times ($p = 0.005$ using a two-tailed test for means). Average breast olefinic apparent T_2 relaxation times were 36.1 ms, 24 % smaller than those of tibial bone marrow (47.8 ms).

Therefore, T_2 corrections should be considered for more accurate comparisons of measures of total fat unsaturation using the optimized long TE methods in breast and tibial bone marrow.

7.3.2 Fat Unsaturation Measures in Different Adipose Tissue

Chapter 5 compared olefinic to methylene ratios as a measure of total fat unsaturation in tibial bone marrow, subcutaneous and breast adipose tissue. No significant differences were found between the three tissues using short TE (PRESS TE = 40 ms) or previously optimized long TE (PRESS TE = 200 ms) spectra. The long TE spectra yielded slightly larger ratios (average of 12.8 % over all three regions) compared to that using short TE (average of 9.6 % over all three regions); likely due to differences in T_2 decay of olefinic and methylene protons and coupling evolution of olefinic protons. Diallylic to methylene ratios (a measure of poly-unsaturation)[34,36,38,41,42] acquired with PRESS with a TE of 40 ms were also studied in the three anatomical regions. The ratios were statistically significantly different in tibial bone marrow compared to subcutaneous ($p = 0.001$) and breast ($p = 0.05$) adipose tissue. Average diallylic to methylene ratios were 1.7 % in tibial bone marrow, 2.2 % in subcutaneous adipose tissue, and 2.3 % in breast adipose tissue. Differences in fat content in different body regions can lead to insights about the role of fats or organs in pathology [41]. A limitation of the work completed in Chapter 5 is the small number of female volunteers for breast adipose tissue measurements (n = 7). It would be beneficial to extend this presented work by investigating further in larger cohorts of volunteers and including other adipose anatomical regions such as liver and spinal bone marrow.

In breast, the water signal significantly overlaps the olefinic peak [2], preventing its quantification and thus measurement of olefinic to methyl or methylene ratios using short TE. Chapter 5 explores using an IR (Inversion Recovery) method for removing the water signal at short TE, providing an alternative to using long TE when T_2 decay is of concern. The T_1 of water was estimated from a water region of the breast of one volunteer as 883 ms, yielding a null time of 613 ms. Using this inversion delay prior to applying a regular PRESS sequence (TE = 40 ms) successfully minimized the water signal, exposing the olefinic peak and enabling its quantification. The IR method yielded an olefinic SNR 5.9 times larger than that obtained using

a long echo time (PRESS TE = 200 ms). The work performed was preliminary and can be expanded by verifying the efficacy of the technique in more volunteers and also expanding its application to other tissues of interest with high water content, such as the liver.

7.3.3 Impact of the Glycerol CH Signal on Olefinic Quantification

The glycerol CH proton at ≈ 5.2 ppm unavoidably overlaps the olefinic proton at ≈ 5.4 ppm at clinical field strengths [43-46], contaminating its quantification for fat unsaturation measures. The significance of the contamination changes with technique and echo time, because of T_2 relaxation and J-coupling evolution of the glycerol CH and olefinic protons, as characterized in Chapter 6 for STEAM and PRESS at 3 T. Furthermore, changes in glycerol CH level with disease can potentially bias olefinic signal variation with disease [47]. In Chapter 6, tricaprylin (a saturated triglyceride containing only glycerol CH protons and no olefinic protons) and oleic acid (a free fatty acid containing only olefinic protons and no glycerol CH protons) were used to assess the response of the glycerol and olefinic protons as a function of STEAM and PRESS TE. STEAM with a TE of 90 ms and PRESS with a TE of 200 ms yielded sufficient olefinic resonance signal (≥ 25 % of signal acquired with short TE) with minimal contamination from the glycerol peak (≤ 5 % of signal acquired with short TE). The estimated contamination of the glycerol peak on the olefinic resonance was ≈ 20 % for STEAM with a TE of 20 ms and ≈ 13 % for PRESS with a TE of 40 ms in tibial bone marrow. A limitation of the work is that the T_2 relaxation is tissue dependent, potentially affecting the optimal timings for minimizing glycerol CH signal.

7.4 Limitations

The work of this thesis demonstrates that optimizing the TE of commonly employed *in-vivo* MRS sequences can enable relative ω-3 fat quantification and improve fat unsaturation measures. Some limitations of this work are addressed in this section.

Optimizations were performed by exploiting J-coupling behavior and considering T_2 relaxation decay. Since the J-coupling relaxation is sequence-dependent, techniques would have to be re-optimized if using a different pulse sequence. The optimizations in this work were performed empirically. A numerical approach could be more efficient once developed; however, while numerical simulations have been widely and successfully applied for predicting the behaviour of the protons of brain metabolites [48-55], their application to fat is challenging due to complex coupling interactions [56,57] that can vary depending on the type of fat [57], and have thus far had limited success [56]. The challenges and future directions with numerical methods are discussed in the next section.

Another limitation that should be addressed is determining thresholds for ω-3 detection with the presented techniques at both 9.4 T and at 3 T. The minimum ω-3 content detectable at 9.4 T was restricted by the size of the mice and the consequent limited voxel size. A limit of ω-3 fat detection was not measured at 3 T. Furthermore, the relative ω-3 fat quantification at 3 T was only performed on phantoms and line broadened to represent expected linewidths in tibial bone marrow; the effect of broader linewidths in different human tissues (such as breast) on the method efficacy was not explored. The methods developed in this research enable quantifying relative total amounts of ω-3 fats, but not separable content of linolenic acid and other types of ω-3 fatty acids.

The optimized sequences use a long TE, yielding signal losses due to T_2 relaxation and J-coupling interactions. Relatively long repetition times and signal averaging result in acquisition times of a few minutes for one spectrum. However, these are general limitations of using *in-vivo* scans and are considered acceptable considering there are no suitable non-invasive alternatives.

7.5 Future Directions

The previous section detailed that the work in this thesis uses empirical methods given the challenges involved with modeling the response of fats. Studies that attempted to model the coupling behaviour of fats were generally limited to fats of only 10 protons [56,58-60], whereas fats in oils [30] and *in-vivo* [32] have in the vicinity of 25- 40 protons. Even for short-chain fatty acids,

discrepancies between modelled and empirical behaviour for some coupling systems were noted [58-60]. Simulations were performed to assess the response of 1-pentene (a 10 proton molecule) to a CPMG (Carr-Purcell-Meiboom-Gill) sequence [58,59], a UDD (Uhrig's dynamical decoupling multipulse echo) sequence [59], and a DIET (Dual Interval Echo Train) sequence [60]. Deviations between the simulations and experimental results were speculated to be caused by stimulated echoes [58-60], lacking precise values for coupling constants [59], differences in T_2 relaxation of fat protons [59], and other effects that were not simulated [58-60]. Another study attempted to model corn oil (a longer chain fatty acid) in response to a fast spin echo sequence and again noted discrepancies with the empirical results, citing imprecise coupling constants, stimulated echo effects, and varying relaxation times of fat protons as possible reasons for the deviations [61]. For the pulse sequences PRESS and STEAM, sources of deviations may primarily be due to incomplete knowledge of the coupling constants in the complex fat molecules [57]. Future work can include validating J-coupling constants and interactions from the literature [62-64] with high-field 2D-NMR of oil samples to potentially enable modelling the response of fats to pulse sequences. Such a model may facilitate optimizing different pulse sequences for ω-3 fat content and fat unsaturation measures and remove the necessity for empirical methods.

The threshold for ω-3 detection at 9.4 T can be potentially enhanced by attempting the optimized method in animals that permit use of a larger fat voxel. Also, using a larger fat voxel would potentially enable measuring the growth of ω-3 fat in adipose tissue with diet over time. In this work, the ω-3 fat content in adipose tissue had already reached a plateau when the mice were large enough to scan. Acquiring additional averages could also enhance the limits of detection at the expense of scanning time. The minimum ω-3 fat content detectable using the method at 3 T was not assessed in this work. This threshold can be determined by forming phantoms with decreasing levels of ω-3 fat content. The efficacy of the 3 T method in samples with broader linewidths should also be explored.

Multi-voxel imaging was not explored in this work. Applying the developed methods in conjunction with a multi-voxel approach could be beneficial, especially since some tumors can be highly heterogeneous [1]. Exploring the optimization of pulse sequences such as LASER (Localized Adiabatic SElective Refocusing) could have potential applications in fat spectroscopy, since LASER uses adiabatic pulses and is thus less sensitive to $\overrightarrow{B_1}$ inhomogeneities

[65]. Moreover, LASER can reduce the effects of J-evolution in fats [65], perhaps providing use in instances where J-coupling evolution is not being exploited as it was in this research.

A potential application of the 9.4 T method presented here is investigating the impact of radiation therapy on fat composition in models of cancer. Studies indicate that fat composition in cancerous tissues differs from benign tissues [29,66] and that fat content may change after cancer radiotherapy treatment [67]. Research revealed that cancer patients have less ω-3 fat in plasma and cell lipids than healthy controls; however, it is unknown if this effect is due to radiotherapy or only the cancer itself [68]. Breast tumor irradiation corresponds to cell signaling pathways in breast tissue [69], and past work has shown that irradiation of *ex-vivo* natural fats preferably causes the destruction of unsaturation content [70], suggesting that changes in ω-3 content could be due to irradiation.

All the work presented in this thesis at 3 T is relevant to the study of disease and diet on pathology. The methods presented for improving fat unsaturation measures and incorporating relative ω-3 fat content can be applied to human studies of diet or pathology, including studying the impact of cancer therapy in cancer patients [67].

7.6 Citations

1. Fardanesh R, Marino MA, Avendano D, Leithner D, Pinker K, Thakur SB. Proton MR spectroscopy in the breast: Technical innovations and clinical applications. J Magn Reson Imaging 2019;50:1033-1046.
2. He Q, Shkarin P, Hooley RJ, Lannin DR, Weinreb JC, Bossuyt VIJ. *In vivo* MR spectroscopic imaging of polyunsaturated fatty acids (PUFA) in healthy and cancerous breast tissues by selective multiple-quantum coherence transfer (Sel-MQC): A preliminary study. Magn Reson Med 2007;58:1079-1085.
3. Yeung DKW, Griffith JF, Antonio GE, Lee FKH, Woo J, Leung PC. Osteoporosis is associated with increased marrow fat content and decreased marrow fat unsaturation: A proton MR spectroscopy study. J Magn Reson Imaging 2005;22:279-285.
4. Karampinos DC, Ruschke S, Dieckmeyer M, et al. Quantitative MRI and spectroscopy of bone marrow. J Magn Reson Imaging 2018;47:332-353.
5. Hu HH, Branca RT, Hernando D, et al. Magnetic resonance imaging of obesity and metabolic disorders: Summary from the 2019 ISMRM Workshop. Magn Reson Med 2020;83:1565-1576.
6. Garaulet M, Hernandez-Morante JJ, Lujan J, Tebar FJ, Zamora S. Relationship between fat cell size and number and fatty acid composition in adipose tissue from different fat depots in overweight/obese humans. Int J Obes 2006;30:899-905.
7. Garaulet M, Pérez-Llamas F, Pérez-Ayala M, et al. Site-specific differences in the fatty acid composition of abdominal adipose tissue in an obese population from a Mediterranean area: relation with dietary fatty acids, plasma lipid profile, serum insulin, and central obesity. Am J Clin Nutr 2001;74:585-591.
8. Johnson NA, Walton DW, Sachinwalla T, et al. Noninvasive assessment of hepatic lipid composition: Advancing understanding and management of fatty liver disorders. Hepatology 2008;47:1513-1523.
9. Cordes C, Baum T, Dieckmeyer M, et al. MR-based assessment of bone marrow fat in osteoporosis, diabetes, and obesity. Front Endocrinol 2016;7:10.3389/fendo.2016.00074 (7 pages).
10. Patsch JM, Li X, Baum T, et al. Bone marrow fat composition as a novel imaging biomarker in postmenopausal women with prevalent fragility fractures. J Bone Miner Res 2013;28:1721-1728.
11. Li Y, Seifert MF, Ney DM, et al. Dietary conjugated linoleic acids alter serum IGF-I and IGF binding protein concentrations and reduce bone formation in rats fed (n-6) or (n-3) fatty acids. J Bone Miner Res 1999;14:1153-1162.
12. Watkins B, Shen C, Adkisson H. Dietary lipids after histomorphometry and concentrations of fatty acids and insulin-like growth factor in chick tibiotarsal bone. The Journal of Nutrition 1996;127:1084-1091.
13. Liu D, Veit HP, Wilson JH, Denbow DM. Long-term supplementation of various dietary lipids alters bone mineral content, mechanical properties, and histological characteristics of Japanese quail. Poult Sci 2003;82:831-839.
14. Robinson LE, Field CJ. Dietary long chain (n-3) fatty acids facilitate immune cell activation in sedentary, but not exercise-trained rats. J Nutr 1998;128:498-504.

15. Henriques VT, Dias CMGC, Franceschini SCC, et al. Omega-3 fatty acids reduce the development of preneoplasic lesions. Rev Nutr 2009;22:237-244.
16. Tou JC, Altman SN, Gigliotti JC, Benedito VA, Cordonier EL. Different sources of omega-3 polyunsaturated fatty acids affects apparent digestibility, tissue deposition, and tissue oxidative stability in growing female rats. Lipids Health Dis 2011;10:179-193.
17. Kaizer LB, N.F., Kriukov V, Tritchler D. Fish consumption and breast cancer risk: an ecological study. Nutr Cancer 1989;12:61-68.
18. Kim J, Lim SY, Shin A, et al. Fatty fish and fish omega-3 fatty acid intakes decrease the breast cancer risk: a case control study. BMC Cancer 2009;9:10.11 186/1471-2407-1479-1216 (11 pages).
19. Elbahnasawy AS, Valeeva ER, El-Sayed EM, Stepanova NV. Protective effect of dietary oils containing omega-3 fatty acids against glucocorticoid-induced osteoporosis. J Nutr Health 2019;52:323-331.
20. Orchard TS, Pan X, Cheek F, Ing SW, Jackson RD. A systematic review of omega-3 fatty acids and osteoporosis. Br J Nutr 2012;107:10.1017/S0007114512001638 (14 pages).
21. Hammad SS, Jones PJ. Dietary fatty acid composition modulates obesity and interacts with obesity-related genes. Lipids 2017;52:803-822.
22. Coelho DF, Pereira-Lancha LO, Chaves DS, et al. Effect of high-fat diets on body composition, lipid metabolism and insulin sensitivity, and the role of exercise on these parameters. Braz J Med Biol Res 2011;44:966-972.
23. Jurešić GC, Percan K, Broznić D. Effect of dietary fatty acid variation on mice adipose tissue lipid content and phospholipid composition. Croat J Food Technol Biotech Nutr 2016;11:128-137.
24. Ouldamer L, Nadal-Desbarats L, Chevalier S, Body G, Goupille C, Bougnoux P. NMR-based lipodomic approach to evaluate controlled dietary intake of lipids in adipose tissue of rat mammary tumor model. J Proteome Res 2016;15:868-878.
25. Field CJ, Clandinin MT. Modulation of adipose tissue fat composition by diet: A review. Nutr Res 1984;4:743-755.
26. Bougnoux P, Koscielny S, Chajès V, Descamps P, Couet C, Calais G. α- Linolenic acid content of adipose breast tissue: a host determinant of the risk of early metastasis in breast cancer. Br J Cancer 1994;70:330-334.
27. Simonsen N, van't Veer P, Strain JJ, et al. Adipose tissue omega-3 and omega-6 fatty acid content and breast cancer in the EURAMIC study. Am J Epidemiol 1998;147:342-352.
28. Machann J, Stefan N, Schabel C, et al. Fraction of unsaturated fatty acids in visceral adipose tissue (VAT) is lower in subjects with high total VAT volume - a combined ^{1}H MRS and volumetric MRI study in male subjects. NMR Biomed 2013;26:232-236.
29. Korteweg MA, Veldhuis WB, Mali WPTM, et al. Investigation of lipid composition of dissected sentinel lymph nodes of breast cancer patients by 7T proton MR spectroscopy. J Magn Reson Imaging 2012;35:387-392.
30. Lundbom J, Heikkinen S, Fielding B, Hakkarainen A, Taskinen M-R, Lundbom N. PRESS echo time behavior of triglyceride resonances at 1.5 T: Detecting ω-3 fatty acids in adipose tissue *in vivo*. J Magn Reson 2009;201:39-47.
31. Škoch A, Jírů F, Dezortová M, et al. Intramyocellular lipid quantification from ^{1}H long echo time spectra at 1.5 and 3 T by means of the LCModel technique. J Magn Reson Imaging 2006;23:728-735.

32. Hodson L, Skeaff CM, Fielding BA. Fatty acid composition of adipose tissue and blood in humans and its use as a biomarker of dietary intake. Prog Lipid Res 2008;47:348-380.
33. Wang J, Wang M-Y, Kuo W-H, Chen K-L, Shih TT-F. Proton MR spectroscopy of normal breasts: Association of risk factors for breast cancer with water and lipid composition of the breast. Magn Reson Imaging 2016;34:524-528.
34. Troitskaia A, Fallone BG, Yahya A. Long echo time proton magnetic resonance spectroscopy for estimating relative measures of lipid unsaturation at 3 T. J Magn Reson Imaging 2013;37:944-949.
35. Bingölbali A, Fallone BG, Yahya A. Comparison of optimized long echo time STEAM and PRESS proton MR spectroscopy of lipid olefinic protons at 3 Tesla. J Magn Reson Imaging 2015;41:481-486.
36. Lundbom J, Hakkarainen A, Söderlund S, Westerbacka J, Lundbom N, Taskinen M-R. Long-TE ^{1}H MRS suggests that liver fat is more saturated than subcutaneous and visceral fat. NMR Biomed 2011;24:238-245.
37. Lundbom J, Bierwagen A, Bodis K, et al. ^{1}H-MRS of femoral red and yellow bone marrow fat composition and water content in healthy young men and women at 3 T. Magn Reson Mater Phy 2019;32:591-597.
38. Lundbom J, Hakkarainen A, Fielding BA, et al. Characterizing human adipose tissue lipids by long echo time ^{1}H-MRS in vivo at 1.5 Tesla: validation by gas chromatography. NMR Biomed 2010;23:466-472.
39. Huovinen V, Viljakainen H, Hakkarainen A, et al. Bone marrow fat unsaturation in young adults is not affected by present or childhood obesity, but increases with age: A pilot study. Metabolism 2015;64:1574-1581.
40. de Bazelaire CMJ, Duhamel GD, Rofsky NM, Alsop DC. MR imaging relaxation times of abdominal and pelvic tissues measured *in vivo* at 3.0 T: Preliminary results Radiology 2004;230:652-659.
41. Machann J, Stefan N, Wagner R, et al. Intra- and interindividual variability of fatty acid unsaturation in six different human adipose tissue compartments assessed by ^{1}H-MRS *in vivo* at 3 T. NMR Biomed 2017;30:e3744 (10 pages).
42. Lundbom J, Bierwagen A, Bodis K, et al. Deep subcutaneous adipose tissue lipid unsaturation associated with intramyocellular lipid content. Metabolism 2016;65:1230-1237.
43. Knothe G, Kenar JA. Determination of the fatty acid profile by ^{1}H-NMR spectroscopy. Eur J Lipid Sci Tech 2004;106:88-96.
44. Vlahov G. Application of NMR to the study of olive oils. Prog Nucl Mag Res Sp 1999;35:341-357.
45. Dimitrov I, Ren J, Sherry D, Malloy C. Fundamental advantages at 7 T allow for fat composition quantification. Medicamundi 2009;53:42-46.
46. Fadzillah NA, Rohman A, Salleh RA, et al. Authentication of butter from lard adulteration using high-resolution of nuclear magnetic resonance spectroscopy and high-performance liquid chromatography. Int J Food Prop 2017;20:2147-2156.
47. Di Pietro G, Capuani S, Manenti G, et al. Bone marrow lipid profiles from peripheral skeleton as potential biomarkers for osteoporosis: A ^{1}H-MR spectroscopy study. Acad Radiol 2016;23:273-283.
48. Kaiser LG, Young K, Matson GB. Numerical simulations of localized high field ^{1}H MR spectroscopy. J Man Reson 2008;195:67-75.

49. Thompson RB, Allen PS. Sources of variability in the response of coupled spins to the PRESS sequence and their potential impact on metabolite quantification. Magn Reson Med 1999;41:1162-1169.
50. Thompson RB, Allen PS. Response of metabolites with coupled spins to the STEAM sequence. Magn Reson Med 2001;45:955-965.
51. Deelchand DK, Iltis I, Henry P-G. Improved quantification precision of human brain short echo-time ^{1}H MRS at high magnetic field: A simulation study. Magn Reson Med 2014;72:20-25.
52. Jalnefjord O, Pettersson P, Ljungberg M. [OA018] Improved absolute metabolite quantification by localized magnetic resonance spectroscopy simulations. Phys Medica 2018;52:7-8.
53. Simpson R, Devenyi GA, Jezzard P, Hennessy TJ, Near J. Advanced processing and simulation of MRS data using the FID appliance (FID-A)—An open source, MATLAB-based toolkit. Magn Reson Med 2017;77:23-33.
54. Kanowski M, Kaufmann J, Braun J, Bernarding J, Tempelmann C. Quantitation of simulated short echo time ^{1} H human brain spectra by LCModel and AMARES. Magn Reson Med 2004;51:904-912.
55. Dobberthein BJ, Tessier AG, Yahya A. Improved resolution of glutamate, glutamine, and γ-aminobutyric acid with optimized point-resolved spectroscopy sequence timings for their simultaneous quantification at 9.4 T. NMR Biomed 2018;31:e3851 (12 pages).
56. Gambarota G. Optimization of metabolite detection by quantum mechanics simulations in magnetic resonance spectroscopy. Anal Biochem 2017;529:65-78.
57. Hamilton G, Middleton MS, Bydder M, et al. Effect of PRESS and STEAM sequences on magnetic resonance spectroscopic liver fat quantification. J Magn Reson Imaging 2009;30:145-152.
58. Stables LA, Kennan RP, Anderson AW, Gore JC. Density matrix simulations of the effects of J coupling in spin echo and fast spin echo imaging J Magn Reson 1999;140:305-314.
59. Stokes A, Feng Y, Mitropoulos T, Warren W. Enhanced refocusing of fat signals using optimized multipulse echo sequences. Magn Reson Med 2013;69:1044-1055.
60. Stables L, Kenna R, Anderson A, Constable R, Gore J. Analysis of J coupling-induced fat suppression in DIET imaging. J Magn Reson 1999;136:143-151.
61. Mulkern RV, Packard AB, Gambarota G. Field dependence of the bright fat effect in fast spin echo imaging: Theory and experiment. Proc Intl Soc Magn Reson Med 2003;11:1107.
62. Oostendorp M, Engelke UFH, Willemsen MAAP, Wevers RA. Diagnosing inborn errors of lipid metabolism with proton nuclear magnetic resonance spectroscopy. Clin Chem 2006;52:1395-1405.
63. Kosugi Y, Matsubara K. Conformational analysis of triacylglycerols by means of Nuclear Magnetic Resonance and Molecular Mechanics. J Jpn Oil Chem Soc 1989;38:415-420.
64. Purcell JM, Morris SG, Susi H. Proton magnetic resonance spectra of unsaturated fatty acids. Anal Chem 1966;38:588-592.
65. Lin M, Kumar A, Yang S. Two-dimensional J-resolved LASER and semi-LASER spectroscopy of human brain. Magn Reson Med 2014;71:911-920.

66. Victor T, Bergman A, Knop R. Detecting fatty acids of dietary origin in normal and cancerous breast tissue by 13C nuclear magnetic resonance spectroscopy. Br J Cancer 1993;68:336-341.
67. Carmona R, Pritz J, Bydder M, et al. Fat composition changes in bone marrow during chemotherapy and radiation therapy. Int J Radiat Oncol 2014;90:155-163.
68. Baracos VE, Mazurak VC, Ma DWL. *n*-3 Polyunsaturated fatty acids throughout the cancer trajectory: influence on disease incidence, progression, response to therapy and cancer-associated cachexia. Nut Res Rev 2004;17:177-192.
69. Meng G, Tang X, Yang Z, et al. Implications for breast cancer treatment from increased autotaxin production in adipose tissue after radiotherapy. FASEB 2017;31:1-15.
70. Hammer C, Wills E. The effect of ionizing radiation on the fatty acid composition of natural fats and on lipid peroxide formation. Int J Radiat Biol Relat Stud Phys Chem Med 1979;35:323-332.

Bibliography

- Machann J, Stefan N, Schabel C, et al. Fraction of unsaturated fatty acids in visceral adipose tissue (VAT) is lower in subjects with high total VAT volume - a combined ^{1}H MRS and volumetric MRI study in male subjects. NMR Biomed 2013;26:232-236.
- Cordes C, Baum T, Dieckmeyer M, et al. MR-based assessment of bone marrow fat in osteoporosis, diabetes, and obesity. Front Endocrinol 2016;7:10.3389/fendo.2016.00074 (7 pages).
- Kumar M, Jagannathan N, Seenu V, Dwivedi S, Julka P, Rath G. Monitoring the therapeutic response of locally advanced breast cancer patients: Sequential *in vivo* proton MR spectroscopy study. J Magn Reson Imaging 2006;24:325-332.
- Korteweg MA, Veldhuis WB, Mali WPTM, et al. Investigation of lipid composition of dissected sentinel lymph nodes of breast cancer patients by 7T proton MR spectroscopy. J Magn Reson Imaging 2012;35:387-392.
- He Q, Shkarin P, Hooley RJ, Lannin DR, Weinreb JC, Bossuyt VIJ. *In vivo* MR spectroscopic imaging of polyunsaturated fatty acids (PUFA) in healthy and cancerous breast tissues by selective multiple-quantum coherence transfer (Sel-MQC): A preliminary study. Magn Reson Med 2007;58:1079-1085.
- Fardanesh R, Marino MA, Avendano D, Leithner D, Pinker K, Thakur SB. Proton MR spectroscopy in the breast: Technical innovations and clinical applications. J Magn Reson Imaging 2019;50:1033-1046.
- Pollesello P, Eriksson O, Höckerstedt K. Analysis of total lipid extracts from human liver by ^{13}C and ^{1}H Nuclear Magnetic Resonance Spectroscopy. Anal Biochem 1996;236:41-48.
- Johnson NA, Walton DW, Sachinwalla T, et al. Noninvasive assessment of hepatic lipid composition: Advancing understanding and management of fatty liver disorders. Hepatology 2008;47:1513-1523.
- Patsch JM, Li X, Baum T, et al. Bone marrow fat composition as a novel imaging biomarker in postmenopausal women with prevalent fragility fractures. J Bone Miner Res 2013;28:1721-1728.
- Yeung DKW, Griffith JF, Antonio GE, Lee FKH, Woo J, Leung PC. Osteoporosis is associated with increased marrow fat content and decreased marrow fat unsaturation: A proton MR spectroscopy study. J Magn Reson Imaging 2005;22:279-285.
- Karampinos DC, Ruschke S, Dieckmeyer M, et al. Quantitative MRI and spectroscopy of bone marrow. J Magn Reson Imaging 2018;47:332-353.
- Oriol A, Valverde D, Capellades J, Cabañas ME, Ribera JM, Arús C. *In vivo* quantification of response to treatment in patients with multiple myeloma by ^{1}H magnetic resonance spectroscopy of bone marrow. Magn Reson Mater Phy 2007;20:93-101.
- Hodson L, Skeaff CM, Fielding BA. Fatty acid composition of adipose tissue and blood in humans and its use as a biomarker of dietary intake. Prog Lipid Res 2008;47:348-380.
- Yeung DKW, Lam SL, Griffith JF, et al. Analysis of bone marrow fatty acid composition using high-resolution proton NMR spectroscopy. Chem Phys Lipids 2008;151:103-109.

- Griffith JF, Yeung DKW, Ahuja AT, et al. A study of bone marrow and subcutaneous fatty acid composition in subjects of varying bone mineral density. Bone 2009;44:1092-1096.
- Ren J, Dimitrov I, Sherry AD, Malloy CR. Composition of adipose tissue and marrow fat in humans by ^{1}H NMR at 7 Tesla. J Lipid Res 2008;49:2055-2062.
- Lundbom J, Hakkarainen A, Fielding BA, et al. Characterizing human adipose tissue lipids by long echo time ^{1}H-MRS in vivo at 1.5 Tesla: validation by gas chromatography. NMR Biomed 2010;23:466-472.
- Lundbom J, Hakkarainen A, Söderlund S, Westerbacka J, Lundbom N, Taskinen M-R. Long-TE ^{1}H MRS suggests that liver fat is more saturated than subcutaneous and visceral fat. NMR Biomed 2011;24:238-245.
- Lundbom J, Bierwagen A, Bodis K, et al. Deep subcutaneous adipose tissue lipid unsaturation associated with intramyocellular lipid content. Metabolism 2016;65:1230-1237.
- Lundbom J, Bierwagen A, Bodis K, et al. ^{1}H-MRS of femoral red and yellow bone marrow fat composition and water content in healthy young men and women at 3 T. Magn Reson Mater Phy 2019;32:591-597.
- Machann J, Stefan N, Schick F. ^{1}H MR spectroscopy of skeletal muscle, liver and bone marrow. Eur J Radiol 2008;67:275-284.
- Machann J, Stefan N, Wagner R, et al. Intra- and interindividual variability of fatty acid unsaturation in six different human adipose tissue compartments assessed by ^{1}H-MRS *in vivo* at 3 T. NMR Biomed 2017;30:e3744 (10 pages).
- Gajdošík M, Hingerl L, Škoch A, et al. Ultralong TE *in vivo* ^{1}H NMR spectroscopy of omega-3 fatty acids in subcutaneous adipose tissue at 7 T. J Magn Reson Imaging 2019;50:71-82.
- Dimitrov IE, Douglas D, Ren J, et al. *In vivo* determination of human breast fat composition by ^{1}H MRS at 7T. Magn Reson Med 2013;67:20-26.
- Tufts LS, Shet K, Liang F, Majumdar S, Li X. Quantification of bone marrow water and lipid composition in anterior cruciate ligament-injured and osteoarthritic knees using three-dimensional magnetic resonance spectroscopic imaging. Magn Reson Imaging 2016;34:632-637.
- Bingölbali A, Fallone BG, Yahya A. Comparison of optimized long echo time STEAM and PRESS proton MR spectroscopy of lipid olefinic protons at 3 Tesla. J Magn Reson Imaging 2015;41:481-486.
- Troitskaia A, Fallone BG, Yahya A. Long echo time proton magnetic resonance spectroscopy for estimating relative measures of lipid unsaturation at 3 T. J Magn Reson Imaging 2013;37:944-949.
- Oostendorp M, Engelke UFH, Willemsen MAAP, Wevers RA. Diagnosing inborn errors of lipid metabolism with proton nuclear magnetic resonance spectroscopy. Clin Chem 2006;52:1395-1405.
- Bottomley PA. Spatial localization in NMR spectroscopy *in vivo*. Ann NY Acad Sci 1987;508:333-348.
- Frahm J, Merboldt K-D, Hänicke W. Localized proton spectroscopy using stimulated echoes. J Magn Reson 1987;72:502-508.
- Ladd ME. Pros and cons of ultra-high-field MRI/MRS for human application. Prog Nucl Mag Res Sp 2018;109:1-50.

- Ocali O, Atalar E. Ultimate intrinsic signal-to-noise ratio in MRI. Magn Reson Med 1989;39:462-473.
- Strobel K, van den Hoff J, Pietzsch J. Localized proton magnetic resonance spectroscopy of lipids in adipose tissue at high spatial resolution in mice *in vivo*. J Lipid Res 2008;49:473-480.
- He D, Mustafi D, Fan X, et al. Magnetic resonance spectroscopy detects differential lipid composition in mammary glands on low fat, high animal fat versus high fructose diets. PLOS ONE 2018;13:e0190929 (12 pages).
- Lee Y, Jee H, Noh H, et al. In vivo ^{1}H-MRS hepatic lipid profiling in nonalcoholic fatty liver disease: an animal study at 9.4 T. Magn Reson Med 2013;70:620-629.
- Yahya A, Tessier AG, Fallone BG. Effect of J-coupling on lipid composition determination with localized proton magnetic resonance spectroscopy at 9.4 T. J Magn Reson Imaging 2011;34:1388-1396.
- Yaligar J, Gopalan V, Wee Kiat O, et al. Evaluation of dietary effects on hepatic lipids in high fat and placebo diet fed rats by *in vivo* MRS and LC-MS techniques. PLOS ONE 2014:0091436 (10 pages).
- de Graaf RA, Klomp DWJ, Luijten PR, Boer VO. Intramolecular zero-quantum-coherence 2D NMR spectroscopy of lipids in the human breast at 7 T. Magn Reson Med 2014;71:451-457.
- Ramamonjisoa N, Ratiney H, Mutel E, et al. *In vivo* hepatic lipid quantification using MRS at 7 Tesla in a mouse model of glycogen storage disease type 1a. J Lipid Res 2013;54:2010-2022.
- Bougnoux P, Koscielny S, Chajès V, Descamps P, Couet C, Calais G. α- Linolenic acid content of adipose breast tissue: a host determinant of the risk of early metastasis in breast cancer. Br J Cancer 1994;70:330-334.
- Lundbom J, Heikkinen S, Fielding B, Hakkarainen A, Taskinen M-R, Lundbom N. PRESS echo time behavior of triglyceride resonances at 1.5 T: Detecting ω-3 fatty acids in adipose tissue *in vivo*. J Magn Reson 2009;201:39-47.
- Škoch A, Tošner Z, Hájek M. The *in vivo* J-difference editing MEGA-PRESS technique for the detection of n-3 fatty acids. NMR Biomed 2014;27:1293-1299.
- Wang J, Wang M-Y, Kuo W-H, Chen K-L, Shih TT-F. Proton MR spectroscopy of normal breasts: Association of risk factors for breast cancer with water and lipid composition of the breast. Magn Reson Imaging 2016;34:524-528.
- Škoch A, Jírů F, Dezortová M, et al. Intramyocellular lipid quantification from ^{1}H long echo time spectra at 1.5 and 3 T by means of the LCModel technique. J Magn Reson Imaging 2006;23:728-735.
- Mosconi E, Fontanella M, Sima DM, et al. Investigation of adipose tissues in Zucker rats using *in vivo* and *ex vivo* magnetic resonance spectroscopy. J Lipid Res 2011;52:330-336.
- Dimitrov I, Ren J, Sherry D, Malloy C. Fundamental advantages at 7 T allow for fat composition quantification. Medicamundi 2009;53:42-46.
- Knothe G, Kenar JA. Determination of the fatty acid profile by ^{1}H-NMR spectroscopy. Eur J Lipid Sci Tech 2004;106:88-96.
- Vlahov G. Application of NMR to the study of olive oils. Prog Nucl Mag Res Sp 1999;35:341-357.
- Viallon M, Leporq B, Drinda S, et al. Chemical-shift-encoded Magnetic Resonance Imaging and Spectroscopy to reveal immediate and long-term multi-organs composition

changes of a 14-days periodic fasting intervention: A technological and case report. Front Nutr 2019;6:1-13.
- Yahya A, Fallone BG. T_2 determination of the J-coupled methyl protons of lipids: *In vivo* illustration with tibial bone marrow at 3T. J Magn Reson Imaging 2010;31:1514-1521.
- Osawa CC, Gonçalves LAG, Ragazzi S. Correlation between free fatty acis of vegetable oils evaluated by rapid tests and by the official method. J Food Compos Anal 2007;20:523-528.
- Mougios V. Exercise biochemistry: Human Kinetics: 2006.
- Fadzillah NA, Rohman A, Salleh RA, et al. Authentication of butter from lard adulteration using high-resolution of nuclear magnetic resonance spectroscopy and high-performance liquid chromatography. Int J Food Prop 2017;20:2147-2156.
- Mundi MS, Koutsari C, Jensen MD. Effects of increased fatty acid availablity on adipose tissue fatty acid storage in men. J Clin Endocrinol Metab 2014;99:E635-E2642.
- Attané C, Estève D, Chaoui K, Schiltz O, Reina N, Muller C. Human bone marrow is comprised of adipocytes with specific lipid metabolism. Cell Reports 2020;30:949-958.
- Ebbert JO, Jensen MD. Fat depots, free fatty acids, and dysipidemia. Nutr 2013;5:498-508.
- Bottomley P. Chapter 1: Basics of NMR. Handbook of Magnetic Resonance Spectroscopy *in vivo*: MRS theory, practice and applications: John Wiley & Sons Ltd; 2016.
- Jensen WB. The origins of the symbols A and Z for atomic weight and number. J Chem Edu 2005;82:1764-1765.
- Constantinides C. Magnetic Resonance Imaging: The basics: CRC Press Taylor Francis Group: 2014.
- Singhal A. The Pearson guide to physical chemistry for the IIT JEE: Pearson India: 2014.
- Pochapsky T, Pochapsky S. NMR for physical and biological scientists: Garland Science Taylor & Francis Group: 2006.
- Krey U, Owen A. Basic theoretical physics: A concise overview: Springer: 2007.
- de Graaf RA. *In vivo* NMR spectroscopy: Principles and techniques. West Sussex PO19 8SQ, England: John Wiley & Sons: 2007.
- Susskind L, Friedman A. Quantum mechanics: the theoretical minimum. New York: Basic Books: 2014.
- Cowan B. Nuclear magnetic resonance and relaxation: Cambridge University Press: 1997.
- Griffiths DJ. Introduction to electrodynamics.: Pearson: 2013.
- Fujita H, T. Z, Yang X, Finnerty MJ, Handa S. RF surface receive array coils: The art of an LC circuit. J Magn Reson Imaging 2013;38:12-25.
- De Zanche N. Birdcage volume coil design. eMagRes 2011: 10.1002/9780470034590/emrstm.9780470031288 (11 pages).
- Elster AD. Questions and Answers in MRI http://mriquestions.com/index.html. 2019.
- Park S-H. MRI Fundamentals. Volume 2021. Department of Bio and Brain Engineering: Korea Advanced Institute of Science and Technology.
- Collins CM. Electromagnetics in magnetic resonance imaging: Physical principles, related applications, and ongoing developments: Morgan & Claypoll Publishers: 2016.
- Hahn EL. Spin echoes. Phys Rev 1950;80:580-602.

- Luo H. Physics-based data analysis for wind turbine condition monitoring. Clean Energy 2017;1:4-22.
- Ordidge RJ, Bendall MR, Gordon RE, Connelly A. Volume selection for *in-vivo* spectroscopy. Magnetic resonance in biology and medicine: Tata McGraw-Hill; 1985.
- Bottomley P. Selective volume method for performing localized NMR spectroscopy. USA; 1984.
- Traber F, Block R, Lamerichs J. ^{1}H metabolite ralxation times at 3.0 Tesla: Measurements of T_1 and T_2 values in normal brain and determination of regional differences in transverse relaxation. J Magn Reson Imaging 2004;19:537-545.
- Helms G. Analysis of 1.5 Tesla proton MR spectra of human brain using LCmodel and an imported basis set. Magn Reson Imaging 1999;17:1211-1218.
- Zhu X, Tomanek B, Sharp J. A pixel is an artifact: On the necessity of zero-filling in fourier imaging. Concepts Magn Reson 2013;42A:32-44.
- Lindon JC, Ferrige AG. Digitisation and data processing in Fourier transform NMR. Prog Nucl Mag Res Sp 1980;14:27-66.
- Barthold E, Ernst RR. Fourier spectroscopy and causality principle. J Magn Reson 1973;11:9-19.
- Balci M. Basic ^{1}H- and ^{13}C- NMR spectroscopy: Elsevier: 2005.
- Harris RK, Lynden-Bell RM. Nuclear magnetic resonance spectoscopy: A physicochemical view: Pitman Publishing: 1983.
- de Graaf R, Rothman D. *In vivo* detection and quantification of scalar coupled ^{1}H NMR resonances. Concepts Magn Reson 2001;13:32-76.
- Keeler J. Chapter 6: Product Operators (from course "Understanding NMR spectroscopy"). University of Cambridge, Department of Chemistry; 2004.
- Goldenberg DP. The Product Operator Formalism: A Physical and Graphical Interpretation. Concepts Magn Reson 2010;36A:49-83.
- Sørensen OW, Eich GW, Levitt MH, Bodenhausen G, Ernst RR. Product operator formalism for the description of NMR pulse experiments. Prog Nucl Mag Res Sp 1983;16:163-192.
- Kay LE, McClung RED. A product operator description of AB and ABX spin systems. J Magn Reson 1988;77:258-273.
- Wilman A, Allen P. The response of the strongly coupled AB system of citrate to typical ^{1}H MRS localization sequences. J Magn Reson B 1995;107:25-33.
- Thompson RB, Allen PS. Response of metabolites with coupled spins to the STEAM sequence. Magn Reson Med 2001;45:955-965.
- Wilman A, Allen P. Observing N-acetyl aspartate via both its N-acetyl and its strongly coupled aspartate groups in *in-vivo* proton Magnetic Resonance Spectroscopy. J Magn Reson B 1996;113:203-213.
- Hamilton G, Middleton MS, Bydder M, et al. Effect of PRESS and STEAM sequences on magnetic resonance spectroscopic liver fat quantification. J Magn Reson Imaging 2009;30:145-152.
- Stables L, Kenna R, Anderson A, Constable R, Gore J. Analysis of J coupling-induced fat suppression in DIET imaging. J Magn Reson 1999;136:143-151.
- Thompson RB, Allen PS. Sources of variability in the response of coupled spins to the PRESS sequence and their potential impact on metabolite quantification. Magn Reson Med 1999;41:1162-1169.

- Yablonskiy DA, Neil JJ, Raichle ME, Ackerman JJ. Homonuclear J coupling effects in volume localized NMR spectroscopy: pitfalls and solutions. Magn Reson Med 1998;39:169-178.
- Snyder J, Wilman A. Field strength dependence of PRESS timings for simultaneous detection of glutamate and glutamine from 1.5 to 7 T. J Magn Reson 2010;203:66-72.
- Hoult DI, Richards RE. The signal-to-noise ratio of the nuclear magnetic resonance experiment. J Magn Reson Imaging 1976;24:71-85.
- Hoult D, Lauterbur PC. The sensitivity of the zeugmatographic experiment involving human samples. J Magn Reson 1979;34:341-344.
- National Academic Press (US). Fats and other lipids. Diet and health: Implications for reducing chronic disease risk; 1989.
- IUPAC-IUB Commission on Biochemical Nomenclature (CBN). The nomenclature of lipids. Eur J Biochem 1977;79:11-21.
- Guillén MD, Ruiz A. High resolution ^{1}H nuclear magnetic resonance in the study of edible oils and fats. Trends Food Sci Technol 2001;12:328-338.
- Fairgrieve-Park L, Fallone CJ, Yahya A. Long TE PRESS and STEAM for measuring the triglyceride glycerol CH_2 protons at 3 T NMR Biomed 2018;32:e4021 (8 pages).
- Kosugi Y, Matsubara K. Conformational analysis of triacylglycerols by means of Nuclear Magnetic Resonance and Molecular Mechanics. J Jpn Oil Chem Soc 1989;38:415-420.
- Stokes A, Feng Y, Mitropoulos T, Warren W. Enhanced refocusing of fat signals using optimized multipulse echo sequences. Magn Reson Med 2013;69:1044-1055.
- Purcell JM, Morris SG, Susi H. Proton magnetic resonance spectra of unsaturated fatty acids. Anal Chem 1966;38:588-592.
- Ansorge R, Graves M. The physics and mathematics of MRI: Morgan & Claypool Publishers: 2016.
- Glover GH, Hayes CE, Pelc NJ, et al. Comparison of linear and circular polarization for Magnetic Resonance Imaging. J Magn Reson 1985;64:225-270.
- Dietrich O, Raya JG, Reeder SB, Reiser MF, Schoenberg S. Measurement of signal-to-noise ratios in MR images: Influence of multichannel coils, parallel imaging, and reconstruction filters. J Magn Reson Imaging 2007;26:375-385.
- Hoult D. The principle of reciprocity in signal strength calculations: A mathematical guide. Concepts Magn Reson 2000;12:173-187.
- Gruber B, Froeling M, Leiner T, Klomp DWJ. RF coils: a practical guide for nonphysicists. J Magn Reson Imaging 2018;48:590-604.
- Johnson JB. Thermal agitation of electricity in conductors. Nature 1927;119:50-51.
- Nyquist H. Thermal agitation of electric charge in conductors. Phys Rev 1928;32:110-113.
- Niederländer B, Blümler P. Simple eddy current compensation by additional gradient pulses. Concepts Magn Reson 2018;47A:e21469 (7 pages).
- Burl M, Young IR. Eddy currents and their control. eMagRes 2007:https://doi.org/10.1002/9780470034590.emrstm9780470030147.
- Canadian Council on Animal Care. Guidelines. https://www.ccac.ca/en/standards/guidelines/. Accessed March 2020.
- Folch J, Lees M, Stanley GHS. A simple method for the isolation and purification of total lipides from animal tissues. J Biol Chem 1957;226:497-509.

- Field CJ, Ryan EA, Thomson ABR, Clandinin MT. Dietary fat and and the diabetic state alter insulin binding and the fatty acyl composition of the adipocyte plasma membrane. Biochem J 1988;253:417-424.
- Cruz-Hernandez C, Goeuriot S, Giuffrida F, Thakkar SK, Destaillats F. Direct quantification of fatty acids in human milk by gas chromatography. J Chromatogr A 2013;1284:174-179.
- Shen J, Rycyna RE, Rothman DL. Improvements on an *in vivo* automatic shimming method [FASTERMAP]. Magn Reson Med 1997;38:834-839.
- Philips. Application Guide Spectroscopy. Volume 4: Achieva Release 3.2 Series.
- Provencher SW. Estimation of metabolite concentrations from localized *in vivo* proton NMR spectra. Magn Reson Med 1993;30:672-679.
- Provencher SW. A constrained regularization method for inverting data represented by linear algebraic or integral equations. Comput Phys Commun 1982;27:213-227.
- Prautzsch H, Boehm W, Paluszny M. Bézier and B-spline techniques: Springer-Verlag 2002.
- Provencher S. LCModel & LCMgui User's Manual. 2018.
- Cavassila S, Deval S, Huegen C, Van Ormondt D, Graveron-Demilly D. Cramér- Rao bounds: an evaluation tool for quantitation. NMR Biomed 2001;14:278-283.
- Kreis R. The trouble with quality filtering based on relative Cramér-Rao lower bounds Magn Reson Med 2016;75:15-18.
- Heo H, S. K, Lee HH, et al. On the utility of short echo time (TE) single voxel ^{1}H–MRS in non–invasive detection of 2–hydroxyglutarate (2HG); Challenges and potential improvement illustrated with animal models using MRUI and LCModel. PLOS ONE 2016;11:e0147794 (18 pages).
- Garaulet M, Hernandez-Morante JJ, Lujan J, Tebar FJ, Zamora S. Relationship between fat cell size and number and fatty acid composition in adipose tissue from different fat depots in overweight/obese humans. Int J Obes 2006;30:899-905.
- Garaulet M, Pérez-Llamas F, Pérez-Ayala M, et al. Site-specific differences in the fatty acid composition of abdominal adipose tissue in an obese population from a Mediterranean area: relation with dietary fatty acids, plasma lipid profile, serum insulin, and central obesity. Am J Clin Nutr 2001;74:585-591.
- Calderan L, Marzola P, Nicolato E, et al. *In vivo* phenotyping of the ob/ob mouse by magnetic resonance imaging and ^{1}H-magnetic resonance spectroscopy. Obesity 2006;14:405-414.
- Chen Y, Jiang Z, Long L, et al. Magnetic Resonance Imaging: Proton density fat fraction for assessment of pancreatic fatty infiltration during progression of T2DM Bama Minipigs. J Magn Reson Imaging 2019;50:1905-1913.
- Hu HH, Branca RT, Hernando D, et al. Magnetic resonance imaging of obesity and metabolic disorders: Summary from the 2019 ISMRM Workshop. Magn Reson Med 2020;83:1565-1576.
- Wang L, Salibi N, Chang G, et al. Assessment of subchondral bone marrow lipids in healthy controls and mild osteoarthritis patients at 3T. NMR Biomed 2011;25:545-555.
- Coelho DF, Pereira-Lancha LO, Chaves DS, et al. Effect of high-fat diets on body composition, lipid metabolism and insulin sensitivity, and the role of exercise on these parameters. Braz J Med Biol Res 2011;44:966-972.

- Hammad SS, Jones PJ. Dietary fatty acid composition modulates obesity and interacts with obesity-related genes. Lipids 2017;52:803-822.
- Orchard TS, Pan X, Cheek F, Ing SW, Jackson RD. A systematic review of omega-3 fatty acids and osteoporosis. Br J Nutr 2012;107:10.1017/S0007114512001638 (14 pages).
- Elbahnasawy AS, Valeeva ER, El-Sayed EM, Stepanova NV. Protective effect of dietary oils containing omega-3 fatty acids against glucocorticoid-induced osteoporosis. J Nutr Health 2019;52:323-331.
- Kaizer LB, N.F., Kriukov V, Tritchler D. Fish consumption and breast cancer risk: an ecological study. Nutr Cancer 1989;12:61-68.
- Kim J, Lim SY, Shin A, et al. Fatty fish and fish omega-3 fatty acid intakes decrease the breast cancer risk: a case control study. BMC Cancer 2009;9:10.11 186/1471-2407-1479-1216 (11 pages).
- McGlory C, Calder PC, Nunes EA. The influence of omega-3 fatty acids on skeletal muscle protein turnover in health, disuse, and disease. Front Nutr 2019;6:10.3389/fnut.2019.00144 (13 pages).
- Baracos VE, Mazurak VC, Ma DWL. *n*-3 Polyunsaturated fatty acids throughout the cancer trajectory: influence on disease incidence, progression, response to therapy and cancer-associated cachexia. Nut Res Rev 2004;17:177-192.
- Simonsen N, van't Veer P, Strain JJ, et al. Adipose tissue omega-3 and omega-6 fatty acid content and breast cancer in the EURAMIC study. Am J Epidemiol 1998;147:342-352.
- Högström M, Nordström P, Nordström A. n-3 Fatty acids are positively associated with peak bone mineral density and bone accrual in healthy men: the NO_2 study. Am J Clin Nutr 2007;85:803-807.
- Albert BB, Derraik JGB, Brennan CM, et al. Higher omega-3 index is associated with increased insulin sensitivity and more favourable metabolic profile in middle-aged overweight men. Sci Rep 2014;4:10.1038/srep06697 (7 pages).
- Tou JC, Altman SN, Gigliotti JC, Benedito VA, Cordonier EL. Different sources of omega-3 polyunsaturated fatty acids affects apparent digestibility, tissue deposition, and tissue oxidative stability in growing female rats. Lipids Health Dis 2011;10:179-193.
- Jurešić GC, Percan K, Broznić D. Effect of dietary fatty acid variation on mice adipose tissue lipid content and phospholipid composition. Croat J Food Technol Biotech Nutr 2016;11:128-137.
- Lau BY, Fajardo VA, McMeekin L, et al. Influence of high-fat diet from differential dietary sources on bone mineral density, bone strength, and bone fatty acid composition in rats. Appl Physiol Nutr Metab 2010;35:598-606.
- Field CJ, Clandinin MT. Modulation of adipose tissue fat composition by diet: A review. Nutr Res 1984;4:743-755.
- Lindeboom L, de Graaf RA. Measurement of lipid composition in human skeletal muscle and adipose tissue with ^{1}H-MRS homonuclear spectral editing. Magn Reson Med 2018;79:619-627.
- Coum A, Ouldamer L, Noury F, et al. *In vivo* MR spectroscopy of human breast tissue: quantification of fatty acid composition at a clinical field strength (3 T). Magn Reson Mater Phy 2016;29:1-4.
- Hamilton G, Schlein AN, Middleton MS, et al. *In vivo* triglyceride composition of abdominal aipose tissue measured by ^{1}H MRS at 3T. J Magn Reson Imaging 2017;45:1455-1463.

- Peterson P, Trinh L, Må nsson S. Quantitative ^{1}H MRI and MRS of fatty acid composition. Magn Reson Med 2020;85:49-67.
- Fallone CJ, McKay RT, Yahya A. Long TE STEAM and PRESS for estimating fat olefinic/methyl ratios and relative ω-3 fat content at 3T. J Magn Reson Imaging 2018;48:169-177.
- Robinson LE, Field CJ. Dietary long chain (n-3) fatty acids facilitate immune cell activation in sedentary, but not exercise-trained rats. J Nutr 1998;128:498-504.
- Lab Supply. Picolab Rodent Diet 20. Accessed March 1 2020. https://www.labsupplytx.com/labdiet/picolab-rodent-diet-20/.
- Brief EE, Whittall KP, Li DKB, MacKay AL. Proton T_2 relaxation of cerebral metabolites of normal human brain over large TE range. NMR Biomed 2005;18:14-18.
- Ouldamer L, Nadal-Desbarats L, Chevalier S, Body G, Goupille C, Bougnoux P. NMR-based lipodomic approach to evaluate controlled dietary intake of lipids in adipose tissue of rat mammary tumor model. J Proteome Res 2016;15:868-878.
- Crémillieux Y, Dumont U, Mazuel L, et al. Online quantification of lactate concentration in microdialysate during cerebral activation using ^{1}H-MRS and sensitive NMR microcoil. Front Cell Neurosci 2019;13:10.3389/fncel.2019.00089 (8 pages).
- Huovinen V, Viljakainen H, Hakkarainen A, et al. Bone marrow fat unsaturation in young adults is not affected by present or childhood obesity, but increases with age: A pilot study. Metabolism 2015;64:1574-1581.
- Al-Nouri DM, Al-Khalifa AS, Shahidi F. Long-term supplementation of dietary omega-6/omega-3 ratios alters bone marrow fatty acid and biomarkers of bone metabolism in growing rabbits. J Funct Foods 2012;4:584-593.
- Lau BYY, Cohen DJA, Ward WE, Ma DWL. Investigating the role of polyunsaturated fatty acids in bone development using animal models. Molecules 2013;18:14203-14227.
- Li Y, Seifert MF, Lim SY, Salem NJ, Watkins BA. Bone mineral content is positively correlated to *n-3* fatty acids in the femur of growing rats. Br J Nutr 2010;104:674-685.
- Liu D, Veit HP, Wilson JH, Denbow DM. Long-term supplementation of various dietary lipids alters bone mineral content, mechanical properties, and histological characteristics of Japanese quail. Poult Sci 2003;82:831-839.
- Li Y, Seifert MF, Ney DM, et al. Dietary conjugated linoleic acids alter serum IGF-I and IGF binding protein concentrations and reduce bone formation in rats fed (n-6) or (n-3) fatty acids. J Bone Miner Res 1999;14:1153-1162.
- Shen J, Rycyna RE, Rothman DL. Improvements on an in vivo automatic shimming method (FASTERMAP). Magn Reson Med 1997;38:834-839.
- Guillén MD, Ruiz A. Rapid simultaneous determination by proton NMR of unsaturation and composition of acyl groups in vegetable oils. Eur J Lipid Sci Technol 2003;105:688-696.
- Ramadan S, Ratai E-M, Wald LL, Mountford CE. *In vivo* 1D and 2D correlation MR spectroscopy of the soleus muscle at 7 T. J Magn Reson 2010;204:91-98.
- Elizondo A, Araya J, Rodrigo R, et al. Polyunsaturated fatty acid pattern in liver and erythrocyte phospholipids from obese patients. Obesity 2007;15:24-31.
- Parker HM, Johnson NA, Burdon CA, Cohn JS, O'Connor HT, George J. Omega-3 supplementation and non-alcoholic fatty liver disease: A systematic review and meta-analysis. J Hepatol 2012;56:944-951.

- Petrus P, Rosqvist F, Edholm D, et al. Saturated fatty acids in human visceral adipose tissue are associated with increased 11-β-hydroxysteroid-dehydrogenase type 1 expression. Lipids Health Dis 2015;14:42-46.
- Velan SS, Said N, Durst C, et al. Distinct patterns of fat metabolism in skeletal muscle of normal-weight, overweight, and obese humans. Am J Physiol Regul Integr Comp Physiol 2008;295:R1060-R1065.
- Andersson A, Nälsén C, Tengblad S, Vessby B. Fatty acid composition of skeletal muscle reflects dietary fat composition in humans. Am J Clin Nutr 2002;76:1222-1229.
- Rodacki CLN, Rodacki ALF, Pereira G, et al. Fish-oil supplementation enhances the effects of strength training in elderly women. Am J Clin Nutr 2012;95:428-436.
- Smith GI, Julliand S, Reeds DN, Sinacore DR, Klein S, Mittendorfer B. Fish oil-derived *n-3* PUFA therapy increases muscle mass and function in healthy older adults. Am J Clin Nutr 2015;102:115-122.
- Gajdošík M, Chadzynski GL, Hangel G, et al. Ultrashort-TE stimulated echo acquisition mode (STEAM) improves the quantification of lipids and fatty acid chain unsaturation in the human liver at 7 T. NMR Biomed 2015;28:1283-1293.
- Laaksonen DE, Nuutinen J, Lahtinen T, Rissanen A, Niskanen LK. Changes in abdominal subcutaneous fat water content with rapid weight loss and long-term weight maintenance in abdominally obese men and women. Int J Obes 2003;27:677-683.
- Querleux B, Cornillon C, Jolivet O, Bittoun J. Anatomy and physiology of subcutaneous adipose tissue by in vivo magnetic resonance imaging and spectroscopy: Relationships with sex and presence of cellulite. Skin Res Technol 2002;8:118-124.
- de Bazelaire CMJ, Duhamel GD, Rofsky NM, Alsop DC. MR imaging relaxation times of abdominal and pelvic tissues measured *in vivo* at 3.0 T: Preliminary results Radiology 2004;230:652-659.
- Robinson MD, Cistola DP. Nanofluidity of fatty acid hydrocarbons as monitored by benchtop time-domain nuclear magnetic resonance. Biochem 2014;53:7515-7522.
- Peterson P, Månsson S. Simultaneous quantification of fat content and fatty acid composition using MR imaging. Magn Reson Med 2013;69:688-697.
- Breitkreutz DY, Fallone BG, Yahya A. Effect of *J* coupling on 1.3-ppm lipid methylene signal acquired with localised proton MRS at 3T. NMR Biomed 2015;28:1324-1331.
- Rakow-Penner R, Daniel B, Yu H, Sawyer-Glover A, Glover GH. Relaxation times of breast tissue at 1.5T and 3T measured using IDEAL. J Magn Reson Imaging 2006;23:87-91.
- Fallone CJ, Yahya A. Effect of triglyceride glycerol CH signal on olefinic resonance quantification with proton magnetic resonance spectroscopy at 3 T. Biomed Phys Eng Express 2019;5:027004 (10 pages).
- Hancu I, Govenkar A, Lenkinski RE, Lee S-K. On shimming approaches in 3T breast MRI. Magn Reson Med 2013;69:862-867.
- Maril N, Collins CM, Greenman RL, Lenkinski RE. Strategies for shimming the breast. Magn Reson Med 2005;54:1139-1145.
- Hernando D, Karampinos DC, King KF, et al. Removal of olefinic fat chemical shift artifact in diffusion MRI. Magn Reson Med 2011;65:692-701.
- Ohno N, Miyati T, Suzuki S, et al. Hybrid quantitative MRI using chemical shift displacement and recovery-based simultaneous water and lipid imaging: A preliminary study. Magn Reson Imaging 2018;50:61-67.

- Del Grande F, Santini F, Herzka DA, et al. Fat-suppression techniques for 3-T MR imaging of the musculoskeletal system. Radiographics 2014;34:217-233.
- Ma Y-J, Zhu Y, Lu X, Carl M, Chang EY, Du J. Short T_2 imaging using a 3D double adiabatic inversion recovery prepared ultrashort echo time cones (3D DIR-UTE-Cones) sequence. Magn Reson Med 2018;79:2555-2563.
- Du J, Takahashi AM, Bae WC, Chung CB, Bydder GM. Dual Inversion Recovery, Ultrashort Echo Time (DIR UTE) imaging: Creating high contrast for short-T_2 species. Magn Reson Med 2010;63:447-455.
- Yu H, Shimakawa A, McKenzie CA, Brodsky E, Brittain JH, Reeder SB. Multiecho water-fat separation and simultaneous R2* estimation with multifrequency fat spectrum modeling. Magn Reson Med 2008;60:1122-1134.
- Di Pietro G, Capuani S, Manenti G, et al. Bone marrow lipid profiles from peripheral skeleton as potential biomarkers for osteoporosis: A ^{1}H-MR spectroscopy study. Acad Radiol 2016;23:273-283.
- Eichmann TO, Kumari M, Haas JT, et al. Studies on the substrate and stereo/regioselectivity of adipose triglyceride lipase, hormone-sensitive lipase, and diacylglycerol-*O*-acyltransferases. J Biol Chem 2012;287:41446-41457.
- Gouw TH, Vlugter JC. Physical properties of triglycerides. I. Density and refractive index. Fett Wiss Technol 1966;7:544-549.
- Johnson WJ, Cosmetic Ingredient Review Expert Panel. Final report on the safety assessment of trilaurin, triarachidin, tribehenin, tricaprin, tricaprylin, trierucin, triheptanoin, triheptylundecanoin, triisononanoin, triisopalmitin, triisostearin, trilinolein, trimyristin, trioctanoin, triolein, tripalmitin, tripalmitolein, triricinolein, tristearin, triundecanoin, glyceryl triacetyl hydroxystearate, glyceryl triacetyl ricinoleate, and glyceryl stearate diacetate. Int J Toxicol 2001;20:61-94.
- Bernardo-Gil G, Esquível M, Ribeiro A. Densities and refractive indices of pure organic acids as a function of temperature. J Chem Eng Data 1990;35:202-204.
- Sales-Cruz M, Aca-Aca G, Sánchez-Daza O, López-Arenas T. Predicting critical properties, density and viscosity of fatty acids, triacylglycerols and methyl esters by group contribution methods. In: Pierucci S, Buzzi Ferraris G, editors. 20th European Symposium on Computer Aided Process Engineering; 2010.
- Kostik V, Memeti S, Bauer B. Fatty acid composition of edible oils and fats. J Hyg Eng Des 2013;4:112-116.
- Orsavova J, Misurcova L, Ambrozova JV, Vicha R, Mlcek J. Fatty acids composition of vegetable oils and its contribution to dietary energy intake and dependence of cardiovascular mortality on dietary intake of fatty acids. Int J Mol Sci 2015;16:12871-12890.
- Roncero JM, Álvarez-Ortí M, Pardo-Giménez A, Gómez R, Rabadán A, Pardo JE. Virgin almond oil: Extraction methods and composition. Grasas Aceites 2016;67:e143 (10 pages).
- Bayrak A, Kiralan M, Ipek A, Arslan N, Cosge B, Khawar KM. Fatty acid compositions of linseed (*Linum Usitatissimum* L.) genotypes of different origin cultivated in Turkey. Biotechnol & Biotechnol Eq 2010;24:1836-1842.
- Tsamouris G, Hatziantoniou S, Demetzos C. Lipid analysis of Greek walnut oil (*Juglans regia* L.). Z Naturforsch 2002;57:51-56.

- Watkins B, Shen C, Adkisson H. Dietary lipids after histomorphometry and concentrations of fatty acids and insulin-like growth factor in chick tibiotarsal bone. The Journal of Nutrition 1996;127:1084-1091.
- Henriques VT, Dias CMGC, Franceschini SCC, et al. Omega-3 fatty acids reduce the development of preneoplasic lesions. Rev Nutr 2009;22:237-244.
- Kaiser LG, Young K, Matson GB. Numerical simulations of localized high field ^{1}H MR spectroscopy. J Man Reson 2008;195:67-75.
- Deelchand DK, Iltis I, Henry P-G. Improved quantification precision of human brain short echo-time ^{1}H MRS at high magnetic field: A simulation study. Magn Reson Med 2014;72:20-25.
- Jalnefjord O, Pettersson P, Ljungberg M. [OA018] Improved absolute metabolite quantification by localized magnetic resonance spectroscopy simulations. Phys Medica 2018;52:7-8.
- Simpson R, Devenyi GA, Jezzard P, Hennessy TJ, Near J. Advanced processing and simulation of MRS data using the FID appliance (FID-A)—An open source, MATLAB-based toolkit. Magn Reson Med 2017;77:23-33.
- Kanowski M, Kaufmann J, Braun J, Bernarding J, Tempelmann C. Quantitation of simulated short echo time ^{1} H human brain spectra by LCModel and AMARES. Magn Reson Med 2004;51:904-912.
- Dobberthein BJ, Tessier AG, Yahya A. Improved resolution of glutamate, glutamine, and γ-aminobutyric acid with optimized point-resolved spectroscopy sequence timings for their simultaneous quantification at 9.4 T. NMR Biomed 2018;31:e3851 (12 pages).
- Gambarota G. Optimization of metabolite detection by quantum mechanics simulations in magnetic resonance spectroscopy. Anal Biochem 2017;529:65-78.
- Stables LA, Kennan RP, Anderson AW, Gore JC. Density matrix simulations of the effects of J coupling in spin echo and fast spin echo imaging J Magn Reson 1999;140:305-314.
- Mulkern RV, Packard AB, Gambarota G. Field dependence of the bright fat effect in fast spin echo imaging: Theory and experiment. Proc Intl Soc Magn Reson Med 2003;11:1107.
- Lin M, Kumar A, Yang S. Two-dimensional J-resolved LASER and semi-LASER spectroscopy of human brain. Magn Reson Med 2014;71:911-920.
- Victor T, Bergman A, Knop R. Detecting fatty acids of dietary origin in normal and cancerous breast tissue by 13C nuclear magnetic resonance spectroscopy. Br J Cancer 1993;68:336-341.
- Carmona R, Pritz J, Bydder M, et al. Fat composition changes in bone marrow during chemotherapy and radiation therapy. Int J Radiat Oncol 2014;90:155-163.
- Meng G, Tang X, Yang Z, et al. Implications for breast cancer treatment from increased autotaxin production in adipose tissue after radiotherapy. FASEB 2017;31:1-15.
- Hammer C, Wills E. The effect of ionizing radiation on the fatty acid composition of natural fats and on lipid peroxide formation. Int J Radiat Biol Relat Stud Phys Chem Med 1979;35:323-332.